Impact-induced phase transformations in elastic solids: a continuum study including numerical simulations for GeO_2

Thesis by
Nancy A. Winfree

In Partial Fulfillment of the Requirements
for the Degree of
Doctor of Philosophy

California Institute of Technology
Pasadena, California

1999

(Defended May 13, 1999)

Acknowledgements

It has been a great privilege to have Jim Knowles as my advisor. His guidance and encouragement have been unyielding. I strive for clarity like his in reasoning and communication. I thank Jim's wife, Jackie Knowles, for the lifetime of support she has provided to him and his students.

It has been a privilege also to work with Tom Ahrens, with whom we have collaborated on this research.

I am grateful to Kalisam Iyer and the Army Research Office for funding this work. I also acknowledge, with sincere appreciation, fellowships from the A.R.C.S. Foundation, the Earle C. Anthony Foundation, the Charles Lee Powell Foundation, and a Scholarship from the American Association of University Women.

Applied Research Associates, Inc., has been gracious in employing me during the final months of my dissertation, and has been supportive as those months turned into a year. Thanks to my colleagues there for their encouragement, and to Dennis Grady for his mentoring.

Kaushik Bhattacharya, Narendra Simha, and Lev Truskinovsky have provided advice and friendship. Tom Hou, James Quirk, and Stewart Silling provided much-needed and greatly appreciated guidance on numerical methods.

Amongst many warm friendships at Caltech, those with Ceca Tatic-Lucic, Mark Duttweiler, Anders Carlson and Ho Seon Shin and his family are especially treasured. I am grateful for bonds with my advisor's recent students, Mark Lusk, Allan Zhong and Sergio Turteltaub.

I am forever thankful for the loving care our children received from the wonderful people of the Children's Center at Caltech, and for the unique environment and outstanding teaching that our older child experienced at The Sequoyah School.

My parents Lela and Clarence have been highly supportive, as have my parents-in-law Maria and Dominic, and the rest of my extended family. A special thanks to my brother-in-law Vianney for the balance he brings to our lives.

Above all, I am thankful for the steadfast support of my husband, Joe Kang, and our children, Dominique and Bianca Kang.

Impact-induced phase transformations in elastic solids: a continuum study including numerical simulations for GeO_2

by

Nancy A. Winfree

In Partial Fulfillment of the
Requirements for the Degree of
Doctor of Philosophy

Abstract

This thesis applies recently developed continuum theories of diffusionless phase transformations in solids to the study of impact problems involving materials which can experience such phase changes. Our objective is to compare the theoretical predictions against certain experimental results.

In the experiments of interest, a face-to-face impact occurs between a disk of amorphous germanium dioxide and another material, either tungsten or an aluminum alloy. The GeO_2 is believed to transform to another phase if sufficient compressive stress is achieved.

We model these experiments using one-dimensional finite elasticity. Phase-changing materials are represented by non-convex potential energy functions. This can produce phase boundaries that propagate *subsonically* or *supersonically* with respect to the slower longitudinal wave speed of the two phases. When a subsonic phase boundary is possible, it is not uniquely determined by the fundamental field equations and jump conditions. Uniqueness is obtained by invoking a *nucleation criterion* to control the initiation of the new phase, and a *kinetic relation* to govern

its evolution.

The experiments considered here are sufficiently long in duration (≈ 3 μs) that several reflections and wave interactions occur, and the analysis becomes analytically intractable. Accordingly, a finite-difference method of Godunov type is employed to analyze these experiments numerically. Methods of Godunov type treat adjoining discretized spatial elements as the two sides of a Riemann problem, which is typically solved *approximately* by linearizing around the initial conditions on each side. Fortuitously, all constitutive models employed in this thesis are such that the required Riemann problems can be solved *exactly* without too much effort.

Simulations utilizing the numerical method demonstrate that the impact response of a material is sensitive to the kinetic relation that enters the model. It appears the theory may offer a plausible description of the experiments, though the restrictions placed on the constitutive models herein seem too severe to provide a good quantitative match to the experimental results.

Contents

List of Figures

List of Tables

Chapter 1

Introduction

In 1975, J. L. Ericksen published *Equilibrium of Bars* [31]; the droll title belies this paper's considerable influence on mechanicians and mathematicians over the ensuing two decades.

Ericksen considered classical equilibrium problems: load controlled or displacement controlled deformations of a one-dimensional bar of elastic material. The elastic material he employed is characterized by a non-monotonic stress-strain curve; continuum mechanicians often excluded such constitutive functions as physically unreasonable, but Ericksen emphasized their connection to displacive phase transformations. With this non-monotonic stress-strain curve, there is a range of loads over which the bar may exist in either of two states of uniform strain; solutions to load controlled problems are thus non-unique. Solutions to the displacement controlled problems are also non-unique, because the bar can achieve a given overall elongation through an infinite combination of spatial intervals that alternate between two phases.

Mechanicians thrive on nonuniqueness.

Thus commenced a storm of theoretical exploration into the mechanics of solids with non-monotonic stress-strain curves. Such *up-down-up* stress-strain curves are natural models of solids which transform between two phases by the application of prescribed stress or deformation. Early work was largely motivated by shape memory alloys, the remarkable properties of which depend upon transformations

between high and low temperature phases; the material displacively transforms from one phase variant to another in response to the loading upon it. These alloys return to their original configuration upon heating above a critical temperature at which they displacively transform back to the high-temperature phase.

There are now models of solid-solid phase transformations which consider both elastic and thermal effects [3,8–10], investigations of multiple losses of monotonicity in the stress-strain curve [1, 100], treatments of stress-strain curves that suffer a change in the sign of the curvature but remain monotonic [78, 98], considerations of surface energy effects at phase interfaces [62], and advances in modeling ferroelectric materials [52]. The theory has even suggested the possibility of developing magnetostrictive materials with far larger mechanical responses than those available today [48, 49, 96]. An excellent bibliography has been assembled by Šilhavý [85].

Successes of the theories for shape memory alloys include modeling their complicated hysteresis behavior [2], accounting for the needle-like, cusp-ended forms of their phase inclusions [77], and the qualitative description of experimentally-observed creep enhanced by a phase transition [53, 80].

The mission herein is to examine how these theories perform for phase transforming materials other than shape memory alloys in situations where inertial effects are important. In particular, we will utilize the purely mechanical models of Abeyaratne and Knowles [3] in exploring shock compression problems in GeO_2, a material known to suffer pressure induced phase transformations [45, 60, 70].

Abeyaratne and Knowles consider the nonuniqueness in solutions to initial-boundary value problems as a constitutive deficiency in the theory, remedied by the introduction of additional constitutive information in the form of a *nucleation criterion* to control the initiation of a new phase, and a *kinetic relation* to govern its evolution. Other workers, also viewing the nonuniqueness as a constitutive deficiency, have restored uniqueness by augmenting the theory such that stress depends not only on strain, but also depends linearly on strain rate (viscosity) and strain gradient (capillarity) [47, 82–84, 88–90, 97]. Although much of the work with such

augmented theories focuses on van der Waals fluids, the method can be applied to solids as well. In the case of the purely mechanical theory, it has been shown that augmenting the theory with linear viscosity and capillarity is equivalent to imposing a particular kinetic relation on a subsonic phase boundary [4, 99]. Recent work has begun to suggest the same for thermoelastic models [72, 101].

This study builds on other efforts to model impact-induced solid to solid phase transformations with the modern theories [12, 29, 58, 74]. The primary extension offered here is the implementation of the theory in a finite difference algorithm developed previously [108,109] with constitutive models that are reasonably descriptive of the behavior of the materials involved in the shock compression experiments we consider.

1.1 Shock compression of solids

The study of shock compression of solids began in earnest with the advent of nuclear weapons in World War II, which required the shock compression of solids by high explosives [17]. Major series of experiments were soon underway, leading to the acquisition of thermodynamic data for many materials, discoveries of new phase transitions, shock-induced chemical synthesis, powder consolidation, and the observation of shock-induced changes in electronic, magnetic, and optical properties.

Properties obtained by experimental shock compression are now utilized in other military applications, particularly the design and analysis of projectiles and armor. Shock compression results have gained new significance with the signing of the Nuclear Test Ban Treaty and the consequent directive that the national laboratories maintain the nuclear stockpile using the best technology available without nuclear testing. Many of the thermomechanical properties required for scientific stewardship of the stockpile are furnished by shock compression research.

Shock compression research extends to civilian applications; explosive welding, compaction, forming, cutting and metal hardening are all industrial techniques in-

volving the shock compression of solids, as is the shock synthesis of industrial-grade diamonds [68].

Geophysicists have been involved in the shock compression of solids from its infancy, as it is the only laboratory technique by which pressures comparable to those deep within the Earth and other planets can be obtained. For the measurement of properties at pressures from 1–3.7 Mbar (the estimated pressure at the center of the Earth), shock compression methods have no competitors [76]. The shock compression behavior of geomaterials provides properties needed to model the thermomechanical behavior of planets.

The literature on the shock compression of solids is vast. Overviews and extensive bibliographies are provided in [17, 68]. Shock compression in phase-changing materials was treated theoretically as early as 1942 by Bethe [20].

1.2 Why study the shock compression of GeO_2?

Historically, the primary motivation for studying the shock compression of GeO_2 has been that germanium-containing systems are structural analogs of silicates, the high-pressure behavior of which is of interest because of its abundance in the Earth. Among the dioxides, only GeO_2 and SiO_2 exhibit both quartz and rutile structures [70]. Both are readily quenched from the melt to form glass, and both combine with other oxides to form the same types of structures. At atmospheric pressure, systems containing GeO_2 often exhibit behaviors found in silicates at much higher pressures [71]. Phase transformations and elastic properties of silicates at high pressures have been predicted from the properties of germanates at lower pressures [70].

The military is interested in GeO_2 because it changes phase near pressures it would experience in an encounter with a ballistic object, and since phase changes generally dissipate energy, it is a candidate for an armor material.

1.3 Phases of GeO_2

At atmospheric conditions, GeO_2 is stable in the *rutile* form [104], a crystalline structure in which the oxygen ions are hexagonally close packed with germanium ions occupying half the octahedral interstitial positions [54]. Each germanium ion therefore sits in the center of an octahedron with an oxygen ion at each apex. The rutile structure has tetragonal symmetry.

Upon heating above 1033 °C at atmospheric pressure, the rutile form transforms to a *quartz* form of hexagonal symmetry, with each germanium ion at the center of a tetrahedron and an oxygen ion at each apex [71]. The corners of the tetrahedra are shared. This transformation is reconstructive, requiring the breaking of bonds and the formation of new ones. The quartz form can be retained upon returning the material to atmospheric conditions. Though it is merely metastable at these conditions, the transformation to the rutile form is so sluggish that the quartz is quite stable [104].

At room temperature and pressure, the density of the rutile and quartz forms are respectively 6.28 g/cm^3 and 4.28 g/cm^3 [104].

The glass formed by quenching from the melt is metastable at room conditions, with a density around 3.62–3.66 g/cm^3 [81, 104]. The local structure is similar to the quartz form in that the germanium ions are at the centers of corner-shared tetrahedra, but the Ge-O-Ge angles are consistent with the absence of long-range ordering [45].

The pressure-temperature phase diagram, Figure 1.1 shows the regions of stability of the rutile, quartz and liquid phases. We are interested in pressures three orders of magnitude greater than those shown in this figure, in a region where the phases are less well understood.

In hydrostatic experiments, some workers have reported that the rutile form transforms to an orthorhombic phase at 28 GPa upon heating to ≈1000 °C [70]. The orthorhombic phase was retained by quenching to room temperature then slowly unloading to atmospheric pressure. At 33 GPa and ambient temperature, the

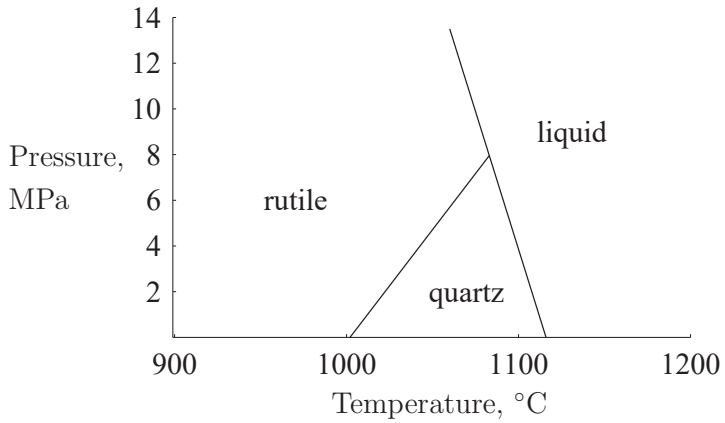

Figure 1.1: Phase diagram for GeO_2, after Wang [104].

densities of the orthorhombic and rutile phases were 6.97 g/cm^3 and 6.79 g/cm^3, respectively. At room conditions, their respective densities were 6.62 g/cm^3 and 6.32 g/cm^3. These findings are controversial [60].

The glass has been found to transform at a hydrostatic pressure of 25 GPa to a phase consistent with the Fe_2N structure, a hexagonally close packed structure of anions with cations randomly distributed in half the octahedral sites [45, 70]. A mechanism has been proposed by which a fourfold coordinated glass can be transformed to a sixfold coordinated structure without the breaking of bonds [92]. Some workers have reported that this new phase transforms back to the glasseous state upon release to ambient conditions [45, 61], but others have retained it [70]. When the new phase was retained, its room temperature density was 6.82 g/cm^3 at 32 GPa and 6.23 g/cm^3 at ambient pressure. Because this hexagonal phase forms only from the glass, and because it has a lower bulk modulus than the rutile phase, it is thought to be less stable at high pressure than the orthorhombic phase formed from the rutile phase [70].

In shock-compression experiments, Jackson and Ahrens [46] exposed both rutile and amorphous GeO_2 to pressures of 11–165 GPa. They found that the rutile form appears to transform to a denser phase above 70 GPa, and the amorphous form appears to transform to a denser phase above 35 GPa. Assuming a particular equation

of state model, the authors show that these results may be explained in terms of both forms transforming to a *common* high-pressure phase. They predicted that the density of this new phase was about 5% greater than the zero-pressure density of the rutile phase. This agrees well with the density of the orthorhombic structure that was later produced under hydrostatic compression from the rutile phase.

The difference between the findings of the hydrostatic and dynamic experiments is significant. Under hydrostatic pressure, the rutile and glass forms of GeO_2 change to two *different* phases, but in dynamic loading they seem to transform to a *common* phase that is consistent with the high pressure phase of the rutile material in the hydrostatic experiments.

There are several possibilities for this discrepancy, the first being that the experiments are suspect. The specimens survive the hydrostatic experiments, and their structure is determined by x-ray diffraction or spectrometry. In shock-compression studies, the specimen is destroyed; predictions about its transformation behavior are based on a particle velocity versus time record that lasts only a few microseconds. One might therefore be inclined to take the hydrostatic work as definitive and ignore the shock compression work. But Jackson and Ahrens argue convincingly that, *whatever* structure the glass transforms to, it must be *more* dense than the rutile phase. In the hydrostatic experiments, the glass transformed to a phase *less* dense than the rutile phase.

To a mechanician knowledgeable about recent theoretical developments in modeling phase transformations, the difference in the results of the two types of experiments may not be a concern, but rather a testimony to the importance of inertial effects in phase transitions. With an appropriate model to describe all four phases (the glass, the rutile, the orthorhombic, and the Fe_2N-like phases) it might be possible to demonstrate that both the static and dynamic results are consistent with modern theories of phase transformations, though some extension of the theories would be necessary.

In this work, the theories employed are sophisticated enough to describe only two

stable or metastable phases. Thus, we have a quandary: we suspect that four or more phases might be relevant in the experiments we examine, but we can accommodate only two. So, what two phases to model? One of our choices is the glasseous form, as the GeO_2 is initially glass in the experiments we will study. Since we are interested in shock compression experiments, the other phase we will try to describe is the high-pressure phase that Jackson and Ahrens predicted in their work. Our model will be presented in Chapter 5.

1.4 Computational methods for phase transformations

Various approaches have been used in computational studies of phase transformations.

Silling [86] employed a finite-difference dynamic relaxation method to model phase changes and localization in elastostatics. He presented results for sample problems involving failure of a soil slope, propagation of shear bands in a soil, necking and Lüders banding, and dendritic formation of phase inclusions near a crack tip. He extended the technique to model the dynamic growth of martensitic plates at a crack tip [87].

Mamiya and Simo [63] incorporated the theories of Abeyaratne and Knowles in a finite element method to model the quasi-static evolution of a maximally dissipative phase boundary in a purely mechanical setting. They later proposed a new element for the description of phase boundaries, using it to consider transformations in anti-plane shear [64]. Their model predicted dendritic formation of the new phase around a screw dislocation.

Swegle [94] considered phase transformations induced by shock compression in quartz. He assumed that the material immediately behind the shock front was a mixture of the quartz and a high-density phase, and used a mass fraction of the high pressure phase to quantify the mixture. The specific volume and internal energy of

the mixture were taken to be the mass-weighted averages of these properties for the individual phases. He examined various kinetics, embodied in expressions that quantified the change of the mass fraction with respect to other parameters, such as time or volume. Such expressions play the role of Abeyaratne and Knowles' kinetic relation in restoring uniqueness.

This thesis makes use of a finite-difference method developed by Zhong, Hou, and LeFloch incorporating the models of Abeyaratne and Knowles for the treatment of propagating phase boundaries in a purely mechanical one-dimensional setting [108,109]. The method of Zhong, Hou, and LeFloch is a modified Godunov technique in which phase boundaries are tracked while shocks are captured.

Chapter 2

Impact experiments

We will examine planar impact experiments conducted by W. Yang and T. J. Ahrens [107] in the 40 mm-bore propellant gun at Caltech's Lindhurst Laboratory of Experimental Geophysics. These experiments have been discussed in a recent publication [22]. The experimental equipment and methods are similar to those described elsewhere [27]. Overviews of experimental techniques can be found in [13, 17].

In brief, a cylindrical Lexan® sabot with a disk called the *flyer plate* mounted on its face is accelerated along an 8 meter gun barrel that extends into an evacuated chamber, where the flyer plate impacts a target assembly. Impact velocities of 1.0–2.5 km/s can be achieved.

Two types of experiments were performed. In a *forward* experiment, a tungsten flyer plate 2–3 mm thick strikes the face of a GeO_2 disk, which is backed by a thin (<2 mm) Al6061-T6 buffer plate, in turn backed by a thick (≈12 mm) LiF window, Figure 2.1. In a *reverse* experiment, a GeO_2 flyer plate 3–4 mm thick strikes the buffer plate, which is backed by the window, Figure 2.2. All plates are disks approximately 25–32 mm in diameter. In both types of experiments, the flyer plate is backed by a disk of polyurethane foam, which provides support to the flyer plate during the sabot's launch but approximates a free surface during impact.

The primary output—known as a *VISAR record*—is a *particle velocity versus time history* of the buffer at its interface with the window, obtained through fiber-

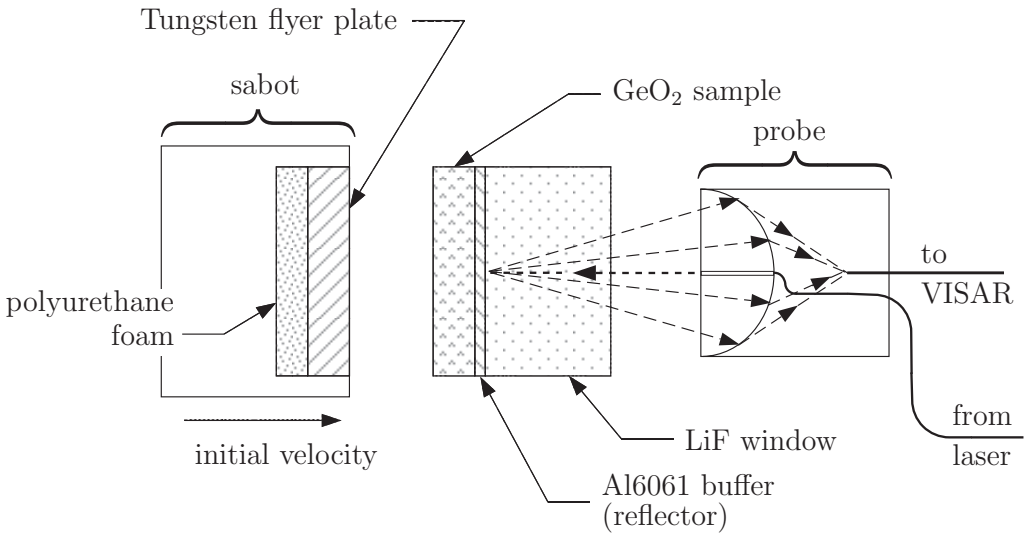

Figure 2.1: Configuration of a forward experiment. VISAR is an acronym for Velocity Interferometer System for Any Reflector.

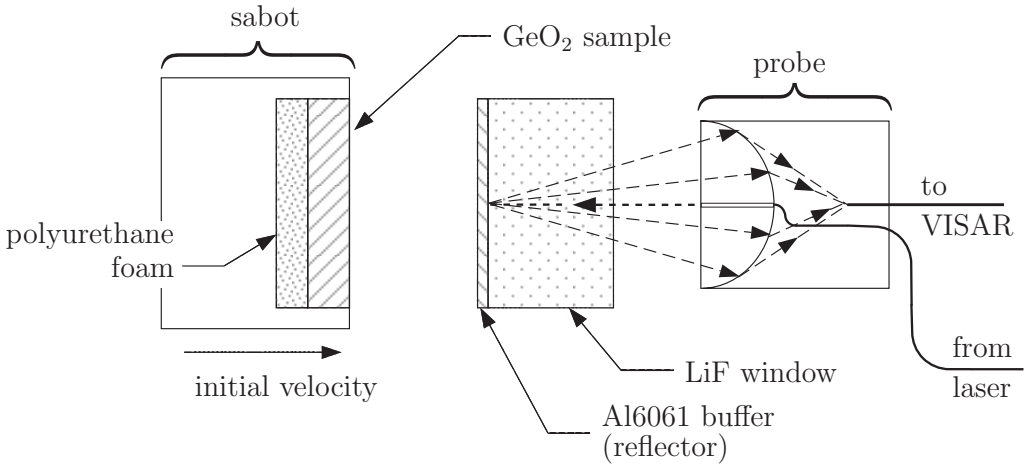

Figure 2.2: Configuration of a reverse experiment.

optic based velocity interferometry. The measurements are taken from a small area surrounding the center of the buffer's diameter. The flyer plate and target are destroyed during the experiment; not even small pieces are recovered afterwards.

A forward experiment provides information about the short-term response of the GeO_2 to impact loading, while a reverse experiment provides information about its

unloading behavior.

One may inquire into the purpose of the buffer plate and window, the choice of materials for them, and their relative thicknesses. Ideally, particle velocities *within* the sample would be recorded, but this is not possible. If velocities were recorded at a *free* surface, compressive waves encountering the free surface would reflect back into the material as rarefaction waves. This is difficult to analyze, particularly if the rarefaction waves interact with other rarefaction waves reflected from the flyer plate's far side and cause either plate to spall. The solution is to back the stationary sample or buffer plate by a thick layer of material which can transmit laser light for interferometry; the thickness is chosen so that the compressive waves encounter the free surface nearest the fiber optics at a "late" time (after the events of interest have occurred). Lithium fluoride is usually the window material of choice because it remains transparent to laser light during the shock loading event.

The buffer provides the necessary reflective surface for the laser light. Al6061-T6 is used because its dynamic compressive response is nearly identical to that of lithium fluoride, minimizing the influence of the buffer. To simplify analysis, the difference in response between the two materials is sometimes ignored.

The disks of the target assembly are bonded at each interface by a thin layer of cyanoacrylate, commonly known as Super Glue®. The influence of the cyanoacrylate is neglected in this thesis. The entire assembly is held in the target chamber by compression at several points on its circumference.

The diameters of the plates are much greater than their thicknesses in order to provide a state of one-dimensional strain surrounding the longitudinal axis. Throughout this work, we assume that the diameters are sufficiently large so that waves emanating from the lateral surfaces do not reach regions near the longitudinal axis—including the region from which the VISAR record is taken—during the duration of the experiments. Within each disk, the material that is unaffected by such edge effects responds as if it were within a disk of infinite lateral extent.

It is important to emphasize that the *time of impact is not known*. In later

chapters, the experimental velocity versus time histories will be freely translated along the time axis to provide the best matches to the simulations.

Before continuing, we address a conflict in terminology. In fields specialized to the shock compression of solids, it is common to refer to the disks in the projectile and target as "plates." In the field of solid mechanics, "plate" is used in a class of problems to describe a body in which one dimension is small, but not negligible, compared to the other two, and the deformation of the body involves a bending deflection normal to the small dimension. Where "plate" is used in this thesis, it is in the first sense.

2.1 Forward shots

Yang and Ahrens [107] obtained the particle velocity histories of Figure 2.3 for the two forward shots described in Table 2.1.

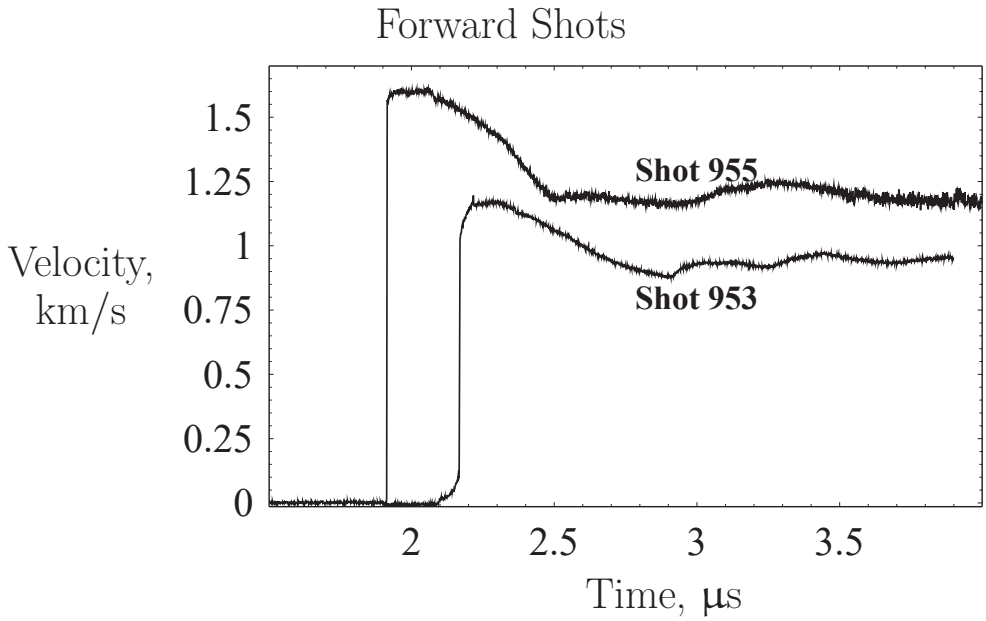

Figure 2.3: Particle velocity histories recorded from the forward experiments.

Forward Shots

	Foam	Tungsten		GeO_2		Al6061	LiF
Shot	Width mm	Velocity km/s	Width mm	Width mm	Density g/cm^3	Width mm	Width mm
953	2.90	1.53	2.627	3.835	3.632	0.743	11.957
955	2.72	1.99	2.645	4.059	3.631	0.923	11.993

Table 2.1: Parameters of the forward experiments.

2.2 Reverse shots

Yang and Ahrens [107] obtained particle velocity histories for four reverse shots, three of which are described in Table 2.2 and presented in Figure 2.4.

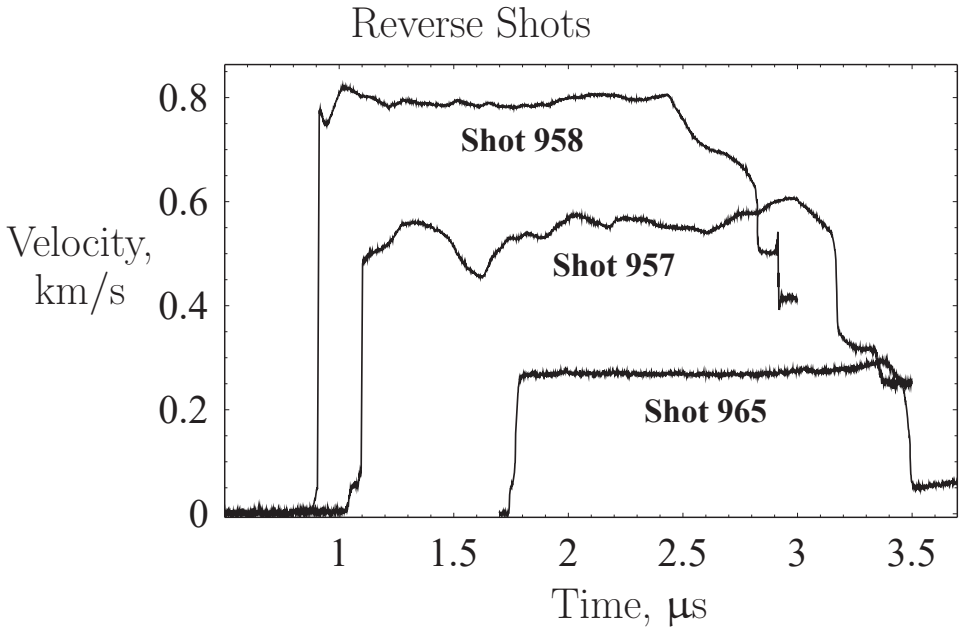

Figure 2.4: Particle velocity histories recorded from the reverse experiments.

Reverse Shots

	Foam	GeO_2			Al6061	LiF
Shot	Width mm	Velocity km/s	Width mm	Density g/cm^3	Width mm	Width mm
957	3.18	1.47	4.087	3.631	1.459	12.029
958	3.18	1.96	4.128	3.633	1.354	12.007
965	3.99	0.62	3.029	3.618	0.774	11.958

Table 2.2: Parameters of the reverse experiments.

In the shot not presented (Shot 956), a 4 mm thick GeO_2 plate reached a velocity of 1.05 km/s. X-ray photographs taken prior to impact indicate that the GeO_2 had

shattered after launch.

Judging from the appearance of the velocity history profiles for Shots 957 and 958, W. Yang suspects that the flyer plates were damaged in these two shots as well [106], though no apparent damage is seen in the X-ray images.

Shot 965 was a fortunate miscircumstance. The experiment had been prepared to achieve a flyer plate velocity of 1 km/s but the velocity actually achieved was only 0.62 km/s. This provides one reverse shot in which there is no reason to suspect any launch-induced damage in the GeO_2.

Chapter 3

Preliminaries

This chapter presents concepts from the purely mechanical, nonlinear continuum theory of elastic bodies in motion. It begins with the basic field equations and constitutive assumptions for the three dimensional theory. A dissipation inequality is introduced, which in turn motivates the introduction of the *driving traction* acting on a discontinuity. This is followed by a brief discussion of how thermodynamic effects would be included in a more complete treatment. The purely mechanical equations are then specialized to the situation of one-dimensional strain in order to model the experiments described in Chapter 2. In this setting, discontinuities in the mechanical fields are classified as either *shocks* or *phase boundaries*, and phase boundaries are further categorized as *subsonic*, *sonic* or *supersonic*. Finally, *fans* are defined and relevant expressions derived.

3.1 Kinematics and balance laws

Consider a body B that occupies a region R in a reference configuration. In a motion of the body, a particle at $\boldsymbol{x}$ in the reference configuration is carried to $\boldsymbol{y}(\boldsymbol{x},t) = \boldsymbol{x} + \boldsymbol{u}(\boldsymbol{x},t)$ at time t, where $\boldsymbol{u}$ is the displacement vector. We assume that the displacement $\boldsymbol{u}$ is continuous with piecewise continuous first and second derivatives.

The *deformation gradient tensor* and the *particle velocity vector* are respectively

$$\boldsymbol{F}(\boldsymbol{x},t) = \operatorname{Grad} \boldsymbol{y} \ , \tag{3.1}$$

$$\boldsymbol{V}(\boldsymbol{x},t) = \frac{\partial \boldsymbol{y}(\boldsymbol{x},t)}{\partial t} \ . \tag{3.2}$$

To ensure that the deformation is one-to-one, the restriction

$$J = \det \boldsymbol{F} > 0 \tag{3.3}$$

is required to hold everywhere for all time.

Where $\boldsymbol{F}$ is smooth, kinematic compatibility requires that

$$\operatorname{Grad} \boldsymbol{V} = \partial \boldsymbol{F}/\partial t \ . \tag{3.4}$$

At any moving regular surface $\Pi(t)$ in the reference configuration across which $\boldsymbol{F}$ is discontinuous, continuity of displacements requires that

$$[\![\boldsymbol{F}]\!]\ell = \boldsymbol{0} \ , \tag{3.5}$$

$$[\![\boldsymbol{V}]\!] = -W[\![\boldsymbol{F}]\!]\boldsymbol{N}_\Pi \ , \tag{3.6}$$

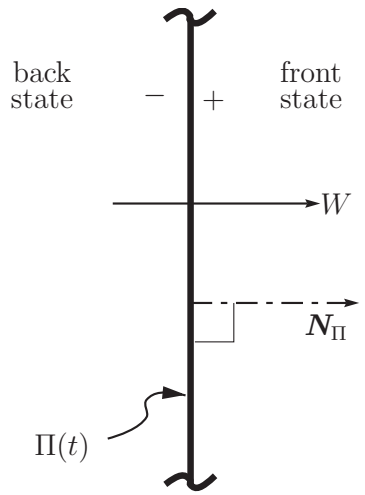

Figure 3.1: A moving discontinuity.

where ℓ is any vector tangent to the surface, and W is the normal velocity of the surface, Figure 3.1. The unit normal to the surface is $\boldsymbol{N}_\Pi$, chosen so that $W \geq 0$. This formulation is purely Lagrangian, but the surface $\Pi(t)$ does have an image in the current ("laboratory") configuration across which the Eulerian fields are discontinuous.

These last expressions employ the *jump notation*, where the *jump* in some quan-

tity Φ across a surface of discontinuity $\Pi(t)$ is

$$[\![\Phi]\!] = \Phi^+ - \Phi^- \ . \tag{3.7}$$

Here Φ^+ and Φ^- are the limiting values of a field Φ on $\Pi(t)$ when approached from the positive and negative sides, respectively. We use the convention that the positive side is that side into which $\boldsymbol{N}_\Pi$ is directed, Figure 3.1. We say that the material on the "+" side of the discontinuity is *ahead* of the discontinuity and is in the *front state*. The material on the "−" side is *behind* the discontinuity and in the *back state*.

Let $\rho_\circ$ denote the *referential mass density* of the body. Let $\boldsymbol{\sigma}(\boldsymbol{x}, t)$ be the *nominal stress tensor*, also known as the *Piola* or *engineering* stress tensor, with units of *force per original area*.

For all regular subregions $\mathcal{R} \subset R$, conservation of linear and angular momentum in the absence of body forces require

$$\frac{d}{dt} \int_{\mathcal{R}} \rho_\circ \, \boldsymbol{V} \, dV = \int_{\partial\mathcal{R}} \boldsymbol{\sigma} \boldsymbol{N} \, dA \ , \tag{3.8}$$

$$\frac{d}{dt} \int_{\mathcal{R}} \boldsymbol{y} \times \rho_\circ \, \boldsymbol{V} \, dV = \int_{\partial\mathcal{R}} \boldsymbol{y} \times \boldsymbol{\sigma} \boldsymbol{N} \, dA \ , \tag{3.9}$$

where $\boldsymbol{N}$ is the field of outward pointing unit normals on the surface $\partial\mathcal{R}$.

At points $(\boldsymbol{x}, t)$ where $\boldsymbol{F}$ is continuous, localization of these balance laws yields

$$\operatorname{Div} \boldsymbol{\sigma} = \rho_\circ \, \dot{\boldsymbol{V}} \ , \tag{3.10}$$

$$\boldsymbol{\sigma} \boldsymbol{F}^T = \boldsymbol{F} \boldsymbol{\sigma}^T \ . \tag{3.11}$$

At a surface of discontinuity, $\Pi(t)$, localization of the balance of linear momentum (3.8) yields the jump condition

$$[\![\boldsymbol{\sigma}]\!] \boldsymbol{N}_\Pi + \rho_\circ [\![\boldsymbol{V}]\!] W = 0 \ . \tag{3.12}$$

Localization of angular momentum yields no new information.

Derivations of the results of this section can be found in many texts. See, for example [21, 65].

3.2 Hyperelastic materials

The consideration of kinematics and the balance laws in the previous section required no specification of the mechanical properties of the material involved, beyond assuming that the material is incapable of supporting contact moments. Connections between the kinematic and mechanical fields are provided by *constitutive equations* which mathematically represent idealized material responses.

Where fields are smooth, kinematic compatibility (3.4) and the balance laws (3.10)–(3.11) for linear and angular momenta provide fifteen scalar equations for twenty-one unknown scalar fields, namely the components of $\boldsymbol{F}$, $\boldsymbol{V}$ and $\boldsymbol{\sigma}$. It is then assumed that the stress is uniquely determined by the motion of the body through *constitutive equations*, providing an additional six equations for the unknowns. Thus, we have twenty-one equations for twenty-one unknowns.

Constitutive models in a purely mechanical setting attempt to account for various effects including elasticity, viscosity, capillarity, and plasticity. We shall restrict our scope to *hyperelastic* constitutive behaviors in homogeneous materials.

In a homogeneous hyperelastic material, the nominal stress derives from an *elastic potential* or *strain energy per unit mass*, $\Psi = \tilde{\Psi}(\boldsymbol{F})$, through

$$\boldsymbol{\sigma} = \tilde{\boldsymbol{\sigma}}(\boldsymbol{F}) = \rho_\circ \frac{\partial \Psi}{\partial \boldsymbol{F}} \,, \tag{3.13}$$

where $\tilde{\boldsymbol{\sigma}}$, the *stress response function*, is a material property. The reader is cautioned that this same title will be bestowed upon a slightly different function for convenience in Section 3.5.2 and will be used only in that sense thereafter.

3.3 The dissipation inequality and the driving traction

Let Γ be the difference between the rate of work of the external forces acting on a subregion $\mathcal{R} \subset R$ and the rate of storage of mechanical energy,

$$\Gamma(t) = \int_{\partial\mathcal{R}} \boldsymbol{\sigma}\boldsymbol{N} \cdot \boldsymbol{V} dA - \frac{d}{dt} \int_{\mathcal{R}} \rho_\circ \left\{ \Psi + \frac{1}{2} \boldsymbol{V} \cdot \boldsymbol{V} \right\} dV \ . \tag{3.14}$$

Thus, Γ represents the rate of dissipation of mechanical energy in the region $\mathcal{R}$. We will impose the *dissipation inequality*,

$$\Gamma(t) \geq 0 \ , \quad \text{for all } t \text{ and for all } \mathcal{R} \ , \tag{3.15}$$

which is a statement that the instantaneous rate of dissipation must be non-negative.

Localization of (3.14) subject to (3.15) yields a trivial result in regions where $\boldsymbol{F}$ is smooth. Across a surface of discontinuity, localization yields

$$\Gamma(t) = [\![\boldsymbol{\sigma}\boldsymbol{N}_\Pi \cdot \boldsymbol{V}]\!] + \rho_\circ [\![\Psi]\!] W + \frac{1}{2} \rho_\circ [\![\boldsymbol{V} \cdot \boldsymbol{V}]\!] W \geq 0 \ . \tag{3.16}$$

Applying the identity

$$[\![\boldsymbol{a} \cdot \boldsymbol{b}]\!] = [\![\boldsymbol{a}]\!] \cdot \langle \boldsymbol{b} \rangle + \langle \boldsymbol{a} \rangle \cdot [\![\boldsymbol{b}]\!] \ , \tag{3.17}$$

where $\langle \cdot \rangle$ denotes the average,

$$\langle \boldsymbol{a} \rangle = \frac{1}{2} \left(\boldsymbol{a}^+ + \boldsymbol{a}^- \right) \ , \tag{3.18}$$

to expand the first and last terms in (3.16), then using the jump conditions (3.5),

(3.6) and (3.12), we arrive at

$$\Gamma(t) = \{\rho_\circ [\![\Psi]\!] - \langle \boldsymbol{\sigma} \rangle \cdot [\![\boldsymbol{F}]\!]\} W \geq 0 \,, \tag{3.19}$$

where, $\langle \boldsymbol{\sigma} \rangle \cdot [\![\boldsymbol{F}]\!] = \mathrm{tr}\,(\langle \boldsymbol{\sigma} \rangle [\![\boldsymbol{F}]\!]^T)$ is the scalar product of the tensors $\langle \boldsymbol{\sigma} \rangle$ and $[\![\boldsymbol{F}]\!]$. This result may be found in [56]; see also [3] and the works of Eshelby [32–34].

In the previous equation, the quantity in braces is defined as the *driving traction*, f, acting on the discontinuity,

$$f = \tilde{f}(\boldsymbol{F}^-, \boldsymbol{F}^+) = \rho_\circ [\![\Psi]\!] - \langle \boldsymbol{\sigma} \rangle \cdot [\![\boldsymbol{F}]\!] \,. \tag{3.20}$$

The dissipation inequality (3.16) can thus be written

$$fW \geq 0 \,. \tag{3.21}$$

A motion of the body is *admissible* if (3.21) holds at each discontinuity and for all time.

A moving discontinuity ($W \neq 0$) is *dissipation-free* when $f = 0$.

3.4 If thermal effects were included

In general, the assumption of constant temperature violates the conservation of energy unless there is a suitable volumetric heat supply. While this violation is usually not severe for slow, or quasi-static, motions, the assumption that the motion is isothermal is not realistic for situations of high-velocity impact [74]. Nonetheless, we adopt it as a useful starting point for examining a new theory, a strategy which has been fruitfully employed by others: see for example [40, 41, 74]. In the following we outline the additional balance principle and the constitutive modifications by which thermal effects could be incorporated if the material were modeled as thermoelastic rather than elastic.

A more complete treatment of a high-velocity impact problem would require that, in addition to the momenta (3.8) and (3.9), thermal and mechanical energies be balanced for all regular subregions $\mathcal{R} \subset R$,

$$\frac{d}{dt}\int_{\mathcal{R}}(\rho_\circ \varepsilon + \frac{1}{2}\rho_\circ \boldsymbol{V}\cdot\boldsymbol{V})dV = \int_{\partial\mathcal{R}} \rho_\circ \boldsymbol{\sigma}\boldsymbol{N}\cdot\boldsymbol{V}dA + \int_{\partial\mathcal{R}} \boldsymbol{q}\cdot\boldsymbol{N}dA\,, \tag{3.22}$$

where $\boldsymbol{q}(\boldsymbol{x},t)$ is the nominal heat flux vector and $\varepsilon(\boldsymbol{x},t)$ the internal energy per unit mass. This expression holds in the absence of body forces and volumetric heat supply. Localization yields

$$\boldsymbol{\sigma}\cdot\dot{\boldsymbol{F}} + \mathrm{Div}\,\boldsymbol{q} = \rho_\circ\dot{\varepsilon}\,, \tag{3.23}$$

$$[\![\boldsymbol{\sigma}\boldsymbol{N}\cdot\boldsymbol{V}]\!] + \rho_\circ[\![\varepsilon + \boldsymbol{V}\cdot\boldsymbol{V}]\!]W + [\![\boldsymbol{q}\cdot\boldsymbol{N}]\!] = 0\,, \tag{3.24}$$

where fields are smooth and across a surface of discontinuity, respectively.

Where fields are smooth, balance of thermal and mechanical energy has added one equation and two unknowns, for a total of 16 scalar field equations and 23 unknowns. It can be motivated that stress, internal energy and heat conduction depend not only upon the motion of the body but also upon a scalar field not present in the equations [21]. Thus the new scalar field of *temperature*, $\theta = \theta(\boldsymbol{x},t)$, is introduced, increasing the unknowns to 24 scalar fields.

The dissipation inequality, (3.14), is replaced by an *entropy inequality* expressing the second law of thermodynamics. The Clausius-Duhem version of the second law requires that for all regular subregions $\mathcal{R} \subset R$,

$$\frac{d}{dt}\int_{\mathcal{R}}\rho_\circ\eta dV - \int_{\partial\mathcal{R}}\boldsymbol{q}\cdot\boldsymbol{N}dA \geq 0\,, \tag{3.25}$$

where $\eta = \eta(\boldsymbol{y}, t)$ is the entropy per unit mass. Localization yields

$$\rho_\circ \dot{\eta} \geq \operatorname{Div} \boldsymbol{q}/\theta \,, \tag{3.26}$$

$$\rho_\circ [\![\eta]\!] W + [\![\boldsymbol{q} \cdot \boldsymbol{N}/\theta]\!] \leq 0 \,, \tag{3.27}$$

where fields are smooth and across a surface of discontinuity, respectively.

Introducing the Helmholtz free energy per unit mass $\Psi = \varepsilon - \theta\eta$, and using (3.24), (3.27) can be manipulated into the form

$$fW \geq 0 \,, \tag{3.28}$$

where

$$f = \rho_\circ [\![\Psi]\!] - \langle \sigma \rangle [\![\boldsymbol{F}]\!] \tag{3.29}$$

is the driving traction.

The constitutive equations must now connect stress, internal energy, and heat flux to the motion and temperature of the body. In a *thermoelastic* material, the stress and entropy derive from a *Helmholtz potential*, $\breve{\Psi} = \breve{\Psi}(\boldsymbol{F}, \theta)$, through

$$\boldsymbol{\sigma} = \breve{\boldsymbol{\sigma}}(\boldsymbol{F}, \theta) = \rho_\circ \breve{\Psi}_{\boldsymbol{F}}(\boldsymbol{F}, \theta) \,, \tag{3.30}$$

$$\eta = \breve{\eta}(\boldsymbol{F}, \theta) = -\breve{\Psi}_\theta(\boldsymbol{F}, \theta) \,. \tag{3.31}$$

Detailed derivations can be found in [3, 85].

One can consider hypothetical materials for which $\breve{\Psi}_{\theta\boldsymbol{F}} = 0$. Deformation and temperature are uncoupled for such materials, and a high-velocity shock compression occurs isothermally without violating the conservation of energy.

3.5 Specialization to one-dimensional deformations

We now specialize the governing equations and constitutive model of the purely mechanical formulation to the problem at hand, namely the analysis of the experiments described in Chapter 2.

3.5.1 Field equations

The disks are regarded as continua of finite thickness in the longitudinal direction and infinite extent radially. Select an orthonormal basis $\boldsymbol{E} = (\boldsymbol{e}_x, \boldsymbol{e}_y, \boldsymbol{e}_z)$ with $\boldsymbol{e}_x$ in the direction of the common axis of the disks. The deformation is assumed to be *uniaxial*; a particle at the point (x, y, z) in a reference configuration is carried at time t to the point $(x + u, y, z)$, where $u = u(x, t)$ is the only non-zero component of the displacement vector $\boldsymbol{u}$.

The *displacement gradient* in the longitudinal direction is

$$\gamma = u_x. \tag{3.32}$$

Subscripts here and elsewhere denote partial differentiation unless otherwise stated. In this thesis, γ will frequently be called *strain* for convenience, though it is *not* a component of the Lagrangian strain tensor $\Phi = (\boldsymbol{F}^T\boldsymbol{F} - \boldsymbol{1})/2$. This is not particularly immoral, since there is a one-to-one correspondence between γ and the component $\Phi_{xx} = \gamma + (\gamma^2)/2$ for all $\gamma > -1$.

The components of $\boldsymbol{F}$ can be written in matrix form,

$$\Big[F\Big] = \begin{bmatrix} 1+\gamma & 0 & 0 \\ 0 & 1 & 0 \\ 0 & 0 & 1 \end{bmatrix}. \tag{3.33}$$

For the deformation to be one-to-one, the restriction (3.3), $\det \boldsymbol{F} > 0$, implies that

$$\gamma > -1 \ . \tag{3.34}$$

The only non-zero component of the particle velocity vector is

$$V = u_t \ . \tag{3.35}$$

Where fields are smooth, kinematic compatibility (3.4) reduces to

$$\dot{\gamma} - V_x = 0 \ . \tag{3.36}$$

We will assume that the symmetry group of the material allows it to sustain uniaxial deformation in the x-direction with no components of shear stress in the x, y or z directions. This is true for uniaxial deformation in *any* direction for an isotropic material, and in certain directions for some anisotropic materials provided the specimen is properly oriented. Conservation of linear momentum (3.10) then reduces to

$$\sigma_x - \rho_\circ \dot{V} = 0 \ , \tag{3.37}$$

where σ is the normal component of $\boldsymbol{\sigma}$ acting on a surface perpendicular to the $\boldsymbol{e}_x$ direction. The balance of angular momentum, (3.11), provides no new information.

We will allow only surfaces of discontinuity which are perpendicular to the longitudinal direction, i.e., $(N_\Pi) = (1, 0, 0)$. The jump conditions for continuity of displacement (3.6) and conservation of linear momentum (3.12) each provide one non-trivial scalar result when applied to uniaxial displacement,

$$[\![V]\!] + W[\![\gamma]\!] = 0 \ , \tag{3.38}$$

$$\rho_\circ [\![V]\!] W + [\![\sigma]\!] = 0 \ . \tag{3.39}$$

For later use, note that these imply

$$\rho_\circ W^2 = \frac{[\![\sigma]\!]}{[\![\gamma]\!]} \,, \tag{3.40}$$

$$\rho_\circ [\![V]\!]^2 = [\![\sigma]\!][\![\gamma]\!] \,. \tag{3.41}$$

Observe that the right side of (3.40) is the slope of the chord passing through the two points (γ^-, σ^-) and (γ^+, σ^+) in the σ, γ plane. Thus, the velocity W of a discontinuity is monotonically related to the slope of this chord.

Since the discontinuity velocity W is real, (3.40) implies that

$$\text{sign}\,([\![\sigma]\!]) = \text{sign}\,([\![\gamma]\!]) \;. \tag{3.42}$$

We also have

$$[\![V]\!] = -\text{sign}\,(W[\![\sigma]\!])\,\frac{1}{\sqrt{\rho_\circ}}\sqrt{[\![\sigma]\!][\![\gamma]\!]}\,. \tag{3.43}$$

The shock compression literature often utilizes the "pressure" P rather than σ, where

$$P = -\sigma \,. \tag{3.44}$$

This conflicts with the standard definition of pressure in continuum mechanics as $P = -(\tau_{xx} + \tau_{yy} + \tau_{zz})/3$, where $\boldsymbol{\tau} = \boldsymbol{\sigma}\boldsymbol{F}/J$ is the *actual* or *Cauchy* stress tensor. One must be cautious when reading the shock compression literature because either definition of pressure might be encountered and not clearly distinguished.

In the shock compression literature one may also encounter the *compression* η, the current density ρ, and the current specific volume v, where

$$\eta = \frac{\rho}{\rho_\circ} = \frac{v_\circ}{v} = J^{-1} > 0 \,. \tag{3.45}$$

Here, $v_\circ = 1/\rho_\circ$ is the specific volume in the reference configuration. By the def-

inition (3.3) of J and the expression (3.33) for the components of $\boldsymbol{F}$, in uniaxial deformation we have

$$\eta = (1+\gamma)^{-1} \, . \tag{3.46}$$

Thus, in compression $\gamma < 0$ and $\eta > 1$, while in extension $\gamma > 0$ and $\eta < 1$.

3.5.2 Hyperelastic material

The normal stress σ acting on a surface perpendicular to the longitudinal direction $\boldsymbol{e}_x$ is computed from the expression (3.13) for the response of a hyperelastic material and the expression (3.33) for the components of $\boldsymbol{F}$ in uniaxial deformation. The result is

$$\sigma = \tilde{\sigma}(\boldsymbol{F}) = \rho_\circ \Psi_{F_{xx}}(\boldsymbol{F}) \, , \tag{3.47}$$

where the subscripts on F designate components of the tensor $\boldsymbol{F}$, not differentiation.

Since $\boldsymbol{F}$ is a function only of γ, we simplify notation by defining $\psi = \hat{\psi}(\gamma) = \rho_\circ \Psi$, so that

$$\sigma = \hat{\sigma}(\gamma) = \psi\,'(\gamma) \, . \tag{3.48}$$

For the remainder of this thesis, $\hat{\sigma}(\gamma)$ will be referred to as the *stress response function.*

The *Lagrangian longitudinal wave speed*, $c = \hat{c}(\gamma)$, which we shall also call the *sound speed*, is defined by

$$c^2 = \frac{\hat{\sigma}\,'(\gamma)}{\rho_\circ} \, . \tag{3.49}$$

The sound speed is real only if $\hat{\sigma}\,'(\gamma)$ is non-negative.

The state of stress in a solid under uniaxial deformation is in general not hy-

drostatic. To illustrate, compare the normal components of stress in the x direction with those in the y and z directions for infinitesimal uniaxial deformations in an isotropic linearly elastic solid. We have:

$$\sigma_{xx} = (\kappa + \frac{4}{3}\mu)\gamma \ , \tag{3.50}$$

$$\sigma_{yy} = \sigma_{zz} = (\kappa - \frac{2}{3}\mu)\gamma < \sigma_{xx} \ , \tag{3.51}$$

where κ is the bulk modulus and μ is the shear modulus. Here, subscripts on σ designate the components of the stress tensor $\boldsymbol{\sigma}$, rather than our usual convention that they designate differentiation. Because the three normal components are not equal, the state of stress is not hydrostatic.

No attempt is made in this thesis to determine the lateral normal components σ_{yy} and σ_{zz}. These components cannot be computed with the little experimental knowledge that we have of the elastic potential Ψ for the materials encountered here.

3.5.3 Driving traction

In uniaxial deformation, the driving traction (3.20) is

$$f = \hat{f}(\gamma^+, \gamma^-) = [\![\psi]\!] - \langle\sigma\rangle[\![\gamma]\!] = \int_{\gamma^-}^{\gamma^+} \hat{\sigma}(\gamma)d\gamma - \langle\sigma\rangle[\![\gamma]\!] \ . \tag{3.52}$$

Thus, $f(t)$ may be interpreted as the area under the curve $\hat{\sigma}(\gamma)$ from (γ^-, σ^-) to (γ^+, σ^+) minus the area under the chord connecting these same points.

Note that the driving traction changes sign but its magnitude stays the same when the discontinuity changes its direction of travel,

$$\hat{f}(\gamma_a, \gamma_b) = -\hat{f}(\gamma_b, \gamma_a) \ , \tag{3.53}$$

for any strain pair (γ_a, γ_b).

The expression for the dissipation inequality, (3.21), is unchanged:

$$fW \geq 0\ . \tag{3.54}$$

3.6 Single and multiple phase materials

Our model of a single phase material is one for which the stress σ is a strictly convex or strictly concave, monotonically increasing function of the displacement gradient γ, Figure 3.2(a). For prescribed longitudinal stress σ on a disk of infinite lateral extent composed of such a material, there is only one equilibrium stress, corresponding to the minimum of the *potential energy*,

$$G(\gamma, \sigma) = \psi(\gamma) - \sigma\gamma. \tag{3.55}$$

The graph of $G(\gamma, \sigma)$ as a function of γ for fixed σ is convex with a single well. In such materials, the conservation principles and dissipation inequality suffice to ensure uniqueness in the problems we will examine [57, 73]. We have little interest in single-phase materials in this work, but it is helpful to understand their behavior, so a brief treatment that applies to them may be found in Appendix A.4.

Two-phase materials will be described by an "up-down-up" stress-strain curve, Figure 3.2(b). In this model, two intervals of the stress-strain curve have positive slope and no inflection points. Each of these intervals represents a distinct metastable phase. They are separated by an interval of negative slope, representing an unstable phase. For any longitudinal stress σ at which the material can exist in either stable phase, the potential energy $G(\gamma, \sigma)$ will have two minima. The material at some location x of our disk of infinite lateral extent is in equilibrium in the *stable phase* if it is in the state corresponding to the *absolute* minimum. It is in a *metastable* equilibrium at the state corresponding to the other minimum. In such materials, the conservation principles and dissipation inequality are *not* sufficient to ensure uniqueness in the problems we will examine. In the next chapter, we will

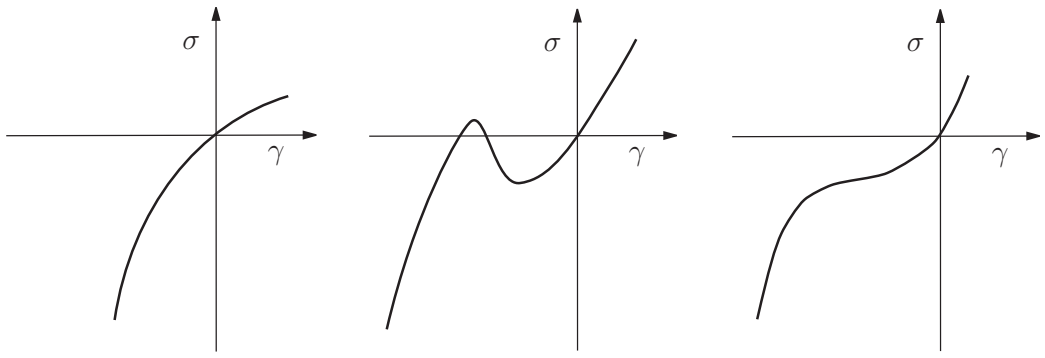

(a) Strictly concave.

(b) Up-down-up.

(c) Monotonic with a change of curvature.

Figure 3.2: Classification of stress response functions. (a) A single phase material is represented by a strictly convex or strictly concave (shown) stress response function. (b) A two phase material is represented by an "up-down-up" stress response function. (c) A material with a monotonic stress response function that is neither strictly concave nor strictly convex is also a phase-changing material.

investigate a particular initial-boundary value problem involving a nonmonotonic stress response function and find that there are an infinite number of solutions that satisfy the dissipation inequality (3.54).

We shall also consider models for which the stress-strain curve is monotonic but neither strictly convex nor strictly concave, Figure 3.2(c). While not commonly associated with phase-changes, solutions to dynamic problems in such materials suffer a lack of uniqueness similar to that for nonmonotonic materials [78]. Abusing terminology in the pursuit of conciseness, intervals demarcated by inflection points will be considered distinct phases.

In the impact experiments of interest, most of the action is in compression. Accordingly, we consider stress-response functions that extend mostly over compression. All of our material models will have three phases. The nomenclature is presented in Figure 3.3. The interval of least compression is the *low pressure phase* (LPP), that of greatest compression the *high pressure phase* (HPP). The interval

between them is the *middle phase* or, in the case of a nonmonotonic stress response function, the *unstable* or *spinodal phase*.

In an equation, the phases are designated with the subscripts 1 for the HPP, 2 for the middle phase, and 3 for the LPP. On a plot of $\hat{\sigma}(\gamma)$, these subscripts increase from left to right. This convention allows the interested reader to readily compare expressions in this thesis to those in publications of Abeyaratne and Knowles, who often describe nonmonotonic materials with phases numbered left to right. The endpoints of the middle phase are (γ_m, σ_m) and (γ_M, σ_M), with the subscript M denoting the endpoint at the more positive *stress*.

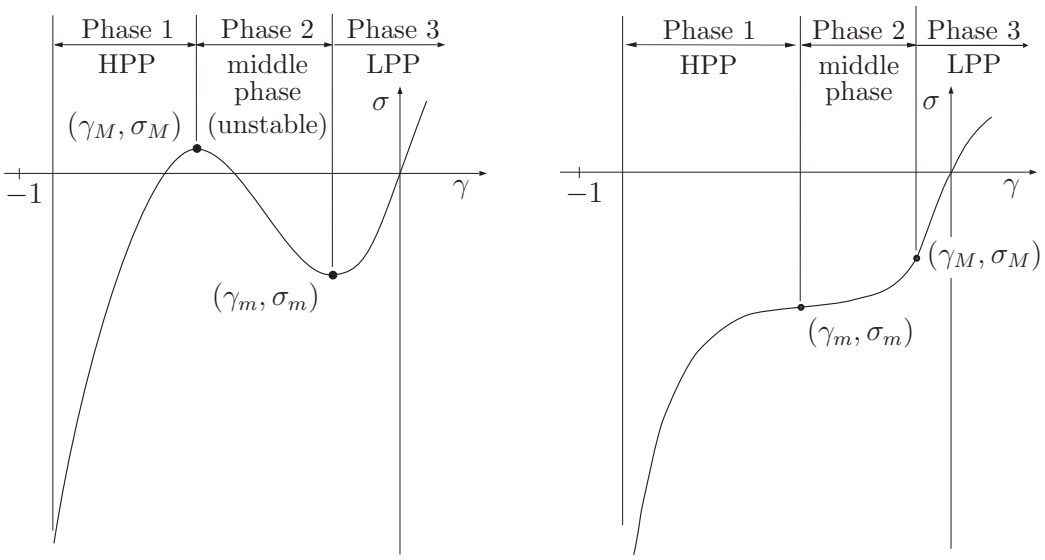

Figure 3.3: Nomenclature for up-down-up stress-strain curves and monotonic stress-strain curves having two inflection points.

The following sections provide a short discussion of discontinuities and fans in phase-changing materials of the type described here. A slightly more general treatment may be found in Appendix A.

3.6.1 Shocks and phase boundaries

In the materials described above, strain discontinuities in the one-dimensional setting can be classified as *shocks* or *phase boundaries*. The following discussion applies *only* to models that have at most one unstable phase; the situation may be more complicated in many-phased materials.

A *shock* is a strain discontinuity for which γ^+ and γ^- are in the *same* phase.

A *phase boundary* is a strain discontinuity for which γ^+ and γ^- are in *different* phases.

Where an expression applies to *any* discontinuity, whether a shock or a phase boundary, the discontinuity velocity will be denoted by W. When an expression applies *only* to phase boundaries, the *phase boundary velocity* will be denoted by $\dot{s}$ instead of W.

An *equilibrium* phase boundary ($\dot{s} = 0$) can exist in an up-down-up material but not in a material for which the stress response function changes convexity but remains monotonic. Consider a body of infinite lateral extent at equilibrium in a uniaxial deformation. By the expressions (3.37) and (3.39) for conservation of linear momentum, the uniaxial normal stress must everywhere be some constant value $\sigma = \sigma^*$. If the body is of an up-down-up material, and if σ^* is within the range of stress where the horizontal line $\sigma = \sigma^*$ intersects the graph of $\sigma = \hat{\sigma}(\gamma)$ more than once, then stationary phase boundaries can exist in the body. The body may be in a single phase or in an infinite combination of alternating stable phases of various thicknesses. If, however, the stress response function of the material changes convexity but remains monotonic, then there is *no* σ^* for which the material can support a stationary phase boundary. In equilibrium, such a body is necessarily in a single phase.

Moving phase boundaries can be categorized as *subsonic*, *sonic* or *supersonic*.

A *subsonic* phase boundary is one for which the Lagrangian speed of propagation

is less than the local sound speed on either side of the phase boundary,

$$|\,\dot{s}\,| \leq \min\left(\hat{c}(\gamma^+), \hat{c}(\gamma^-)\right) . \tag{3.56}$$

A *sonic* phase boundary is one for which the speed of propagation is equal to the lesser of the local wave speeds on either side of the phase boundary,

$$|\,\dot{s}\,| = \min\left(\hat{c}(\gamma^+), \hat{c}(\gamma^-)\right) . \tag{3.57}$$

A *supersonic* phase boundary is one for which the speed of propagation is greater than the local wave speed on one side of the phase boundary,

$$|\,\dot{s}\,| > \min\left(\hat{c}(\gamma^+), \hat{c}(\gamma^-)\right) . \tag{3.58}$$

3.6.2 Fans

For problems that involve no length or time scales, we introduce the similarity variable $\xi = \pm x/t$ and assume that

$$\hat{\gamma}(x,t) = \tilde{\gamma}(\xi) , \qquad \hat{V}(x,t) = \tilde{V}(\xi) , \tag{3.59}$$

corresponding to scale invariant solutions. Observe that $\xi =$ constant is a ray in the x, t plane, and we are seeking solutions that are constant on any ray. Where fields are smooth, the compatibility equation (3.36) and the equation of motion (3.37) become ordinary differential equations,

$$V_\xi + \xi\gamma_\xi = 0 , \tag{3.60}$$

$$\rho_\circ \xi V_\xi + \sigma_\gamma \gamma_\xi = 0 . \tag{3.61}$$

Solving for ξ,

$$\xi = \pm\sqrt{\frac{\hat{\sigma}\,'(\gamma)}{\rho_\circ}}\,. \tag{3.62}$$

We will be interested exclusively in solutions that involve only stable phases, i.e., $\hat{\sigma}\,'(\gamma) \geq 0$ everywhere. Under this restriction, any non-constant smooth solution of the ordinary differential equations (3.60) and (3.61) is called a *fan*.

If the particle velocity V is known on any ray in a fan, it can be calculated on every other ray in the fan. Consider any two positive rays, $\xi^+ > \xi^- > 0$. By (3.60) and (3.62),

$$\int_{\xi^+}^{\xi^-} V_\xi d\xi = -\frac{1}{\sqrt{\rho_\circ}} \int_{\xi^+}^{\xi^-} \sqrt{\sigma_\xi}\,\gamma_\xi d\xi\,.$$

Integrating the left side and changing the variable of integration on the right

$$V^- - V^+ = -\frac{1}{\sqrt{\rho_\circ}} \int_{\gamma^+}^{\gamma^-} \sqrt{\hat{\sigma}\,'(\gamma)}d\gamma\,. \tag{3.63}$$

The superscripts "+" and "-" indicate the value of a quantity at ξ^+ and ξ^-, respectively.

For negative rays, $\xi^+ < \xi^- < 0$, the corresponding result is

$$V^- - V^+ = +\frac{1}{\sqrt{\rho_\circ}} \int_{\xi^+}^{\xi^-} \sqrt{\hat{\sigma}\,'(\gamma)}d\gamma\,. \tag{3.64}$$

Appendix A provides an additional, short treatment of fans and discontinuities.

3.6.3 The Maxwell stress

Consider a two-phase material with a non-monotonic stress response function. In an equilibrium mixture, two phases are separated by a stationary phase boundary,

$\dot{s} = 0$. By the jump condition (3.38), the stress must be identical on the two sides of the phase boundary: $\sigma^+ = \sigma^-$. The stress $\sigma_\circ$ at which the driving traction vanishes is the *Maxwell stress*. It is found by solving for $\sigma_\circ = \sigma^+ = \sigma^-$ with $f = 0$ in the expression (3.52) for the driving traction. On a stress-strain curve, the two areas between the curve and the line segment from (γ^-, σ^-) to (γ^+, σ^+) are equal at the Maxwell stress, Figure 3.4.

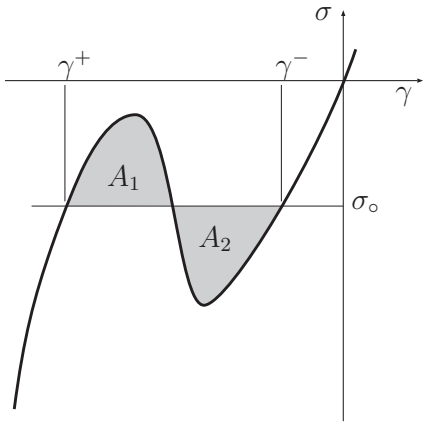

Figure 3.4: The driving traction on a stationary phase boundary vanishes at the Maxwell stress $\sigma_\circ$. The area A_1 above the horizontal line segment from $(\gamma^+, \sigma_\circ)$ to $(\gamma^-, \sigma_\circ)$ but below the curve $\sigma = \hat{\sigma}(\gamma)$ equals the area A_2 below the horizontal line segment and above the curve.

Chapter 4

Loci of contact states and constitutive models

This chapter introduces an initial-boundary value problem that is the cornerstone to understanding predictions of the present model as regards the response of the plates in the impact experiments. Once we are able to solve this initial-boundary value problem, it is a trivial step to treat impact problems and Riemann problems. Initial-boundary value problems, impact problems, and Riemann problems are the foundation of the numerical method introduced in Chapter 6.

We begin with an initial-boundary value problem with either a constant prescribed velocity boundary condition or a constant prescribed stress boundary condition. In this context, the notions of *possible state*, *contact states* and the *locus of contact states* are introduced. The locus of contact states will be particularly useful, as it describes all boundary conditions that can be accommodated by similarity solutions for prescribed initial conditions. This locus is related to the *Hugoniot curve* and *release isentrope* of the shock compression literature.

We then consider a particular form of the nonmonotonic stress response function, used in later chapters to describe GeO_2. For this material, we construct all forms of possible states and examine a representative locus of contact states in the σ, V plane. It will be seen that there are initial-boundary value problems for which the locus of contact states does not select a unique solution.

This lack of uniqueness motivates the introduction of new constitutive information, in the form of *kinetic relations* and *nucleation criteria*. Suitably restricted, these constitutive properties restore uniqueness.

We next consider the 3-phase monotonic stress response function that will be our model for the ancillary materials. Solutions to initial-boundary value problems for this type of stress-response function are also not unique. To restore uniqueness, we prescribe *a priori* a *particular* kinetic relation and nucleation criterion. We construct all forms of possible states that satisfy these restrictions and present a representative locus of contact states.

Finally, we describe how loci of contact states are used to solve impact problems and Riemann problems.

4.1 An initial-boundary value problem

We will consider an initial-boundary value problem that has been well examined [11, 74, 75, 79]. The presentation here closely follows that of Pence [74, 75].

Consider the half-space $x > 0$ with constant initial conditions

$$\hat{\gamma}(x,0) = \gamma_R \,, \quad \hat{V}(x,0) = V_R \quad \text{for } x \geq 0 \,. \tag{4.1}$$

The subscript R refers to the *right-hand* problem, Figure 4.1. For times $t > 0$, either

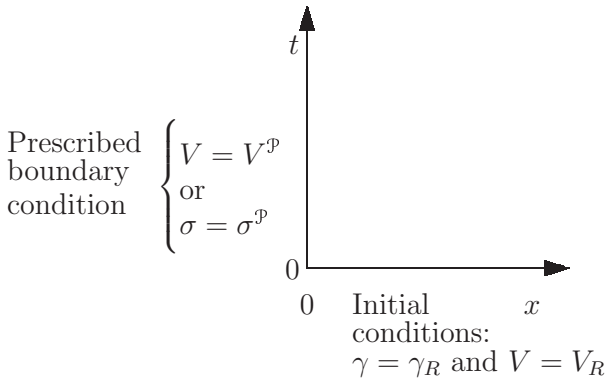

Figure 4.1: An initial-boundary value problem.

a constant velocity or a constant stress condition is prescribed on $x = 0$:

$$\hat{V}(0,t) = V^{\mathcal{P}} \text{ for } t > 0 \,, \tag{4.2}$$

or

$$\hat{\sigma}(0,t) = \sigma^{\mathcal{P}} \text{ for } t > 0 \,. \tag{4.3}$$

The superscript $\mathcal{P}$ indicates a "prescribed" quantity.

We wish to satisfy the field equations and jump conditions (3.36)-(3.39), for all $x > 0$, $t > 0$ subject to the initial conditions (4.1) and *either* (4.2) *or* (4.3).

Because the formulation of the problem involves no length or time scales, introduce $\xi = x/t$ and assume that the fields are scale-invariant:

$$\hat{\gamma}(x,t) = \tilde{\gamma}(\xi) \,, \qquad \hat{V}(x,t) = \tilde{V}(\xi) \,. \tag{4.4}$$

For a given stress response function, $\hat{\sigma}(\gamma)$, we call any pair of piecewise smooth functions $(\tilde{\gamma}(\xi), \tilde{V}(\xi))$ defined for $\xi \geq 0$ a *possible state* if the pair

1. satisfies the initial conditions,

2. satisfies the field equations,

3. satisfies the dissipation inequality (3.54) at any strain discontinuity.

Our definition of a possible state is the same as Pence's notion of a *candidate dynamical state* [74, 75], except that we include the last requirement.

Thus, a *possible state* is an admissible scale-invariant solution to the field equations in the quadrant $x > 0$, $t > 0$, subject to the initial conditions but not subject to boundary conditions. It is composed of some combination of *elementary waves*, namely fans, shocks, and phase boundaries, as in Figure 4.2.

The particular composition of a possible state depends on the initial conditions, the stress response function and, for a phase changing material, on the material

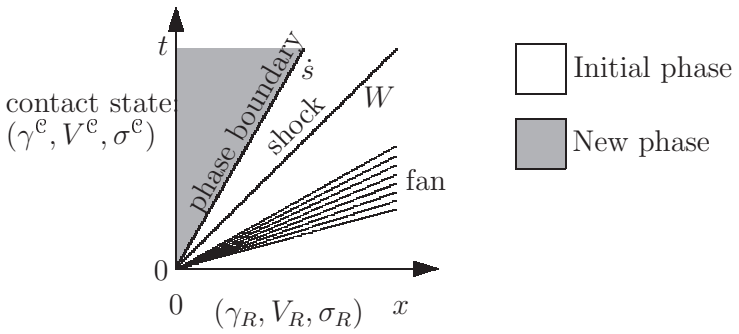

Figure 4.2: A similarity solution to an initial-boundary value problem is composed of some combination of elementary scale-invariant solutions to the balance equations. The elementary solutions are shocks, phase boundaries, and fans.

properties that govern phase nucleation and propagation.

For each possible state, let $\gamma^{\mathcal{C}}$, $V^{\mathcal{C}}$, and $\sigma^{\mathcal{C}}$ denote the values of the deformation gradient, particle velocity and stress on the *contact interface* $x = 0$,

$$\gamma^{\mathcal{C}} = \tilde{\gamma}(0) \,, \qquad V^{\mathcal{C}} = \tilde{V}(0) \,, \qquad \sigma^{\mathcal{C}} = \hat{\sigma}(\gamma^{\mathcal{C}}) \,. \tag{4.5}$$

The superscript $\mathcal{C}$ denotes a *contact value*, and the trio $(\gamma^{\mathcal{C}}, V^{\mathcal{C}}, \sigma^{\mathcal{C}})$ will be called a *contact state*.

A possible state is a solution to the initial-boundary value problem with *prescribed contact velocity* $V^{\mathcal{P}}$ if :

$$V^{\mathcal{C}} = V^{\mathcal{P}} \,. \tag{4.6}$$

A possible state is a solution to the initial-boundary value problem with *prescribed contact stress* $\sigma^{\mathcal{P}}$ if:

$$\sigma^{\mathcal{C}} = \sigma^{\mathcal{P}} \,. \tag{4.7}$$

4.2 Locus of contact states

Pence [74, 75] considered the set of all contact states in the σ, V plane; an example of this *locus of contact states* or *contact locus* is shown in Figure 4.3 for a single-phase concave material model $\hat{\sigma}(\gamma)$. The topography of a locus of contact states is dependent on the material, on the initial deformation gradient γ_R and the initial velocity V_R. We will say that a locus of contact states is *based* at the initial state (γ_R, V_R). The locus based at $(0, 0)$ is the *principal locus of contact states*. Changes in the initial particle velocity V_R merely translate the figure vertically.

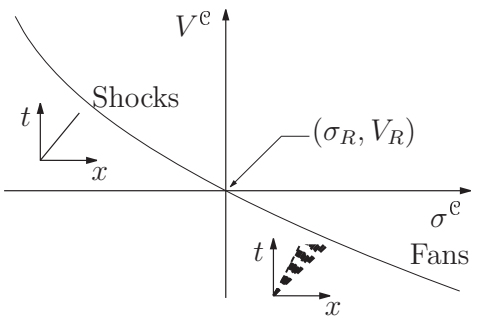

Figure 4.3: Locus of contact states for a concave material. The axes cross at (σ_R, V_R), i.e., where the locus is based. The only solutions supported by this material are those composed of a single shock or a single fan.

As shown in Appendix A, the locus of contact states on the right half-space $x > 0$ for any single-phase material is a curve of negative slope passing through the initial state (γ_R, V_R). The intersection of this locus with a horizontal line at the prescribed contact velocity, $V^{\mathcal{P}}$, selects a unique solution $V^{\mathcal{C}} = V^{\mathcal{P}}$. Likewise, a vertical line at the prescribed contact stress selects a unique solution $\sigma^{\mathcal{C}} = \sigma^{\mathcal{P}}$.

The shock compression literature has long embraced the locus of contact states, but with different terminology. Occasionally, the term *wave curve* appears in a sense nearly equivalent to that of the locus of contact states [67]. More typically, the terms *Hugoniot* and *release isentrope* substitute for the locus in specific circumstances.

If a possible state is constructed of a *single compressive* strain discontinuity, then the contact state $(\gamma^{\mathcal{C}}, V^{\mathcal{C}}, \sigma^{\mathcal{C}})$ is known in the shock compression literature as a *Hugoniot state* for the isothermal problem. For prescribed initial conditions (γ_R, V_R), the locus of all Hugoniot states is *the Hugoniot* based at the initial conditions (γ_R, V_R). The *principal Hugoniot* is based at $(0, 0)$.

The locus of all contact states $(\gamma^{\mathcal{C}}, V^{\mathcal{C}}, \sigma^{\mathcal{C}})$ for possible states constructed only

of *expansive fans* is the *release isentrope* from the prescribed initial conditions in the isothermal problem.

4.3 The trilinear model

We will describe GeO_2 with a special up-down-up model known as the *trilinear* model, Figure 4.4. Its stress response function is:

$$\hat{\sigma}(\gamma) = \begin{cases} \text{undefined} & \text{for } \gamma < \gamma_Z \ , \\ \hat{\sigma}_1(\gamma) & \text{for } \gamma_Z \le \gamma \le \gamma_M \ , \\ \hat{\sigma}_2(\gamma) & \text{for } \gamma_M < \gamma < \gamma_m \ , \\ \hat{\sigma}_3(\gamma) & \text{for } \gamma_m \le \gamma \le \gamma_F \\ \text{undefined} & \text{for } \gamma > \gamma_F \ , \end{cases} \tag{4.8}$$

where each function $\hat{\sigma}_i(\gamma)$ is of the form

$$\hat{\sigma}_i(\gamma) = \bar{E}_i \gamma + d_i \ . \tag{4.9}$$

We will require the tangent modulus to be negative in the middle interval and positive in the other two phases:

$$\bar{E}_1 > 0 \ , \qquad \bar{E}_2 < 0 \ , \qquad \bar{E}_3 > 0 \ . \tag{4.10}$$

This model has been used extensively by Abeyaratne and Knowles: see, for example, [4, 5, 7].

Each of the segments $\hat{\sigma}_i(\gamma)$ is invertible. Each inverse is represented by $\hat{\gamma}_i(\sigma)$.

We will insist that $\hat{\sigma}(\gamma)$ be continuous over $\gamma \in [\gamma_Z, \gamma_F]$. This requires that

$$\bar{E}_2 = \frac{\sigma_m - \sigma_M}{\gamma_m - \gamma_M} \ , \tag{4.11}$$

$$d_2 = \frac{1}{2}\{\sigma_M + \sigma_m - \bar{E}_2(\gamma_M + \gamma_m)\} \ . \tag{4.12}$$

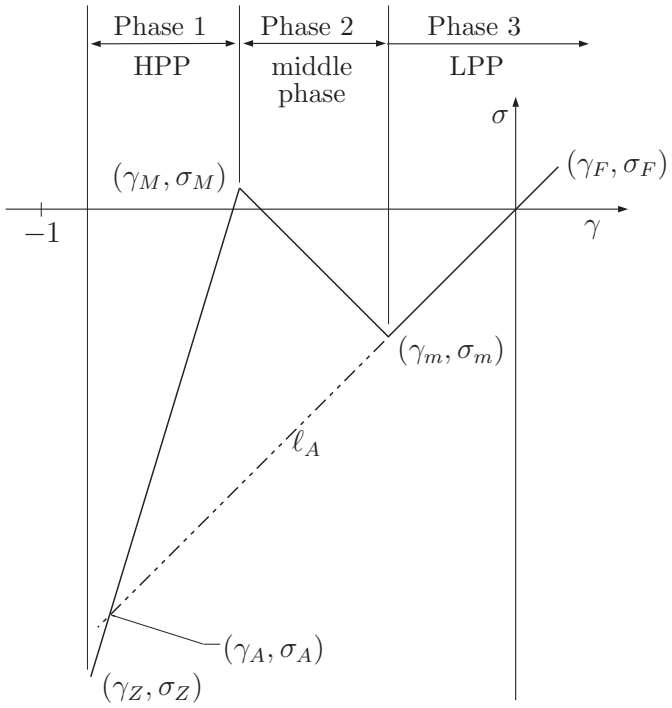

Figure 4.4: Stress response function of a trilinear material.

The equations for the stable branches intersect at (γ_A, σ_A),

$$\gamma_A = -\frac{d_1 - d_3}{\bar{E}_1 - \bar{E}_3}\,, \tag{4.13}$$

$$\sigma_A = \frac{d_3\bar{E}_1 - d_1\bar{E}_3}{\bar{E}_1 - \bar{E}_3}\,. \tag{4.14}$$

Define the *transformation strain* γ_T by

$$\gamma_T \;=\; \hat{\gamma}_1(0) - \hat{\gamma}_3(0) \;=\; \frac{d_3\bar{E}_1 - d_1\bar{E}_3}{\bar{E}_1\bar{E}_3}\,. \tag{4.15}$$

For a material like that of Figure 4.4, for which $\sigma_M > 0$, γ_T is the *static transformation strain* at $\sigma = 0$. For other materials, the meaning is less physical. The definition of transformation strain varies between authors.

We will require expressions for the driving traction, derived in the next section.

4.3.1 Driving traction

Consider a phase boundary with the + side in phase 3 and the − side in phase 1, Figure 4.5(a). From the expression (3.52) for the driving traction in uniaxial deformation and the expressions (4.8)-(4.15) for the stress response function of a trilinear material, the following equivalent expressions can be found for the driving traction

$$\hat{f}(\gamma^+,\gamma^-) = \frac{1}{2}\left\{\left(\sigma_M-\sigma^+\right)\left(\gamma_m-\gamma^-\right)+\left(\sigma_m-\sigma^-\right)\left(\gamma^+-\gamma_M\right)\right\}\ , \tag{4.16a}$$

$$= \frac{1}{2}\{\ (d_1-d_3)\left(\gamma_m+\gamma_M-\gamma^--\gamma^+\right) + \left(\bar{E}_1-\bar{E}_3\right)\left(\gamma_m\gamma_M-\gamma^-\gamma^+\right)\}\ , \tag{4.16b}$$

$$= \frac{1}{2}\{\ \gamma_T\left(\sigma^++\sigma^--\sigma_m-\sigma_M\right) + \frac{\bar{E}_1-\bar{E}_3}{\bar{E}_1\bar{E}_3}\left(\sigma_M\sigma_m-\sigma^+\sigma^-\right)\}\ , \tag{4.16c}$$

$$= \frac{\gamma_T}{2\sigma_A}\left\{\sigma_A\left(\sigma^++\sigma^--\sigma_m-\sigma_M\right)+\sigma_M\sigma_m-\sigma^+\sigma^-\right\}\ . \tag{4.16d}$$

Now consider a phase boundary with the + side in phase 1 and the − side in phase 3, Figure 4.5(b). Recalling that $\hat{f}(\gamma_a,\gamma_b) = -\hat{f}(\gamma_b,\gamma_a)$ by (3.53), the driving

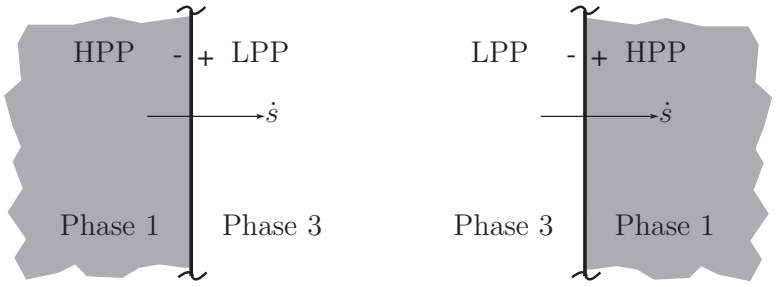

(a) A low pressure to high pressure phase boundary.

(b) A high pressure to low pressure phase boundary.

Figure 4.5: Phase boundaries in a trilinear material.

traction is easily found to be

$$\hat{f}(\gamma^+,\gamma^-) = -\frac{1}{2}\left\{\left(\sigma_M-\sigma^-\right)\left(\gamma_m-\gamma^+\right)+\left(\sigma_m-\sigma^+\right)\left(\gamma^--\gamma_M\right)\right\}\ , \tag{4.17a}$$

$$= -\frac{1}{2}\left\{\ (d_1-d_3)\left(\gamma_m+\gamma_M-\gamma^+-\gamma^-\right) + \left(\bar{E}_1-\bar{E}_3\right)\left(\gamma_m\gamma_M-\gamma^+\gamma^-\right)\ \right\}\ , \tag{4.17b}$$

$$= -\frac{1}{2}\left\{\ \gamma_T\left(\sigma^-+\sigma^+-\sigma_m-\sigma_M\right) + \frac{\bar{E}_1-\bar{E}_3}{\bar{E}_1\bar{E}_3}\left(\sigma_M\sigma_m-\sigma^-\sigma^+\right)\ \right\}\ , \tag{4.17c}$$

$$= -\frac{\gamma_T}{2\sigma_A}\left\{\sigma_A\left(\sigma^-+\sigma^+-\sigma_m-\sigma_M\right)+\sigma_M\sigma_m-\sigma^-\sigma^+\right\}\ . \tag{4.17d}$$

4.3.2 The Maxwell stress

The Maxwell stress for a trilinear material is

$$\sigma_\circ = \sigma_A + \sqrt{(\sigma_A-\sigma_M)\,(\sigma_A-\sigma_m)}\ . \tag{4.18}$$

This was found by setting $f=0$ in the expression (4.16d) or (4.17d) for the driving traction, then assuming that $\sigma_\circ=\sigma^+=\sigma^-$ and solving for $\sigma_\circ$.

4.3.3 Possible states for any initial-boundary value problem

It will be assumed that the material is initially in a stable phase:

$$\gamma_R \le \gamma_M\ , \qquad \text{or} \qquad \gamma_R \ge \gamma_m\ . \tag{4.19}$$

The forms of possible states for any initial-boundary value problem depend on the relative values of the moduli $\bar{E}_3$ and $\bar{E}_1$ of the low and high pressure phases, and on whether the intersection point (γ_A,σ_A) lies within the bounds $[\gamma_Z,\ \gamma_F]$. For definiteness, we assume that the high pressure phase is stiffer than the low pressure phase, and that the intersection of the line segments of the two stable phases lies

within the high pressure phase:

$$\bar{E}_1 > \bar{E}_3 \,, \tag{4.20}$$

$$-1 < \gamma_Z < \gamma_A < \gamma_M < \gamma_m \,. \tag{4.21}$$

The possible states are found by constructing every combination of waves that satisfies the initial conditions and the boundary conditions, then eliminating those that violate the dissipation inequality. If the material is initially in the *low pressure phase*, three types of solutions survive this procedure, Figures 4.6(a)–4.6(c):

1. If the contact strain $\gamma^{\mathfrak{C}}$ is in the LPP, then the solution is a shock, Figure 4.6(a).

2. If the contact strain $\gamma^{\mathfrak{C}}$ is in the HPP and $\gamma^{\mathfrak{C}} > \gamma_A$, then the solution is a shock followed by a subsonic phase boundary, Figure 4.6(b). Solutions with $\sigma^{\mathfrak{C}} > \sigma_\circ$ violate the dissipation inequality, so we have $\sigma^{\mathfrak{C}} \leq \sigma_\circ$.

3. If the contact strain $\gamma^{\mathfrak{C}}$ is in the HPP and $\gamma^{\mathfrak{C}} \leq \gamma_A$, then the solution is a sonic or supersonic phase boundary, Figure 4.6(c).

If the material is initially in the *high pressure phase*, there are only two survivors, Figures 4.6(d)–4.6(e):

1. If the contact strain $\gamma^{\mathfrak{C}}$ is in the HPP, then the solution is a shock, Figure 4.6(d).

2. If the contact strain $\gamma^{\mathfrak{C}}$ is in the LPP, then the solution is a shock followed by a subsonic phase boundary, Figure 4.6(e). Solutions with $\sigma^{\mathfrak{C}} < \sigma_\circ$ violate the dissipation inequality, so we have $\sigma^{\mathfrak{C}} \geq \sigma_\circ$.

The procedure by which these possible states are found was nicely detailed by Lin [58] for a Riemann problem involving a more general up-down-up material, and by Abeyaratne and Knowles [5] for a Riemann problem in a particular trilinear material.

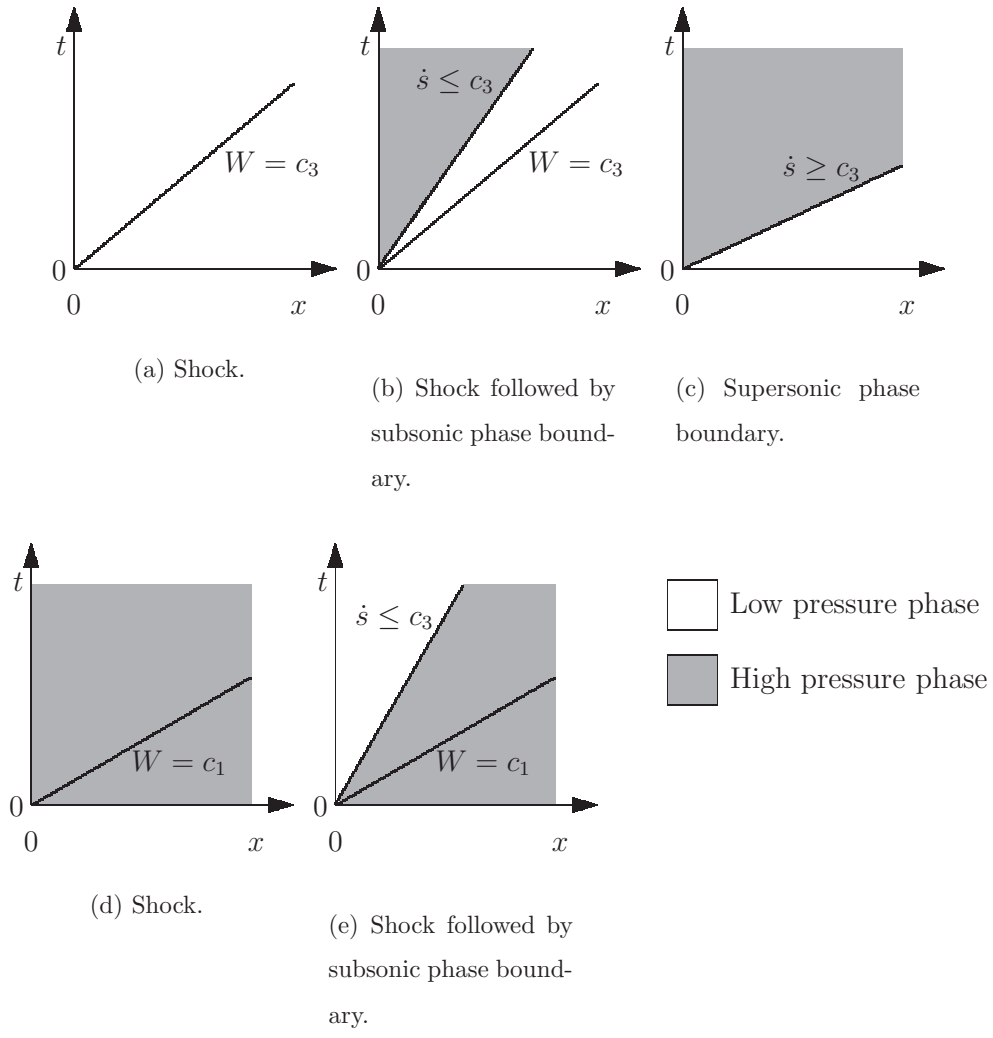

(a) Shock.

(b) Shock followed by subsonic phase boundary.

(c) Supersonic phase boundary.

(d) Shock.

(e) Shock followed by subsonic phase boundary.

Figure 4.6: Forms of the possible states to an initial-boundary value problem for a trilinear material initially in the low pressure phase (top) or the high pressure phase (bottom).

4.3.4 Locus of contact states

To determine the locus of contact states for prescribed initial conditions, we find in the next several sections the contact locus for each of the different types of solutions just presented. The locus we seek is the union of the individual ones. Figure 4.7 shows the result for the principal locus of contact states.

Some of the resulting expressions are similar whether the material is initially in

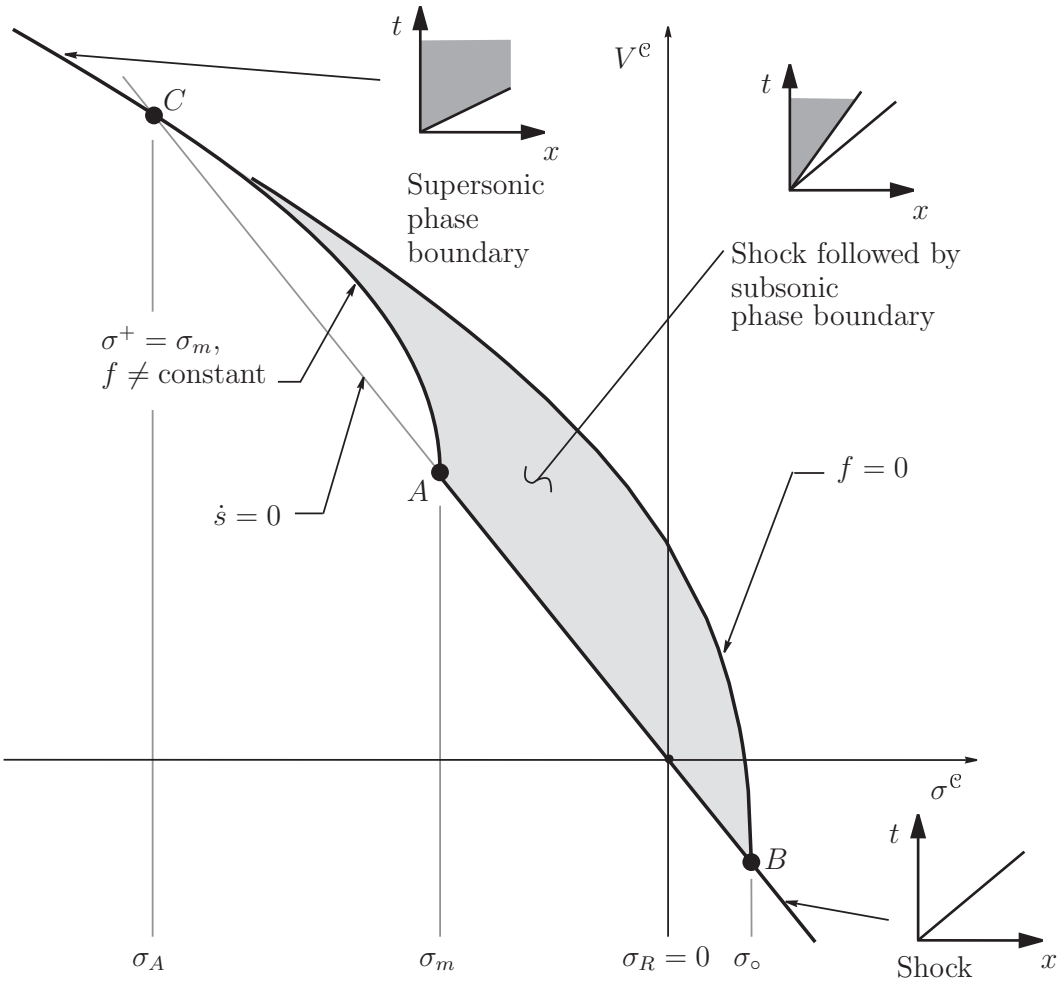

Figure 4.7: Principal locus of contact states for a trilinear material on the positive half space $x > 0$. To reach contact stresses $\sigma^{\mathfrak{C}} < \sigma_A$, the similarity solution must be a supersonic phase boundary, Figure 4.6(c). For contact stresses $\sigma^{\mathfrak{C}} > \sigma_\circ$, the similarity solution must be a shock, Figure 4.6(a). For contact values $(\sigma^{\mathfrak{C}}, V^{\mathfrak{C}})$ in ABC or on the boundaries AC or BC, the similarity solution must be a shock followed by a phase boundary of nonzero velocity, Figure 4.6(b). Contact values on the AB boundary of ABC can be reached by two different forms of similarity solutions, either a shock or a shock followed by a phase boundary of zero velocity $\dot{s} = 0$. The principal Hugoniot is the union of the loci for compressive shocks and supersonic phase boundaries: namely the line segment AB and the locus $\sigma^{\mathfrak{C}} < \sigma_A$.

the low pressure phase or the high pressure phase. When this is true, the expression is written in a general way using $\bar{E}_R$, d_R for parameters in the initial phase.

Locus of contact states for shocks

Specializing the jump conditions to the case of a linear phase, the locus of contact states for solutions composed of a single shock is found to be a straight line segment in the $(\sigma^{\mathcal{C}}, V^{\mathcal{C}})$ plane,

$$V^{\mathcal{C}} = V_R - \frac{1}{\sqrt{\bar{E}_R \rho_\circ}}(\sigma_R - \sigma^{\mathcal{C}}) \ , \tag{4.22}$$

$$\sigma^{\mathcal{C}} \in \begin{cases} [-1, \sigma_M] & \text{if } \gamma_R \in \text{Phase 1} \\ [\sigma_m, \sigma_F] & \text{if } \gamma_R \in \text{Phase 3} \end{cases} \tag{4.23}$$

Equation (4.22) will be called the *shock locus*. In Figure 4.7, it is the line segment on which A and B lie; it extends from point A to $\sigma^{\mathcal{C}} = \sigma_F$, which is off the right side of the figure.

Because $\hat{\sigma}_i(\gamma)$ is linear in each phase, every shock travels at the *known* characteristic wave speed of the phase,

$$W = c_R \ . \tag{4.24}$$

Locus of contact states for supersonic phase boundaries

Since we are focusing on materials for which the high pressure phase is stiffer than the low pressure phase, a phase boundary can be supersonic only if the material on the + side is in phase 3, the low pressure phase.

Specializing the jump condition (3.41) for $\gamma_R \in$ Phase 3 and $\gamma^{\mathcal{C}} \in$ Phase 1, the contact values $(\sigma^{\mathcal{C}}, V^{\mathcal{C}})$ are found to lie on a hyperbola in the σ, V plane:

$$\frac{\left(\sigma^{\mathcal{C}} - \alpha\right)^2}{\left(\sqrt{\rho_\circ K}\right)^2} - \frac{[\![V]\!]^2}{\left(\sqrt{K/\bar{E}_1}\right)^2} = 1 \ , \tag{4.25}$$

where

$$\sigma^{\mathfrak{C}} < \sigma_A \ , \tag{4.26}$$

$$[\![V]\!] = V_R - V^{\mathfrak{C}} \ , \tag{4.27}$$

$$\alpha = \frac{\bar{E}_3 \left(\sigma_R + d_1\right) + \bar{E}_1 \left(\sigma_R - d_3\right)}{2\bar{E}_3} \ , \tag{4.28}$$

$$K = \frac{\left(\bar{E}_1 d_3 - d_1 \bar{E}_3 + \sigma_R \left(\bar{E}_3 - \bar{E}_1\right)\right)^2}{4\rho_\circ \bar{E}_3^2} \geq 0 \ . \tag{4.29}$$

Properties of this hyperbola include:

$$\text{center: } \left(\sigma^{\mathfrak{C}} = \alpha, [\![V]\!] = 0\right) \ , \tag{4.30}$$

$$\text{asymptotes: } [\![V]\!] = \pm \frac{1}{\sqrt{\bar{E}_1 \rho_\circ}} \left(\sigma^{\mathfrak{C}} - \alpha\right) \ , \tag{4.31}$$

$$\text{vertical tangents: } \sigma^{\mathfrak{C}} = \begin{cases} \sigma_R \ , \\ d_1 + \frac{\bar{E}_1}{\bar{E}_3} \left(\sigma_R - d_3\right) \ . \end{cases} \tag{4.32}$$

Two special points $(\sigma^{\mathfrak{C}}, V^{\mathfrak{C}})$ lie on the hyperbola:

$$(\sigma^{\mathfrak{C}}, V^{\mathfrak{C}}) = (\sigma_R \ , V_R) \ , \tag{4.33}$$

$$(\sigma^{\mathfrak{C}}, V^{\mathfrak{C}}) = \left(\sigma_A \ , V_R - \frac{1}{\sqrt{\bar{E}_3 \rho_\circ}} (\sigma_R - \sigma_A)\right) \ . \tag{4.34}$$

By (4.32) and (4.33), the hyperbola and one of its vertical tangents passes through the front state. By (4.34) and (4.22), it intersects the expression for the shock locus at $\sigma^{\mathfrak{C}} = \sigma_A$.

The dissipation inequality is satisfied by the portion of the locus (4.25)-(4.29) where $[\![\sigma]\!][\![V]\!] \geq 0$. In Figure 4.7, this is the solid curve to the left of point C.

Locus of contact states for subsonic phase boundaries

A subsonic phase boundary is in general preceded by a shock, Figures 4.6(b) and 4.6(e). Denote the constant state of the material between the shock and the phase boundary by $(\gamma^+, V^+, \sigma^+)$. The jump conditions must be satisfied across both the shock with propagation velocity $W = c_R$ and the phase boundary with propagation velocity $\dot{s}$,

$$V^+ - V_R + \frac{1}{\sqrt{\bar{E}_R \rho_\circ}}(\sigma_R - \sigma^+) = 0 \,, \tag{4.35}$$

$$W = c_R \,, \tag{4.36}$$

$$V^+ - V^{\mathfrak{C}} + \dot{s}(\gamma^+ - \gamma^{\mathfrak{C}}) = 0 \,, \tag{4.37}$$

$$\rho_\circ (V^+ - V^{\mathfrak{C}})\dot{s} + (\sigma^+ - \sigma^{\mathfrak{C}}) = 0 \,, \tag{4.38}$$

$$\sigma_R \in [-1, \sigma_M] \;, \quad \sigma^{\mathfrak{C}} \in [\sigma_\circ, \sigma_F] \quad \text{if } \gamma_R \in \text{Phase 1} \,, \tag{4.39}$$

$$\sigma_R \in [\sigma_m, \infty] \;, \quad \sigma^{\mathfrak{C}} \in [\sigma_\circ, \sigma_A] \quad \text{if } \gamma_R \in \text{Phase 3} \,, \tag{4.40}$$

subject, of course, to $\hat{f}(\gamma^+, \gamma^-) \geq 0$ from the dissipation inequality.

Equations (4.35)-(4.40) provide *four* equations for the *five* unknowns γ^+,V^+, $\dot{s}$, γ^-, and V^-. The locus of contact states is therefore not a curve but a *region* in the σ, V plane. In Figure 4.7 this is ABC. The region is bounded by three special contact loci, AB, BC and CA. The first of these, AB, is the locus of *stationary* phase boundaries $\dot{s} = 0$: it lies on the shock locus. The second boundary locus, BC, is the one on which the driving traction vanishes. It is found by enforcing $f = 0$ in the appropriate expression (4.16c) or (4.17c) for the driving traction, in conjunction with (4.35)-(4.38) and either (4.39) or (4.40). The result is a lengthy polynomial of third order in $\sigma^{\mathfrak{C}}$ and second order in $V^{\mathfrak{C}}$. On the final locus, CA, the driving traction takes the maximum possible value for each subsonic phase boundary velocity. This maximum value is found by exploiting the interpretation of f as the signed area between $\hat{\sigma}(\gamma)$ and the chord connecting the two points γ^- and γ^+. For a given $\dot{s} < c_3$, this area is maximized when $(\gamma^+, \sigma^+) = (\gamma_m, \sigma_m)$ for a LPP to HPP transformation,

and when $(\gamma^+, \sigma^+) = (\gamma_M, \sigma_M)$ for a HPP to LPP transformation. Thus, the CA boundary is found by fixing (γ^+, σ^+) appropriately. The resulting expression is a hyperbola identical in form to the one for supersonic phase boundaries, (4.25), but with $\sigma^+ = \sigma_m$ substituting for σ_R if the initial state is in the LPP or with $\sigma^+ = \sigma_M$ substituting for σ_R if the initial state is in the HPP, and with V^+ computed from (4.35) substituting for V_R.

It is important to emphasize that the intermediate state $(\gamma^+, V^+, \sigma^+)$ *between* the shock wave and the phase boundary is not represented in Figure 4.7. Because this is a state behind a shock passing into material at the initial state, all intermediate pairs (σ^+, V^+) lie on the shock locus. Thus, though two contact states may be close together in ABC, their phase boundary velocities and their corresponding "+" states can be dramatically different. Consider two extremes. If the contact state $(\sigma^{\mathfrak{C}}, V^{\mathfrak{C}})$ lies *anywhere* on CA in Figure 4.7, then the intermediate state (σ^+, V^+) lies at the point A. On the other hand, if the contact state $(\sigma^{\mathfrak{C}}, V^{\mathfrak{C}})$ lies on BC, then the intermediate pair (σ^+, V^+) varies as the contact state varies along BC. In particular, if the contact state $(\sigma^{\mathfrak{C}}, V^{\mathfrak{C}})$ is at the point B, then the intermediate pair (σ^+, V^+) is also at B. But as the contact state moves toward C, the intermediate pair (σ^+, V^+) moves in the positive σ direction along the shock locus. It is possible, then, that the intermediate + state can be *less* compressed than the initial state even though the contact state is more *compressed* than the initial state. In other words, a *compressive* phase boundary can be preceded by a *rarefactive* shock!

4.3.5 Kinetic relations

Consider Figure 4.7. A horizontal line drawn at any velocity $V^{\mathfrak{C}} = V^{\mathfrak{P}}$ above point C or below point B has a unique intersection with the locus of contact states. Likewise, a vertical line drawn at any stress left of point C or right of point B has a unique intersection with the locus. Thus, there is a unique solution to any initial-boundary value problem with initial conditions $\gamma_R = 0$, $V_R = 0$ and constant boundary conditions if the prescribed boundary conditions $V^{\mathfrak{P}}$ or $\sigma^{\mathfrak{P}}$ fall outside of

the region ABC.

On the other hand, if the prescribed boundary conditions fall within the region ABC or on its boundaries, then there is an infinite set of admissible solutions available for the initial-boundary value problem. Solutions to these initial-boundary value problems are not unique.

Abeyaratne and Knowles, viewing this lack of uniqueness associated with the presence of a phase boundary as a constitutive deficiency, introduce a *kinetic relation* [5]. A kinetic relation prescribes that the driving traction on a subsonic phase boundary is related to the phase boundary velocity through a *kinetic response function*, $\mathcal{F}_{ab}$,

$$f = \mathcal{F}_{ab}(\dot{s}) \ , \tag{4.41}$$

where a indicates the phase *ahead* of the phase boundary (the + or parent phase) and b the phase *behind* it (the − or product phase).

The kinetic relation is relevant only for subsonic phase boundaries, as there is no lack of uniqueness and therefore no need for this additional constitutive information for supersonic phase boundaries or in the absence of phase changes.

The kinetic relation must satisfy the dissipation inequality (3.54), and we expect that $\mathcal{F}_{ab}(\dot{s}) = -\mathcal{F}_{ab}(-\dot{s})$. With these restrictions, the region comprising the set of all available pairs $(\dot{s}, \mathcal{F}_{ab}(\dot{s}))$ for specified parent and product phases a and b can be determined, Figure 4.8. The kinetic response function (4.41) must lie in the shaded region of this figure. If the graph of $f = \mathcal{F}_{ab}(\dot{s})$ coincides with the boundary $f = 0$, the kinetic relation is said to be *non-dissipative*. If the graph of $f = \mathcal{F}_{ab}(\dot{s})$ lies on the top boundary of the first quadrant and on the bottom boundary in the third quadrant, the kinetic relation $\mathcal{F}_{ab}(\dot{s})$ maximizes the driving traction for any prescribed phase boundary velocity. This last kinetic relation is called the *maximum dissipation* kinetic relation, also affectionately known as *the roof*.

The roof has a useful interpretation. Recall by (3.52) that the driving traction $f = f(\gamma^+, \gamma^-)$ is the sum of the signed areas between $\hat{\sigma}(\gamma)$ and the chord connecting

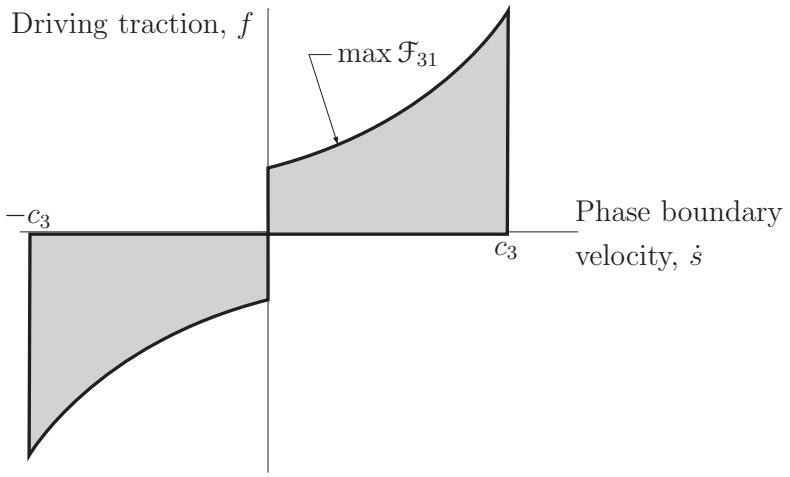

Figure 4.8: The region of possible pairs $(\dot{s}, f)$ for the trilinear material initially in phase 3, the low pressure phase. The curve for the kinetic response function expressed by (4.41) must lie in the shaded region. The top boundary in the first quadrant and the bottom boundary in the third quadrant is "the roof."

the points (γ^-, σ^-) and (γ^+, σ^+). By inspection, $|f|$ is maximized for a given phase boundary velocity $\dot{s}$ when a chord of slope $\rho_\circ \dot{s}^2 = [\![\sigma]\!]/[\![\gamma]\!]$ connects (γ^+, σ^+) and (γ^-, σ^-) without crossing $\hat{\sigma}(\gamma)$. For a transformation from the *low* to the *high* pressure phases, this can only happen when the strain ahead of the phase boundary is $\gamma^+ = \gamma_m$. For a transformation from the *high* to the *low* pressure phases, this can only happen when the strain ahead of the phase boundary is $\gamma^+ = \gamma_M$. Therefore, the intermediate values (γ^+, σ^+) are always known when the roof is the kinetic relationship.

Figure 4.9 will help us to understand how a kinetic relation in the f, $\dot{s}$ plane maps onto the contact locus. Here, loci for several constant values of driving traction f and for different constant phase boundary velocities $\dot{s}$ are shown. The former are described by polynomials similar to the one which describes the locus $f = 0$, and the latter are all straight lines.

We will consider only kinetic response functions that are continuous for all subsonic phase boundary velocities $|\dot{s}| \leq c_3$ except possibly for a discontinuity at $\dot{s} = 0$.

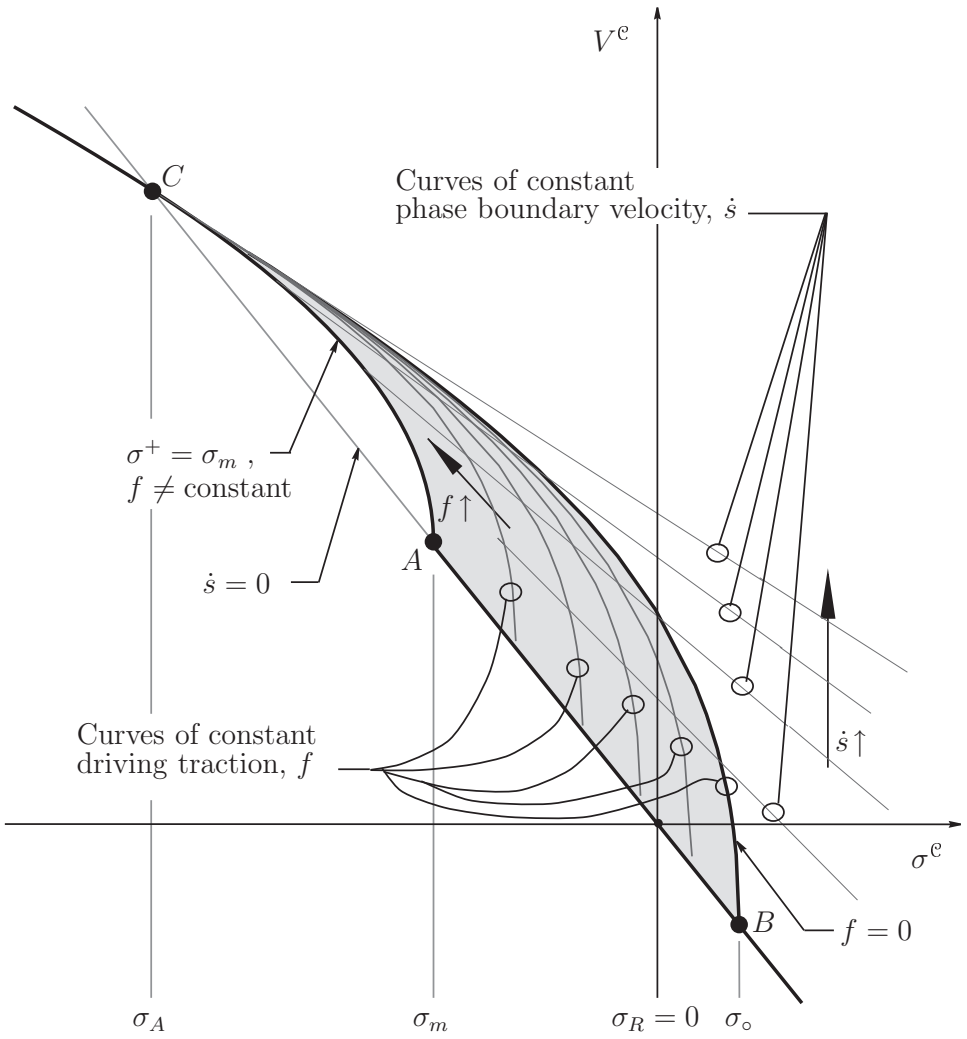

Figure 4.9: In the region ABC, loci of contact states for constant driving traction and for constant phase boundary velocity can be found.

We will also restrict attention to kinetic response functions that are increasing functions of the phase boundary velocity $\dot{s}$:

$$\mathcal{F}'_{ab}(\dot{s}) \geq 0 \, . \tag{4.42}$$

As we can tell by the loci of constant driving traction and the loci of constant phase boundary velocity in Figure 4.9, any kinetic relation subject to these restrictions

selects a locus of contact states in ABC that is continuous and of negative slope $dV^{\mathcal{C}}/d\sigma^{\mathcal{C}} < 0$. One end of this locus is at some point X on the line AB and the other is at C, Figure 4.10. At most one solution is available on this curve for any prescribed contact stress or particle velocity.

Kinetic response functions that relinquish (4.42) can select a nonmonotonic locus of contact states in ABC, and there will be cases in which two (or more) solutions are available on this curve for prescribed boundary conditions. These nonmonotone kinetic relations can produce stick-slip behavior in the phase boundary motion [79].

We will introduce nomenclature for the discontinuities associated with the fastest and slowest phase boundaries that can be supported by a kinetic relationship. A value ϕ associated with the *fastest* phase boundary supported by a kinetic relationship $\mathcal{F}_{ab}(\dot{s})$ will be designated ${\phi_{ab}}^{(\text{fastest})}$. For example, the velocity for a low pressure to high pressure phase boundary will be $\dot{s}_{31}^{(\text{fastest})}$ and the stress ahead of the phase boundary will be $\sigma_{31}^{+\,(\text{fastest})}$. Because $\hat{\sigma}(\gamma)$ is not defined for all γ, we may have $\dot{s}_{ab}^{(\text{fastest})} < \min(c_1, c_3)$: this will be discussed in Section 4.3.7.

A value ϕ associated with the *slowest* phase boundary supported by a kinetic relation $\mathcal{F}_{ab}$ will be designated ${\phi_{ab}}^{(\text{slowest})}$. For our trilinear materials, $\dot{s}_{31}^{(\text{slowest})} = \dot{s}_{13}^{(\text{slowest})} = 0$: it would be a greater velocity for a phase-changing material with monotonic $\hat{\sigma}(\gamma)$.

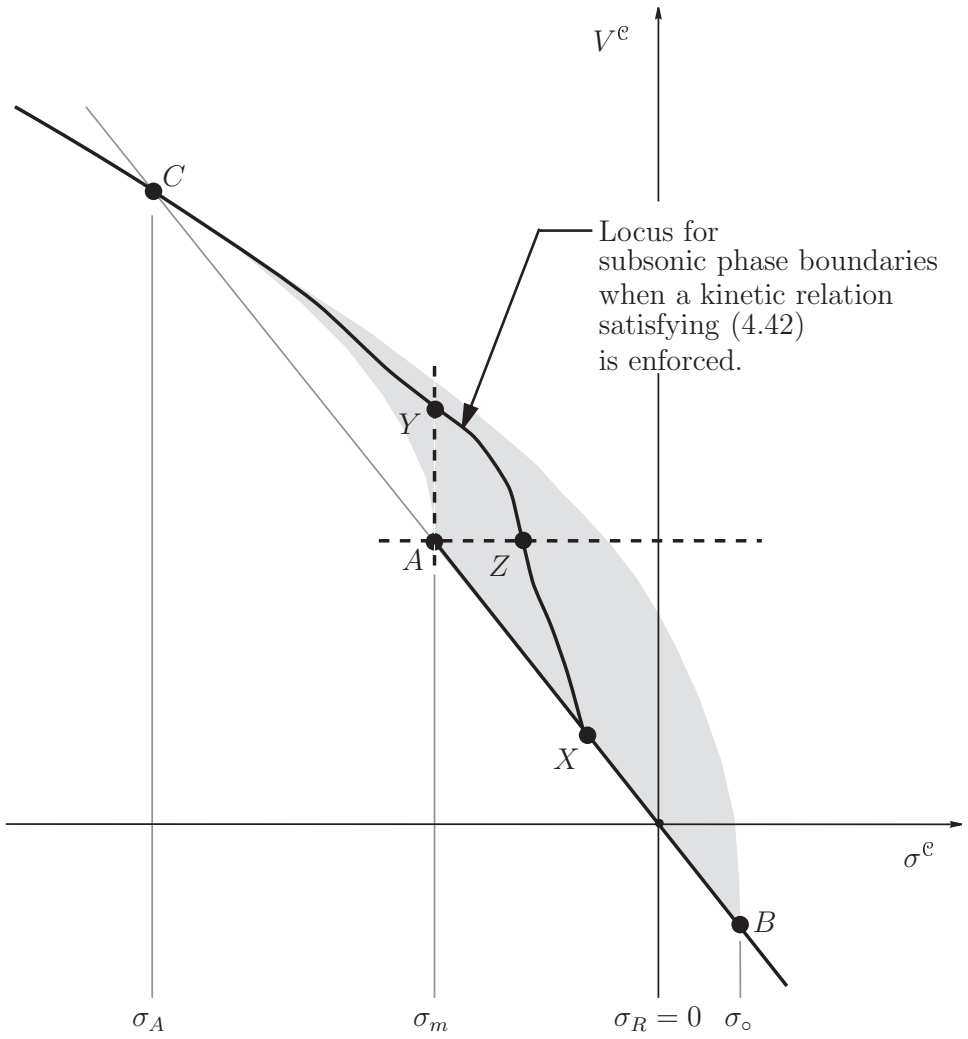

Figure 4.10: Principal locus of contact states for a trilinear material with a kinetic relation enforced. The points Y and Z are described in Section 4.3.6.

4.3.6 Nucleation criteria

Even with (4.42) in force, non-uniqueness remains. In general, there are still *two* loci that satisfy the initial-boundary value problem with prescribed contact velocity $V^{\mathcal{P}}$ if a horizontal line $V^{\mathcal{C}} = V^{\mathcal{P}}$ intersects *both* the contact locus and the locus for subsonic phase boundaries with a kinetic relation enforced. In Figure 4.10, this is the situation when $V^{\mathcal{C}} = V^{\mathcal{P}}$ intersects both AX and XZ. On AX, solutions consist

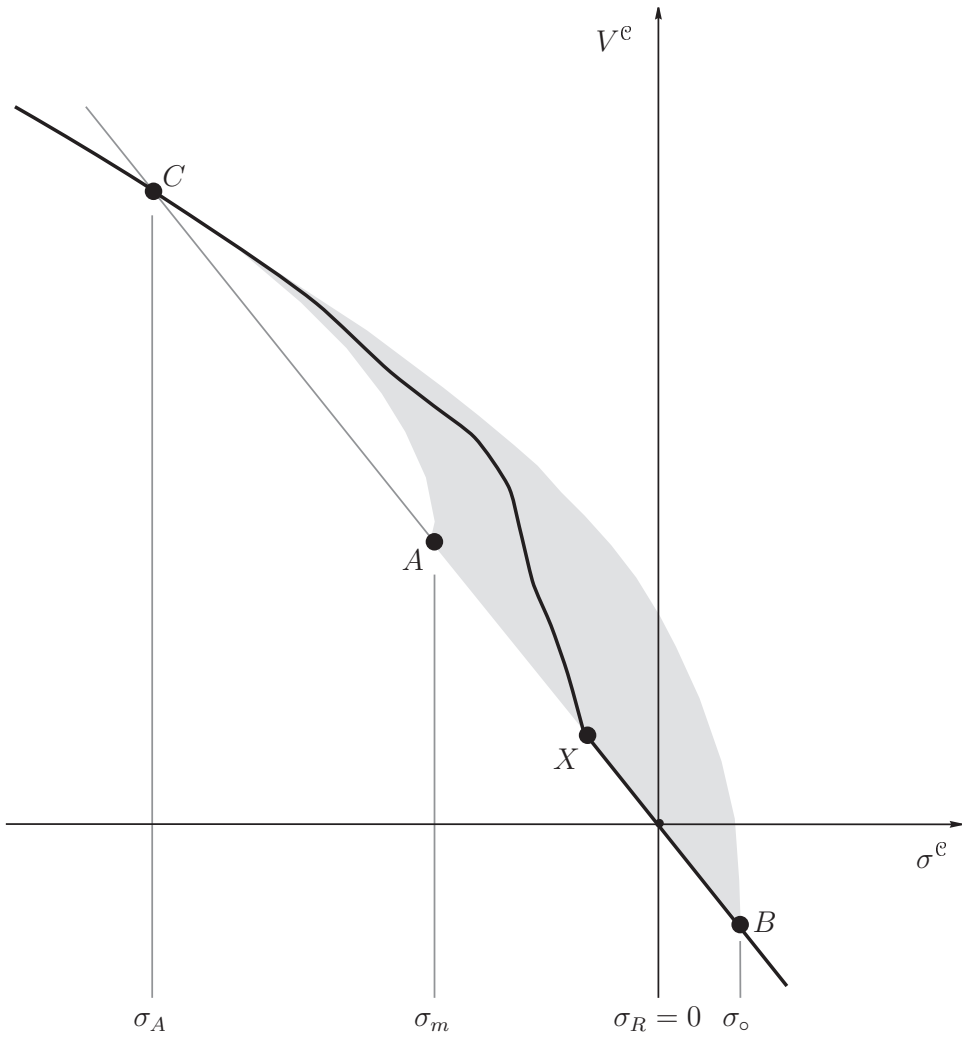

Figure 4.11: Principal locus of contact states for a trilinear material with a kinetic relation and nucleation criterion enforced.

of a single shock with no phase boundary. On XZ, they involve a shock followed by a subsonic phase boundary. Likewise, both AX and XY offer solutions for the initial-boundary value problem with prescribed contact stress $\sigma^{\mathfrak{P}}$ between σ_m and the stress at point X.

This remaining lack of uniqueness is resolved by introducing a *nucleation criterion*. This criterion decrees that a new subsonic boundary appears when the driving

traction is at least as great as some critical value,

$$f \geq f^c_{ab} \, . \tag{4.43}$$

In this thesis, the critical driving traction for nucleation f^c_{ab} is always chosen to be equal to the traction that overcomes the resistance $\mathcal{F}_{ab}(0^+)$ to phase boundary motion,

$$f^c_{ab} = \mathcal{F}_{ab}(0^+) \, . \tag{4.44}$$

This ensures continuity of the locus of contact states, Figure 4.11. When the driving traction equals or exceeds $f^c_{ab} = \mathcal{F}_{ab}(0^+)$, a subsonic phase boundary nucleates and the solution on CX is chosen. Otherwise, a solution on AX is selected.

Other values of the critical driving traction f^c_{ab} cause the locus of contact states to be discontinuous; it was anticipated that this situation would cause numerical instabilities and it was avoided in this work.

In summary, a monotonic kinetic relation, coupled with a properly restricted nucleation criterion, selects a particular continuous monotonic locus. Uniqueness has been achieved.

4.3.7 The alternate kinetic relation

There are situations when a kinetic relationship requires the strain γ^+ ahead of the phase boundary or the strain γ^- behind the phase boundary to fall outside of the defined range $\gamma \in [\gamma_Z, \gamma_F]$ of our trilinear model. We will demonstrate this with an example.

Consider a transformation from the low-pressure phase to the high-pressure phase in a trilinear material for which the high-pressure phase is stiffer than the low pressure phase, $\bar{E}_1 > \bar{E}_3$, and the stress-response function of the low-pressure passes through the origin, $d_3 = 0$. Assume that the phase boundary is governed by a dissipation-free kinetic relationship: $\mathcal{F}_{31}(\dot{s}) = 0$. Set $\hat{f}(\gamma^+, \gamma^-) = 0$ in the expression

(4.16c) for the driving traction and solve for γ^+. The result is

$$\gamma^+ = -\frac{d_1\gamma^- - d_1(\gamma_M + \gamma_m) + \gamma_M\gamma_m(\bar{E}_3 - \bar{E}_1)}{d_1 + (\bar{E}_1 - \bar{E}_3)\gamma^-} \,. \tag{4.45}$$

Evaluating the derivative of the right side with respect to γ^-, we find that it is always negative and that it approaches $-\infty$ as $\gamma^- \to \gamma_A$. Thus, as γ^- decreases in the high-pressure phase toward the limiting value γ_A for a subsonic phase boundary, γ^+ increases toward $+\infty$ in the low-pressure phase. Since the low-pressure phase is undefined for $\gamma > \gamma_F$, we have a problem. Solving (4.45) for $\gamma^+ = \gamma_F$, we find that any

$$\gamma^- < \frac{d_1(\gamma_F - \gamma_M - \gamma_m) + (\bar{E}_3 - \bar{E}_1)\gamma_M\gamma_m}{d_1 + (\bar{E}_1 - \bar{E}_3)\gamma_F} \tag{4.46}$$

forces $\gamma^+ > \gamma_F$.

Other kinetic relationships can also force $\gamma^+ > \gamma_F$, though at different values of γ^-. Furthermore, if the expressions for the low and high pressure phases intersect at $\gamma_A < \gamma_Z$, the same type of problem occurs for the transformation from the low pressure to the high pressure phase.

We can think of these situations as truncating the space f, $\dot{s}$ in which a kinetic relationship $\mathcal{F}_{ab}(\dot{s})$ can lie, Figure 4.12.

In this work, when a prescribed kinetic response function $\mathcal{F}_{ab}(\dot{s})$ can only be enforced with a value of γ^+ for which the stress response function $\hat{\sigma}(\gamma)$ is undefined, the *boundary* of the truncated space is prescribed as an *alternate kinetic relation*. The alternate kinetic relation is conveniently enforced by setting $\gamma^+ = \gamma_{ab}^{+\,(\text{fastest})}$.

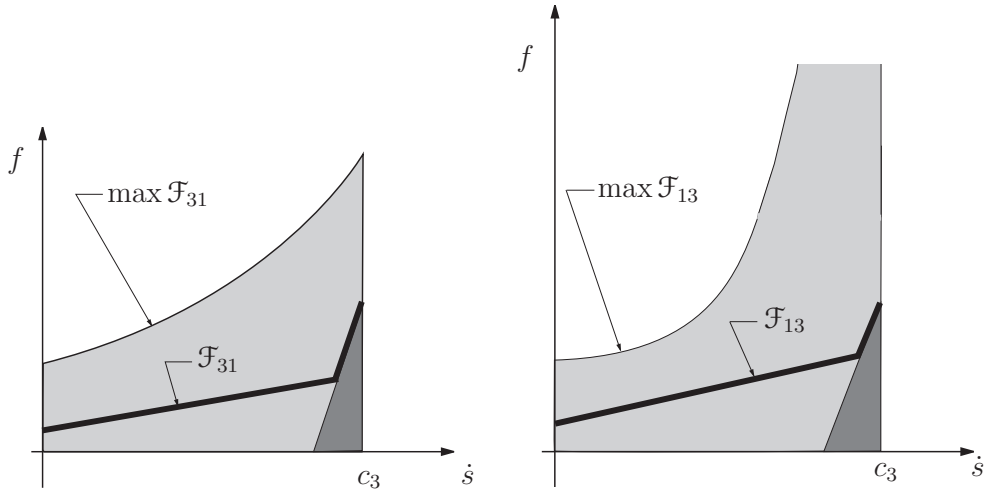

(a) Low pressure to high pressure transformation.

(b) High pressure to low pressure transformation.

Figure 4.12: Because the trilinear model is undefined outside of $\gamma \in [\gamma_Z, \gamma_F]$, the space of possible kinetic relationships is truncated. Light shading indicates the space still available, dark shading the space that would be available if $\hat{\sigma}(\gamma)$ were defined for all γ. Where a kinetic relationship enters one of these missing areas, we will instead enforce the *boundary* of the missing space as the *alternate kinetic relationship*. Examples are shown by the heavy lines. (Only the first quadrants are shown, the reflections in the third quadrants are identical.)

4.4 The concave-convex model

Materials other than GeO_2 to be encountered here will be described by a *concave-convex material model*, Figure 4.4. The stress response function is:

$$\hat{\sigma}(\gamma) = \begin{cases} \text{undefined} & \text{for } \gamma < \gamma_Z \ , \\ \hat{\sigma}_1(\gamma) = \bar{K}\gamma\left(1 + s_1\gamma\right)^{-2} & \text{for } \gamma_l \leq \gamma \leq \gamma_m \ , \\ \hat{\sigma}_2(\gamma) = a - b\left(-\gamma\right)^n \quad n \neq -1 & \text{for } \gamma_m < \gamma < \gamma_M \ , \\ \hat{\sigma}_3(\gamma) = \bar{E}\gamma & \text{for } \gamma_M \leq \gamma \leq \gamma_F \ , \\ \text{undefined} & \text{for } \gamma > \gamma_F > 0 \ . \end{cases} \tag{4.47}$$

We will require that the slope of the middle phase be less than that of the low pressure phase,

$$\sigma_2'(\gamma_M) < \sigma_3'(\gamma_M) \ . \tag{4.48}$$

The expressions for the low and high pressure phases intersect in the low pressure phase at the origin $(0, 0)$ and in the high pressure phase at (γ_A, σ_A). The tangent to the middle phase at (γ_M, σ_M) intersects the high pressure phase at (γ_B, σ_B). The points (γ_A, σ_A) and (γ_B, σ_B) are significant because the form of the solution can depend on the value of the contact stress σ^{c} relative to σ_A and σ_B.

4.4.1 Possible states for the initial-boundary value problem

Though $\hat{\sigma}(\gamma)$ is monotonic, its curvature changes sign. While not commonly identified with phase-changing materials because equilibrium mixtures of phases cannot occur, solutions to *dynamic* problems with these types of stress response functions suffer the same lack of uniqueness observed for nonmonotonic stress response functions [78]. In particular, the non-uniqueness arises in an initial-boundary value problem when the initial strain is in segment 1 or 3. As it did for a nonmonotonic

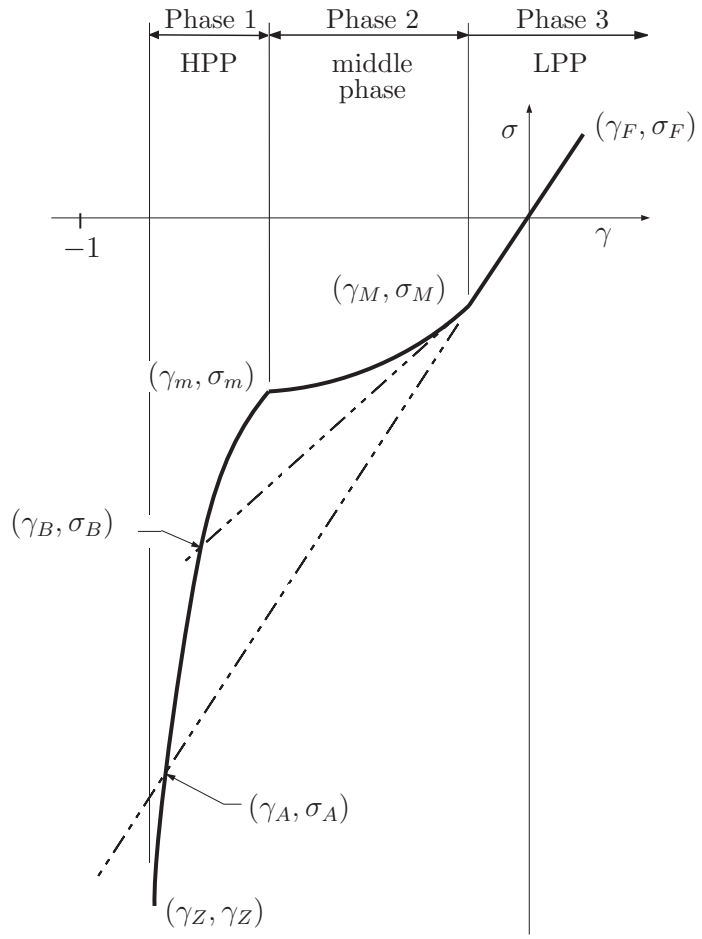

Figure 4.13: Stress response function of a concave-convex material.

$\hat{\sigma}(\gamma)$, the introduction of a kinetic relationship and a nucleation criterion restores uniqueness.

We consider only one type of kinetic relation for this monotonic model, namely the kinetic relation that maximizes the driving traction f for any subsonic phase boundary velocity $\dot{s}$. This choice will be motivated in Chapter 5.

As it did for the trilinear model, this particular kinetic relation has a useful geometric property for the concave-convex model. Recall that by (3.52) the driving traction $f = f(\gamma^+, \gamma^-)$ is the sum of the signed areas between $\hat{\sigma}(\gamma)$ and the chord connecting the points (γ^-, σ^-) and (γ^+, σ^+). By inspection, for a given phase boundary velocity $\dot{s}$, the driving traction $| f |$ is maximized when a chord of slope

$\rho_\circ \dot{s}^2 = [\![\sigma]\!]/[\![\gamma]\!]$ connects (γ^+, σ^+) and (γ^-, σ^-) without crossing $\hat{\sigma}(\gamma)$. Therefore, the only subsonic phase boundaries this kinetic relation permits are those for which the deformation gradient ahead of the boundary is at a point of discontinuity in the slope of the stress-strain curve, i.e., at γ_M or γ_m. (Indeed, since the wave speed is discontinuous at these values of γ, the phase boundary velocity could be classified subsonic or supersonic, but perhaps should not be classified at all. We use subsonic for convenience.) All other phase boundaries are either sonic or supersonic.

Because this kinetic relationship can be implemented through this geometrical understanding, it is not necessary here to write an expression specializing it to the concave-convex material model. This is fortunate, as the expression would be quite cumbersome.

We now find all possible states for our initial-boundary value problem, imposing this kinetic relation when necessary to ensure uniqueness. The solutions can be classified according to the initial phase of the material.

If the material is initially in the *low pressure phase*, five distinct forms of possible states satisfy the maximum driving traction kinetic relation, Figure 4.14. These solutions are shown in relationship to the stress-strain curve in Figure 4.15. They are:

1. If the contact strain $\gamma^{\mathfrak{C}}$ is in the LPP, then the solution is a shock, Figures 4.14(a) and 4.15(a).

2. If the contact strain $\gamma^{\mathfrak{C}}$ is in the middle phase, then the solution is a shock in the LPP to (γ_M, σ_M), followed by a fan in the middle phase, Figures 4.14(b) and 4.15(b).

3. If the contact strain $\gamma^{\mathfrak{C}}$ is in the HPP and $\gamma^{\mathfrak{C}} > \gamma_B$, then the solution is a shock to (γ_M, σ_M), followed by a fan in the middle phase and a sonic phase boundary on the fan's trailing edge, Figures 4.14(c) and 4.15(c). Ahead of the phase boundary, $\gamma = \gamma_t$, the strain at the tangent point of a chord drawn tangent to the middle phase from $(\gamma^{\mathfrak{C}}, \sigma^{\mathfrak{C}})$.

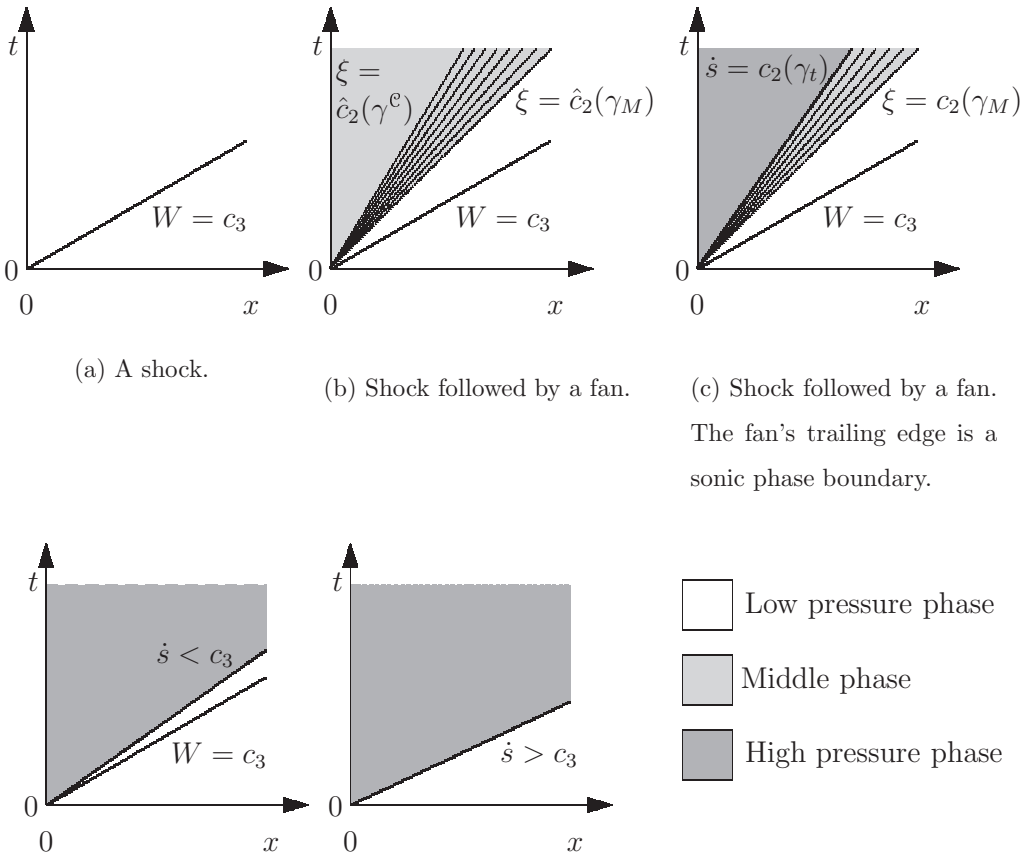

(a) A shock.

(b) Shock followed by a fan.

(c) Shock followed by a fan. The fan's trailing edge is a sonic phase boundary.

(d) Shock followed by a phase boundary.

(e) Supersonic phase boundary.

Figure 4.14: The kinetic relation that maximizes the driving traction f results in five forms of possible solutions in a concave-convex material initially in the low pressure phase.

4. If the contact strain γ^{c} is in the HPP and $\gamma_B > \gamma^{\mathrm{c}} > \gamma_A$, then the solution is a shock to (γ_M, σ_M), followed by a phase boundary, supersonic with respect to the middle phase at (γ_M, σ_M), Figures 4.14(d) and 4.15(d).

5. If the contact strain γ^{c} is in the HPP and $\gamma^{\mathrm{c}} < \gamma_A$ then the solution is a phase boundary, supersonic with respect to the LPP, Figures 4.14(e) and 4.15(e).

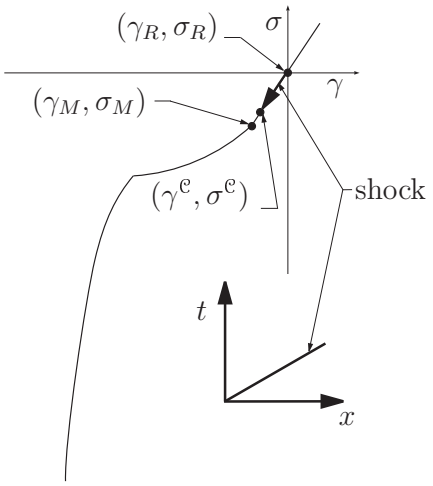

(a) Shock in the LPP.

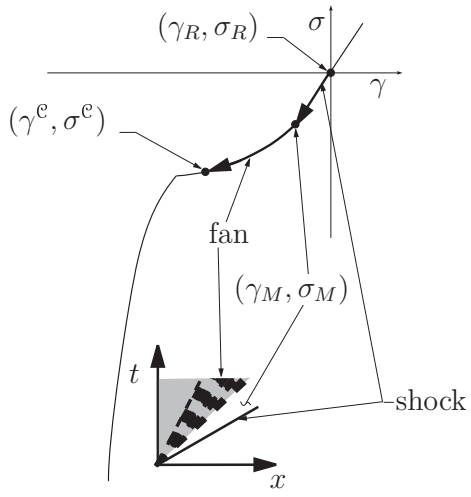

(b) Shock followed by a fan.

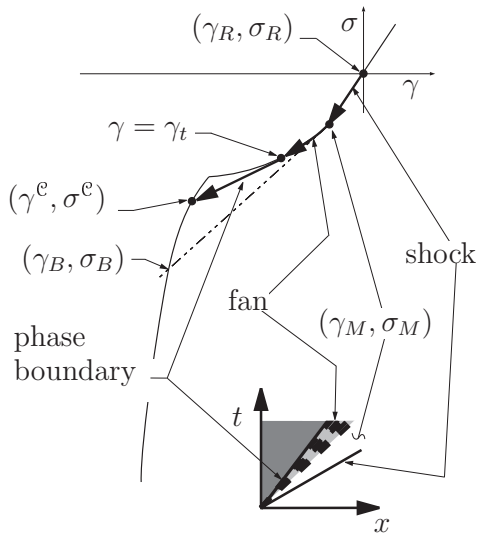

(c) Shock followed by a fan with a sonic phase boundary on the trailing edge of the fan.

Figure 4.15: Relation between the stress-strain curve and the five types of possible states shown in Figure 4.14 for initial conditions in the low pressure phase.

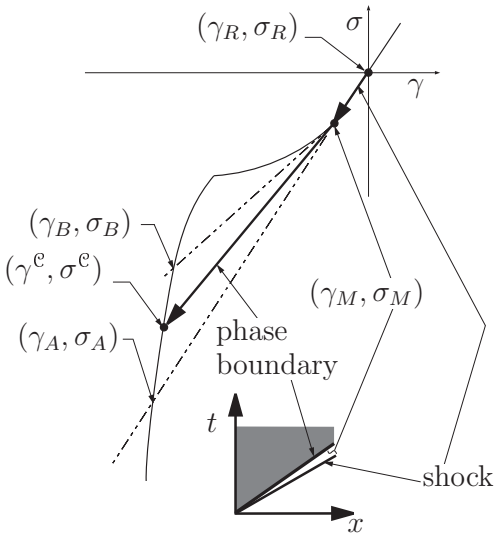

(d) Shock followed by a phase boundary.

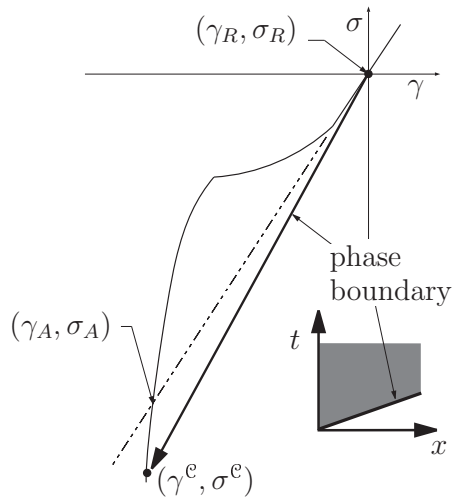

(e) Supersonic phase boundary.

Figure 4.15: (Continued)

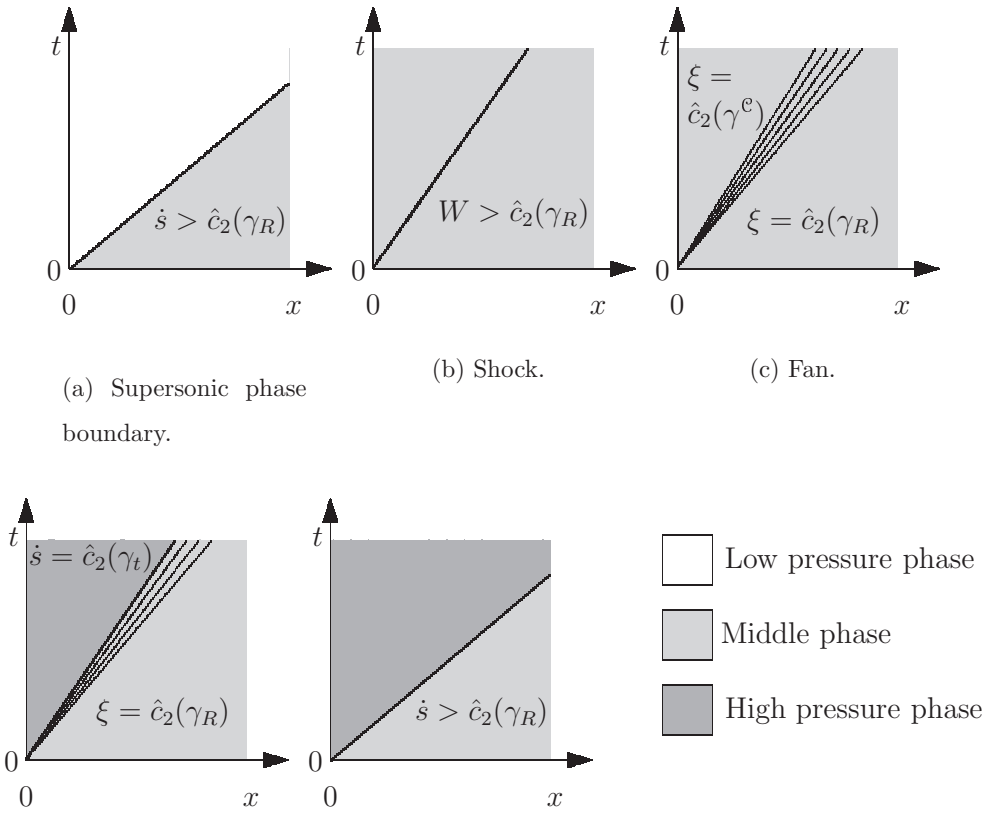

(a) Supersonic phase boundary.

(b) Shock.

(c) Fan.

(d) Fan. The trailing edge is a sonic phase boundary.

(e) Supersonic phase boundary.

Figure 4.16: Possible states in a concave-convex material initially in the middle phase. All phase boundaries for which the middle phase is the parent phase are sonic or supersonic with respect to the middle phase, and the solutions are uniquely determined by the balance equations and the entropy inequality. A kinetic relation is not needed and cannot be accommodated.

If the material is initially in the *middle phase*, then five other forms arise. It is helpful to construct a line tangent to $\hat{\sigma}(\gamma)$ at γ_R. The intersection of this tangent with the HPP occurs at $\gamma = \gamma_B{}'$. When γ^{e} is in the HPP but greater than $\gamma_B{}'$, it is also helpful to construct a chord from $(\gamma^{\mathrm{e}}, \sigma^{\mathrm{e}})$ tangent to the middle phase at some value $\gamma = \gamma_t$. The five forms of the possible states, shown in Figure 4.16, are then:

1. If the contact strain $\gamma^{\mathcal{C}}$ is in the LPP, the solution is a supersonic phase boundary, Figure 4.16(a).

2. If the contact strain $\gamma^{\mathcal{C}}$ is in the middle phase but more positive than the initial strain, $\gamma^{\mathcal{C}} > \gamma_R$, then the solution is a shock, Figure 4.16(b).

3. If the contact strain $\gamma^{\mathcal{C}}$ is in the middle phase but more negative than the initial strain, $\gamma^{\mathcal{C}} < \gamma_R$, then the solution is a fan, Figure 4.16(c).

4. If the contact strain $\gamma^{\mathcal{C}}$ is in the HPP and $\gamma^{\mathcal{C}} > \gamma_B{}'$, then the solution is a fan that ends at $\gamma = \gamma_t$. On the trailing edge of the fan is a sonic phase boundary, Figure 4.16(d).

5. If the contact strain $\gamma^{\mathcal{C}}$ is in the HPP and $\gamma^{\mathcal{C}} < \gamma_B{}'$ then the solution is a supersonic phase boundary, Figure 4.16(e).

Finally, if the *high pressure phase* is the initial phase, four forms of solutions are possible, Figure 4.17:

1. If the contact strain $\gamma^{\mathcal{C}}$ is in the HPP and more negative than the initial strain, $\gamma^{\mathcal{C}} < \gamma_R$, then the solution is a shock, Figure 4.17(a).

2. If the contact strain $\gamma^{\mathcal{C}}$ is in the HPP and more positive than the initial strain, $\gamma^{\mathcal{C}} > \gamma_R$, then the solution is a fan, Figure 4.17(b).

3. If the contact strain $\gamma^{\mathcal{C}}$ is in the middle phase then the solution is a fan to $\gamma = \gamma_m$ followed by a supersonic phase boundary, Figure 4.17(c).

4. If the contact strain $\gamma^{\mathcal{C}}$ is in the LPP then the solution is a fan to $\gamma = \gamma_m$ followed by a supersonic phase boundary, Figure 4.17(d).

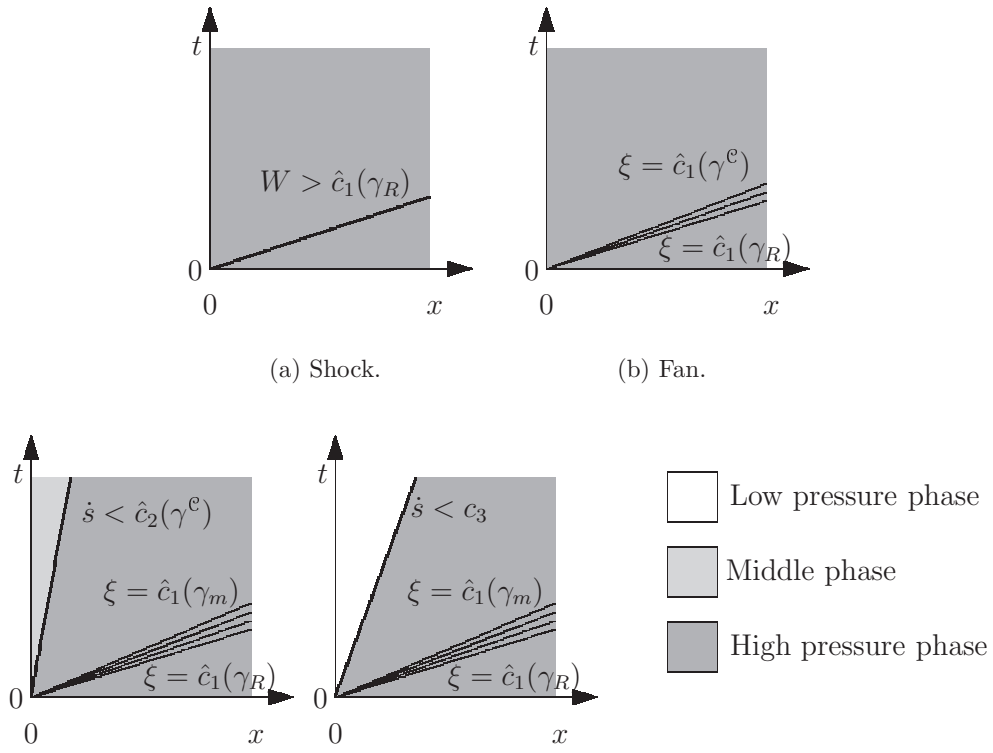

(a) Shock.

(b) Fan.

(c) Fan followed by a phase boundary.

(d) Fan followed by a phase boundary.

Figure 4.17: Forms of possible solutions in a concave-convex material initially in the high pressure phase with the kinetic relation that maximizes the driving traction.

4.4.2 Locus of contact states

The locus of contact states for prescribed initial conditions is the union of the loci for each of the different types of solutions compatible with the initial conditions. Figure 4.18 shows the result for the principal locus of contact states. The following sections present some of the equations needed to determine the loci for shocks and fans.

For an *arbitrary* elastic material, it is not possible to find analytic expressions for the change in particle velocity across a fan, as the expression (3.63) for fans requires integration of $\sqrt{\hat{\sigma}'(\gamma)}$. Fortuitously, this integral *can* be found analytically

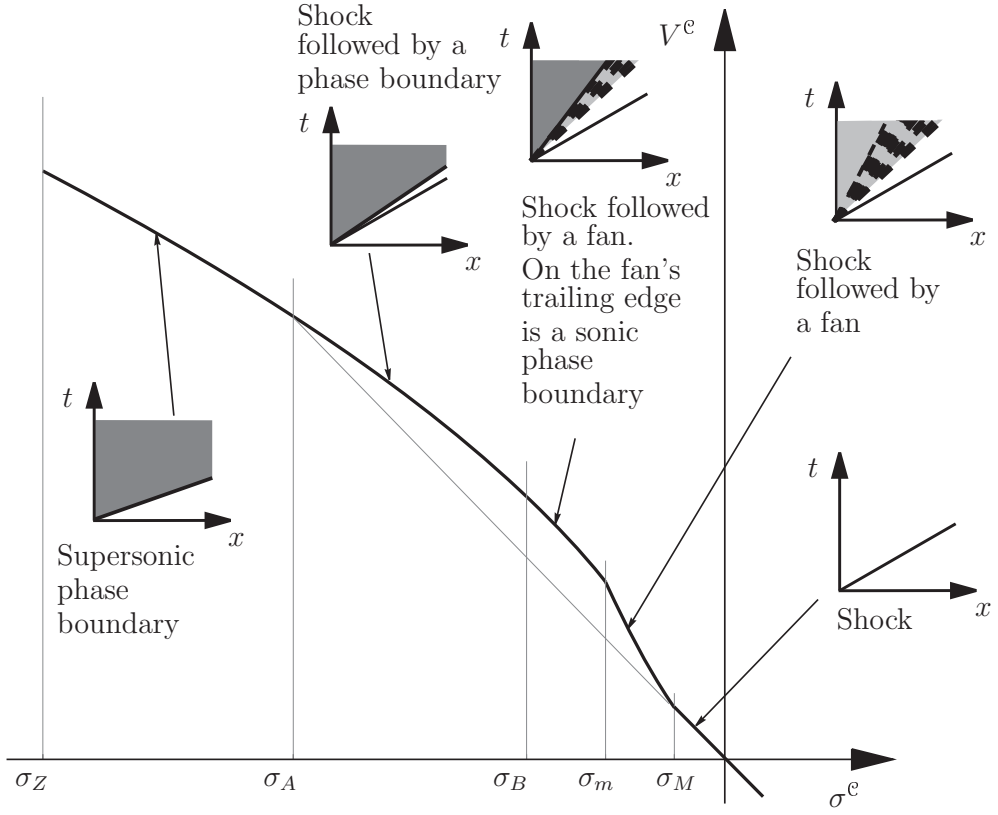

Figure 4.18: Principal locus of contact states for a concave-convex material.

for each of the three phases of the concave-convex material model; the resulting expressions are provided in this section and are coded into the program described in later chapters.

In this material model, any phase can transform to any other phase across a phase boundary, for a total of six kinds of transformations. Since the form of the expression for $\hat{\sigma}(\gamma)$ is different for each phase, the jump conditions give rise to a unique expression for each of these six kinds of transformations. These six expressions are not presented here, as there is little to be gained from them: they are awkward, not readily simplified, and not explicitly coded into the computer program used in later chapters. When a phase boundary is involved, the contact stress σ^{c} and contact particle velocity V^{c} are better expressed by the jump conditions and the stress-strain relationship $\hat{\sigma}(\gamma)$ as parametric functions of γ^{c}.

Elementary waves within the LPP

Within the low pressure phase, the stress and strain are linearly related, and there is no distinction between a shock and a fan. The balance equations are satisfied by

$$V^+ - V^- = \frac{\text{sign}\,(W)}{\sqrt{\bar{E}\rho_\circ}}(\sigma^+ - \sigma^-)\,, \tag{4.49}$$

$$W^2 = \bar{E}/\rho_\circ\,, \tag{4.50}$$

across any discontinuity.

Elementary waves within the middle phase

The expression $\hat{\sigma}(\gamma)$ for the middle phase can be inverted, yielding

$$\hat{\gamma}_2(\sigma) = -\left(\frac{a-\sigma}{b}\right)^{1/n}\,. \tag{4.51}$$

The local wave speed $c = \hat{c}(\gamma)$ is given by

$$c^2 = \frac{bn(-\gamma)^{n-1}}{\rho_\circ}\,. \tag{4.52}$$

Within a fan, the change in particle velocity between any two positive rays ξ^+ and ξ^- is calculated from (3.63),

$$V = V^+ - \frac{2\sqrt{nb^{1/n}}}{\sqrt{\rho_\circ}\,(1+n)}\left\{\left(a-\sigma^-\right)^{\frac{1+n}{2n}} - \left(a-\sigma^+\right)^{\frac{1+n}{2n}}\right\}\,. \tag{4.53}$$

Terms in γ were eliminated by (4.51).

To find the jump in particle velocity across a shock and to determine the shock propagation velocity, use (4.51) in the jump conditions (3.40) and (3.41) to find the

jump in particle velocity in the σ, V plane. The result is:

$$V^- = V^+ + \text{sign}\left([\![\sigma]\!]\right) \frac{1}{\sqrt{\rho_\circ b^{1/n}}} \sqrt{(\sigma^+ - \sigma^-)\left\{-\left(a-\sigma^+\right)^{1/n} + \left(a-\sigma^-\right)^{1/n}\right\}}\,, \quad (4.54)$$

$$W^2 = \frac{-\left(\sigma^+ - \sigma^-\right) b^{1/n}}{\rho_\circ \left\{\left(a-\sigma^+\right)^{1/n} - \left(a-\sigma^-\right)^{1/n}\right\}}\,. \quad (4.55)$$

$$(4.56)$$

Elementary waves within the HPP

Within the high pressure phase, the inverse of $\hat{\sigma}(\gamma)$ is

$$\hat{\gamma}(\sigma) = \frac{\bar{K} - 2s_1\sigma - \sqrt{\bar{K}(\bar{K} - 4s_1\sigma)}}{2s_1^2\sigma}\,. \quad (4.57)$$

The local wave speed $c = \hat{c}(\gamma)$ in this phase is given by

$$c^2 = \frac{\bar{K}(1 - s_1\gamma)}{\rho_\circ(1+s_1\gamma)^3}\,. \quad (4.58)$$

The change in particle velocity between any two positive rays $\xi = c^+$ and $\xi = c^-$ within a fan is calculated from (3.63).

$$V^- = V^+ - \frac{\sqrt{\bar{K}}}{\rho_\circ s_1}\left(-2\sqrt{\frac{1-s_1\gamma}{1+s_1\gamma}} + \arcsin(-s_1\gamma)\right)_{\gamma^+}^{\gamma^-}\,, \quad (4.59)$$

where γ^- and γ^+ are evaluated on $\xi = c^-$ and $\xi = c^+$, respectively.

This expression, in conjunction with $\hat{\sigma}(\gamma)$ for this phase, parametrically describes the locus of available (V^-, σ^-) for prescribed (V^+, σ^+).

4.5 Riemann problems and impact problems

A *Riemann problem* is an initial value problem for a single material occupying the interval on $-\infty < x < \infty$, Figure 4.19. The initial conditions are piecewise constant with a discontinuity only at $x = 0$.

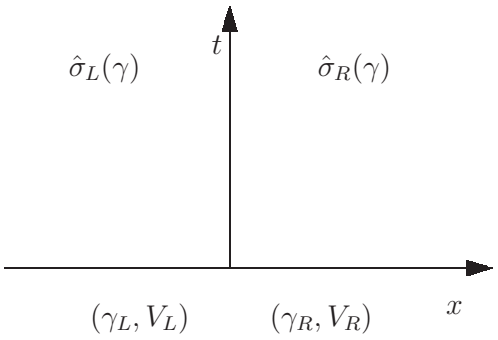

Figure 4.19: A single-material or bimaterial Riemann problem. In a single-material Riemann problem, the stress response function $\hat{\sigma}_L(\gamma)$ for $x < 0$ is identical to the stress response function $\hat{\sigma}_R(\gamma)$ for $x > 0$. In a bimaterial Riemann problem, the stress response functions are different on the left and right half-spaces.

We will define a *bimaterial Riemann problem* as a problem identical to a Riemann problem except that the material in $x < 0$ differs from the material in $x > 0$.

In either type of Riemann problem, the jump conditions (3.38)-(3.39) must be satisfied across the contact discontinuity at $x = 0$ with $W = 0$. The jump conditions become:

$$[\![V]\!] = 0 \,, \tag{4.60}$$

$$[\![\sigma]\!] = 0 \,. \tag{4.61}$$

Thus, the solution to either the single material or bimaterial Riemann problem is the intersection of the locus of contact states for the right-hand problem and the locus for the left-hand problem, as shown in Figure 4.20.

In this thesis, an *impact problem* is either a Riemann problem or a bimaterial Riemann problem with the constraint that the interface $x = 0$ cannot support ten-

sion. If the jump conditions (4.60)-(4.61) at $x = 0$ are satisfied by $\sigma^+ = \sigma^- > 0$ at some time $t^\dagger$, the two half spaces must separate. The Riemann solution is then discarded, and the Riemann problem is replaced by two initial-boundary value problems, each with the boundary conditions $\sigma^{\mathcal{P}} = 0$ for times $t > t^\dagger$. After separation, the current spatial positions y must be computed for each of the newly free surfaces, as a "re-impact" may occur. Thus, the solution to an impact problem is found by solving

$$[\![V]\!] = 0 \,, \quad \text{if } \sigma^+ = \sigma^- < 0 \,, \tag{4.62}$$

$$\sigma^+ = 0 \,, \quad \sigma^- = 0 \quad \text{otherwise} \,, \tag{4.63}$$

subject to the prescribed initial conditions.

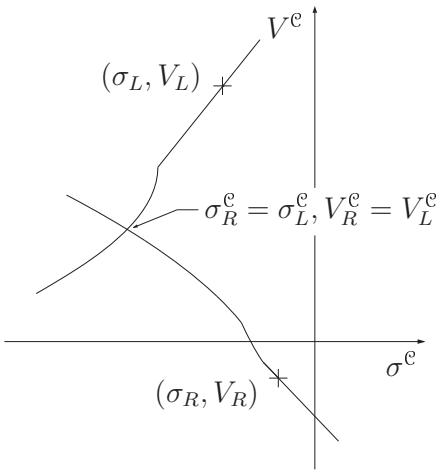

Figure 4.20: The intersection of the contact locus for each half space $x < 0$ and $x > 0$ provides the solution for a single material or bimaterial Riemann problem. This technique is known as *the impedance match method* in the shock compression literature [14]. In this example, the upper curve is the locus of contact states based at (σ_L, V_L) for a trilinear material on the left half space $x < 0$. The lower curve is the locus based at (σ_R, V_R) for a concave-convex material on the right half space $x > 0$.

Chapter 5

Elastic models for the experimental materials

Each of the five different plate materials utilized in the experiments will be described by a stress response function $\hat{\sigma}(\gamma)$ intended to represent the material's experimentally observed response to uniaxial compression at high strain rates.

The phase-changing material, germanium dioxide, is modeled as an up-down-up trilinear material. In Section 4.3.3 we saw that an initial-boundary value problem in this type of material gives rise to massive non-uniqueness in the solution space. This non-uniqueness is remedied by the introduction of a kinetic relation and a nucleation criterion. Since one of our primary objectives is to illustrate the effect of changing the kinetic relation in the model for GeO_2, we utilize three forms of kinetic relation for this material. The first is the *roof*, introduced in Section 4.3.5. This kinetic relation maximizes the driving traction for any given phase boundary velocity, and has been shown to be analogous to the concept of maximum plastic work [6]. We also use a *linear kinetic relation*,

$$\mathcal{F}_{ab}(\dot{s}) = g_{ab} + h_{ab}\,\dot{s}\;, \qquad g_{ab} \geq 0\;, \quad h_{ab} \geq 0, \tag{5.1}$$

where g_{ab} and h_{ab} are positive parameters which may be chosen freely so long as the resulting expression lies within the region of possible $(\dot{s}, f)$ pairs for a subsonic

phase boundary, Figure 4.8. Recall that the first subscript refers to the phase *ahead* of the phase boundary and the second subscript to the phase *behind* it, as described in Section 4.3.5. The final kinetic relation considered is the *non-dissipative kinetic relation*, also introduced in Section 4.3.5: it is a special case of (5.1) with $g_{ab} = 0$, $h_{ab} = 0$.

The kinetic relation governing the transformation from one phase to the other is prescribed independently of that for the reverse transformation, i.e., $\mathcal{F}_{31}(\dot{s}) \neq \mathcal{F}_{13}(\dot{s})$.

The nucleation criterion utilized in this work is always

$$f^c_{ab} = \mathcal{F}_{ab}(0^+) \ . \tag{5.2}$$

This nucleation criterion always selects a solution with a phase change over a solution with no phase change when both solutions are possible. More general nucleation conditions were avoided as they were expected to cause difficulties numerically.

With the exception of some very special kinetic relations, the stress ahead of a phase boundary is problem-dependent, and it is inappropriate to speak of a unique stress at which transformation occurs. The kinetic relation we call the roof is one of these special cases: with the roof, the (γ, σ) pair ahead of a phase boundary always assumes a particular value, either (γ_m, σ_m) or (γ_M, σ_M).

In the shock compression literature, many materials are considered to possess a well-defined *Hugoniot elastic limit* at which yield occurs in uniaxial shock compression tests. For the reasons given in the previous paragraph, using the roof to model the kinetic relation in these materials allows imitation of this behavior in compression. Of the four ancillary materials we must model, both of the metals and the lithium fluoride are thought to yield at a unique Hugoniot elastic limit. Therefore, the roof is the only kinetic relation considered for these three materials in this thesis. The roof also has the benefit of being simple to implement, as it can be enforced without computing the driving traction.

This same kinetic relation is chosen for the foam, which exhibits a "lock-up" behavior when the open pores in it collapse under compression to some particular

uniaxial deformation [38]. The roof does a reasonable job of mimicking this behavior as well.

5.1 Elastic model for germanium dioxide

The trilinear model is used to represent germanium dioxide because of the simplicity of the model as regards phase transitions. In truth, neither phase of the germanium dioxide has a linear behavior. Our challenge is to rationally select linear relationships for each phase such that significant features of the experimentally obtained velocity-time histories of Chapter 2 are adequately reproduced.

We begin by choosing an unstressed reference configuration in the low pressure phase. Requiring $\hat{\sigma}_3(0) = 0$ necessitates that the intercept d_3 in this phase be zero:

$$d_3 = 0 \ . \tag{5.3}$$

We will utilize data from eight shock compressions experiments on GeO_2 glass by Jackson and Ahrens [46]. The initial density of the GeO_2 was $\rho_\circ = 3.655$ g/cm^3. The deformation in these experiments was longitudinal, and the resulting stress σ ranged from -4.1 GPa to -142 GPa.

In one of Jackson and Ahrens' experiments, the impact produced two discontinuities in the GeO_2. Assuming that the faster of these two discontinuities, at $W = 3.53 \pm 0.04$ km/s, is a shock in the glass phase, we find that the longitudinal modulus is 45.5 ± 1 GPa. In the simulations, the value used is $\bar{E}_3 = 45.2$ GPa.

Ultrasonic measurements of wave speeds in *hydrostatic* experiments suggest that the longitudinal wave speed is around 3.6–3.7 km/s in the reference configuration, decreases with increasing pressures to about 3.5 km/s at ≈ 2 GPa, then increases with increasing pressures to 7 km/s at 8 GPa [35, 93, 105]. These are measurements taken in the current configuration, and it is difficult to assess their applicability to the shock compression experiments because the loading is different. Nonetheless, they hint that the *real* low pressure behavior is not linear.

Now consider the high pressure phase. In Jackson and Ahrens' experiments, it appears that at least the five data points with the greatest compression, from σ = -35 GPa to σ = -142 GPa, belong to the high pressure phase. Each of these data points corresponds to a single experiment, and in each experiment, impact produced only one detectable discontinuity in the GeO_2. It was found that the discontinuity velocity and the jump in particle velocity across the discontinuity were linearly related. This behavior is common to many materials; in Section 5.3, it is seen to lead to the concave, high-pressure expression for the concave-convex materials. Thus, over the interval in which these five data points lie, the GeO_2 responds in a manner that can be attributed to a single phase.

The challenge here is to represent the high pressure phase by a linear stress response function. Several different linear functions were investigated, and simulations of Shot 955 were run for each. This shot is special in that the impact is predicted to initiate a *supersonic* phase boundary for most material models. When this occurs, kinetic relations do not enter into the early part of the simulation, and we can concentrate on refining the high pressure phase to best capture the experimental results. Indeed, depending on the material model, it often occurs that no kinetic relationship is utilized during the *entire* simulation.

Options that were examined for modeling the high pressure phase included fitting a line to Jackson and Ahrens' five strongest shots, to their six strongest shots, and to their three shots in the range σ = -16 GPa to σ = -35 GPa. Hopes were high for this latter fit, because simulations for the experiments described in Chapter 2 were predicting stresses no more compressive than about -40 GPa; tuning the model to the data available in this range seemed a clever thing to do. Hopes were dashed when none of these relationships produced satisfactory predictions: Figure 5.1.

Another technique was explored, based on Jackson and Ahrens' estimation that the density of the high pressure phase would be 6.59 g/cm^3 in a stress-free state σ =0. To achieve this density by one-dimensional deformation, we must have $\gamma_T \approx$ -0.446 . Therefore, models with $\gamma_T \approx$ -0.446 were tested, selecting a slope by

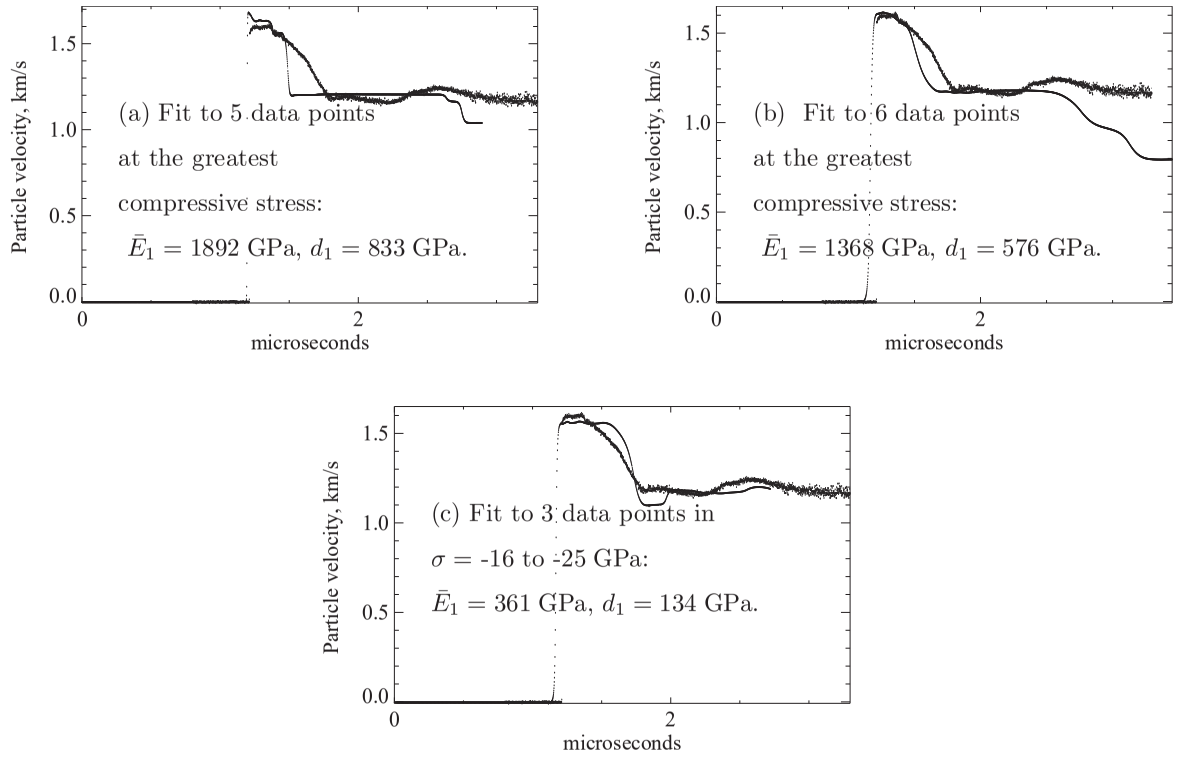

Figure 5.1: Particle velocity versus time predictions at the interface of the aluminum and lithium fluoride in Shot 955 using a trilinear model for GeO_2 with different expressions for the high pressure phase. Predictions are the thin lines, the experimentally obtained VISAR record the heavier lines. The HPP was fit to data points from [46]: the captions describe which points were used. In all of these simulations, a supersonic phase boundary transformed the material to the high pressure phase, and no reverse phase boundary nucleated. The match between these simulations and the experimental results was judged unacceptable.

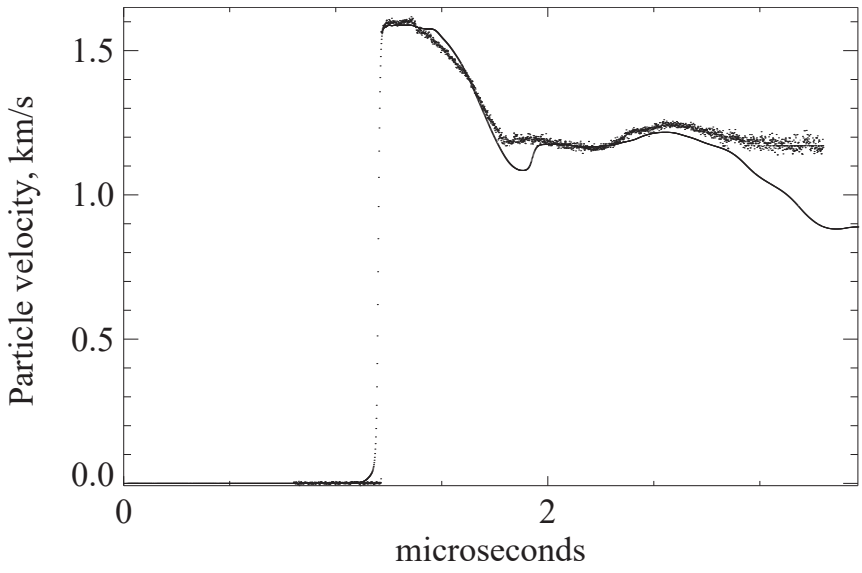

Figure 5.2: Particle velocity versus time prediction for Shot 955 using a concave-convex model for GeO_2. Prediction is shown in the thinner line, and the experimentally obtained VISAR record in the heavier line.

averaging the slopes from $(\gamma_T, 0)$ to each point of some subset of Jackson and Ahrens' high pressure phase data. Predictions with these types of models did not show much improvement.

Here it was hypothesized that the fidelity we sought just could not be obtained with a trilinear model. The hypothesis was tested by turning briefly to concave-convex models of GeO_2. Keeping $\bar{E}_3 = 45.2$ GPa in the low pressure phase, the parameters for the high pressure phase were taken from Jackson and Ahrens' fit to their high pressure data: $\bar{K} = 1.44$ GPa, $s_1 = 1.84$. The strains γ_m and γ_M were adjusted to obtain the best match to Shot 955. When kinetics were required, maximum dissipation kinetics were utilized, as this is the only option written into the numerical program for concave-convex models.

The best prediction resulting from this procedure for Shot 955 (Figure 5.2) and an accurately constructed x, t diagram (Figure 5.3) confirm the hypothesis: in the x, t diagram, notice the broad fan that forms in the GeO_2 from the wave that enters

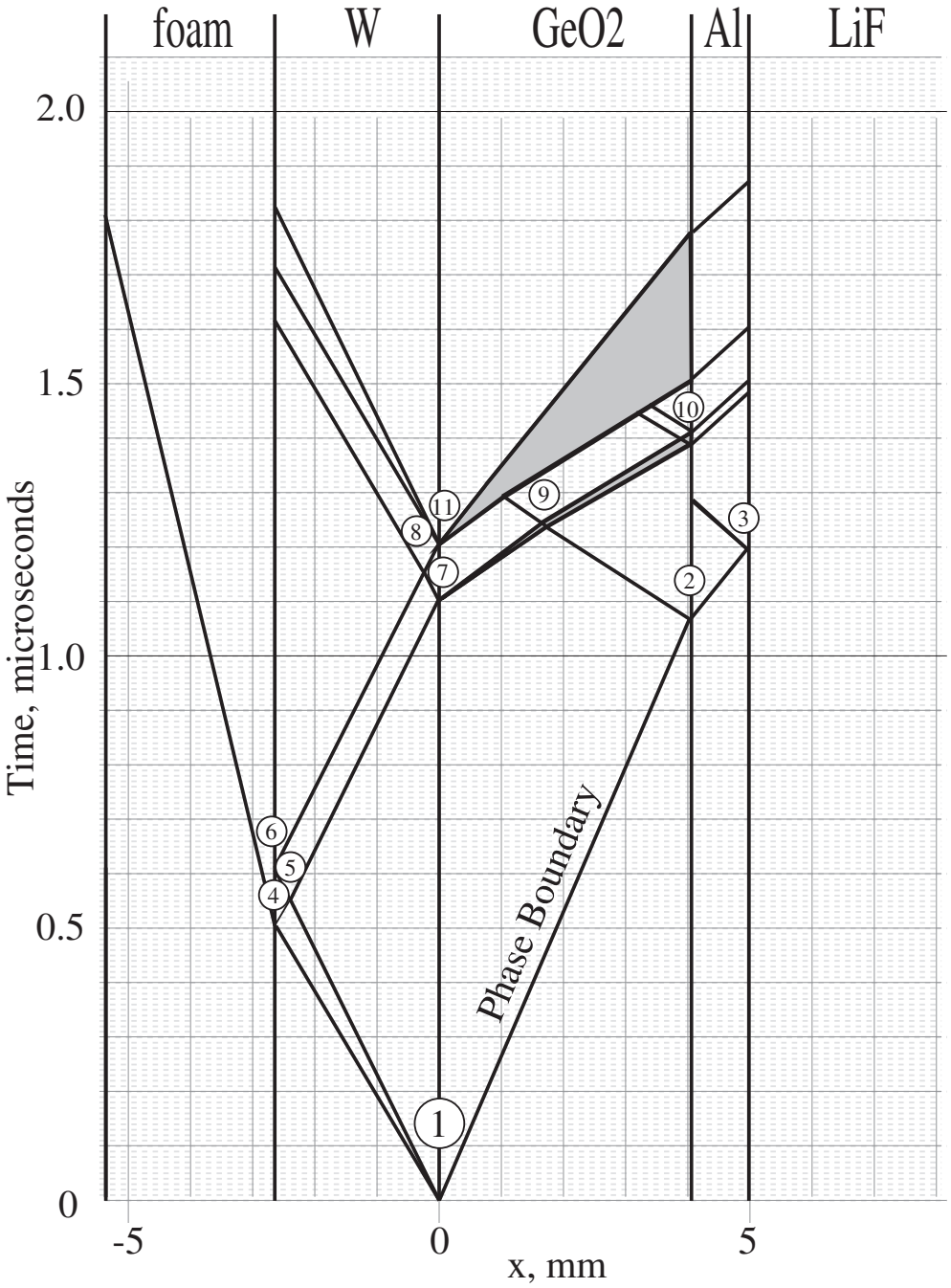

Figure 5.3: x, t diagram for Shot 955 with a concave-convex model of GeO_2. Waves transmitted into the LiF are not shown, nor are most of the waves that travel into the foam.

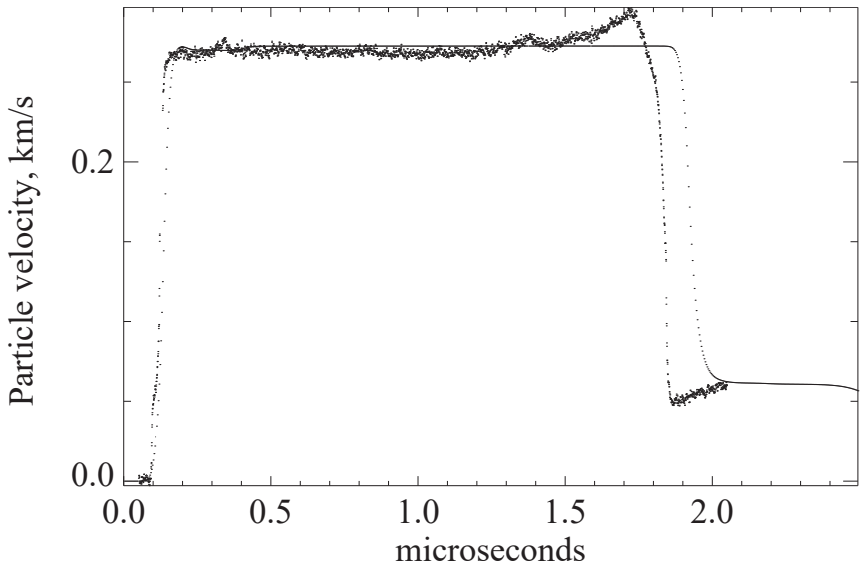

Figure 5.4: Predicted particle-velocity history of Shot 965 using a concave-convex model for GeO_2.

it at $x = 0$ and $t \approx 1.2$ μs. It is difficult to extend this diagram much farther in time, but this fan is clearly responsible in part for a better match to the slope of the experimentally recorded VISAR profile between $t = 1.4$–1.7 μs than was achieved with any trilinear model.

It is important to emphasize that this concave-convex model of GeO_2 produced a supersonic phase boundary in Shot 955. The GeO_2 remained in the high pressure phase for the duration of the simulation. No kinetic relationship was required or utilized. Thus, all differences between the predictions of the concave-convex model and the predictions of trilinear models that produced supersonic phase boundaries with no reverse phase change are caused strictly by the differences in their high pressure phases. The differences in their middle phases and in their kinetic relationships are irrelevant. Even their low pressure phases are irrelevant.

In contrast to the reasonable predictions for Shot 955, the combination of this concave-convex model for GeO_2 with the maximum dissipation kinetic relation gave poor results for Shot 965 and especially for Shot 953, Figures 5.4 and 5.5.

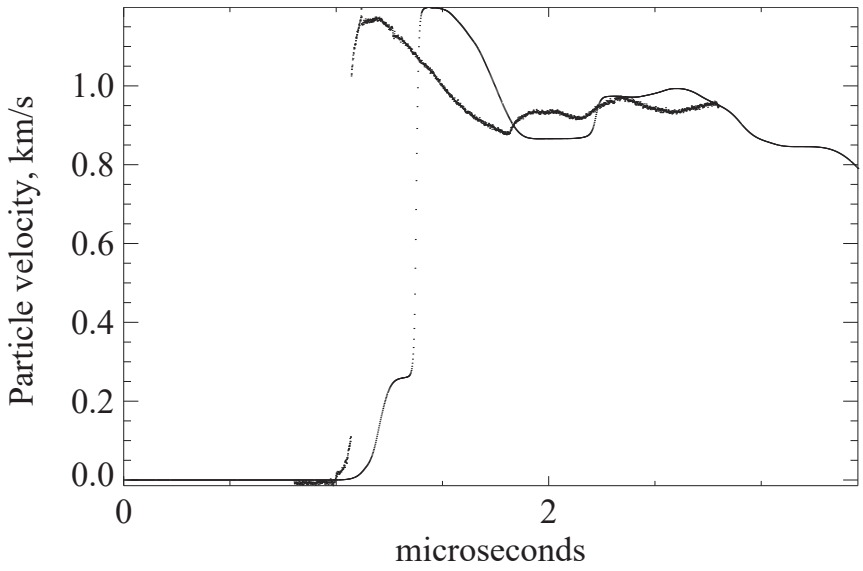

Figure 5.5: Predicted particle-velocity history of Shot 953 using a concave-convex model for GeO_2.

These were both exciting and discouraging discoveries. They were exciting because they suggested that a kinetic relation other than the roof might really be involved in the transformations. They were discouraging because they created a desire to study kinetic relations in materials with curvature in the high-pressure phase, but by this time, key routines of the program had been customized to accommodate only trilinear up-down-up materials. Perhaps it would suffice to vary kinetic relations in concave-convex materials, but this possibility was even more remote: there had never been an accommodation in the program for any kinetic relation besides the roof for monotonic materials.

Conceding that the trilinear model would not reproduce some of the features of the experimental VISAR profile, it was decided to select a linear high pressure phase that would at least reproduce the peak velocity of the VISAR record of Shot 955 and dwell at that velocity for about the right length of time. Largely through trial and error, this was achieved with $\bar{E}_1 = 800$ GPa, $d_1 \approx 330$ GPa, Figure 5.6. These are the parameters that will be used most extensively in Chapter 7.

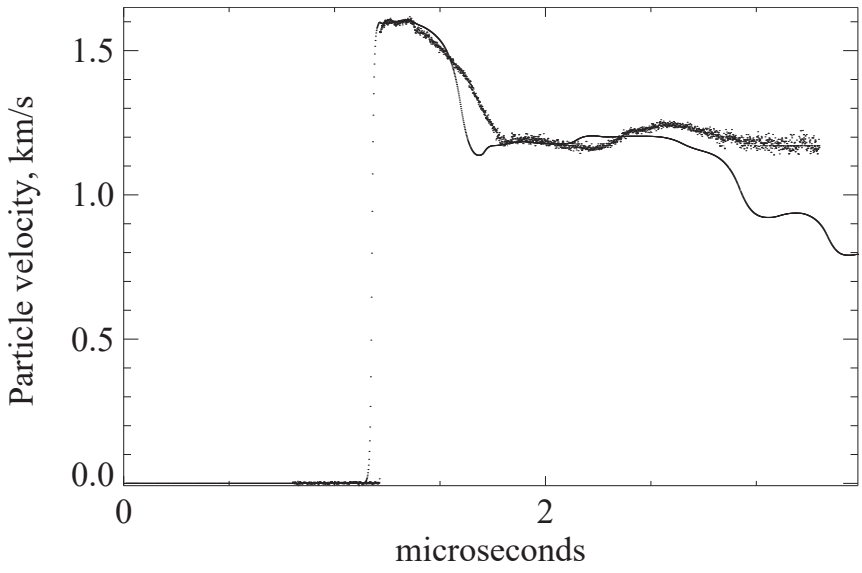

Figure 5.6: Predicted particle-velocity history of Shot 955 using the chosen trilinear model of GeO_2: $\bar{E}_1 = 800$ GPa, $d_1 \approx 330$ GPa.

The x, t diagram of Figure 5.3 was constructed after a considerable number of simulations had been conducted with this new trilinear model. When the diagram was completed, it was realized that it could have aided in selecting a linear high pressure phase to meet our goals. This x, t diagram was constructed with the help of routines that solve Riemann problems, and these provided the strain, stress, and particle velocity at each of the numbered locations. Our requirement to reproduce the peak velocity of the VISAR record is met by forcing the high pressure phase to reproduce states 1 and 2. This results in $\bar{E}_1 = 700$ GPa, $d_1 = 294$ GPa. To capture the duration of the peak VISAR velocity, the wave that travels from point 6 to point 11 should travel through the GeO_2 in the same time as the front of the fan that currently leaves point 11. Since this fan encounters several other waves in the GeO_2, we do not know its velocity exactly, but we can graphically estimate that its average velocity is around 13.5 km/s. Achieving this velocity in a linear high pressure phase requires that $\bar{E}_1 = 664$ GPa. Though we can't reproduce both the peak VISAR velocity *and* it's dwell time at the peak with just a linear high pressure

phase, at least the moduli estimated by the two different methods are in the same ballpark.

A simulation of Shot 955 was conducted with this last model, $\bar{E}_1 = 700$ GPa, $d_1 = 294$ GPa. The prediction was at best only a minor improvement over that obtained with the model that had already been chosen, so no more simulations were run with the new model.

We should expect either of these models to do poorly for the other shots: the other shots achieve lower pressures in the GeO_2, and the data points of Jackson and Ahrens indicate that the high pressure phase is much less stiff at these lower pressures: for instance, $\bar{E}_1 \approx 682$, 355, and 207 GPa at $\sigma \approx$ -27, -17, and -11 GPa, respectively.

5.1.1 Choosing extents of each phase

Having selected $\bar{E}_1$, d_1, $\bar{E}_3$, and d_3, all that remains is to prescribe the limiting strains γ_Z, γ_M, γ_m, and γ_F.

We will select $\gamma_Z = -0.510$, the most compressed state achieved in the experiments of Jackson and Ahrens [46]. To suppress "fracture" during the simulations, we choose the ridiculous value $\gamma_F = 100.0$.

The best we are able to do for γ_M and γ_m is to estimate bounds from the literature.

Jackson and Ahrens argued that the high pressure phase was retained when it was returned to a stress-free state. We will accept this, which requires

$$\sigma_M > 0 \ . \tag{5.4}$$

Their lowest pressure shot induced two discontinuities in the GeO_2: their data indicates that $\sigma = 4.1$ GPa behind the first discontinuity. If we assume that the

material behind the first discontinuity was in the low pressure phase, we have:

$$\sigma_m \leq 4.1 \text{ GPa} . \tag{5.5}$$

The low pressure and high pressure phases are not allowed to overlap in γ:

$$\gamma_M \leq \gamma_m . \tag{5.6}$$

Jackson and Ahrens, utilizing results of their own experiments and enthalpies of transformation obtained by Navrotsky [71], estimated that the transformation energy from the glassy phase to the high pressure phase is $\Psi(\gamma_T)$ = -0.253 kJ/g. We will impose this as a requirement on the trilinear model

$$\psi(\gamma_T) = \int_{\gamma_T}^{0} \hat{\sigma}(\gamma) d\gamma . \tag{5.7}$$

By the expression (3.52) for the driving traction in uniaxial deformation,

$$\psi(\gamma_T) = \hat{f}(0, \gamma_T) + \frac{1}{2}(\hat{\sigma}(\gamma_T) + \hat{\sigma}(0))(-\gamma_T) . \tag{5.8}$$

But $\hat{\sigma}(\gamma_T) = \hat{\sigma}(0) = 0$, and by (4.16c) for the driving traction in a trilinear material,

$$2\psi(\gamma_T) + \gamma_T \sigma_m = \sigma_M(\sigma_m \frac{\bar{E}_1 - \bar{E}_3}{\bar{E}_1 \bar{E}_3} - \gamma_T) . \tag{5.9}$$

This is a strong constraint: the selection of either σ_m or σ_M determines the other.

We use the principal contact locus to impose a final requirement. For any pair (γ_M, σ_M) and (γ_m, σ_m) selected, draw the contact locus in the σ, V plane. On the plot, overlay the data points obtained by Jackson and Ahrens. As shown in Figure 5.7, when γ_M is near to γ_m, two data points lie within the region ABC that corresponds to subsonic phase boundaries. As γ_M and γ_m move apart subject to (5.9), the CA boundary moves toward the BC boundary, and the region ABC shrinks, Figure 5.8. Eventually, the two data points no longer lie within ABC, nor

do they lie anywhere on the contact locus. Therefore, we eliminate any combination of γ_M and γ_m that cause either of these two data points to lie outside of ABC.

Satisfying (5.9), we find that preventing these two data points from falling left of the CA boundary is a much greater restriction than (5.4) or (5.5). In particular, (γ_M, σ_M) and (γ_m, σ_m) can be no farther apart in γ than:

$$(\gamma_M, \sigma_M) = (-0.3929, 15.9 \text{ GPa}) \ , \quad (\gamma_m, \sigma_m) = (-0.25, \text{-}11.3 \text{ GPa}) \ . \tag{5.10}$$

The pair that is closest together in strain without violating (5.6) is:

$$(\gamma_M, \sigma_M) = (-0.346, 53.4 \text{ GPa}) \ , \quad (\gamma_m, \sigma_m) = (-0.346, \text{-}15.6 \text{ GPa}) \ . \tag{5.11}$$

For definiteness, select:

$$(\gamma_M, \sigma_M) = (-0.352, \ 48.86 \text{ GPa}) \ , \quad (\gamma_m, \sigma_m) = (-0.340, \ \text{-}15.368 \text{ GPa}) \ . \tag{5.12}$$

This pair of points satisfies the all of the constraints and each point of the pair is between their respective extremes in (5.10)-(5.11).

In summary, this material is described by:

$$\rho_\circ = 3.629 \text{ g/cm}^3 \ , \tag{5.13}$$

$$\hat{\sigma}(\gamma)[\text{GPa}] = \begin{cases} \text{undefined} & \text{for } \gamma < -0.510 \ , \\ \hat{\sigma}_1(\gamma) = 800.0\gamma + 330.212 & \text{for } -0.510 < \gamma \leq -0.352 \ , \\ \hat{\sigma}_2(\gamma) = -5494.807\gamma - 1883.602 \ , & \text{for } -0.352 < \gamma \leq -0.340 \ , \\ \hat{\sigma}_3(\gamma) = 45.2\gamma \ , & \text{for } -0.340 < \gamma \leq 100.0, \\ \text{undefined} & \text{for } \gamma > 100.0 \ . \end{cases} \tag{5.14}$$

It has a longitudinal wave speed of $c_3 = (\bar{E}_3/\rho_\circ)^{1/2} = 3.53$ km/s.

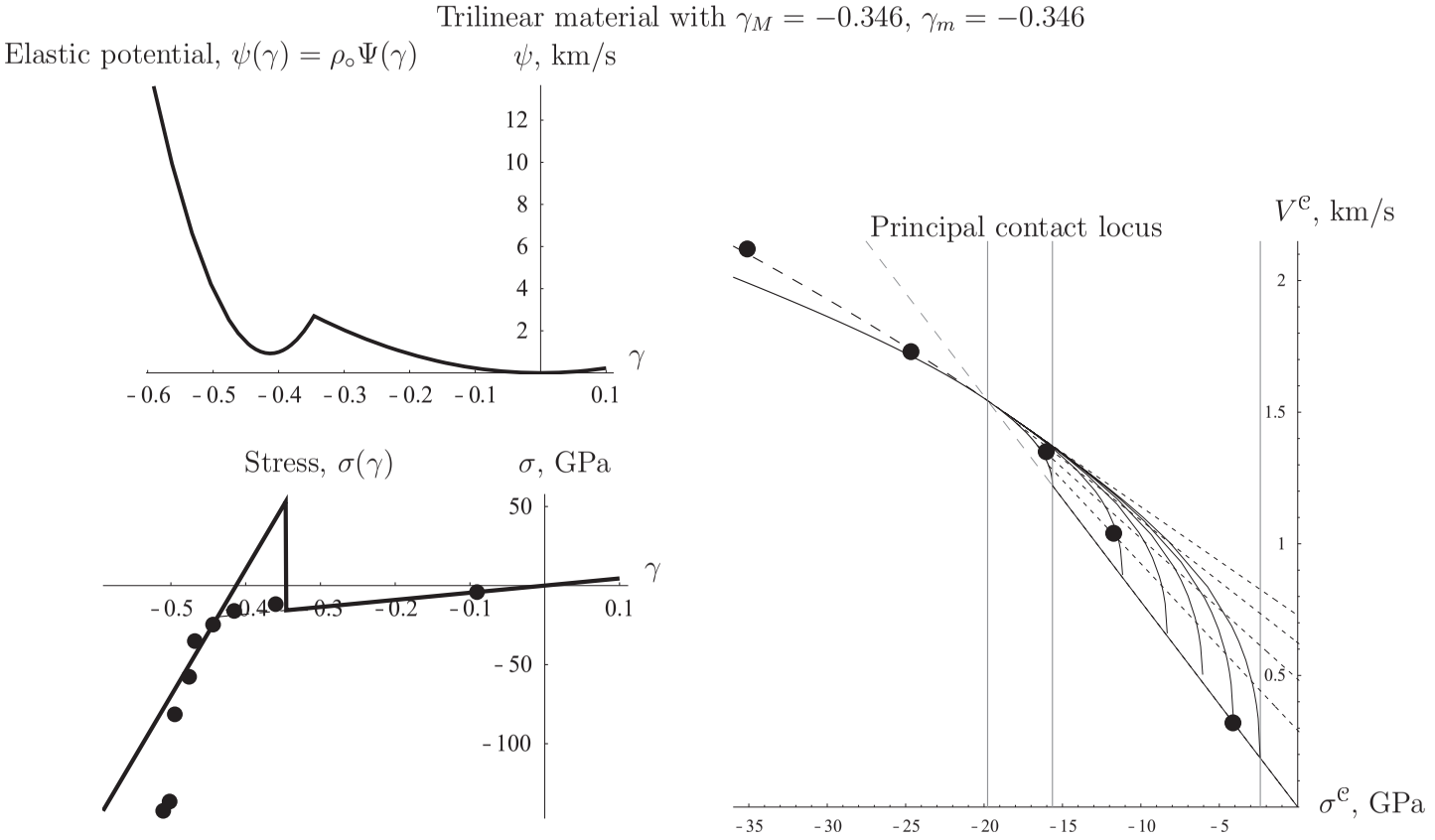

Figure 5.7: Trilinear model and principal contact locus subject to constraints (5.4)-(5.6) and (5.9), with $\gamma_M \approx \gamma_m$, (5.11). Circles are data points from Jackson and Ahrens, [46]. The contact locus in the supersonic regime ($\sigma \lesssim 19.8$ GPa) is the dashed curve immediately above the solid curve. (The solid curve is an extension of the hyperbola that describes the maximum dissipation contact locus for subsonic phase boundaries.)

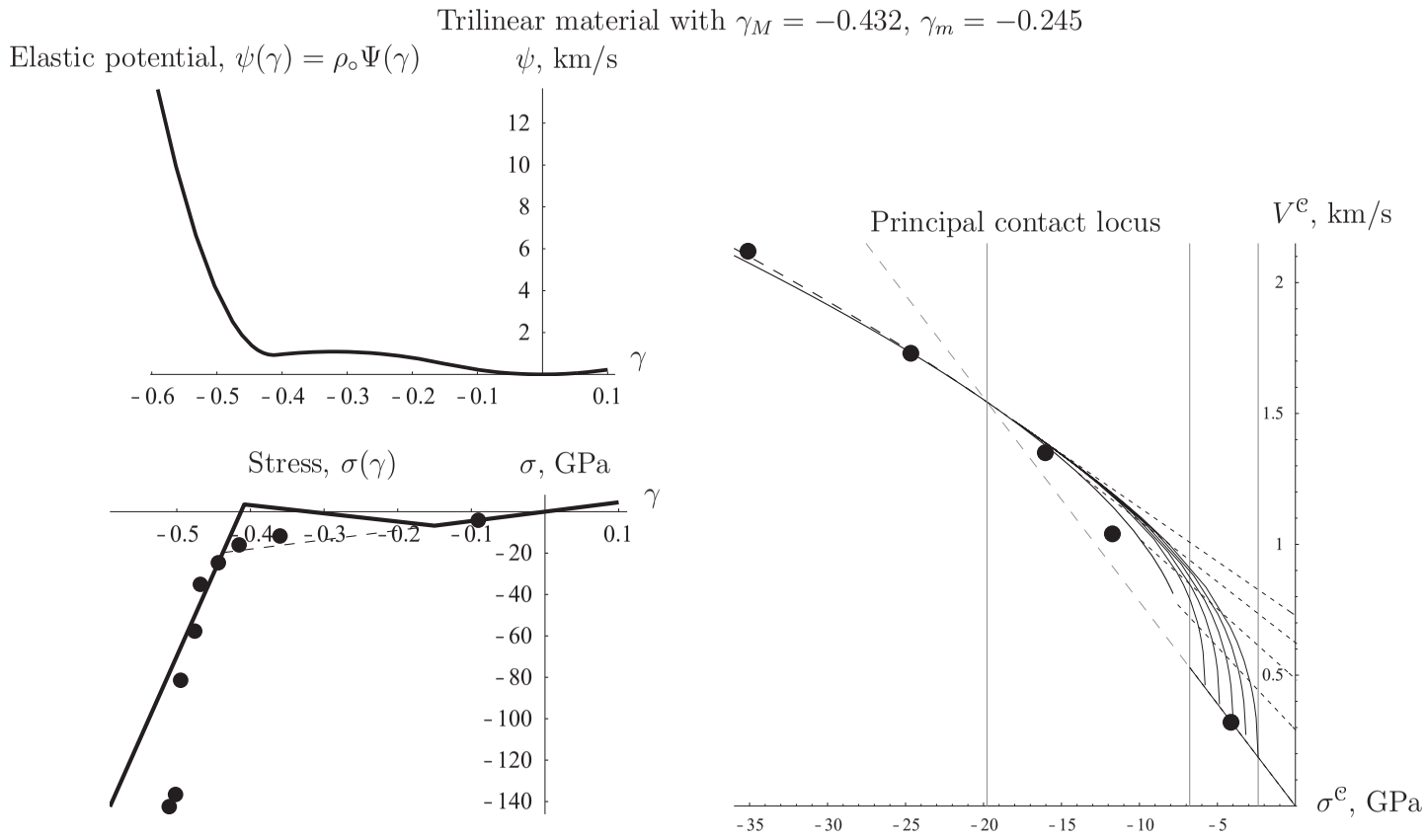

Figure 5.8: Trilinear model if $\gamma_M = -0.408$, $\gamma_m = -0.150$. Because data points in the range of stress that can only be reached by a subsonic phase boundary are outside of the contact locus ABC, this material is eliminated as a candidate. The contact locus in the supersonic regime ($\sigma \lesssim 19.8$ GPa) is the dashed curve immediately above the solid curve. (The solid curve is an extension of the hyperbola that describes the maximum dissipation contact locus for subsonic phase boundaries. A portion of this locus is missing because of plotting difficulties.)

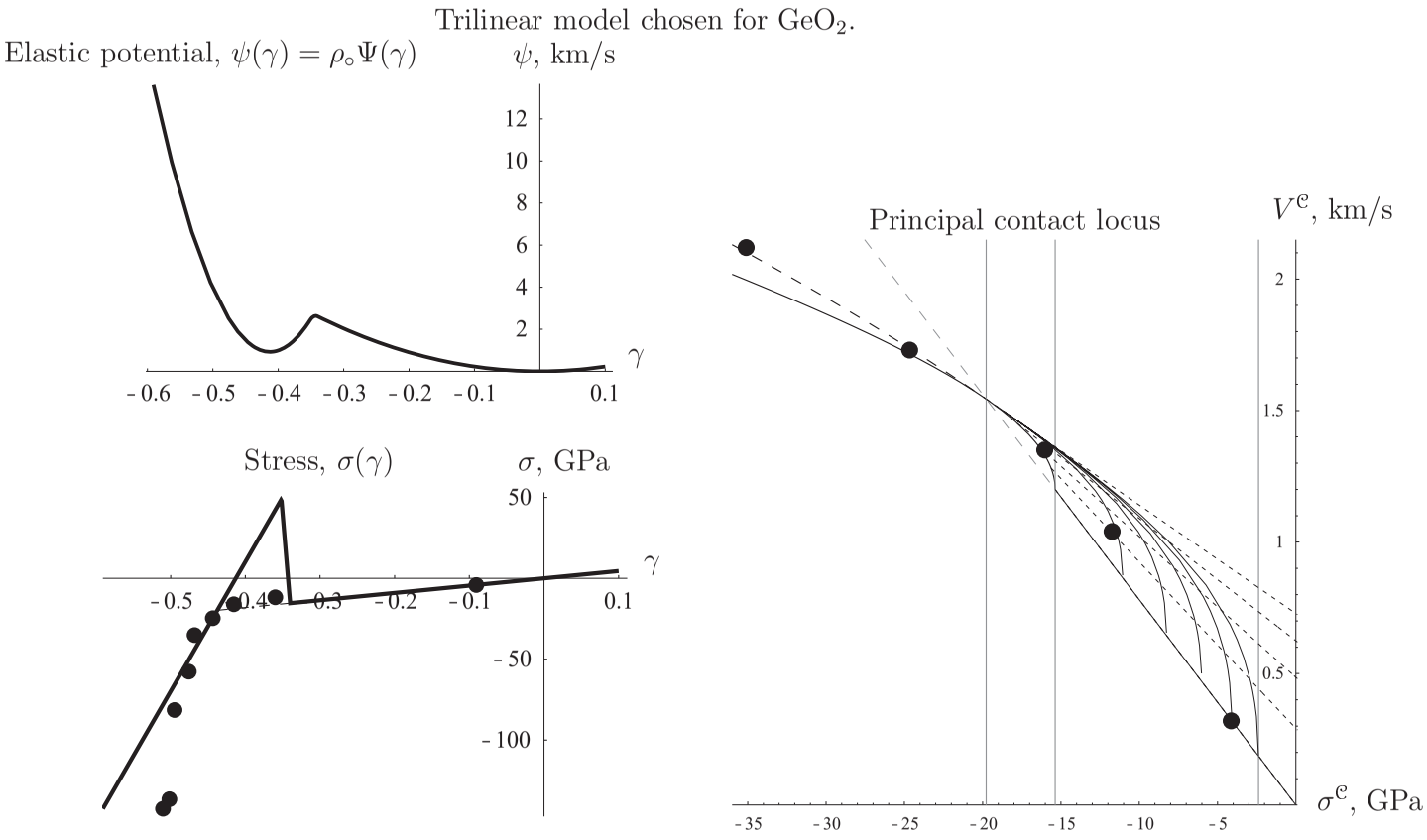

Figure 5.9: Trilinear model and contact locus selected for GeO_2. The contact locus in the supersonic regime ($\sigma \lesssim 19.8$ GPa) is the dashed curve immediately above the solid curve. (The solid curve is an extension of the hyperbola that describes the maximum dissipation contact locus for subsonic phase boundaries.)

5.2 Kinetic relations for the germanium dioxide

In Chapter 7 we will examine results of a number of simulations that have been conducted using the material model (5.14). Linear kinetic relations $\mathcal{F}_{ab}(\dot{s}) = g_{ab} + h_{ab}\,\dot{s}$ are prescribed, and the coefficients g_{ab} and h_{ab} are varied between simulations. The roof $\mathcal{F}_{ab}(\dot{s}) = \mathcal{F}^{\text{roof}}_{ab}(\dot{s})$ is also prescribed in some simulations.

All kinetic relations that we examine will remain below the roof; that is $\mathcal{F}_{ab}(\dot{s}) < \mathcal{F}^{\text{roof}}_{ab}(\dot{s})$ for all $|\,\dot{s}\,| < c_3 = 3.53$ km/s. The roof $\mathcal{F}^{\text{roof}}_{ab}(\dot{s})$ is plotted for the transformation from the low pressure phase to the high pressure phase in Figure 5.10 and for the reverse transformation (from the high pressure phase to the low pressure phase) in Figure 5.11.

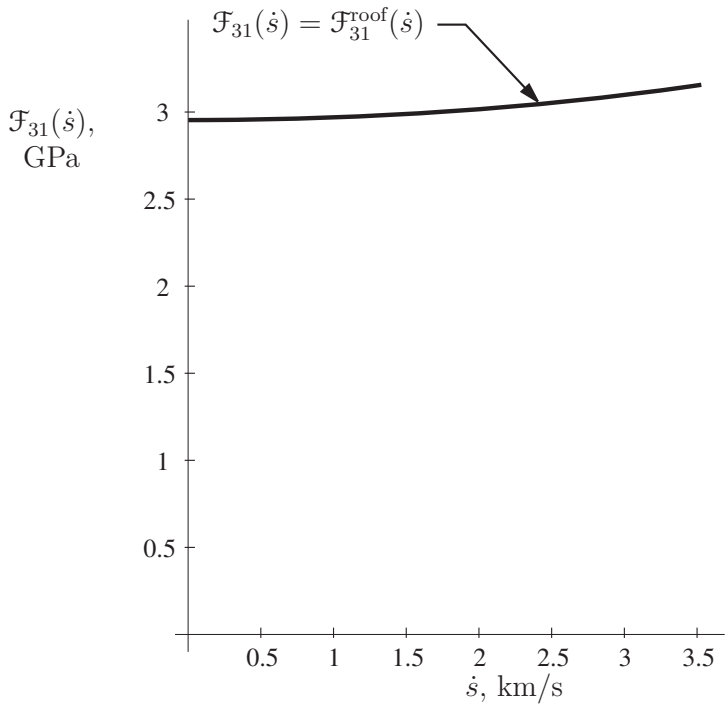

Figure 5.10: The roof or maximum-dissipation kinetic relation for the transformation from the low pressure phase to the high pressure phase.

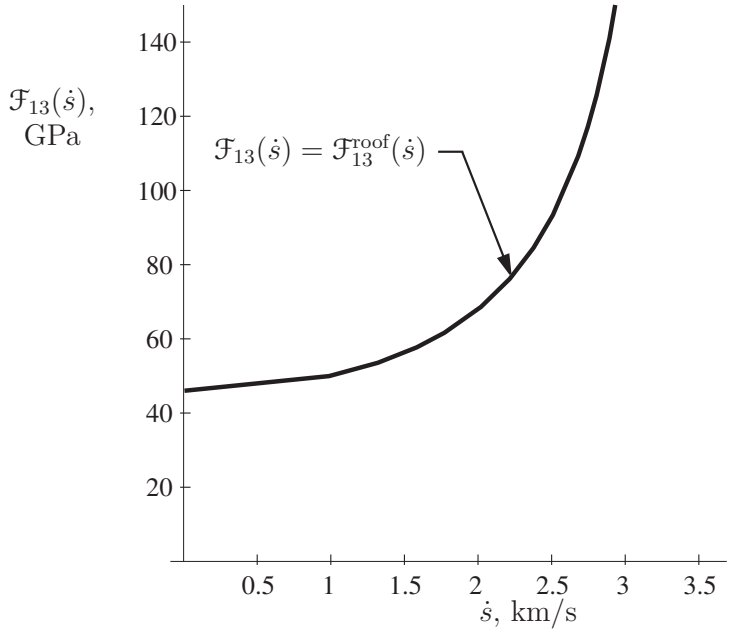

Figure 5.11: The roof or maximum-dissipation kinetic relation for the transformation from the high pressure phase to the low pressure phase.

5.3 Elastic models for the ancillary materials

Under uniaxial shock compression, lithium fluoride, Al6061-T6, and tungsten each exhibit three regimes of behavior: a linearly elastic regime, a regime with plasticity, and a highly compressed regime which is usually modeled as thermoelastic. (Under conditions of high confining pressures, plastic-like deformation occurs even in normally brittle materials like ceramics [23, 43].) In this work, no attempt is made to accurately describe plastic or thermoelastic behavior; all three regimes are taken to be elastic. In particular, these materials will be modeled with the concave-convex material model.

The foam responds in a similar fashion, except that "crushing" replaces plasticity, and will also be modeled with the concave-convex model.

Recall the $\hat{\sigma}(\gamma)$ relation for the concave-convex model:

$$\hat{\sigma}(\gamma) = \begin{cases} \text{undefined} & \text{for } \gamma < \gamma_Z \ , & (5.15a) \\ \hat{\sigma}_1(\gamma) = \bar{K}\gamma\,(1+s_1\gamma)^{-2} & \text{for } \gamma_l \le \gamma \le \gamma_m \ , & (5.15b) \\ \hat{\sigma}_2(\gamma) = a - b\,(-\gamma)^n \quad n \neq -1 & \text{for } \gamma_m < \gamma < \gamma_M \ , & (5.15c) \\ \hat{\sigma}_3(\gamma) = \bar{E}\gamma & \text{for } \gamma_M \le \gamma \le \gamma_F \ , & (5.15d) \\ \text{undefined} & \text{for } \ \gamma > \gamma_F > 0 \ . & (5.15e) \end{cases}$$

We now discuss the motivation for the form of each segment of this stress response function, and how the expression for each was obtained.

The low pressure phase models the longitudinal response for small deformations, $|\,\gamma_M\,| \ll 1$, where it is adequate to describe the material by linear elasticity. In particular, the deformation gradient γ is approximately equal to the longitudinal component ϵ of the linearized strain tensor:

$$\gamma \approx \epsilon \qquad \text{if } \ |\,\gamma_M\,| \ll 1 \ . \tag{5.16}$$

The modulus $\bar{E}$ is the usual longitudinal modulus of linear elasticity for isotropic materials:

$$\bar{E} = \lambda + 2\mu = \kappa + \frac{4}{3}\mu \ , \tag{5.17}$$

where λ, μ, and κ are Lame's modulus, the shear modulus, and the bulk modulus, respectively.

The lower bound (γ_M, σ_M) for this interval of the stress response function is the value at which yield is thought to occur. This point is computed from published values of the yield stress $Y_\circ$ at very high strain rates. The von Mises yield criterion predicts that for loading in longitudinal strain in the x direction, yield first occurs

when

$$\sigma - \sigma_L = -Y_\circ \ , \tag{5.18}$$

where the subscript L indicates either of the equivalent lateral directions.

Imposing the usual assumptions that volumetric strain is purely elastic and that the elastic deformation can be described by linear isotropic theory, the lateral stress can be computed,

$$\sigma_L = \lambda(\epsilon^e + \epsilon^p) + \mu\epsilon^p \ . \tag{5.19}$$

The strains ϵ^e and ϵ^p are respectively the elastic and plastic strains in the longitudinal direction, so that $\epsilon = \epsilon^e + \epsilon^p$.

When yield first occurs, $\epsilon^p = 0$ and $\epsilon^e = \epsilon_M$. Equations (5.16), (5.18), (5.19), and the expression (5.15d) of $\hat{\sigma}(\gamma)$ in the low pressure phase can be solved at this condition to obtain

$$(\gamma_M, \sigma_M) = \left(\frac{-Y_\circ}{2\mu}, -\bar{E}\frac{Y_\circ}{2\mu} \right) \ . \tag{5.20}$$

The linear segment can end at a tensile "fracture" limit, $\gamma_F > 0$ above which σ drops to zero for any γ. This is intended to imitate a spall behavior, but in all simulations γ_F was taken to be sufficiently great that γ_F was never reached.

The middle phase is modeled by a power law relation intended to mimic the loading behavior in plasticity. Unfortunately, it is difficult to determine values for a, b, and n from the literature, and in the end all simulations were done with this segment taken to be a straight line by setting $n = 1$. The parameters a and b were then set to produce a line between the adjoining two segments from γ_m to γ_M, where γ_m is the upper bound for which the expression (5.15b) of the stress response function in the high pressure segment is experimentally verified.

The expression for the high pressure phase derives from a response common to

many materials, including those here. For a great variety of materials, it has been found that, over a substantial range of data, the velocity W of a single compressive discontinuity passing through an initially unstressed material at rest is linearly related to the resulting particle velocity V^- behind that discontinuity. For a right-traveling discontinuity ($W > 0$),

$$W = s_0 + s_1 V^- \ . \tag{5.21}$$

Discussions of this remarkable relationship can be found in [28, 50, 51]. The parameters s_0 and s_1 have been compiled for many materials [16, 66, 91].

Satisfying the jump conditions (3.38)-(3.39) subject to (5.21) leads to the expression (5.15b) for $\hat{\sigma}(\gamma)$ in the high pressure phase, where

$$\bar{K} = \rho_\circ s_0^2 \ . \tag{5.22}$$

The bounds γ_m and γ_Z are the extremes for which (5.21) has been verified experimentally. No extrapolation of (5.15b) beyond these bounds was required in this thesis; any extrapolation must be done with caution, especially since (5.15b) is singular at $\gamma = -s_1^{-1}$ and has negative slope for $\gamma > s_1^{-1}$.

Table 5.1 lists the parameters for the ancillary material models, and Figure 5.12 depicts their stress response functions.

Parameters for the foam warrant a brief discussion. The values s_0 and s_1 were approximated with expressions in the appendices of [38]:

$$s_0 = \frac{\rho_{\circ\circ}}{\rho_{\circ\circ} - \rho_\circ} \ , \tag{5.23}$$

$$s_1 = \sqrt{\frac{s_0 P_c}{\rho_\circ}} \ , \tag{5.24}$$

where $\rho_{\circ\circ}$ is the density of the matrix material and P_c is a characteristic crush parameter. (Readers referring to [38] are advised that the definitions of $\rho_\circ$ and $\rho_{\circ\circ}$ in that report are interchanged with respect to those here.) Assume that

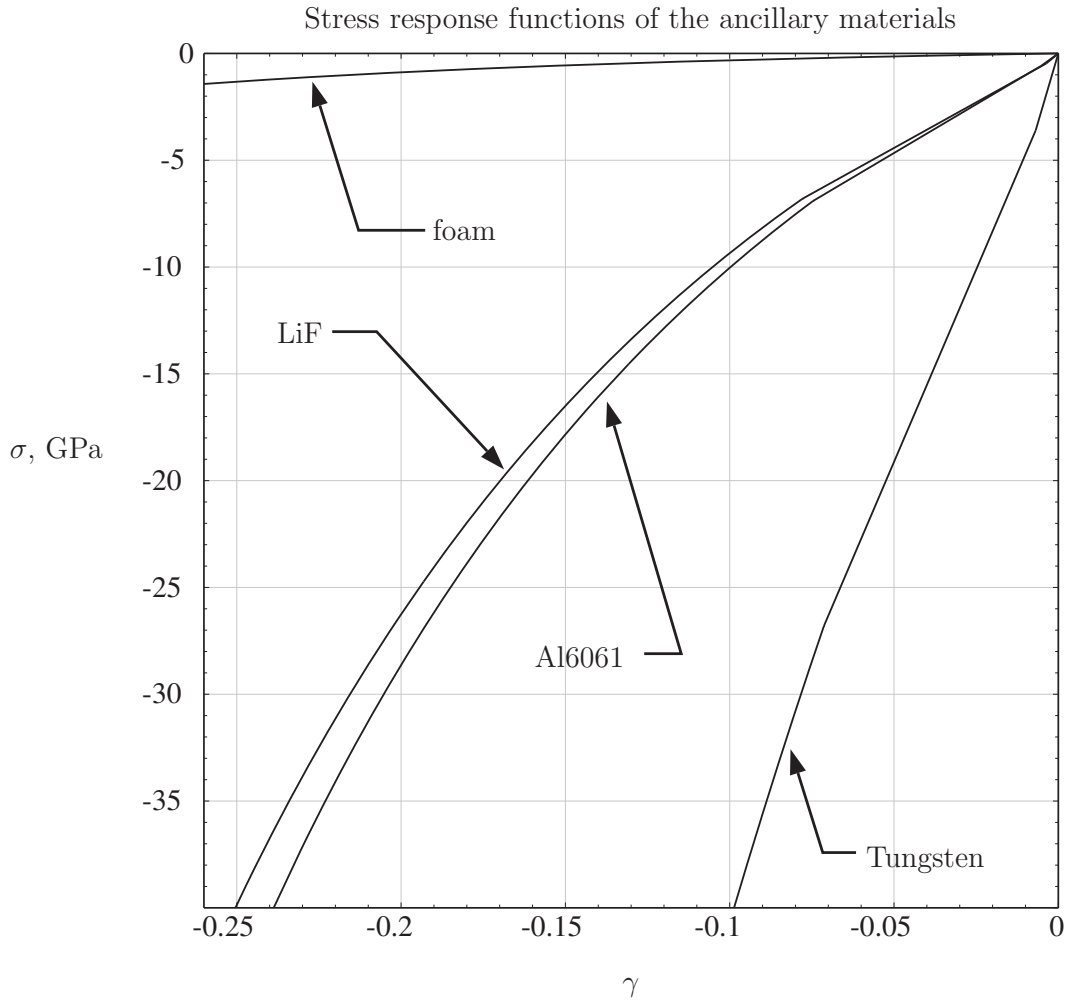

Figure 5.12: Stress response models of the ancillary materials, plotted over the range of stress encountered in the simulations of later chapters.

$\rho_{\circ\circ} = 1.2\,\mathrm{g/cm^3}$ [18]. Take $P_c = 22.5\,\mathrm{MPa}$, based on properties for a 40 $\mathrm{lb/ft^3}$ polyurethane foam in Table II-1 of [38].

For the low pressure phase, the longitudinal modulus $\bar{E}$ is calculated from (5.17) by taking Young's modulus to be 0.06 GPa [18] and assuming that Poisson's ratio is 1/3. The resulting expression for the low pressure phase intersects the high pressure phase at $\gamma_A \approx$ -0.14. We will arbitrarily divide the interval between this point and the origin equally between the low pressure phases and the middle phase, and will force the middle phase to have a slope equal to half of that of the low pressure phase. These bold assumptions can be tolerated because the foam plays a relatively minor role in the particle-velocity histories of the experiments.

	Al6061	LiF	Tungsten	Foam
$\rho_\circ$, g/cm^3	2.703 [91]	2.638 [91]	19.235	0.61
$\bar{E}$, GPa	111 [59, 91]	128 [55, 91]	523 [66]	0.09 [18]
a, GPa	-0.105472	-0.156736	-1.12036	-.00315
b, GPa	91.124	85.3662	360.039	0.045
n	1	1	1	1
s_0, km/s [91]	5.24	5.15	4.03	2.034 [38]
s_1	1.40 [91]	1.35 [91]	1.237 [91]	0.273 [38]
$Y_\circ$, GPa	0.29 [91]	0.36 [91]	2.2 [91]	–
γ_M	-0.00525362	-0.00367347	-0.006875	-0.07
σ_M, GPa	-0.584203	-0.470327	-3.59563	-0.0063
γ_m	-0.0746 [66]	-0.0779 [66]	-0.0713 [66]	-0.1073
σ_m GPa	-6.90332	-6.80677	-26.791	-7.977

Table 5.1: Model parameters for the ancillary materials. The longitudinal modulus, $\bar{E}$, was computed for Al6061 from μ [91] and κ [59], for lithium fluoride from μ [91] and κ [55], and for tungsten from the wave speeds and density in [91]. Tungsten and foam densities were measured in the experiments of Chapter 2. Parameters a, b, and n for the power law segment were determined so that (γ_M, σ_M) and (γ_m, σ_m) were connected with a straight line (see text). The values γ_m, σ_m, γ_M, σ_M were found as described in the text. See the text for a discussion of the foam's parameters. Other values are from the references cited in the table.

5.4 Summary

Figure 5.13 shows the stress response functions described by $\sigma = \hat{\sigma}(\gamma)$ for the five materials. Figure 5.14 illustrates their principal contact loci in compression.

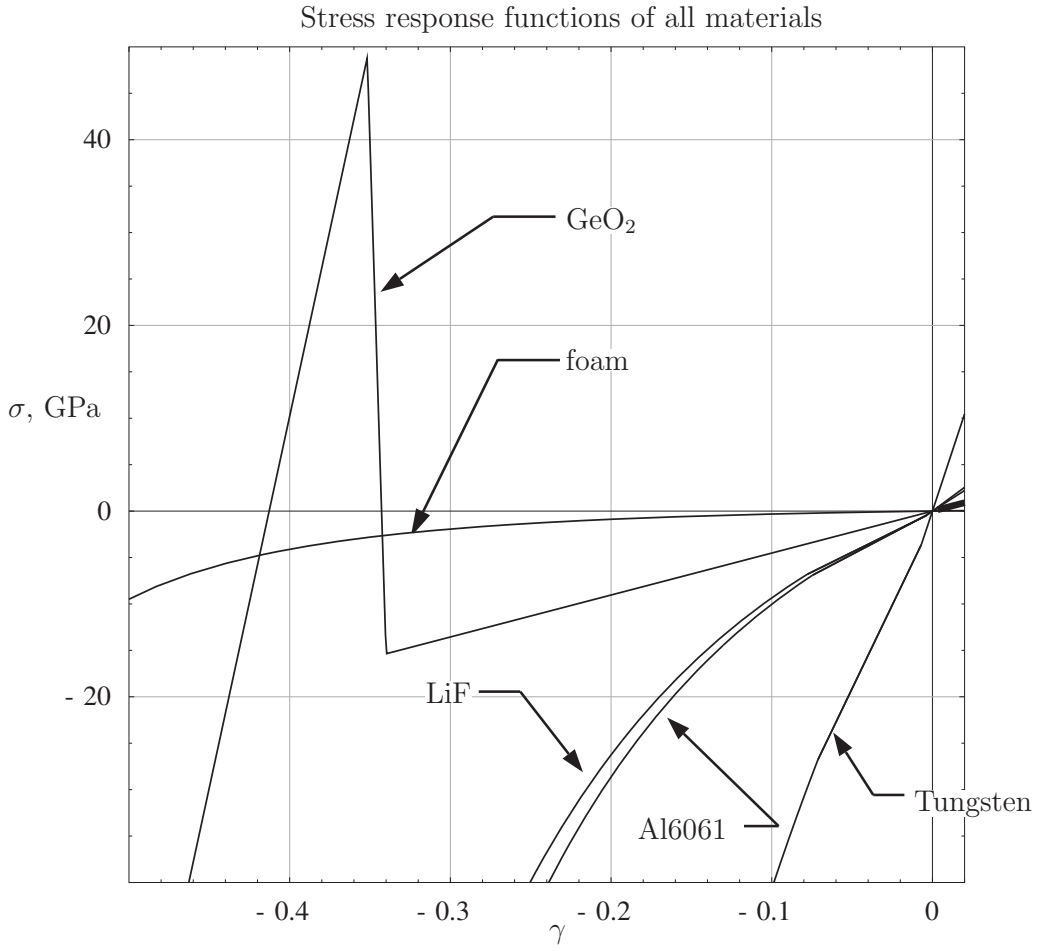

Figure 5.13: Stress response models of all materials over the range of stress encountered in the simulations.

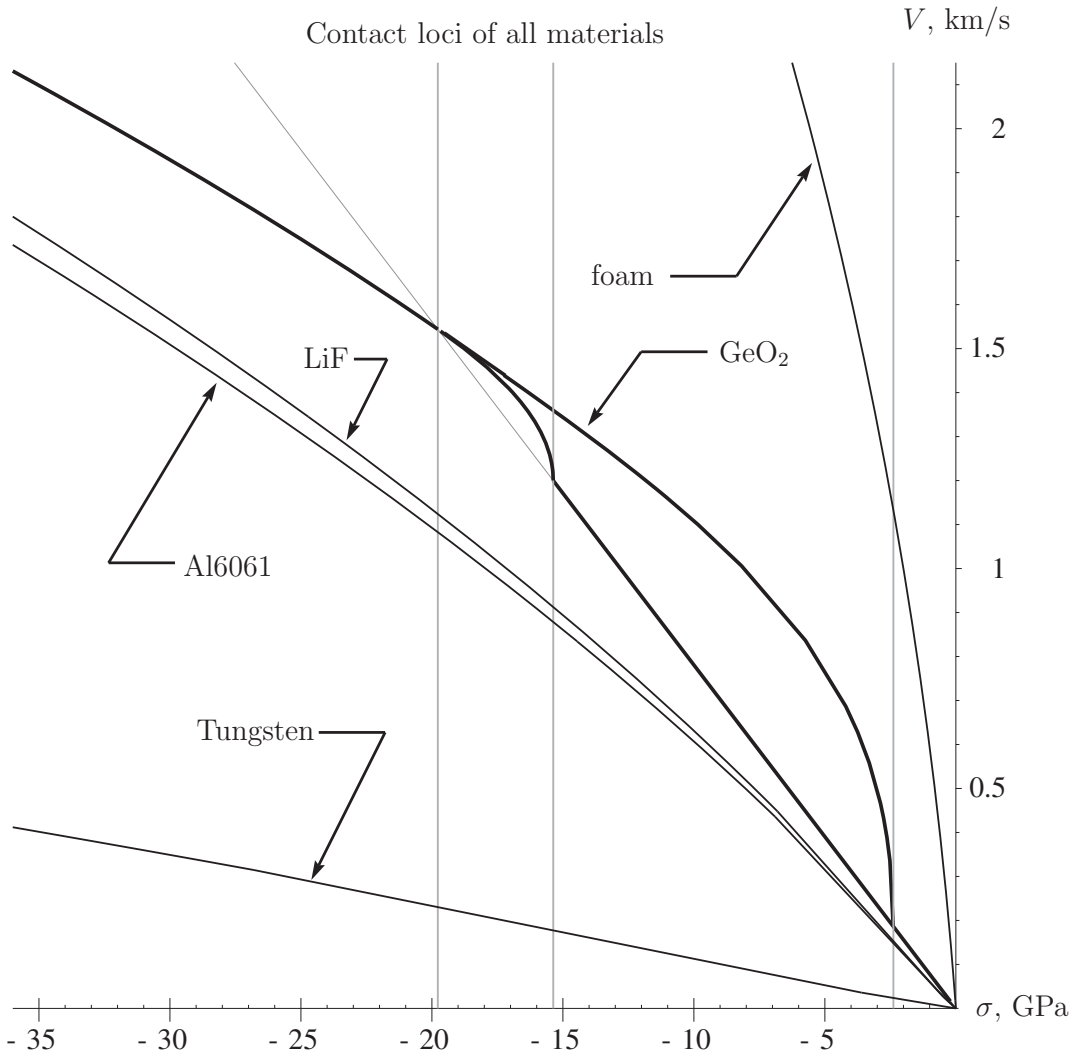

Figure 5.14: Principal contact loci for the material models. The vertical lines indicate σ_A, σ_m, and $\sigma_\circ$ for the GeO_2.

Chapter 6

Numerical method

The computational method employed in this work is based on one developed by Zhong, Hou and LeFloch [109] for the treatment of one-dimensional problems involving both phase boundaries and shocks. Their technique builds on *front tracking* and *shock capturing* methods utilized for shock waves in computational fluid dynamics.

Front tracking schemes compute a shock front sharply without numerical dissipation, but they are difficult to implement when shock wave interactions are involved [108].

Shock capturing schemes spread shock fronts out over a few mesh cells, adequate for many applications. Implementation is relatively straight-forward, and no modifications are required to accommodate shock wave interactions. Of particular interest to us are the shock capturing methods based on the first-order Godunov method and its higher order extensions, which have received a great deal of attention in recent years [19, 24, 25, 30, 37, 39, 103].

In capturing, strain and velocity are averaged within each cell. In a cell containing multiple phases, the average strain could fall in a range corresponding to an unstable phase, but unstable phases do not arise in the physical model if they aren't there initially [5]. Naïve application of capturing schemes may lead to unphysical solutions when phase transformations are involved.

One treatment for this difficulty is to approximate the behavior of a multiphase

cell by an effective single phase, the properties of which are computed from the stable phases within the cell. This is the approach taken in most codes of which the author is aware, both "research codes" [69] and established "production codes" like CTH, Wondy, and SHARC.

Zhong, Hou and LeFloch's approach is a hybrid scheme; phase boundaries are tracked, and shocks are captured. When a phase boundary is present, gridpoints are adjusted so that the boundary passes *between* cells rather than *through* a cell. In this way, mixed-phase cells are not generated.

Any numerical method based on a Godunov scheme must find the solution of certain canonical initial-boundary value problems, Riemann problems, and impact problems at the cell boundaries. For a general elastic material, finding the exact solution to these problems requires costly numerical integration of the $\sqrt{\hat{\sigma}'(\gamma)}$ term that arises in the expression (3.63) for fans. To make matters worse, this integral must be evaluated repeatedly as the program iterates to find the intersection of the loci of contact states for the right and left sides of a Riemann problem or impact problem. For these reasons, an important part of most Godunov-based methods is the implementation of an *approximate Riemann solver* to find these solutions.

Bucking the trend, no approximate Riemann solver is employed here. Recall from Chapter 4 that the integral that causes the grief can be found analytically for the material models we consider. We take advantage of this to construct *exact Riemann solvers* for these models, using bisection algorithms to find the crossings of the contact loci. The bisection algorithm was chosen as a root-finder for robustness; it is guaranteed to find the root of an equation of one variable in a prescribed interval if the function is continuous and has a single root in that interval.

This chapter presents the numerical approach used in this work. It begins by reviewing Godunov methods, working from the first-order to the second order method. Next, the hybrid scheme of Zhong, Hou, and LeFloch is introduced. Then a section highlights the features that are special to our particular implementation, including remedies for some time-step problems caused by phase boundaries. Two sections

then outline some of the mechanics of the code, describing data structures and routines that are utilized by the exact Riemann solvers. These mechanics aid in understanding the program and the Riemann solvers in particular. The final section presents an overview of the exact Riemann solvers.

The phrase "Riemann solver" is used loosely: in this document it includes not only routines that solve Riemann problems, but also routines that solve initial-boundary value problems.

6.1 Godunov methods

In a landmark paper of 1959, Godunov proposed that the local characteristic structure obtained by solving a Riemann problem could be used to define a numerical method of treating balance equations [36].

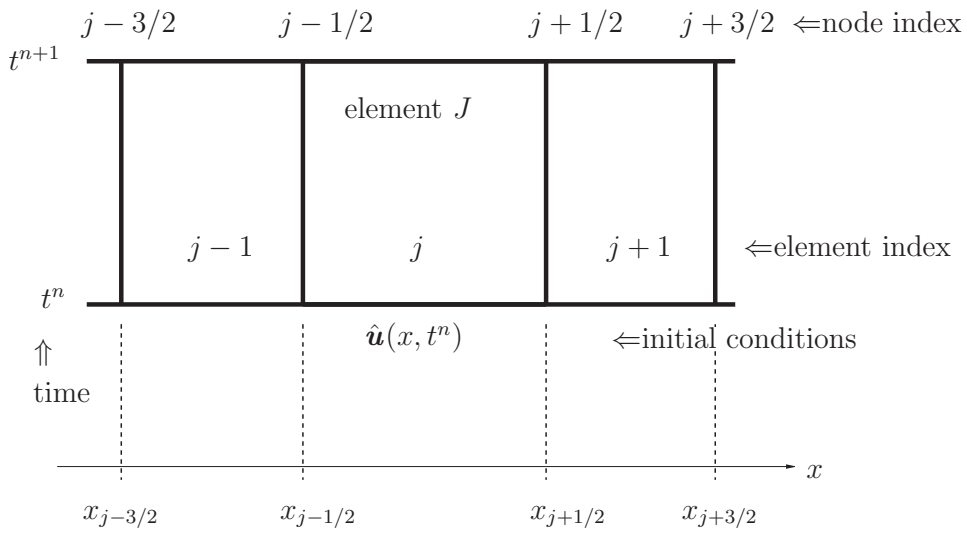

Figure 6.1: Numerical grid and notation.

Consider the element J on the discretized space and time grid of Figure 6.1. For an elastic material, an integral form of the balance laws for this element is

$$\iint_J \{\boldsymbol{u}_t + \boldsymbol{g}_x(\boldsymbol{u})\} dx dt = 0 \,. \tag{6.1}$$

Here $\boldsymbol{u}$ is the *vector of conserved quantities* and $\boldsymbol{g}$ is the *flux vector*,

$$\boldsymbol{u} = \hat{\boldsymbol{u}}(x,t) = \begin{Bmatrix} V \\ \gamma \end{Bmatrix} , \qquad \boldsymbol{g}(\boldsymbol{u}) = \hat{\boldsymbol{g}}(x,t) = \begin{Bmatrix} -\hat{\sigma}(\gamma)/\rho_\circ \\ -V \end{Bmatrix} , \tag{6.2}$$

and

$$\boldsymbol{g}_x(\boldsymbol{u}) = \boldsymbol{g}\,'(\boldsymbol{u})\boldsymbol{u}_x = \begin{pmatrix} 0 & -\hat{\sigma}'(\gamma)/\rho_\circ \\ -1 & 0 \end{pmatrix} \begin{Bmatrix} V_x \\ \gamma_x \end{Bmatrix} . \tag{6.3}$$

Applying Green's Theorem to (6.1),

$$\int_{\partial J} \{\boldsymbol{g}(\boldsymbol{u})dt - \boldsymbol{u}dx\} = 0. \tag{6.4}$$

Writing this out for each of the four sides of the element J,

$$\int_{x_{j-1/2}}^{x_{j+1/2}} \hat{\boldsymbol{u}}(x,t^n)dx + \int_{t^n}^{t^{n+1}} \hat{\boldsymbol{g}}(x_{j+1/2},t)dt + \int_{x_{j+1/2}}^{x_{j-1/2}} \hat{\boldsymbol{u}}(x,t^{n+1})dx + \int_{t^{n+1}}^{t^n} \hat{\boldsymbol{g}}(x_{j-1/2},t)dt = 0 \tag{6.5}$$

Denote the duration of the n^{th} time-step by

$$(\Delta t)^n = t^{n+1} - t^n , \tag{6.6}$$

and the width of cell J at time t^n by

$$(\Delta x)_j^n = x_{j-1/2}^n - x_{j+1/2}^n . \tag{6.7}$$

The *cell average* of $\boldsymbol{u}$ in cell J at time t^n is

$$\bar{\boldsymbol{U}}_j^n = \frac{1}{(\Delta x)_j^n} \int_{x_{j-1/2}}^{x_{j+1/2}} \hat{\boldsymbol{u}}(x, t^n) dx \ . \tag{6.8}$$

The *time average flux* on the $j + 1/2$ boundary from time t^n to t^{n+1} is

$$\boldsymbol{G}_{j+1/2}^n = \frac{1}{(\Delta t)^n} \int_{t^n}^{t^{n+1}} \hat{\boldsymbol{g}}(x_{j+1/2}, t) dt \ . \tag{6.9}$$

Solving (6.5) for the cell average of the conserved quantities at the end of the time-step,

$$\bar{\boldsymbol{U}}_j^{n+1} = \bar{\boldsymbol{U}}_j^n - \frac{(\Delta t)^n}{(\Delta x)_j^n} \left(\boldsymbol{G}_{j+1/2}^n - \boldsymbol{G}_{j-1/2}^n \right) \ . \tag{6.10}$$

6.1.1 First-order Godunov method

In the first-order Godunov method, the conditions $\boldsymbol{u}(x, t^n)$ at the start of each time-step are approximated by the averages in each cell, $\ldots\ \bar{\boldsymbol{U}}_{j-1}^n,\ \bar{\boldsymbol{U}}_j^n,\ \bar{\boldsymbol{U}}_{j+1}^n\ \ldots$. Neighboring cells are then treated as the two halves of a Riemann problem. Assume that the solutions to all of the Riemann problems can be found, and let $\boldsymbol{U}_{J,j+1/2}^{*,n}$ be the solution at the cell boundary $x_{j+1/2}$ in the cell J. Now assume that all solutions are constant along the grid boundaries over the time interval $t \in (t^n, t^{n+1})$. Then the flux vectors computed from $(6.2)_2$ are constant on each cell boundary, and computation of the average flux vector (6.9) is a trivial matter. The cell averages for the next time-step are computed from (6.10), and the process repeats.

The solution $\boldsymbol{U}_{J,j+1/2}^{*,n}$ will *not* be constant if waves arising from neighboring Riemann problems propagate to $x_{j+1/2}$. If waves cross the cell boundaries, the solution is no longer constant on the boundaries, oscillations arise and the numerical method becomes unstable. This difficulty is prevented by restricting the time-step

$(\Delta t)^n$ such that

$$(\Delta t)^n < \min_j \frac{(\Delta x)_j^n}{c_j^n} \qquad \text{for all elements } J \ , \tag{6.11}$$

where c_j^n is the highest wave speed of the material in cell J during the n^{th} time-step.

In practice, the wave speed c_j^n is not known everywhere in a cell and the maximum wave speed in any cell is only approximated, perhaps by the wave speed at the start of the time-step, $(c)_j^n \approx (\hat{\sigma}\,'(\gamma_j^n)/\rho_\circ)^{1/2} = \pm\lambda_j^n$. Here, $\pm\lambda_j^n$ are the eigenvalues of $\boldsymbol{g}\,'(\bar{\boldsymbol{U}}_j^n)$. The restriction is then expressed as the *CFL condition*,

$$\lambda_j^n \frac{(\Delta t)^n}{(\Delta x)_j^n} < 1 \ . \tag{6.12}$$

In a linear system, the restriction (6.12) allows waves from neighboring Riemann problems to interact during a time-step, but the interaction and resulting waves are entirely contained within a cell during the time-step. In non-linear systems, the interaction within a cell may produce waves that travel faster than the interacting waves, and (6.12) is inadequate to contain these new waves within the cell. In non-linear systems, then, (6.12) is replaced by

$$\lambda_j^n \frac{(\Delta t)^n}{(\Delta x)_j^n} < \tau \ , \tag{6.13}$$

where the *Courant number* $\tau < 1$ is chosen (often by trial and error) to prevent numerical oscillations from arising. The more strongly non-linear the problem, the lower τ must be.

In the simulations for this thesis, a Courant number of $\tau = 0.8$ is typical.

6.1.2 Second-order Godunov method

Considerable effort has been expended to extend Godunov's approach to higher order [102, 103]. In brief, the method is made higher order in space by approximating the conditions at the start of each time-step by piecewise polynomial functions of higher-

order than the piecewise constant functions used above (which are of order zero). Neighboring cells are still treated as the two halves of a Riemann problem, with initial conditions prescribed by the polynomial functions evaluated at the boundary between the cells.

We consider only the second-order extension of the Godunov method. At the start of the n^{th} time-step, $\hat{\boldsymbol{u}}(x, t^n)$ is approximated within each cell by a linear function $\boldsymbol{U}_j^n(x)$:

$$\boldsymbol{U}_j^n(x) = \bar{\boldsymbol{U}}_j^n + \frac{1}{(\Delta x)_j^n}(x - x_j)\delta_j^n \boldsymbol{U} \qquad \text{for } x_{j-1/2} < x < x_{j+1/2} \,, \tag{6.14}$$

where $\delta_j^n \boldsymbol{U}$ is an estimate of the first derivative within the cell,

$$\delta_j^n \boldsymbol{U} = \frac{\bar{\boldsymbol{U}}_{j+1}^n - \bar{\boldsymbol{U}}_{j-1}^n}{(\Delta x)_j^n + \frac{1}{2}((\Delta x)_{j+1}^n + (\Delta x)_{j-1}^n)} \,. \tag{6.15}$$

At each cell boundary, the flux vector $\boldsymbol{g}$ is approximated by solving the Riemann problem defined by the cell boundary values. If the first order numerical flux at the $j + 1/2$ cell boundary is defined by

$$\boldsymbol{G}_{j+1/2}^{*n} = \boldsymbol{G}^*(\bar{\boldsymbol{U}}_j^n, \bar{\boldsymbol{U}}_{j+1}^n) \,, \tag{6.16}$$

then the spatially second-order numerical flux is:

$$\boldsymbol{G}_{j+1/2}^{**n} = \boldsymbol{G}^*(\boldsymbol{U}_j^n(x_{j+1/2}), \boldsymbol{U}_{j+1}^n(x_{j-1/2})) \,. \tag{6.17}$$

The cell average $\bar{\boldsymbol{U}}_j^{n+1}$ at the end of the time-step is found from (6.10):

$$\bar{\boldsymbol{U}}_j^{n+1} = \bar{\boldsymbol{U}}_j^n - \frac{(\Delta t)^n}{(\Delta x)_j^n}\left(\boldsymbol{G}_{j+1/2}^{**n} - \boldsymbol{G}_{j-1/2}^{**n}\right) \,. \tag{6.18}$$

Unfortunately, this scheme is linearly *unconditionally unstable*, though "weakly so" [42]! It is remedied by second-order *time* differencing, achieved by adding a correction to the flux term $\boldsymbol{G}_{j+1/2}^{**n}$. The correction term used in this thesis is the

flux for first-order Riemann problems at the half-time-step. In particular, the recipe is:

Step 1. Begin the n^{th} time-step with the average value $\bar{\boldsymbol{U}}_j^n$ in each cell J computed from (6.18).

Step 2. Use (6.14)–(6.15) to define a linear approximation $\boldsymbol{U}_j^n(x)$ to the solution in each cell J. The spatial average of $\boldsymbol{U}_j^n(x)$ across the cell must equal $\bar{\boldsymbol{U}}_j^n$.

Step 3. Define a Riemann problem at each cell interface, using $\boldsymbol{U}_j^n(x_{j+1/2})$ and $\boldsymbol{U}_{j+1}^n(x_{j-1/2})$ as initial values for the left and right sides of the Riemann problem at $j+1/2$.

Step 4. Solve each Riemann problem. Let $\boldsymbol{G}_{j+1/2}^{**n}$ be the computed flux vector at the $j+1/2$ interface.

Step 5. Estimate the time-step $(\Delta t)^n$ by (6.13), where λ_j^n is the maxiumum value of the eigenvector in the cell J between $x_{j-1/2}^n$ and $x_{j+1/2}^n$ at time t^n.

Step 6. Compute the cell average $\bar{\boldsymbol{U}}_j^{n+1/2}$ at the half time-step,

$$\bar{\boldsymbol{U}}_j^{n+1/2} = \bar{\boldsymbol{U}}_j^n - \frac{(\Delta t)^n}{2(\Delta x)_j^n}\left(\boldsymbol{G}_{j+1/2}^{**n} - \boldsymbol{G}_{j-1/2}^{**n}\right) . \tag{6.19}$$

Step 7. At the half time-step, define another Riemann problem at each cell interface, using $\bar{\boldsymbol{U}}_j^{n+1/2}$ and $\bar{\boldsymbol{U}}_{j+1}^{n+1/2}$ as the initial values for the left and right sides of the Riemann problem at $j+1/2$.

Step 8. Solve each of these half-time-step Riemann problems. Let $\boldsymbol{G}_{j+1/2}^{*n+1/2}$ be the computed flux vector at the $j+1/2$ cell boundary.

Step 9. Compute the new cell average $\bar{\boldsymbol{U}}_j^{n+1}$ at the end of the time-step using the cell average at the half time-step and the flux computed for the second

half of the time-step, so that

$$\bar{\boldsymbol{U}}_j^{n+1} = \bar{\boldsymbol{U}}_j^{n+1/2} - \frac{(\Delta t)^{n+1/2}}{(\Delta x)_j^n}\left(\boldsymbol{G}_{j+1/2}^{*n+1/2} - \boldsymbol{G}_{j-1/2}^{*n+1/2}\right) . \tag{6.20}$$

Step 10. Repeat for the $(n+1)^{\text{st}}$ time-step.

We now have a scheme that is second-order in both time and space. This method, however, produces numerical oscillations when the estimated gradient $\delta_j^n \boldsymbol{U}$ in a cell is larger than, or of sign opposite to, the gradient computed using the cell's mean value $\bar{\boldsymbol{U}}_j^n$ and only one of the two adjacent mean values $\bar{\boldsymbol{U}}_{j+1}^n$ or $\bar{\boldsymbol{U}}_{j-1}^n$. These oscillations are annoying in some types of problems, but in considering a phase-changing material, they are disastrous: in benchmark problems that can be solved analytically, they nucleate phase transformations in locations where transformations should not appear. The oscillations are prevented by limiting $\delta_j^n \boldsymbol{U}$ in each cell with a function known as a *slope limiter* [42]. In this thesis, the *minmod* slope limiter is used.

The minmod slope limiter is

$$\delta_j^n \boldsymbol{U} = 2 \text{ minmod}\left(\frac{\bar{\boldsymbol{U}}_{j+1}^n - \bar{\boldsymbol{U}}_j^n}{(\Delta x)_{j+1}^n + (\Delta x)_j^n}, \frac{\bar{\boldsymbol{U}}_j^n - \bar{\boldsymbol{U}}_{j-1}^n}{(\Delta x)_j^n + (\Delta x)_{j-1}^n}\right) \tag{6.21}$$

where the *minmod function* is

$$\begin{aligned} \text{minmod}\,(a,b) &= \begin{cases} a & \text{if } |a|<|b| \text{ and } ab>0 , \\ b & \text{if } |b|<|a| \text{ and } ab>0 , \\ 0 & \text{if } ab<0 , \end{cases} \\ &= \frac{1}{2}(\text{sign}\,(a)+\text{sign}\,(b))\min(|a|,|b|) . \end{aligned} \tag{6.22}$$

Equation (6.21) is used in place of (6.15) in Step 2, providing an oscillation-free, second-order Godunov method.

6.1.3 Adjustment for cells with a neighbor of a different material

When a cell has either a free boundary or a neighbor involving a different material, the scheme must be first-order in this cell to avoid oscillations. This is readily accomplished by prescribing that the slope $\delta_j^n \boldsymbol{U} = 0$ in any such cell.

6.2 Zhong, Hou, and LeFloch's hybrid scheme

The Godunov method requires the computation of cell averages of $\boldsymbol{U}$. This average should not be used when a cell contains both stable phases of an up-down-up material, as the resulting average γ may fall in the unstable phase.

Zhong, Hou, and LeFloch resolved this with a hybrid scheme [109]. They employed a second-order Godunov method in any cell with no phase boundary. In a cell of mixed phase, the position of the phase boundary or boundaries is *tracked*, and the grid points are shifted to follow each phase boundary. In this way, a phase boundary passes *between* cells rather than through them, and cells of mixed phases are avoided.

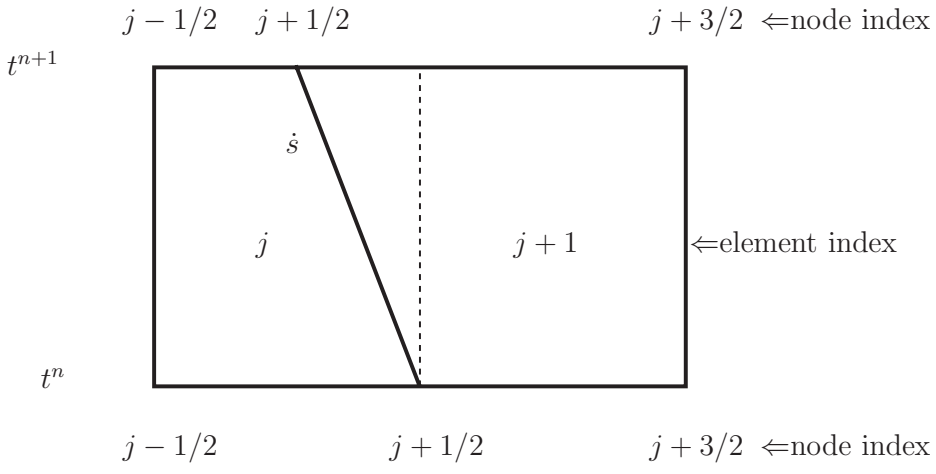

Figure 6.2: Shifting scheme of Zhong, Hou, and LeFloch.

They accomplished the tracking with a shifting scheme, Figure 6.2. The vertical dotted line at $j + 1/2$ indicates the boundary between the cells in the absence of a phase boundary. The interface $j + 1/2$ is shifted with the phase boundary propagating at velocity $\dot{s}$. The new average $\bar{\boldsymbol{U}}_j^{n+1}$ in the cell J is found by applying Green's theorem to the balance equations over the cell.

When neighboring cells are of different phases, the scheme must again revert to first-order to avoid oscillations.

6.3 Modifications in this thesis

In concave-convex materials, the second-order, slope-limited Godunov method described above is applied without modification, as there is no difficulty with the cell average of γ falling in an unstable phase.

For a trilinear material, Zhong, Hou, and LeFloch's scheme is implemented with a minor modification. Rather than *shifting* grid points to track a phase boundary, we *split* any cell containing a phase boundary. The concept is illustrated in Figure 6.3, where the shaded areas represent a new left cell (index l) and a new right cell (index r) in the original cell J. The borders of the new cells lie on the phase boundaries, which propagate at velocities $\dot{s}_l$ and $\dot{s}_r$. Two boundaries are shown so the expressions can be written for a general case, but usually only one is present in a given cell.

At the end of the time-step, the widths of the new cells are $(\Delta x)_l^{n+1} = \dot{s}_l(\Delta t)^n$ and $(\Delta x)_r^{n+1} = -\dot{s}_r(\Delta t)^n$. The width of cell J decreases to $(\Delta x)_j^{n+1} = (\Delta x)_j^n - (\Delta x)_l^{n+1} - (\Delta x)_r^{n+1}$.

The numerical method reverts to first order in these cells and computation of the cell average of $\boldsymbol{u}$ is made only at the full time-step. This is trivial for the new cells: the solutions $\boldsymbol{U}_{l,j-1/2}^{*,n}$ and $\boldsymbol{U}_{r,j+1/2}^{*,n}$ behind the left and right phase boundaries are constant during the time-step. The cell averages are simply these solutions:

$$\bar{\boldsymbol{U}}_l^n = \boldsymbol{U}_{l,j-1/2}^{*,n}\,, \qquad \bar{\boldsymbol{U}}_r^n = \boldsymbol{U}_{r,j+1/2}^{*,n}\,. \tag{6.23}$$

For the element J, the average at the end of the time-step is:

$$\bar{\boldsymbol{U}}_j^{n+1} = \Bigg(\Big\{ \bar{\boldsymbol{U}}_j^n - \frac{(\Delta t)^n}{(\Delta x)_j^n} \big(\boldsymbol{G}_{j+1/2}^n - \boldsymbol{G}_{j-1/2}^n \big) \Big\} (\Delta x)_j^n \\ - \bar{\boldsymbol{U}}_l^n (\Delta x)_l^{n+1} - \bar{\boldsymbol{U}}_r^n (\Delta x)_r^{n+1} \Bigg) / (\Delta x)_j^{n+1} \ . \quad (6.24)$$

Note that the term in {} on the first line is the right side of (6.10).

Splitting a cell increases the number of cells by one at each time-step for each phase boundary. These new cells can be extremely small for a slowly moving phase boundary. The time-steps can become too small to be useful unless some remedies are applied.

If a given small cell J has a neighboring cell of the same material and phase, the two cells can be combined. At the end of each time-step, the program used here looks for cells of widths below a specified fraction (typically 0.4) of the original mesh width. If such a cell has a neighboring cell of the same phase, it is merged with that neighbor. In the (rare) cases when both neighbors are of the same phase, the given cell is merged with the smaller of the neighbors, but all three are merged if the two neighbors are of equal width. The width of a merged cell is the sum of the widths of the individual cells, and the new cell average value $\bar{\boldsymbol{U}}_j^{n+1}$ is the width-weighed sum of the averages of the individual cells.

We have just created a new difficulty. After several time-steps, so many small cells may have merged into a continually growing neighbor that the neighbor cell becomes much wider than the initial mesh. Accordingly, before the start of the new time-step, the program splits any cell of width greater than a specified multiple (typically slightly more than 2) of the original mesh width into two halves.

Another time-step difficulty arises either when two phase boundaries are approaching each other, or one phase boundary is approaching the edge of the plate. At some point, only one cell remains between the two phase boundaries or between the phase boundary and the boundary of the plate. From that time forward, the CFL condition prevents the phase boundary from ever traversing the intervening

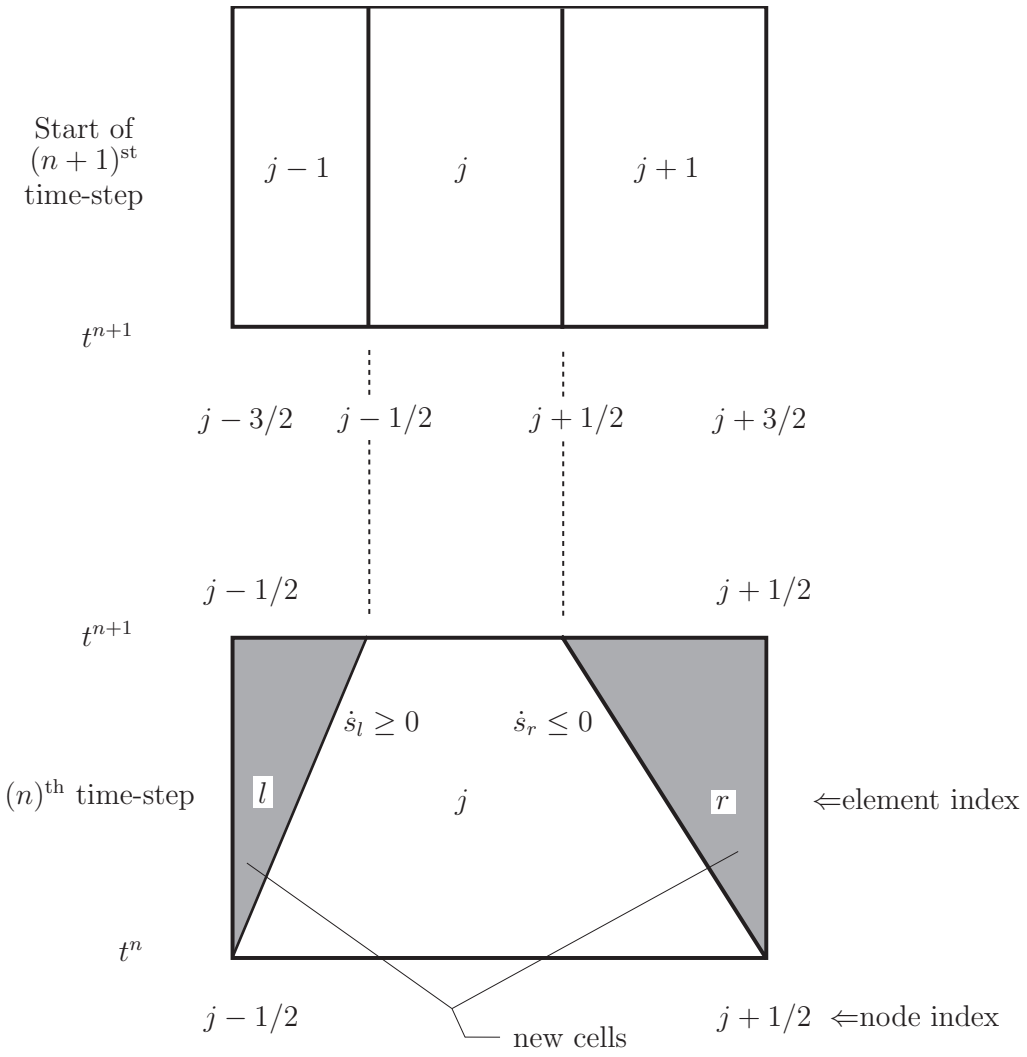

Figure 6.3: Splitting of a grid element that contains phase boundaries. In the lower figure, the phase boundaries are propagating into the cell during the time-step. At the end of the time-step, the cell is split into the three cells shown in the upper figure.

cell. The intervening cell and the time-step get smaller and smaller, and the program soon crashes.

There is a remedy for this very serious problem. If a phase boundary is entering the last cell of a plate, or if a phase boundary is entering on *each* side of a cell, the program *ignores* the CFL condition in this cell. Instead, it allows a time-step that causes the phase boundary to exactly cross the last cell, or that allows the two phase boundaries to exactly meet. The troublesome intervening cell then has zero width and is removed. Of course, if this time-step would violate the CFL condition in any other cell, the CFL condition is honored instead. Eventually, however, the intervening cell becomes so small that the time-step computed by this alternative method is less than that required by the CFL condition in any other cell.

The other common situation in which a phase boundary causes very small time-steps is when a very slowly moving phase boundary nucleates. The new phase initially fills one small cell, which grows slowly. The time-steps must be small to satisfy the CFL condition in the small cell. As long as the cell grows, the time-step slowly increases, and the reasonable time-steps may may be recovered in a reasonable period of computational time. No special provisions were added to the program to handle this situation: as a result, cases involving certain combinations of impact conditions, kinetic relations and material models were encountered for which the simulations could not be completed. Sub-cycling in time would be an appropriate improvement for this situation.

6.4 Data structures

In the last section, the element indices $\ldots\ j-1,\ j,\ j+1\ \ldots$ were used for discussion: they are not actually used in the program. Instead, the program defines a *data structure* for each element. A data structure is a collection of various types of variables that can be treated as a single unit within the program. More details about structures and lists in the "C" language can be found in texts such as [26,44].

The data structures for all of the elements are in a doubly linked list: the data structure for each element points to the data structures for its left and right neighboring elements. A new cell is readily inserted by allocating the memory for its structure, setting its links to point to its neighbors, then changing the neighbors' links to point to it. A cell is removed by changing the links that point to it to point to the new neighboring cells, then freeing the memory for the data structure of the cell being removed. It is not necessary to know how many cells there are, nor the index j of any cell. The program progresses from one cell to another by starting at the first cell and following the links to the end. There are special pointers to the first and last cells so the program knows where in memory the list begins and ends.

Data structures are used extensively in the program, and they tell a great deal about the program's operation. The use of pointers within these structures avoids many time-consuming conditional statements (*if*, *else*, *case*, *switch*).

The most important structures and their most important contents are:

`material` Describes a material. There is one of these structures for each material in the simulation. This structure contains:

- The density $\rho_\circ$.
- The intersection point (γ_A, σ_A) of the expressions for the low pressure phase and the high pressure phase, and a pointer to the **`phase`** in which it occurs.
- Pointers `p_slowest_phase_boundary`[0]-[1], to two **`discontinuity`** structures describing the *slowest* phase boundaries $\dot{s}_{31}^{(\text{slowest})}$ and $\dot{s}_{13}^{(\text{slowest})}$ allowed by the forward and reverse kinetic relationships $\mathcal{F}_{31}(\dot{s})$ and $\mathcal{F}_{13}(\dot{s})$.
- Pointers `p_fastest_phase_boundary`[0]-[1] to the **`discontinuity`** structures describing the *fastest* phases boundaries $\dot{s}_{31}^{(\text{fastest})}$ and $\dot{s}_{13}^{(\text{fastest})}$ that can be supported by the foward and reverse kinetic relationships $\mathcal{F}_{31}(\dot{s})$ and $\mathcal{F}_{13}(\dot{s})$.

- Pointers to the first **phase** and last **phase** of the material.
- `p_compressive_function`, a pointer to the routine that computes a similarity solution in this material when it undergoes a *compressive* deformation. (Here, compressive refers to the strain in the deformed state relative to the initial state, namely $\gamma^{\mathrm{c}} < \gamma_{\circ}$.)

  In particular, `p_compressive_function` points to **ConcaveConvexCompression**, **TrilinearRoofCompression**, or **TrilinearGeneralKineticsCompression**.
- `p_expansive_function`, a pointer to the routine that computes a similarity solution in this material when it undergoes an *expansive* deformation. (Again, the deformation is defined relative to the initial condition, so an expansive deformation has $\gamma^{\mathrm{c}} > \gamma_{\circ}$)

  In particular, `p_expansive_function` points to **ConcaveConvexExpansion**, **TrilinearRoofExpansion**, or **TrilinearGeneralKineticsExpansion**.
- Pointers to the user-specified parameters (g_{13} and h_{13}), and (g_{31} and h_{31}). A pointer is set to NULL if the transformation is governed by the roof kinetic relation.
- Pointers `p_kinetic_relationship`[0]-[1] to routines that compute $\mathcal{F}_{31}(\dot{s})$ and $\mathcal{F}_{13}(\dot{s})$. A pointer is set to NULL if the transformation is governed by the roof kinetic relation.

phase Describes a phase. In this work, there are three of these structures for each material, though the data structures were designed to accommodate more. Each contains:

- The parameters ($\bar{E}$ and d or $\bar{K}$ and s_1) for the phase.
- The values of strain and stress at each endpoint of this phase.
- The area under the curve $\hat{\sigma}(\gamma)$ in this phase, and the velocity changes

across compressive and expansive deformations that span the phase. These are used to speed up calculations for waves that span an entire phase.

- Pointers to functions that compute $\hat{\sigma}(\gamma)$, $\hat{\gamma}(\sigma)$, $\hat{\sigma}'(\gamma)$, $\int_0^\gamma \hat{\sigma}(\gamma^*)d\gamma^*$, and $\int_0^\gamma \sqrt{\hat{\sigma}'(\gamma^*)}d\gamma^*$ for this phase. For our materials, these are all analytical functions, but other functions such as table look-up or numerical integration could be used.
- Pointer to the **material** to which this phase belongs.
- Pointers to the "previous" (more compressed) **phase** and the "next" (less compressed) **phase**.

plate Describes a plate. It contains:

- The user-specified Courant number for this **plate**.
- Pointer to the **material** that makes up this **plate**.
- Pointer to the previous **plate** (smaller x) and next **plate** (larger x).
- Pointers to the first **element** and last **element** of this **plate**.
- Pointer to the routine for solving Riemann problems between **element**s within this **plate**.
- Pointer to the routine for solving the Riemann problem between the last **element** of this **plate** and the first **element** of the next **plate**. If this is the last **plate**, the pointer is NULL.
- Pointer to the routine for solving initial-boundary value problems on free-surfaces of this **plate**. Though a given **plate** may have no free surfaces at the start of the simulation, free surfaces can develop by fracture within a **plate** or by separation between **plate**s.
- Pointer to the slope limiter function for this **plate**. Only the MINMOD limiter is currently implemented.

- A flag to indicate the current boundary condition (free, in contact and tension allowed, in contact but no tension allowed) on the right side of the **plate**.

element Describes an element. It contains:

- The current width $(\Delta x)^n$ of the **element**.
- The Lagrangian location x of the right side of the **element**.
- The current (Eulerian) location $y(x,t) = x + u(x,t)$ of the right side of the **element**.
- The current slope computed from the slope limiter function.
- Pointers to **solution** structures for the left and right side problems. There is one pointer to the **solution** within the **element** at its left side and one to the **solution** within the **element** at its right side. In the indicial notation of the previous sections, these would be the solutions $\boldsymbol{U}^{*,n+1/2}_{j,j-1/2}$ and $\boldsymbol{U}^{*,n+1/2}_{j,j+1/2}$ or $\boldsymbol{U}^{*,n+1}_{j,j-1/2}$ and $\boldsymbol{U}^{*,n+1}_{j,j+1/2}$ for cell J, though our **solution** structure holds more information than just $\boldsymbol{U}$.
- Pointer to the **plate** in which this **element** lies.

solution Describes a solution to an initial-boundary value problem or a Riemann problem. During a root-finding process, initial conditions and current guesses are held in these type of structures (a smaller structure with a name like "`state`" would suffice for the initial conditions). This structure contains:

- Values of γ, V, σ for some state.
- Status flags to indicate which of these values have or have not yet been computed.
- `p_phase`, a pointer to the **phase** that the **material** is in for the given γ or σ. This pointer is especially important for up-down-up

materials: since the phase cannot necessarily be determined from σ, the program must have another way of indicating the phase.

- Speeds of the fastest and slowest waves computed in the solution. The fastest wave is used in computing the time-step. If a phase boundary occurs, its velocity (required to split the cell) is given by the slowest wave.
- `type_of_phase_boundary`, an integer that flags the kind of phase change. The integers are referred to by name: NoPhaseChange, Subsonic, Supersonic.

`discontinuity` This structure describes a discontinuity. The program uses it only for subsonic phase boundaries in up-down-up materials. It contains:

- The driving traction f.
- The phase boundary velocity $\dot{s}$.
- The jump in particle velocity across the discontinuity $[\![V]\!] = V^+ - V^-$.
- The strain and stress on each side of the discontinuity: γ^+, σ^+, γ^-, σ^-.

6.5 Routines used by the Riemann solvers

The Riemann solvers seek intersections of the contact loci for the left and right sides of a problem. Let $V_L^{\mathcal{C}} = \mathcal{V}_L(\gamma^{\mathcal{C}})$ and $V_L^{\mathcal{C}} = \mathcal{V}_R(\gamma^{\mathcal{C}})$ be the contact velocities at the contact strain $\gamma^{\mathcal{C}}$ for the left and right sides of a Riemann problem, respectively. Let $V_\circ^{\mathcal{C}} = \mathcal{V}_\circ(\gamma^{\mathcal{C}})$ be the contact velocity for the contact strain $\gamma^{\mathcal{C}}$ when we are discussing a general case. By virtue of the relations presented in Chapter 4, these functions are known for all of the model materials and for all initial conditions.

In the program, calculation of the contact velocity involves a number of routines, outlined in the remainder of this section.

6.5.1 Routines that determine the current phase

Two routines can determine what phase a particular strain or stress lies in:

`PhaseForGivenStrain` This routine receives a value of strain γ and a pointer to the **`material`**, then returns a pointer to the **`phase`** for that strain.

`PhaseForGivenStress` This routine receives a value of stress σ and a pointer to the **`material`**, then returns a pointer to the **`phase`** for that stress. It works only for monotonic materials.

6.5.2 Routines that compute stress or strain in a phase

Recall that the **`phase`** structure holds pointers `pstressfunction` and `pstrainfunction` to routines that compute $\hat{\sigma}(\gamma)$ and $\hat{\gamma}(\sigma)$. Since there are currently three types of phases (the linear phases, the concave phase of the concave-convex material, and the convex phase of the concave-convex material), there are six routines. Rather than name and describe each of the six, we just name and describe the two categories:

`StressForGivenStrain` These types of routines receive a value of strain γ and a pointer to a **`phase`** i, then return the stress $\hat{\sigma}_i(\gamma)$.

Each pointer **`phase`**→`pstressfunction` points to a routine of this type.

`StrainForGivenStress` These types of routines receive a value of stress σ and a pointer to a **`phase`** i, then return the strain $\hat{\gamma}_i(\sigma)$.

Each pointer **`phase`**→`pstrainfunction` points to a routine of this type.

6.5.3 A routine to compute f, W, and $[\![V]\!]$

The following utility is called from many other routines:

`DrivingTractionAndVelocityOfDiscontinuity` This routine receives a **`discontinuity`** structure in which γ^+, σ^+, γ^-, σ^- have been set. From

these values, it computes and sets all other members of the **discontinuity**: f, $\dot{s}$, and $[\![V]\!]$.

6.5.4 Routines that find contact velocity at prescribed contact strain or stress for monotonic materials

Two routines find similarity solutions and compute the particle velocity on a contact locus for initial-boundary value problems in concave-convex materials.

For concave-convex materials, **material**→p_compressive_function points to **ConcaveConvexCompression**, and **material**→p_expansive_function points to **ConcaveConvexExpansion**.

ConcaveConvexCompression The purpose of this routine is to compute the contact velocity $\mathcal{V}_\circ(\gamma^{\mathfrak{C}})$ at a specified contact strain $\gamma^{\mathfrak{C}}$ or contact stress $\sigma^{\mathfrak{C}}$ for prescribed initial conditions $(\gamma_\circ, V_\circ)$ in a concave-convex material. It is called for compressive deformations (i.e., when $\gamma^{\mathfrak{C}} < \gamma_\circ$ or $\sigma^{\mathfrak{C}} < \sigma_\circ$). The maximum dissipation kinetic relationship is enforced.

ConcaveConvexCompression receives pointers to two **solution** structures, frontstate and backstate. The structure frontstate contains the initial state $\gamma_\circ$, $\sigma_\circ$, $V_\circ$. In backstate, either a contact strain $\gamma^{\mathfrak{C}}$ and/or a contact stress $\sigma^{\mathfrak{C}}$ has been set. (If both are set, they are consistent, i.e., $\sigma^{\mathfrak{C}} = \hat{\sigma}(\gamma^{\mathfrak{C}})$.) **ConcaveConvexCompression** also receives a pointer to the **material**, and an integer whatside, where whatside=−1 if the initial conditions are on the left-side of an initial-boundary value problem, and whatside=+1 if the initial conditions are on the right-side.

The routine examines the status flags in backstate that indicate whether $\gamma^{\mathfrak{C}}$ and/or $\sigma^{\mathfrak{C}}$ is current. Then it calls **PhaseForGivenStrain** or **PhaseForGivenStress** as appropriate to set the pointer backstate→phase to the correct **phase**. Next,

StressForGivenStrain or **StrainForGivenStress** is called if needed to calculate the current value of $\sigma^{\mathfrak{C}}$ from $\gamma^{\mathfrak{C}}$ or vice-versa. The corresponding status flag is toggled to indicate that the newly computed value is now current.

With this housekeeping complete, **ConcaveConvexCompression** determines what kind of solution is required to reach $\gamma^{\mathfrak{C}}$ from $\gamma_\circ$ with maximum dissipation kinetics (the roof). The situations presented in Section 4.4, and the resulting forms of the possible states, are explicitly coded into the routine. Once the form of the solution is determined, **ConcaveConvexCompression** calls other routines to compute the particle velocity ${V_\circ}^{\mathfrak{C}}$.

For example, if **ConcaveConvexCompression** determines that the solution must be a shock, it calls a routine named **SinglePhaseShock**, which works for any shock (compressive or expansive) in any phase in any material. **SinglePhaseShock** computes

$$
\begin{aligned}
{V_\circ}^{\mathfrak{C}} &= V_\circ + \operatorname{sign}\left(W[\![\sigma]\!]\right) \frac{1}{\sqrt{\rho_\circ}} \sqrt{[\![\sigma]\!][\![\gamma]\!]} \,, \\
W &= \texttt{whatside} \sqrt{\frac{[\![\sigma]\!]}{\rho_\circ [\![\gamma]\!]}} \,,
\end{aligned}
$$

where

$$
[\![\sigma]\!] = \sigma_\circ - \sigma^{\mathfrak{C}} \,, \qquad [\![\gamma]\!] = \gamma_\circ - \gamma^{\mathfrak{C}} \,.
$$

It stores $V^{\mathfrak{C}}$ and W in `backstate` and returns control to **ConcaveConvexCompression**, which then returns control to the routine that called it.

ConcaveConvexExpansion This routine is identical to **ConcaveConvexCompression** except that it works for *expansive*

deformations.

6.5.5 Routines that describe a kinetic relation

Most kinetic relationships require a routine that returns $\mathcal{F}_{ab}(\dot{s})$ for specified $\dot{s}$ and specified front phase a and back phase b. The roof is a notable exception, as it can be implemented without knowing the form of $\mathcal{F}_{ab}(\dot{s})$.

If kinetics other than the roof are utilized for a **`material`**, then a pointer in that **`material`** structure points to one of these routines. There is one pointer for the LPP→HPP transformation and one for the HPP→LPP, so the kinetic relationship is specified independently for each transformation. Their coefficients (g_{ab} and h_{ab} for a linear kinetic relationship) are also specified independently.

Since the program currently implements only one type of kinetic relationship other than the roof, the only routine in this category is:

`LinearKineticRelation` Receives $\dot{s}$, a pointer to the **`material`**, and an integer that flags whether to compute $\mathcal{F}_{13}(\dot{s})$ or $\mathcal{F}_{31}(\dot{s})$. Computes and returns the appropriate choice of $\mathcal{F}_{13}(\dot{s}) = g_{13} + h_{13}\dot{s}$ or $\mathcal{F}_{31}(\dot{s}) = g_{31} + h_{31}\dot{s}$.

6.5.6 Routines that find a discontinuity to satisfy a kinetic relation

In this section we encounter two root-finding algorithms based on the bisection method. The principle of the bisection algorithm is simple. Start with a continuous function $\hat{h}(w)$ on some interval $w \in [w_1, w_2]$. If $\hat{h}(w_1)$ and $\hat{h}(w_2)$ have opposite signs, then the function must have a zero in that interval. Evaluate $\hat{h}(w_m)$ at the midpoint w_m of the interval and examine its sign. The root must lie in the half-interval where $\hat{h}(w)$ changes sign. Replace the original interval with this half-interval and repeat the process. When the interval is "small enough," the zero has been found to within the required accuracy.

The routines here return a **`discontinuity`** that satisfies the material's kinetic

relationship $\mathcal{F}_{ab}(\dot{s})$ for a specified transformation (LPP to HPP or vice versa). Both routines work in the first quadrant of the $\dot{s}$, f plane—the calling routine must change the signs of $\dot{s}$ and f for left-going phase boundaries—and require that $\mathcal{F}_{ab}(\dot{s})$ be a non-decreasing function of $\dot{s}$. Each routine receives pointers to the **phase** structures on the "+" and "-" sides of the discontinuity.

These routines are only used for kinetic relations expressed as an equation relating f and $\dot{s}$. In particular, they are *not* used for the roof (maximum dissipation) kinetic relationship: in a general up-down-up material, we might not even be able to find the equation relating f and $\dot{s}$ on the roof. Fortunately, the maximum dissipation kinetic relationship can be implemented by forcing $\gamma^+ = \gamma_M$ or $\gamma^+ = \gamma_m$ ahead of a phase boundary.

SatisfyKineticRelationForPhaseBoundaryVelocity This routine receives a specified phase boundary velocity $\dot{s}$ and finds the pair (γ^-, γ^+) that satisfies the kinetic relationship for this $\dot{s}$. It returns NULL if no such pair exists.

It begins by calling **LinearKineticRelation** to find $\mathcal{F} = \mathcal{F}_{ab}(\dot{s})$ for this transformation. (Actually, it calls whatever routine is pointed to by **material**→p_kinetic_relationship for this transformation, but **LinearKineticRelation** is the only such routine implemented.)

Then the routine constructs the function $\hat{h}(\gamma^+) = \hat{f}(\gamma^-, \gamma^+) - \mathcal{F}$ and iterates in γ^+ to find the root of the function. Here, $\gamma^- = \tilde{\gamma}(\gamma^+)$ is the strain in the product phase that satisfies the jump conditions across a phase boundary of specified velocity $\dot{s}$ for strain γ^+ in the parent phase. Geometrically, γ^- is the intercept of the "−" phase of the stress response function $\hat{\sigma}(\gamma)$ with a chord of slope $\rho_\circ \dot{s}^2$ drawn through (γ^+, σ^+). Because we are interested only in trilinear up-down-up models, the routine explicitly calculates

$$\gamma^- = \tilde{\gamma}(\gamma^+) = (d^- - \sigma^+ - \rho_\circ \dot{s}^2 \gamma^+)/(\rho_\circ \dot{s}^2 - \bar{E}^-) \; .$$

The routine's search interval is $\gamma^+ \in [\gamma_1^+, \gamma_2^+]$, where γ_1^+, γ_2^+ are the smallest and greatest values of γ on the "+" phase of $\hat{\sigma}(\gamma)$ for which a line of slope $\rho_\circ \dot{s}^2$ intercepts the "−" phase.

For each guess of γ^+ tested as a root, the routine computes $\gamma^- = \tilde{\gamma}(\gamma^+)$, then calls a **`StressForGivenStrain`** routine twice to compute $\sigma^+ = \hat{\sigma}(\gamma^+)$ and $\sigma^- = \hat{\sigma}(\gamma^-)$. It places all four of these quantities into a **`discontinuity`** structure, then calls **`DrivingTractionAndVelocityOfDiscontinuity`** to get the driving traction $\hat{f}(\gamma^-, \gamma^+)$. If $\hat{f}(\gamma^-, \gamma^+) = \mathcal{F}$ within the requested accuracy, then the phase boundary satisfies the kinetic relationship, and the **`discontinuity`** structure is returned to the calling routine. Otherwise, another guess of γ^+ is made and the process repeats.

The only use of this routine is to fill in the **`discontinuity`** structures pointed to by **`material`**→`p_slowest_phase_boundary`[0]-[1] and **`material`**→`p_fastest_phase_boundary`[0]-[1] for the up-down-up materials before the program starts looping in time. To fill in the structures pointed to by **`material`**→`p_slowest_phase_boundary`[0]-[1], this routine is called with $\dot{s} = 0$ for both the low-to-high ([0]) and high-to-low pressure ([1]) transformations. To fill in **`material`**→`p_fastest_phase_boundary`[0]-[1], it is called for both transformations with $\dot{s} = \min(c_1, c_3)$. Because the stress-response models are undefined outside of $\gamma \in [\gamma_Z, \gamma_F]$, the routine may return NULL in this latter case. If this happens, a bisection algorithm iterates in $\dot{s}$ to find the maximum phase boundary velocity that can be supported by the material model with the kinetic relationship enforced.

`SatisfyKineticRelationForStressMinus` This routine receives a specified stress σ^- and finds the pair (γ^+, σ^+) that satisfies the kinetic relationship. It returns NULL if no such pair exists.

The routine begins by calling—through the pointer it received to the "–" phase—a **StrainForGivenStress** routine to compute γ^-. It sets the values of γ^- and σ^- in a **discontinuity** structure.

It next checks whether $\sigma^- \in [\sigma_{ab}^{-\,(\text{slowest})}, \sigma_{ab}^{-\,(\text{fastest})}]$ (these values are accessed by the pointers **material**→p_slowest_phase_boundary[0]-[1] and **material**→p_fastest_phase_boundary[0]-[1]).

If σ^- is *not* in this range, then the kinetic relation specified by the user forces γ^+ to fall outside of $\gamma \in [\gamma_Z, \gamma_F]$. The routine abandons the user's kinetic relation and instead enforces the alternate kinetic relationship described in Section 4.3.7 by setting $\gamma^+ = \gamma^{+\,(\text{fastest})}_{ab}$, $\sigma^+ = \sigma^{+\,(\text{fastest})}_{ab}$. Then it returns control to the routine that called it.

If σ^- *is* in this range, the routine constructs the function $\hat{h}(\gamma^+) = \hat{f}(\gamma^-, \gamma^+) - \mathcal{F}_{ab}(\dot{s}^\dagger)$ and iterates in γ^+ to find the root of this function. Here, $\dot{s}^\dagger = \dot{\mathcal{S}}(\gamma^+) = \sqrt{[\![\sigma]\!]/(\rho_\circ [\![\gamma]\!])}$ is the speed of the phase boundary for the current guess γ^+.

The search interval is better understood in terms of stress σ^+ than strain γ^+. For a low-pressure phase to high-pressure phase transformation,

$$\sigma^+ \in [\max(\sigma^-, \sigma_m), \sigma_F] \;\Rightarrow \gamma^+ \in [\hat{\gamma}_3(\max(\sigma^-, \sigma_m)), \gamma_F] \; . \tag{6.25}$$

For a high-pressure phase to low-pressure phase transformation,

$$\sigma^+ \in [\sigma_A, \min(\sigma^-, \sigma_M)] \;\Rightarrow \gamma^+ \in [\gamma_A, \hat{\gamma}_1(\min(\sigma^-, \sigma_M))] \tag{6.26}$$

For each guess of γ^+ tested as a root, the routine calls **StressForGivenStrain** to compute σ^+. It sets γ^+ and σ^+ in the **discontinuity** structure (which already contains γ^- and σ^-) and calls **DrivingTractionAndVelocityOfDiscontinuity** to compute $\hat{f}(\gamma^-, \gamma^+)$ and $\dot{s}^\dagger$ for this discontinuity. Then it passes $\dot{s}^\dagger$ to

LinearKineticRelation to find $\mathcal{F}_{ab}(\dot{s}^\dagger)$. If $\hat{f}(\gamma^-, \gamma^+) = \mathcal{F}_{ab}(\dot{s}^\dagger)$ within the requested accuracy, then the root has been found, and the **discontinuity** is returned to the calling routine. Otherwise, another guess of γ^+ is made and the process repeats.

6.5.7 Routines that find contact velocity at prescribed contact stress in a trilinear material

There are four routines that find similarity solutions to initial-boundary value problems in trilinear materials, enforcing the kinetic relationships at subsonic phase boundaries.

If $\mathcal{F}_{31}(\dot{s}) = \mathcal{F}_{31}^{\text{roof}}(\dot{s})$, **material**→`p_compressive_function` points to **TrilinearRoofCompression**. For any other forward kinetic relationship $\mathcal{F}_{31}$, this pointer points to **TrilinearGeneralKineticsCompression**.

If $\mathcal{F}_{13}(\dot{s}) = \mathcal{F}_{13}^{\text{roof}}(\dot{s})$, **material**→`p_expansive_function` points to **TrilinearRoofExpansion**, otherwise it points to **TrilinearGeneralKineticsExpansion**.

TrilinearGeneralKineticsCompression The purpose of this routine is to compute the particle velocity ${V_\circ}^{\mathcal{C}} = \mathcal{V}_\circ(\gamma^{\mathcal{C}})$ on the contact locus at a specified contact strain $\gamma^{\mathcal{C}}$ for prescribed initial conditions $(\gamma_\circ, V_\circ)$. It is called for compressive deformations in a trilinear material. The calling routine must have already determined whether the solution will contain a phase boundary, and whether the phase boundary is subsonic or supersonic. This routine enforces the kinetic relationship $\mathcal{F}_{31}(\dot{s})$ for subsonic phase boundaries.

TrilinearGeneralKineticsCompression receives pointers to `frontstate`, containing the initial state $\gamma_\circ$, $\sigma_\circ$, $V_\circ$, and to `backstate`, containing a contact strain $\gamma^{\mathcal{C}}$ and a contact stress $\sigma^{\mathcal{C}}$. The pointer `backstate`→`phase` has been set to indicate the phase for $\gamma^{\mathcal{C}}$. The routine

also receives a pointer to the **material**, and the integer whatside, which it passes along to routines that it calls. The backstate→type_of_phase_boundary has been set before this routine is called.

This routine switches on backstate→type_of_phase_boundary.

If backstate→type_of_phase_boundary= NOPHASECHANGE, then the routine calls **SinglePhaseShock**, which was briefly described on page 123.

If backstate→type_of_phase_boundary= SUPERSONIC, then the routine calls **MultiPhaseDiscontinuity**, a routine identical to **SinglePhaseShock** except that γ^+ and γ^- may be in different phases.

If backstate→type_of_phase_boundary= SUBSONIC, then the routine passes backstate to **SatisfyKineticRelationForStressMinus** to find the strain γ^+ and stress σ^+ ahead of the phase boundary, and the jump in particle velocity across it. It sets γ^+ and σ^+ into a **discontinuity** named intermediatestate, the passes this and frontstate to **SinglePhaseShock** to find the particle velocity V of the intermediatestate. Finally, it calls **MultiPhaseDiscontinuity** with intermediatestate and backstate to update the particle velocity V of backstate.

TrilinearGeneralKineticsCompression then returns to the program that called it.

TrilinearGeneralKineticsExpansion This routine is nearly identical to **TrilinearGeneralKineticsCompression**, but it works for expansive deformations. (In retrospect, there is no need for seperate routines, they differ only in whether they call **material**→p_kinetic_relationship[0] or [1]. An integer variable ForwardOrReverse, either 0 or 1, could be passed in to indicate the correct function.)

TrilinearRoofCompression This routine is identical **TrilinearGeneralKineticsCompression**, except for its behavior in this situation:

If `backstate→type_of_phase_boundary`= SUBSONIC, the routine sets $\gamma^+ = \gamma_m$ and $\sigma^+ = \sigma_m$ into a **discontinuity** named `intermediatestate`, the passes `intermediatestate` and `frontstate` to **SinglePhaseShock** to find the particle velocity V of the `intermediatestate`. Finally, it calls **MultiPhaseDiscontinuity** with `intermediatestate` and `backstate` to update the particle velocity V of the `backstate`.

There is no need to call a root-finding algorithm to satisfy the kinetic relationship.

TrilinearRoofExpansion This routine is nearly identical to **TrilinearRoofCompression**, but since it works for expansive deformations, it sets $\gamma^+ = \gamma_M$ and $\sigma^+ = \sigma_M$ into `intermediatestate`.

6.5.8 A routine that determines the form of solution for prescribed contact stress in a trilinear material

The variable `backstate→type_of_phase_boundary` must be set before any of the four routines described in the previous section are called. The following routine is responsible for setting this variable, and for calling these four functions.

FindSolutionGivenContactStressInNonMonotonicMaterial This routine receives `frontstate`, which points to a **solution** containing the initial state $\gamma_\circ$, $\sigma_\circ$, $V_\circ$, and `backstate`, which points to a **solution** containing a contact stress $\sigma^{\mathfrak{C}}$. Neither the contact strain $\gamma^{\mathfrak{C}}$ nor the phase are known: this routine must determine them. The routine also receives a pointer to the **material**, and the integer `whatside`, which it passes along to routines that it calls.

For clarity, the description that follows assumes the initial conditions are in the low pressure phase of a trilinear material for which the intersection point (γ_A, σ_A) occurs within the high pressure phase. In truth, the routine is written to accommodate any up-down-up material, and it differentiates the phases not by which one is high or low pressure, but by where their expressions intersect.

The routine must determine whether the contact stress can be reached by a supersonic phase boundary, a subsonic phase boundary, or no phase boundary at all, then set the flag `backstate→type_of_phase_boundary` appropriately.

First the routine checks whether $\sigma^{\mathcal{C}} < \sigma_A$: if so, the solution must be a supersonic phase boundary, and `backstate→type_of_phase_boundary` is set to SUPERSONIC.

If the solution is not a supersonic phase boundary, the routine checks whether $\sigma_A \leq \sigma^{\mathcal{C}} < \sigma_m$: if so, the solution must involve a subsonic phase boundary and the routine sets `backstate→type_of_phase_boundary` to SUBSONIC.

If neither of these cases is true, the routine then checks whether $\sigma^{\mathcal{C}} > \sigma_{31}{}^{(\text{slowest})}$: if so, no phase change is involved, and it sets `backstate→type_of_phase_boundary` to SUBSONIC.

Finally, if $\sigma_m \leq \sigma^{\mathcal{C}} < \sigma_{31}{}^{(\text{slowest})}$, the solution can be either a shock or it can involve a subsonic phase boundary. The nucleation criteria is applied to choose between these two solutions. The only nucleation criteria currently implemented selects the solution with a phase boundary over the one without, so the routine sets `backstate→type_of_phase_boundary` to SUBSONIC.

Having determined whether a phase boundary is present, the routine sets `backstate→phase`, and calls **`StrainForGivenStress`** to compute $\gamma^{\mathcal{C}}$

from $\sigma^{\mathcal{C}}$. Finally, it calls **material**→p_compressive_function or **material**→p_expansive_function to compute the particle velocity at the contact state, then returns to the routine that called it.

6.6 Riemann solvers

Having described the routines that the Riemann solvers utilize, we can now describe the Riemann solvers themselves.

Let us list the types of problems that may be encountered at any time-step:

1. *Initial-boundary value problem with stress-free surface in a concave-convex material.* This type of problem must be solved for any element adjacent to a free surface of a concave-convex material.

2. *Single material Riemann problem in a concave-convex material.* Within any of the ancillary materials, all the Riemann problems between neighboring elements are of this type.

3. *Bimaterial Riemann problem involving only concave-convex materials.* The elements adjacent to the interface between plates of two different ancillary materials define a Riemann problem of this type.

4. *Initial-boundary value problem with stress-free surface in a trilinear material.* This situation occurs for any element adjacent to a free surface in a trilinear material.

5. *Single or bimaterial Riemann problem involving a trilinear material.* This occurs if either (or both) of two adjoining cells involves a trilinear material.

There is a different routine for each of these situations:

FreeEdgeInMonotonicMaterial This routine is for case 1, where the free-surface requirement that $\sigma^{\mathcal{P}} = 0$ implies $\gamma^{\mathcal{P}} = 0$. The routine sets the

initial conditions $\gamma_\circ$, $\sigma_\circ$, $V_\circ$ into a **solution** structure named `frontstate`, sets the free-surface conditions $\gamma^{\mathfrak{C}} = 0$, $\sigma^{\mathfrak{C}} = 0$ into another **solution** structure named `backstate`. Then it determines whether the deformation will be expansive or compressive, and calls the routine pointed to by **material**→`p_expansive_function` or **material**→`p_compressive_function` as appropriate. (Currently, these are **ConcaveConvexExpansion** and **ConcaveConvexCompression**.)

RiemannProblemForOneMonotonicMaterial This routine is for case 2. It uses a bisection algorithm that exploits the fact that the stress-response function $\hat{\sigma}(\gamma)$ is monotonic and identical on both sides of the Riemann problem. This allows the routine to iterate in the variable $\gamma^{\mathfrak{C}}$ rather than $\sigma^{\mathfrak{C}}$ because the jump condition $[\![\sigma]\!] = 0$ implies $[\![\gamma]\!] = 0$. The bisection algorithm finds the root of $\hat{h}(\gamma^{\mathfrak{C}}) = \mathcal{V}_R(\gamma^{\mathfrak{C}}) - \mathcal{V}_L(\gamma^{\mathfrak{C}})$. The search interval could be set to $\gamma^{\mathfrak{C}} \in [\gamma_Z, \gamma_F]$, but it is narrowed significantly by recognizing that the solution must lie in a region accessible to both sides of the problem. Utilizing results of Appendix A, Figure 6.4 is constructed as an example. In this figure, the intersection of the loci for the right and left sides of the problem must lie in one of the two open regions, and the search interval is therefore restricted to $\gamma \in [\gamma_R, \gamma_F]$. Going even further, we test whether the contact locus for the right side passes above or below the initial conditions (σ_L, V_L) for the left side. If $\mathcal{V}_R(\gamma_L) - V_L > 0$ then the bisection algorithm searches only over $\gamma \in [\gamma_L, \gamma_F]$. If $\mathcal{V}_R(\gamma_L) - V_L < 0$ then the search is restricted to $\gamma \in [\gamma_L, \gamma_R]$. Once the search interval has been restricted, the routine determines whether **material**→`p_compressive_function` or **material**→`p_expansive_function` should be called for each half of the Riemann problem to compute $\mathcal{V}_R(\gamma^{\mathfrak{C}})$ and $\mathcal{V}_L(\gamma^{\mathfrak{C}})$ for each guess $\gamma^{\mathfrak{C}}$.

Indeed, the ability to restrict the search in this way was the motivation for writing separate compression and expansion routines for each material model. If a single routine were written, it would have to make a decision

each time it was called as to whether the deformation was going to be compressive or expansive. Since these functions are called *many* times during a root-finding process, placing the decision at a higher level saves many conditional statements (*if*, *else*, *case*, *switch*) for each grid interface and for each time-step.

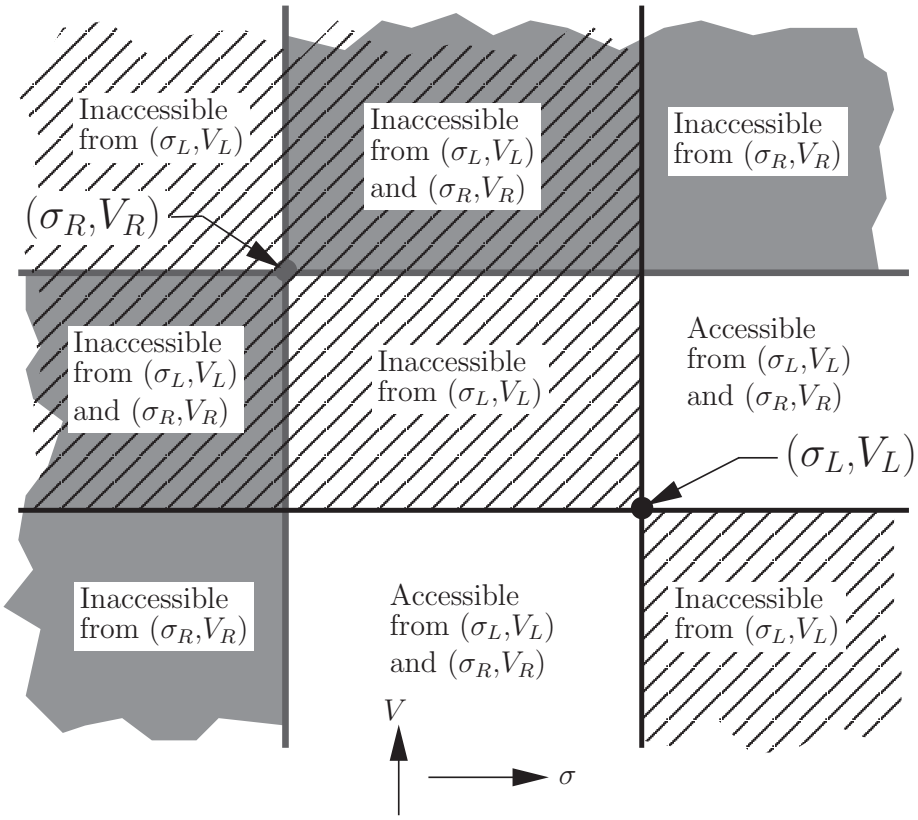

Figure 6.4: For a Riemann problem involving materials with monotonic stress response functions, the striped regions cannot be accessed via the locus of contact states for the left side, and solid regions are inaccessible for the right side. The solution must lie in one of the two open areas. The σ and V arrows indicate the direction of the axes but are not intended to imply an origin.

`RiemannProblemForTwoMonotonicMaterials` This is a bisection algorithm for case 3. It is similar to **`RiemannProblemForOneMonotonicMaterial`** except that now the

search for a root must be done in the variable stress $\sigma^{\mathcal{C}}$ rather than strain $\gamma^{\mathcal{C}}$, since the material is different on the two sides of the problem. In particular, the search is for a root of $\hat{h}(\sigma^{\mathcal{C}}) = \mathcal{V}_R(\gamma_R^{\mathcal{C}}) - \mathcal{V}_L(\gamma_L^{\mathcal{C}})$, where $\gamma_R^{\mathcal{C}} = \hat{\gamma}_R(\sigma^{\mathcal{C}})$ and $\gamma_L^{\mathcal{C}} = \hat{\gamma}_L(\sigma^{\mathcal{C}})$. The search interval is again restricted, this time to the interval of stress $\sigma^{\mathcal{C}}$ that can be reached by both the right and left contact loci. As the search interval must be defined for both materials, it cannot extend beyond $\sigma^{\mathcal{C}} \in [\max\{(\sigma_Z)_L, (\sigma_Z)_R\}, \min\{(\sigma_F)_L, (\sigma_F)_R\}]$.

`FreeEdgeInUpDownUpMaterial` This routine is for case 4. It receives a **`solution`** named **`frontstate`** and sets the boundary condition $\sigma^{\mathcal{P}} = 0$ into a **`solution`** named `backstate`. Then it calls **`FindSolutionGivenContactStressInNonMonotonicMaterial`**.

`RiemannProblemForUpDownUpMaterial` This routine is for case 5. It is similar to **`RiemannProblemForTwoMonotonicMaterials`**, but the search interval cannot be restricted. The root finding algorithm searches over the entire range of stress $\sigma^{\mathcal{C}}$ for which the stress response function is defined for both the left and right materials,
$\sigma^{\mathcal{C}} \in [\max\{(\sigma_Z)_L, (\sigma_Z)_R\}, \min\{(\sigma_F)_L, (\sigma_F)_R\}]$.

Chapter 7

Numerical investigations

This chapter investigates how the response of the trilinear model we developed for GeO_2 in Chapter 5 is influenced by the kinetic relationships that govern subsonic phase boundaries. In particular, we will simulate the impact experiments described in Chapter 2 with the numerical method described in Chapter 6. Unless otherwise stated, the model for GeO_2 is held fixed and only the kinetic relations are varied.

Recall that five experiments were conducted. In the two forward experiments, Shots 955 and 953, a tungsten flyer plate traveling at 1.99 km/s or 1.53 km/s, respectively, impacted a stationary GeO_2 plate. In the three reverse experiments, Shots 965, 957, and 958, a GeO_2 flyer plate traveling at 0.62 km/s, 1.47 km/s, or 1.96 km/s, respectively, impacted a stationary plate of Al6061. Predictions for each of these shots are presented in individual sections in the order just listed.

Using the model described by (5.14), each experiment was simulated with several different forward kinetic relations $f = \mathcal{F}_{31}(\dot{s})$. The first goal was to find a forward kinetic relation *with no dependence on the phase boundary velocity* $\dot{s}$ to optimize the match between the predicted particle-velocity history and the experimental VISAR recording for that shot. After the kinetic relations $\mathcal{F}_{31}(\dot{s}) = g_{31}$ that result in the best match for each shot are identified, linear kinetic relations $\mathcal{F}_{31}(\dot{s}) = g_{31} + h_{31}\dot{s}$ are examined in a separate section.

The kinetic relation $f = \mathcal{F}_{13}(\dot{s})$ governing the reverse transformation was also

varied for each experiment, but usually only after the forward kinetic relation that provided the best match to the early part of the experimental VISAR record was found.

In the final two sections of the chapter, modifications are made to the trilinear model of GeO_2 to force certain phenomena otherwise absent in the simulations to occur. The first modification allows the low pressure to nucleate from the high pressure phase in a simulation of Shot 955. The second modification suppresses phase transitions in the simulations altogether, and will be used in simulations of Shots 955 and 953. (With the proper choice of the forward kinetic relation, phase transformations can be avoided with our *current* model for the other three shots, so this modified model is not applied to those three shots.)

In this chapter, where we discuss kinetic relations in simulations, it is to be understood that these kinetic relations are used for subsonic phase boundaries only. The input file for the program specifies kinetic relations for both forward and reverse transformations, but the program enforces them only at subsonic phase boundaries.

Reference to any material is intended to be a reference to its model as described in Chapter 5, and descriptions of events refer to the events in the simulations as opposed to the actual experiments.

The critical driving traction f_{ab}^c selected for the nucleation criterion is always the driving traction prescribed by the kinetic relation at a stationary phase boundary, $f_{ab}^c = \mathcal{F}_{ab}(0^+)$. When two similarity solutions to an initial-boundary value problem are possible, one involving a phase boundary and the other involving only a shock, this nucleation criterion selects the solution with the phase boundary.

For each shot, contact loci for the initial impact will be presented. In terms of a bimaterial Riemann problem, our convention for these loci will be that the flyer plate is on the left side ($x < 0$) and the plate it hits is on the right side ($x > 0$).

Likewise, in the simulations, the flyer plate and foam backing have Lagrangian coordinates $x < 0$, and the stationary plates have Lagrangian coordinates $x > 0$. The impact of the flyer plate and target occurs at $x = 0$.

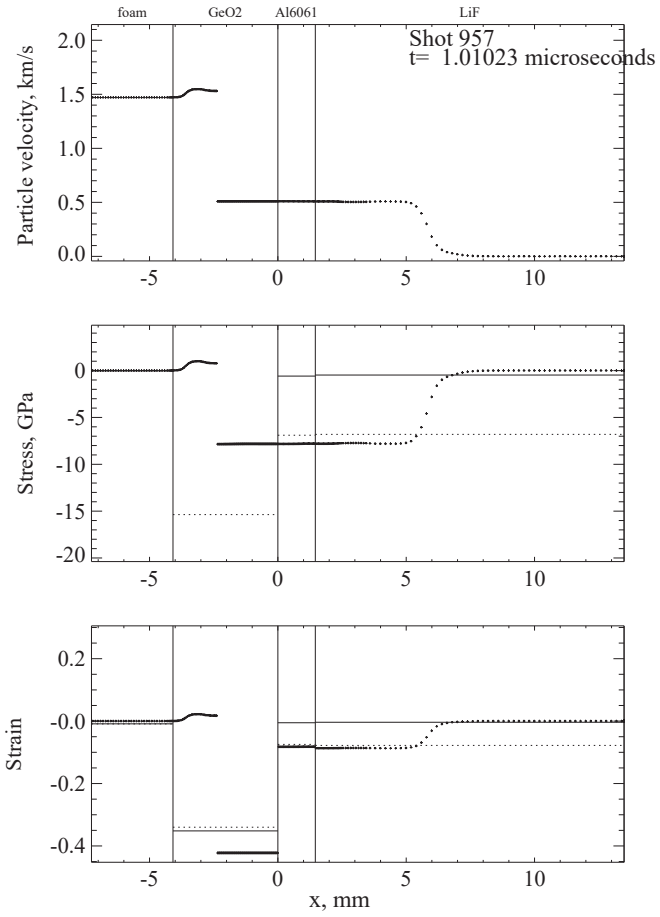

Figure 7.1: An example of predicted spatial distributions of particle-velocity, stress, and strain.

Predicted spatial distributions of particle-velocity, stress and strain in Lagrangian coordinates will be presented for some of the simulations: an example is shown in Figure 7.1. The time given in the figure is the time elapsed since the initial impact of the flyer plate and target. Plate boundaries are shown as vertical lines, and the material of each plate is indicated above the topmost frame. Though the lithium fluoride window is shown in Figure 7.1, in the remainder of this chapter most of the window will be cropped to increase the size of the figures, and the time since impact will be given below the figures.

In Figure 7.1, the average value of particle-velocity, stress and strain in each

discretized element is indicated with a small "+" marker. Where the elements are especially fine, the markers can overlap and appear to be a heavy solid line.

In the strain frame, a dashed line and a solid line are drawn across each plate at the respective strains $\gamma = \gamma_m$ and $\gamma = \gamma_M$ that delimit the phases for the material of that plate. At any position x, these lines allow a visual determination of the phase of the particle whose referential location is x. In particular, the GeO_2 is in the *low pressure phase when its strain is above the dashed line, and in the high pressure phase when the strain is below the solid line.* In our example, Figure 7.1, the GeO_2 is in the low pressure phase for $x \lesssim$ -2.3 mm and in the high pressure phase for $x \gtrsim$ -2.3 mm. The discontinuity at $x \approx$ -2.3 mm is a phase boundary.

Dashed and solid lines are also drawn at σ_m and σ_M respectively in the stress frames, though the solid line at $\sigma_M =$ 48.86 GPa for the GeO_2 is off the scale.

7.1 Shot 955

Because their contact loci intersect to the left of point C in Figure 7.2, it is predicted that the impact of the tungsten flyer plate onto the GeO_2 produces a supersonic phase boundary in the GeO_2. This phase boundary does not require and cannot be subjected to a forward kinetic relation $f = \mathcal{F}_{31}(\dot{s})$ unless its velocity drops into a subsonic range, and this can happen only if other waves interact with the phase boundary, abruptly changing its velocity, before it travels across the GeO_2. This does not happen in simulations of this shot: as seen in the spatial distributions of Figure 7.3, the GeO_2 fully transforms to the high pressure phase before the wave that reflects from the tungsten-foam interface can reach the phase boundary. As expected, the strain discontinuity propagating across the GeO_2 in the bottom frames of Figures 7.3(a) and 7.3(b) is a supersonic phase boundary: its propagation velocity is $\dot{s} \approx 3.87$ km/s, greater than the maximum speed possible for a subsonic phase boundary, $c_3 = 3.529$ km/s. Notice that no wave propagates ahead of the phase boundary, in agreement with the presentation of Section 4.3.3 and Figure 4.6(c).

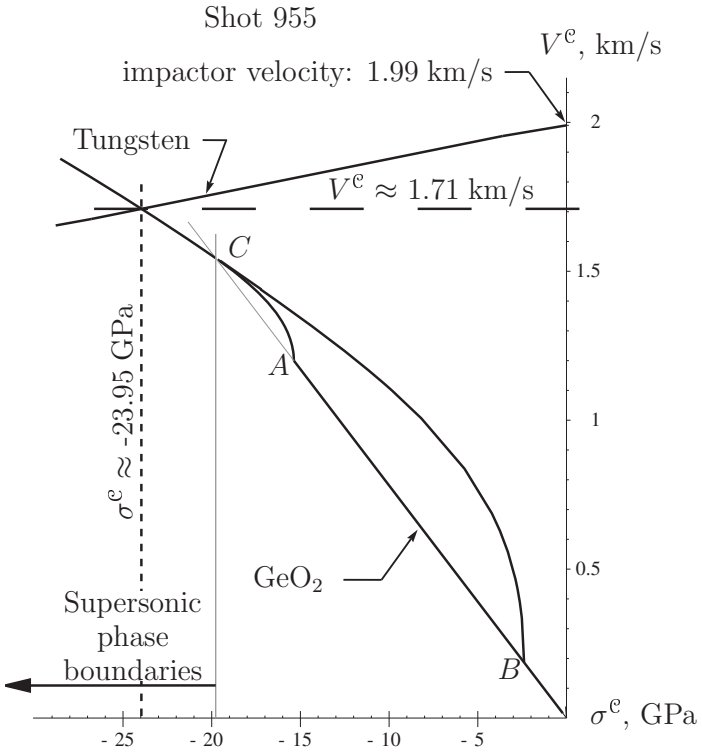

Figure 7.2: The loci of contact states for tungsten and GeO_2 based at the initial impact conditions in Shot 955. Because their intersection is left of point C, there will be a supersonic phase boundary in the GeO_2.

In the spatial distributions, we see that the predicted particle-velocity and stress behind the waves that propagate away from the impact interface agree well with the values of $V^{\mathcal{C}} = 1.71$ km/s and $\sigma^{\mathcal{C}} =$ -23.95 GPa estimated from the intersection of the contact loci in Figure 7.2.

The predicted particle-velocity history for this model is given in Figure 7.4.

Since the phase boundary propagates entirely across the GeO_2 undisturbed from its nucleation site, there is no opportunity for it to reverse direction and, therefore, no opportunity for the reverse kinetic relationship $f = \mathcal{F}_{13}(\dot{s})$ to influence its propagation. The reverse kinetic relationship can still play a role at later times if the low pressure phase nucleates from the high pressure phase, but even in the situation most favorable for this—namely the combination of the dissipation-free

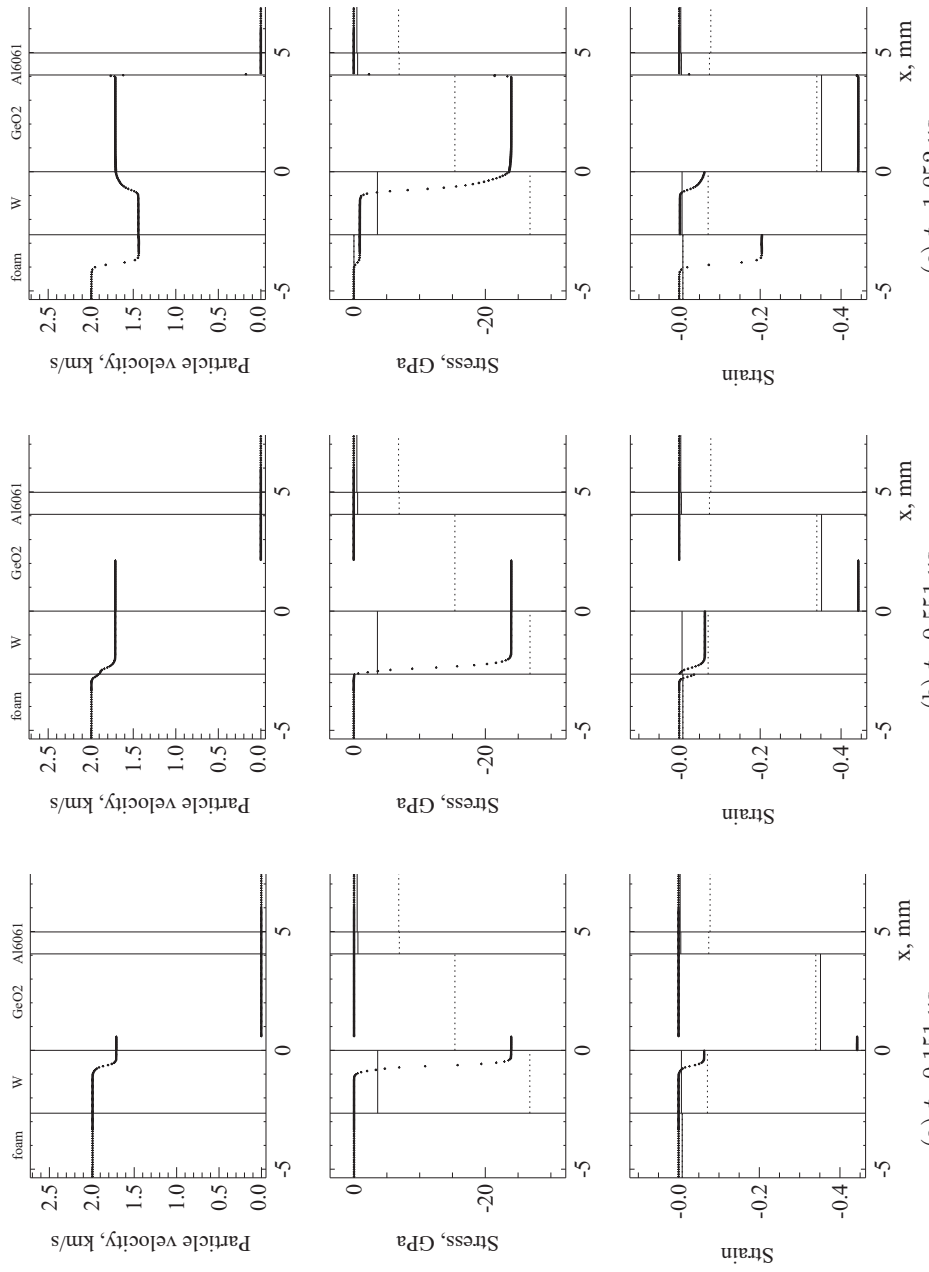

(a) t=0.151 µs (b) t=0.551 µs (c) t=1.052 µs

Figure 7.3: Predicted spatial distributions of particle-velocity, stress and strain in Shot 955. The supersonic phase boundary, seen in (a) and (b), has traveled completely across the GeO_2 in (c) before any reflected wave could reach it.

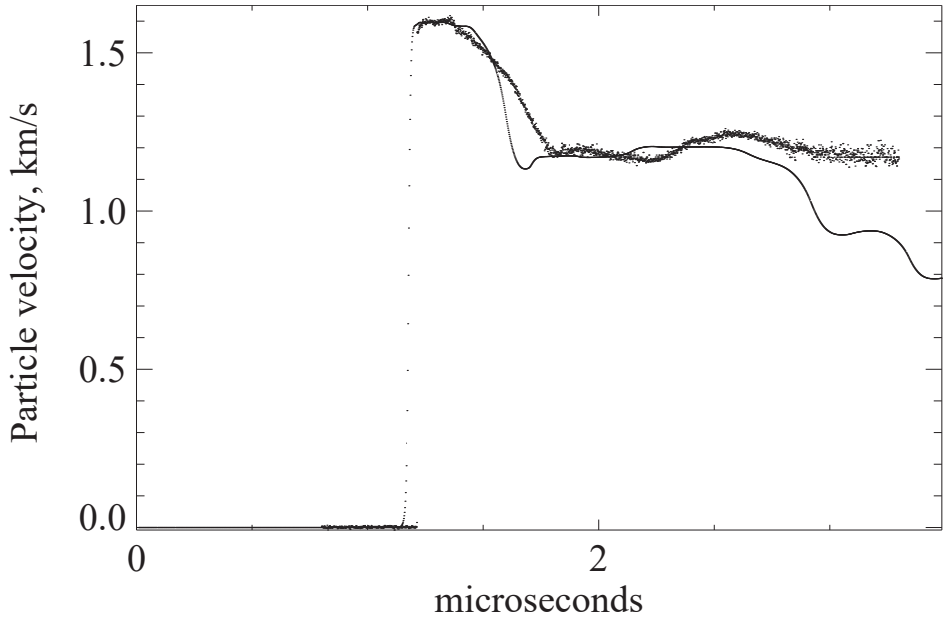

Figure 7.4: Predicted particle-velocity history (light curve) at the interface between the Al6061 and LiF compared to the VISAR record (heavy curve) for Shot 955. (This figure is identical to Figure 5.6.)

reverse kinetic relation $\mathcal{F}_{13}(\dot{s}) = 0$ with a critical driving traction of $f_{13}^{c} = 0$ for nucleation—the low pressure phase does not reappear. The results of simulations with the dissipation-free reverse kinetic relation were identical to those with the maximum-dissipation reverse kinetic relation, confirming that the reverse kinetic relation played no role at all during the duration of the simulation.

In conclusion, the model predicts a supersonic phase boundary in the GeO_2 that fully transforms it to the high pressure phase, no reverse transformation is predicted for any choice of reverse kinetic relation, and subsonic phase boundaries are not predicted. Neither a forward nor reverse kinetic relation is ever utilized.

7.2 Shot 953

Because the contact locus for the tungsten flyer plate crosses the region ABC of the locus for the GeO_2 target, Figure 7.5, the impact can induce a subsonic phase

boundary but not a supersonic phase boundary. Furthermore, since there is no point of intersection on the shock locus AB, there is no solution that involves only a shock and no phase boundary: impact *must* nucleate a subsonic phase boundary for *all* choices of kinetic relations $f = \mathcal{F}_{31}(\dot{s})$ and *any* nucleation criteria chosen for the forward transformation.

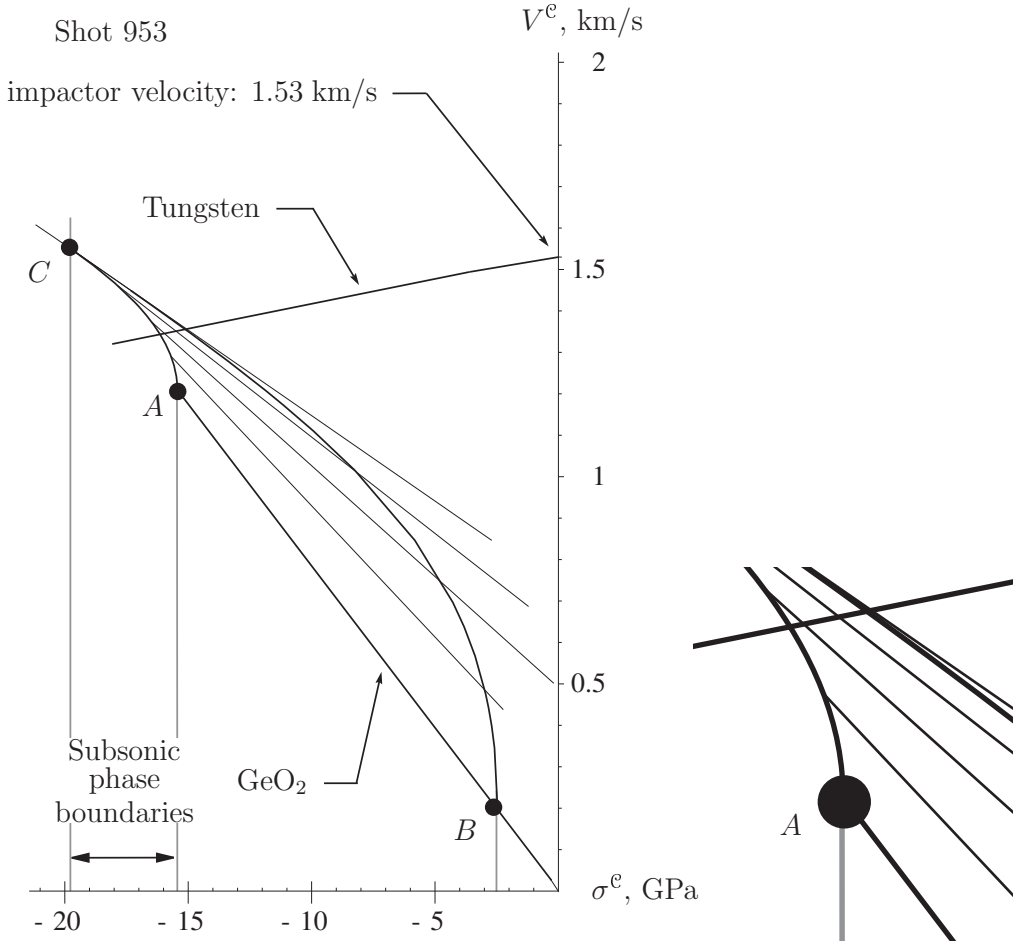

(a) Contact loci.

(b) Enlargement around the intersection of the loci.

Figure 7.5: The intersection of the loci of contact states for the initial impact of Shot 953 indicates that the solution must involve a subsonic phase boundary.

Using the lines of constant phase boundary velocity in Figure 7.5, we can esti-

mate the velocities of the slowest and fastest phase boundaries that can be nucleated by the impact. In this figure and all remaining similar figures in this chapter, these lines are drawn at increments of $\Delta\dot{s} = 0.882$ km/s. In the enlargement of Figure 7.5(b), it is seen that tungsten's contact locus crosses the AC boundary between $\dot{s} = 0.882$–1.765 km/s: the velocity of the *slowest* phase boundary that can be induced by the impact lies in this range. The intersection on the BC locus indicates that the velocity of the *fastest* phase boundary will be in the range $\dot{s} = 2.647$–3.528 km/s, below the maximum speed possible for a subsonic phase boundary, $c_3 = 3.529$ km/s.

Over a dozen simulations, each using a different foward kinetic relation, were conducted for this shot. The maximum dissipation kinetic relation $\mathcal{F}_{31}(\dot{s}) = \mathcal{F}_{31}^{\text{roof}}(\dot{s})$ and the dissipation-free kinetic relation $\mathcal{F}_{31}(\dot{s}) = 0$ were included amongst these. As expected, all simulations did indeed predict that a phase transition was nucleated. Until the phase boundaries were disturbed by other waves, their velocities were within the ranges predicted in the previous paragraph: the velocity of the slowest phase boundary, achieved with the maximum dissipation forward kinetic relation, was $\dot{s} = 1.54$ km/s, while the velocity of the fastest phase boundary, achieved with the dissipation-free forward kinetic relation, was $\dot{s} = 3.41$ km/s.

Particle-velocity histories for four of these simulations, using forward kinetic relationships $\mathcal{F}_{31}(\dot{s})$ having no dependence on $\dot{s}$, are presented in Figure 7.6. Only the roof $\mathcal{F}_{13}(\dot{s}) = \mathcal{F}_{13}^{\text{roof}}(\dot{s})$was used for the reverse kinetic relationship in the simulations shown in this figure.

The driving traction $f = \hat{\mathcal{F}}_{31}(\dot{s}) = g_{31}$ is constant for each of the kinetic relations used for Figure 7.6; there is no dependence on the phase boundary velocity $\dot{s}$. The constant values differ by only $\Delta g_{31} = 0.05$ GPa between Figures 7.6(b) and 7.6(c), and by only $\Delta g_{31} = 0.025$ GPa between Figures 7.6(c) and 7.6(d). The resulting predictions of particle-velocity history are very similar for these three simulations, except between times $t \approx 1.2$–1.3 μs. In Figure 7.6(b), the predicted particle velocity becomes negative in this period of time. In Figure 7.6(d), it becomes positive,

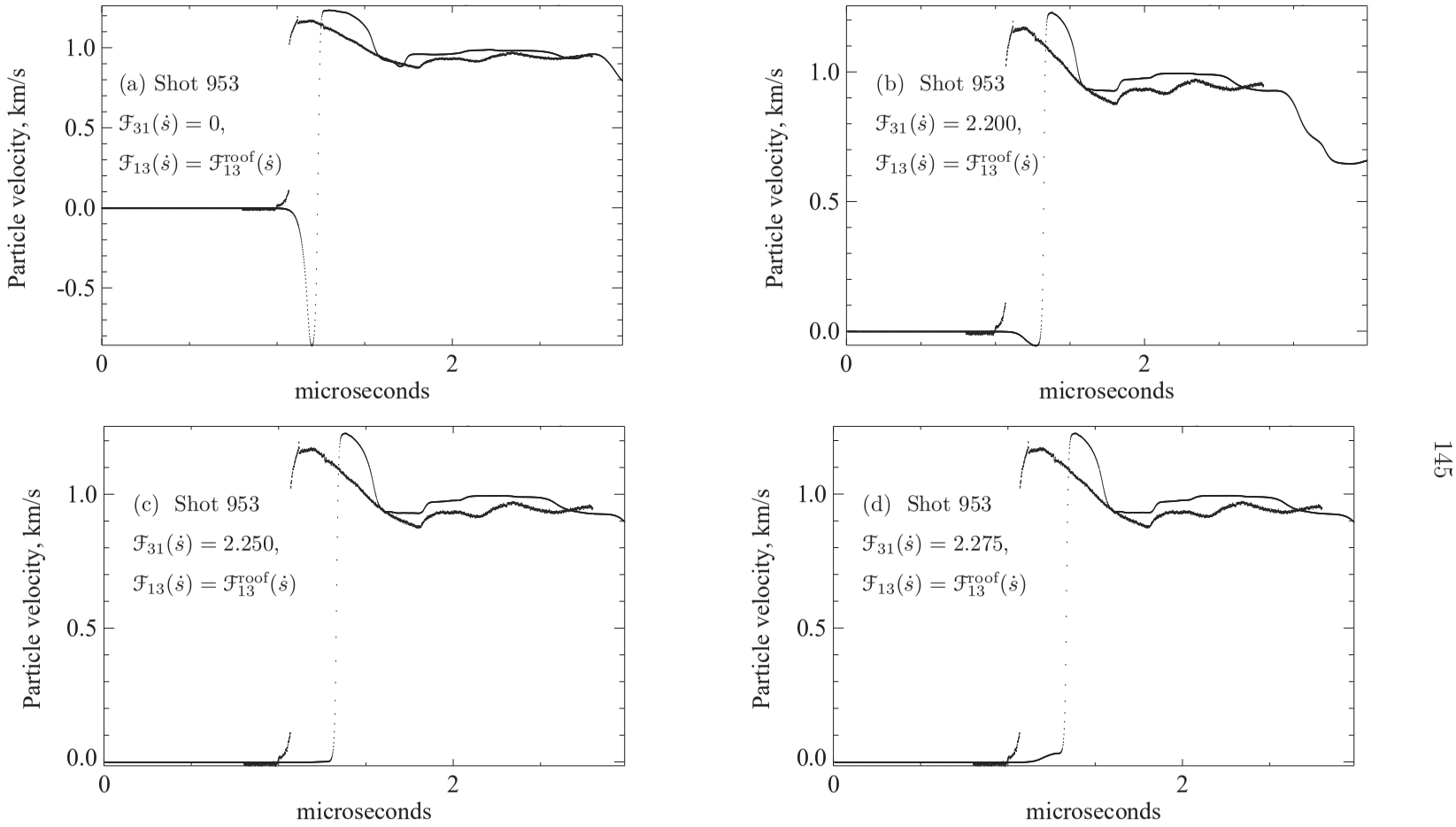

Figure 7.6: Predicted particle-velocity histories for Shot 953 using different kinetic relations for the transformation from the low pressure phase to the high pressure phase.

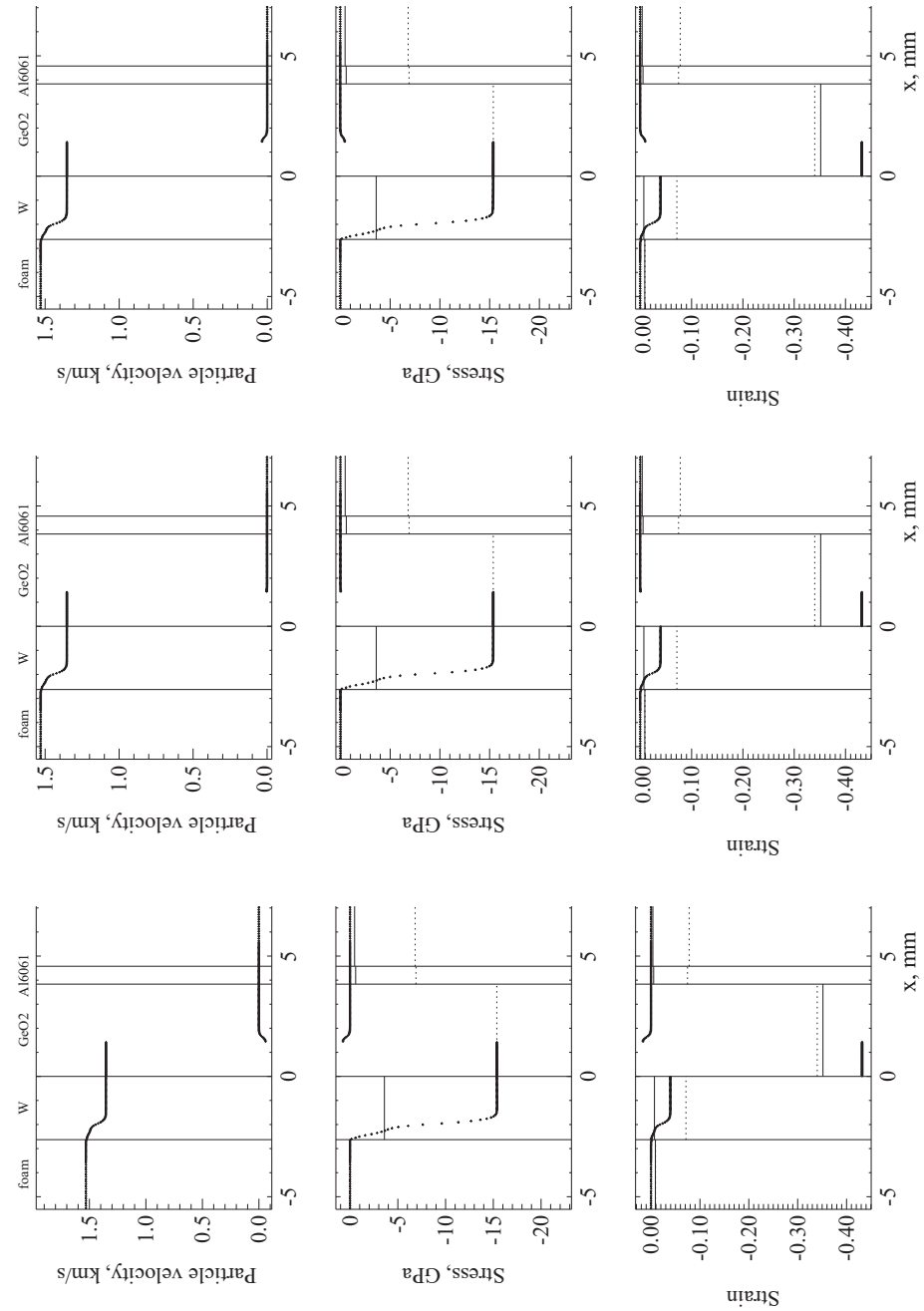

(a) t=0.456 µs, $\mathcal{F}_{31}(\dot{s}) = 2.200$, $\mathcal{F}_{13}(\dot{s}) = \mathcal{F}_{13}^{\text{roof}}(\dot{s})$.

(b) t=0.455 µs, $\mathcal{F}_{31}(\dot{s}) = 2.250$, $\mathcal{F}_{13}(\dot{s}) = \mathcal{F}_{13}^{\text{roof}}(\dot{s})$.

(c) t=0.456 µs, $\mathcal{F}_{31}(\dot{s}) = 2.275$, $\mathcal{F}_{13}(\dot{s}) = \mathcal{F}_{13}^{\text{roof}}(\dot{s})$.

Figure 7.7: Spatial distributions in Shot 953 at approximately equal times for the three different forward kinetic relations of Figures 7.6(b)–7.6(d). Just ahead of the phase boundary, the GeO_2 is (a) in tension, (b) nearly undisturbed, and (c) in compression.

and in Figure 7.6(c), the material remains nearly quiescent in this period of time. In the following paragraphs, we discuss how the sign of the predicted particle-velocity in this time interval depends on whether a *tensile* or *compressive* shock wave propagates ahead of the phase boundary.

Recall that a subsonic phase boundary in a trilinear material is in general preceded by a shock wave. When a forward kinetic relation $f = g_{31}$ with no dependence on $\dot{s}$ is prescribed, there is a special value of $g_{31} \approx 2.25$ GPa at which the predicted jumps in particle-velocity, stress, and strain vanish across the shock. In this situation, though the phase boundary is subsonic, there is no shock ahead of it, Figure 7.7(b). When the phase boundary reaches the aluminum buffer, it creates a compressive wave in the aluminum. This compressive wave causes the rapid increase in the particle-velocity at $t \approx 1.3$ μs in Figure 7.6(c).

If a forward kinetic relationship $f = g_{31}$, with $g_{31} \lesssim 2.25$ GPa is prescribed, then the shock ahead of the phase boundary is predicted to take the material into *tension*, Figure 7.7(a). Behind the shock, the particle-velocity is *negative*. This shock wave passes into the aluminum and encounters the lithium fluoride at $t \approx 1.2$ μs, causing the particle-velocity to become negative in the predicted particle-velocity histories of Figures 7.6(a) and 7.6(b).

When a forward kinetic relationship $f = g_{31}$, with $g_{31} \gtrsim 2.25$ GPa is prescribed, the shock ahead of the phase boundary is predicted to take the material into *compression*, Figure 7.7(c). The particle-velocity is *positive* behind this shock. The shock causes the predicted particle-velocity to become positive at $t \approx 1.2$ μs, Figure 7.6(d). Larger values of $f = g_{31}$ caused greater increases in this initial part of the particle-velocity history.

Thus we see that the initial change in the predicted particle-velocity history for this shot is very sensitive to the forward kinetic relationship. Observe that the experimental VISAR record for this experiment displays a small rise in particle-velocity followed by a much larger jump. Of the simulations conducted for this shot, Figure 7.6(d) comes the closest to capturing this feature of the experimental

recording, so we choose it as the best that our trilinear model is capable of for this shot.

In all the predictions of Figure 7.6, the velocity decreases from its peak value much more rapidly than in the experimental record. This is consistent with the limitation imposed by using a linear stress-strain curve for the high pressure phase, as discussed in Section 5.1. This limitation causes more discrepancy in the forward shots than in the reverse shots. Using a model with a lower modulus, the predicted velocity history can be made to remain longer at its peak value, but the decrease is still too rapid because the release wave is prevented by the model from generating a fan in the GeO_2.

The simulations discussed so far all utilized the roof for the kinetic relation governing the reverse transformation (from the high pressure phase to the low pressure phase). Simulations using the same two forward kinetic relationships as Figure 7.6(c) and Figure 7.6(d) were repeated with the dissipation-free kinetic relation $\mathcal{F}_{13}(\dot{s}) = 0$ for the reverse transformation, but there was no change in the results. For either of these two forward kinetic relations, the initial impact initiates a fast but subsonic phase boundary that propagates entirely across the GeO_2 before any large disturbance can reach it. The disturbances that the phase boundary *does* encounter are too small to reverse its direction *even when the dissipation-free reverse kinetic relation, which presents* no *barrier to a reversal of direction of the phase boundary, is prescribed*. Thus, for these two forward kinetic relations, there is no opportunity for *any* reverse kinetic relation to influence the propagation of the phase boundary nucleated by the impact. Furthermore, for these two forward kinetic relations, once the low pressure phase is gone, it is gone for good: it never nucleates from the high pressure phase even for the dissipation-free reverse kinetic relation, which is the reverse kinetic relation that is most favorable for the low pressure phase to reappear. In summary, changing the reverse kinetic relation does not change the results of these simulations because the phase boundary nucleated by the impact never has the opportunity to reverse direction, and no other phase boundaries ever nucleate.

A simulation of this shot using a Mie-Grüneisen equation of state for both the low and high pressure phases of GeO_2 has recently been published by Chen et al. [22]. In the Mie-Grüneisen equation of state, the internal energy is a function of temperature and density. Furthermore, this equation of state is capable of describing a non-linear relationship between pressure and volume. In these senses it is more sophisticated than the trilinear model used in this thesis. Phase transformations in the GeO_2 were described by a mixed phase, with the percentage of the high pressure phase linearly increasing with compression.

Chen and colleagues compared an "irreversible phase change" model to a "reversible phase change model." In the irreversible model, the high pressure phase does not transform back to the glass phase upon release, while in the reversible model it does. In both models, the GeO_2 "enters a mixed phase at $\sim$ 8 GPa." They find that predictions with the irreversible phase change model are a much closer fit to the experiment than predictions with the reversible phase change model. Their fit to the VISAR record for this shot with the irreversible model is considerably better than any obtained here for this shot with the trilinear model.

Chen et al. also report that simulations were conducted for the other shots in this series, but that the predictions were *best* for Shot 953. This is especially interesting, as our predictions using the trilinear model are much *worse* for Shot 953 than for any of the other shots.

7.3 Shot 965

In Shot 965, the contact locus of the aluminum buffer intersects the region ABC of the contact locus of the GeO_2 impactor, Figure 7.2. Therefore, this impact can nucleate a subsonic but not a supersonic phase boundary. Since the contact locus of the aluminum crosses the boundary AB, which is part of the shock locus for GeO_2, there are *also* solutions that involve only a shock and *no* phase boundary. Thus, there will be some threshold value of the critical driving traction f_{31}^c that allows a

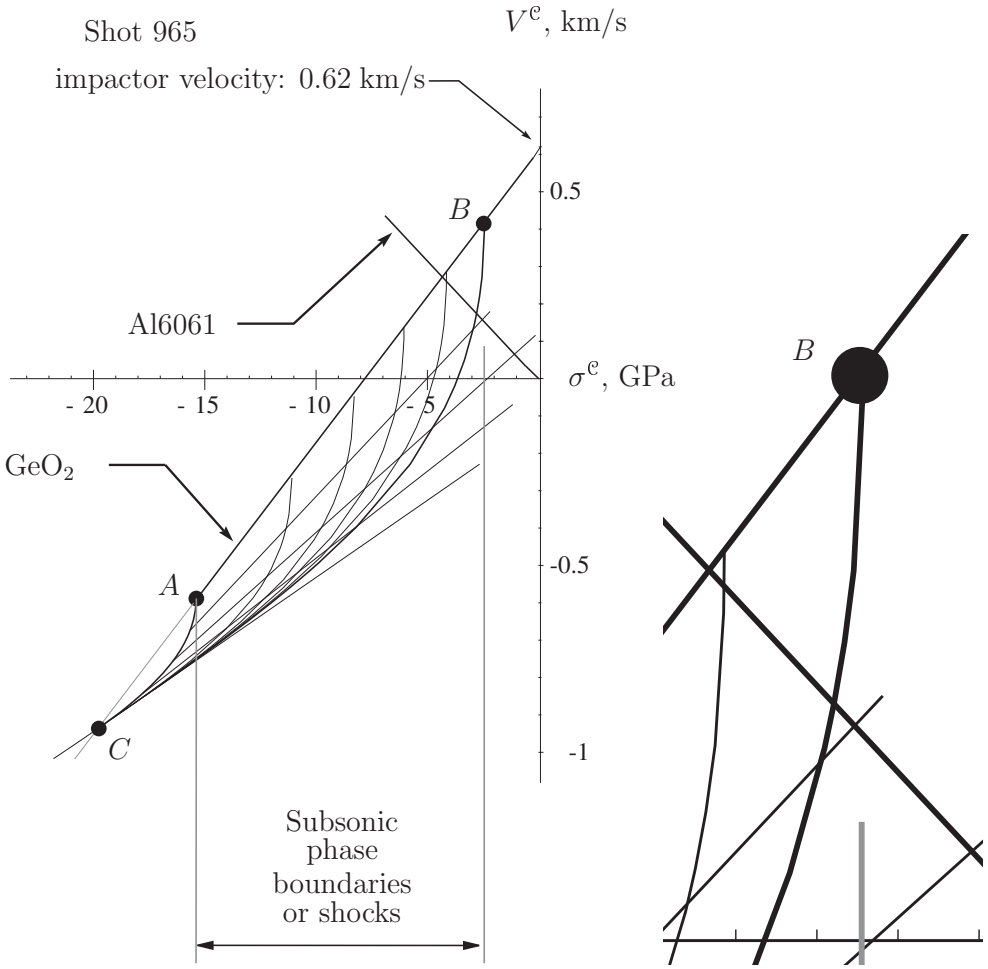

(a) Contact loci.

(b) Enlargement around the intersection of the loci.

Figure 7.8: The loci of contact states for aluminum and GeO_2 based at the initial impact conditions in Shot 965. Because the locus of the aluminum crosses the region ABC, any phase boundary in the GeO_2 will be subsonic. Solutions with no phase boundary are also possible, since the locus of the aluminum crosses shock locus which lies on the boundary AB.

phase boundary to nucleate. If a critical driving traction greater than this threshold value is prescribed, no phase boundary nucleates.

The loci of constant driving traction in Figure 7.2 help us estimate what the

threshold value of the critical driving traction must be. In this figure and all similar figures to follow, these loci are at increments $\Delta f = 0.591$ GPa. The contact locus of the aluminum intersects AB just left of the curve $f = 0.591$ GPa. Thus, the impact can nucleate a phase boundary only if we prescribe $f_{31}^c \lesssim 0.6$ GPa.

Since the only critical driving traction implemented in the computer program is of the form $f_{ab}^c = \mathcal{F}_{ab}(0^+)$, we can only vary the critical driving traction f_{31}^c by varying the kinetic relation $f = \mathcal{F}_{31}(\dot{s})$. We will stick to kinetic relations that have no dependence on the phase boundary velocity $\dot{s}$, so that our threshold value of the critical driving traction is the greatest value of g_{31} that allows a phase boundary to nucleate.

The fastest phase boundary occurs with a dissipation-free kinetic relation, the locus for which lies on the BC boundary of the region ABC. The contact locus of the aluminum intersects the BC boundary near the line of constant phase boundary velocity $\dot{s} = 0.882$ km/s. Therefore, any phase boundary induced by this impact can propagate no faster than $\dot{s} \approx 0.88$ km/s unless and until it encounters other waves.

Simulations were conducted using kinetic relationships with no dependence on $\dot{s}$, $\mathcal{F}_{31}(\dot{s}) = g_{31}$. The roof was used as the kinetic relationship for the reverse transformation. Phase boundaries nucleated for *all* $g_{31} \leq 0.6$, and for *no* $g_{31} \geq 0.75$, in good agreement with the prediction made in the previous paragraphs. The simulations predict a decrease in the particle-velocity history with decreasing $g_{31} \leq 0.6$, Figure 7.9. Figure 7.10 presents spatial distributions of particle-velocity, stress and strain at approximately equivalent times for the kinetic relations used in the predictions of Figures 7.9(a), 7.9(b) and 7.9(d). These spatial distributions depict three extreme cases: no phase boundary, a very slow phase boundary, and the fastest phase boundary possible. The fastest phase boundary velocity was $\dot{s} = 0.78$ km/s, consistent with the upper bound estimated from Figure 7.2.

The velocity of the very slow phase boundary seen in Figure 7.10(b) was $\dot{s} = 0.119$ km/s, and its velocity decreased at later times when other waves disturbed it. The high pressure phase behind this phase boundary never grew wider than $\Delta x =$

0.2 mm. It is remarkable that the generation of this sliver of high pressure phase dissipated enough energy to decrease the predicted particle-velocity at the top of the "plateau" in Figure 7.9(b) by approximately 4% compared to the prediction with no phase boundary, Figure 7.9(a). This sliver of high pressure phase resulted in the best match to the experimental VISAR record for this shot, based on a comparison of predicted and measured particle velocities along most of the "plateau."

Now we examine the effect of the reverse kinetic relationship. As long as the phase boundary travels undisturbed from its nucleation site, the reverse kinetic relationship plays no role. The first disturbance encountered by the phase boundary is a wave reflected from the interface between the aluminum and the lithium fluoride, but it is very weak and does not cause the phase boundary to reverse direction for any of the simulations. The next disturbance to the phase boundary occurs when the shock wave that precedes the phase boundary in the GeO_2 reflects from the interface with the foam, and this *is* sufficient to reverse the direction of the phase boundary transformation if the reverse kinetic relationship allows it. When the phase boundary reverses direction, the material through which it passes is transformed from the high pressure phase back to the low pressure phase.

In the spatial distributions of Figures 7.11 and 7.12, we see—for a particular choice of a forward kinetic relation—that the phase boundary changes direction when the transformation from the high pressure phase to the low pressure phase is governed by a dissipation-free kinetic relation, Figure 7.11, but not when it is governed by the maximum-dissipation kinetic relation, Figure 7.12. The influence of the reverse kinetic relation manifests itself in the "tail" of the predicted particle-velocity history, Figure 7.13. Even when the phase boundary slows down or reverses direction, this information may not reach the interface between the aluminum and the lithium fluoride—where we compare the predicted particle-velocity history to the VISAR record—during the time of the simulation. This occurred for the combination of $\mathcal{F}_{31}(\dot{s}) = 0$, $\mathcal{F}_{13}(\dot{s}) = 0$: the predicted particle-velocity history profile from this simulation is identical to that with $\mathcal{F}_{31}(\dot{s}) = 0$, $\mathcal{F}_{13}(\dot{s}) = \mathcal{F}_{13}^{\text{roof}}(\dot{s})$, but their

spatial distributions become different sometime in the interval $t = 2.42$-2.47 μs.

A simulation was conducted for a forward kinetic relationship having a linear dependence on $\dot{s}$, namely $\mathcal{F}_{31}(\dot{s}) = 1.500 + 0.388\dot{s}$. This kinetic relation lies entirely above the threshold for nucleation; as expected, no phase boundary nucleated, and the result was identical to that of Figure 7.9(a).

The particle velocity in the VISAR record of the experiment increases near the end of the plateau, at about $t = 1.3$–1.7 μs in Figure 7.9. No simulation of Shot 965 using this trilinear model predicted an increase in this time interval. As shall be seen in the following sections, a rise *was* found for the other reverse shots: the increase was caused by the reflection of an expansive shock that precedes the phase boundary. It is expected that an expansive wave could be produced for Shot 965 with a different trilinear model. A likely candidate for this different model could be found by modifying the current model, retaining the expressions for the low and high pressure phases but making the delimiting strains γ_M and γ_m less negative. For a prescribed kinetic relation of the form $f = g_{31} =$ constant, this forces the strain γ^+ ahead of a phase boundary moving into the low pressure phase to become less negative. As γ_M and γ_m are increased subject to the constraint $\gamma_M \leq \gamma_m < 0$, then γ^+ is eventually forced to become positive for $f = g_{31} = 0$ and for other values of g_{31} that are "small enough." When γ^+ is positive, the shock in front of the phase boundary is expansive, and this could lead to an increase in the predicted particle-velocity near the end of the plateau.

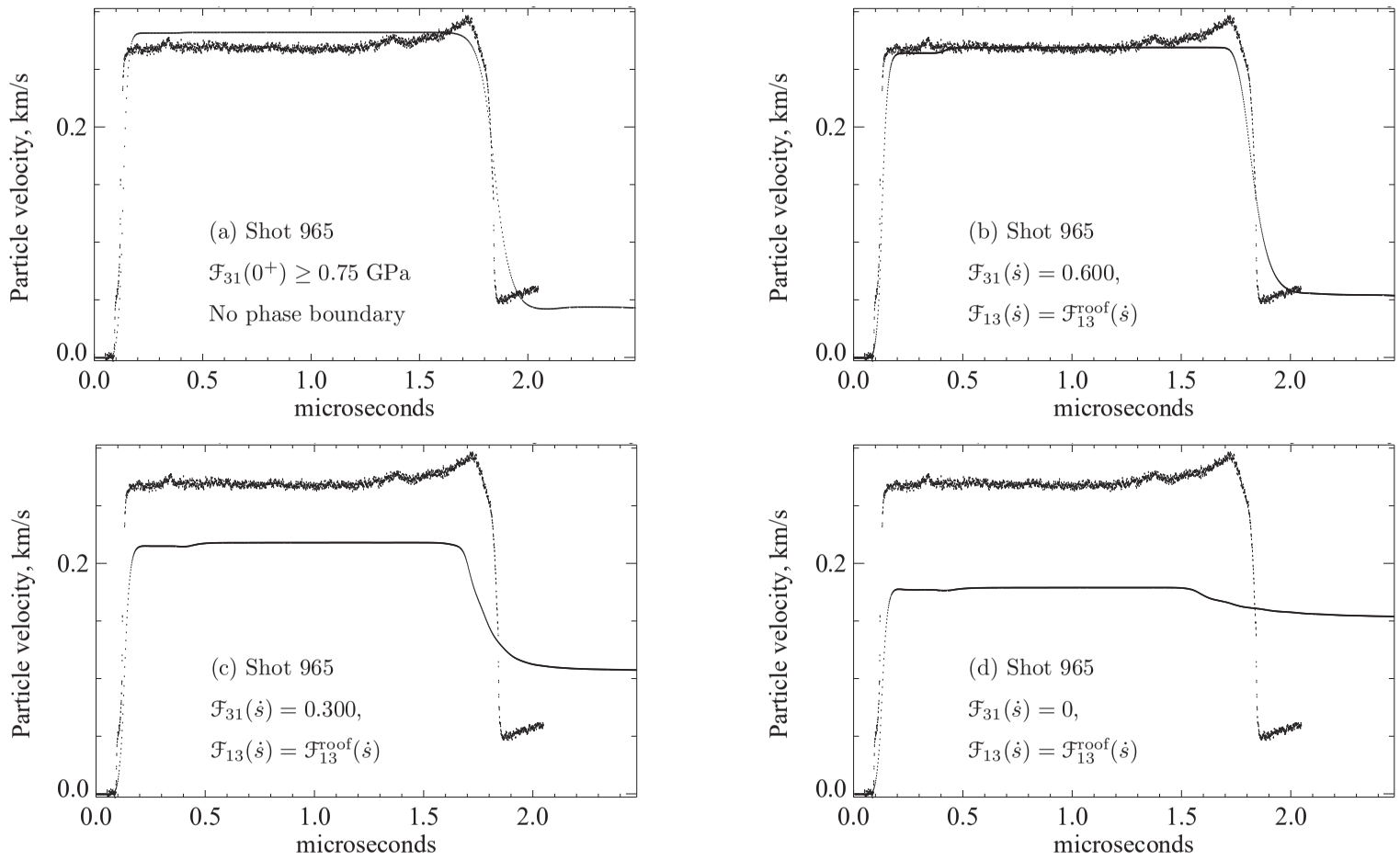

Figure 7.9: Predicted particle-velocity histories for Shot 965 using different forward kinetic relationships $f = \mathcal{F}_{31}$. The impact is predicted to induce (a) no phase boundary, (b) a phase boundary with a velocity of $\dot{s} = 0.119$ km/s, (c) a phase boundary with a velocity of $\dot{s} \approx 0.45$ km/s, (d) a phase boundary with a velocity of 0.78 km/s, the maximum that can be induced by this impact.

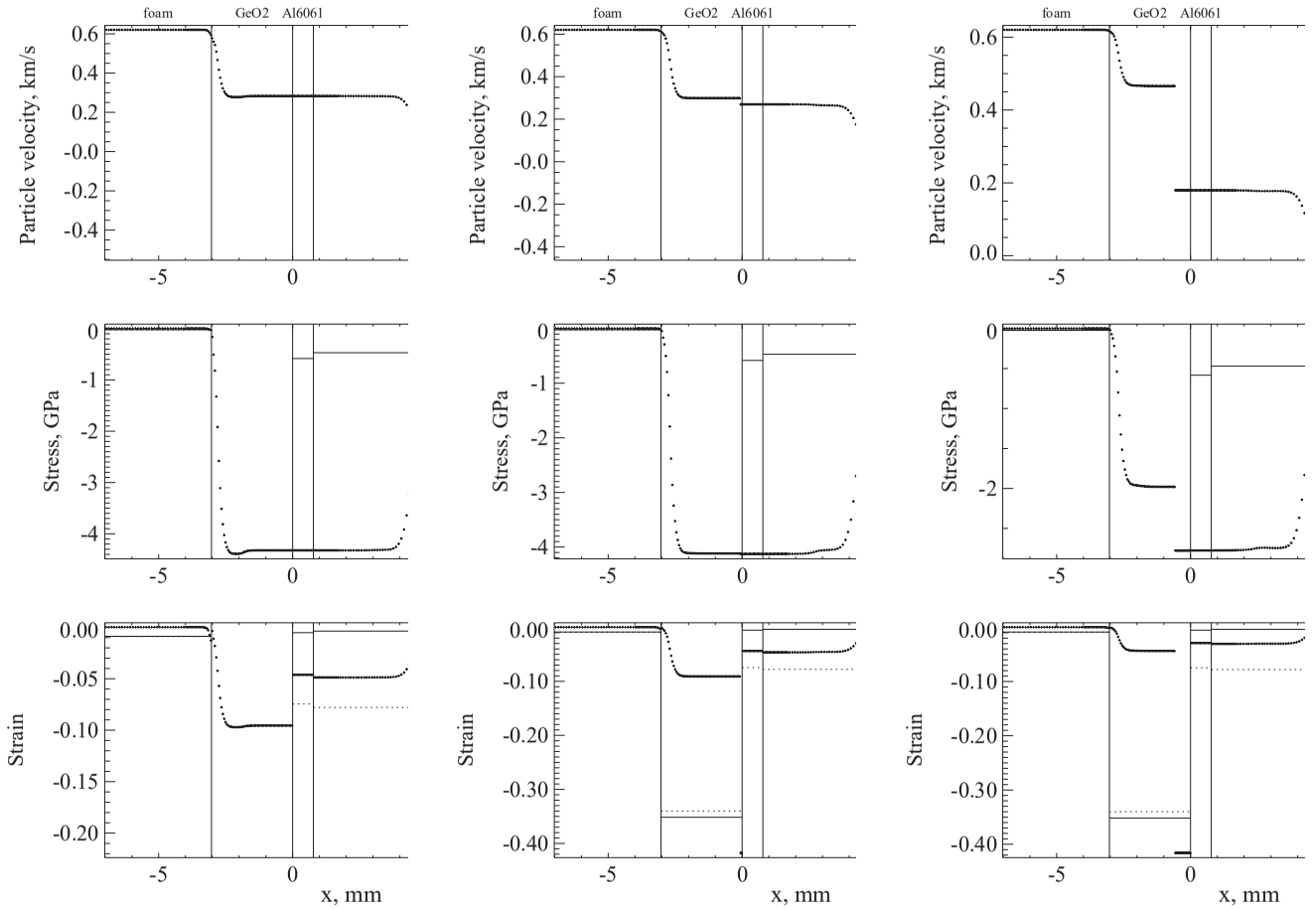

(a) t=0.789 μs,
$\mathcal{F}_{31}(0) \geq 0.75$ GPa.

(b) t=0.759 μs,
$\mathcal{F}_{31}(\dot{s}) = 0.600$, $\mathcal{F}_{13}(\dot{s}) = \mathcal{F}_{13}^{\text{roof}}(\dot{s})$.

(c) t=0.756 μs,
$\mathcal{F}_{31}(\dot{s}) = 0$, $\mathcal{F}_{13}(\dot{s}) = \mathcal{F}_{13}^{\text{roof}}(\dot{s})$.

Figure 7.10: Spatial distributions at approximately equal times for the three forward kinetic relations used in Figures 7.9(a), 7.9(b), and 7.9(d). (a) No phase transformation. (b) A very slow phase boundary: only 3 or 4 cells at $\gamma \approx$ -0.42 on the right side of the GeO_2 have transformed to the HPP. (c) The fastest phase boundary that can be induced by this impact: about 0.6 mm of the material has transformed to the HPP.

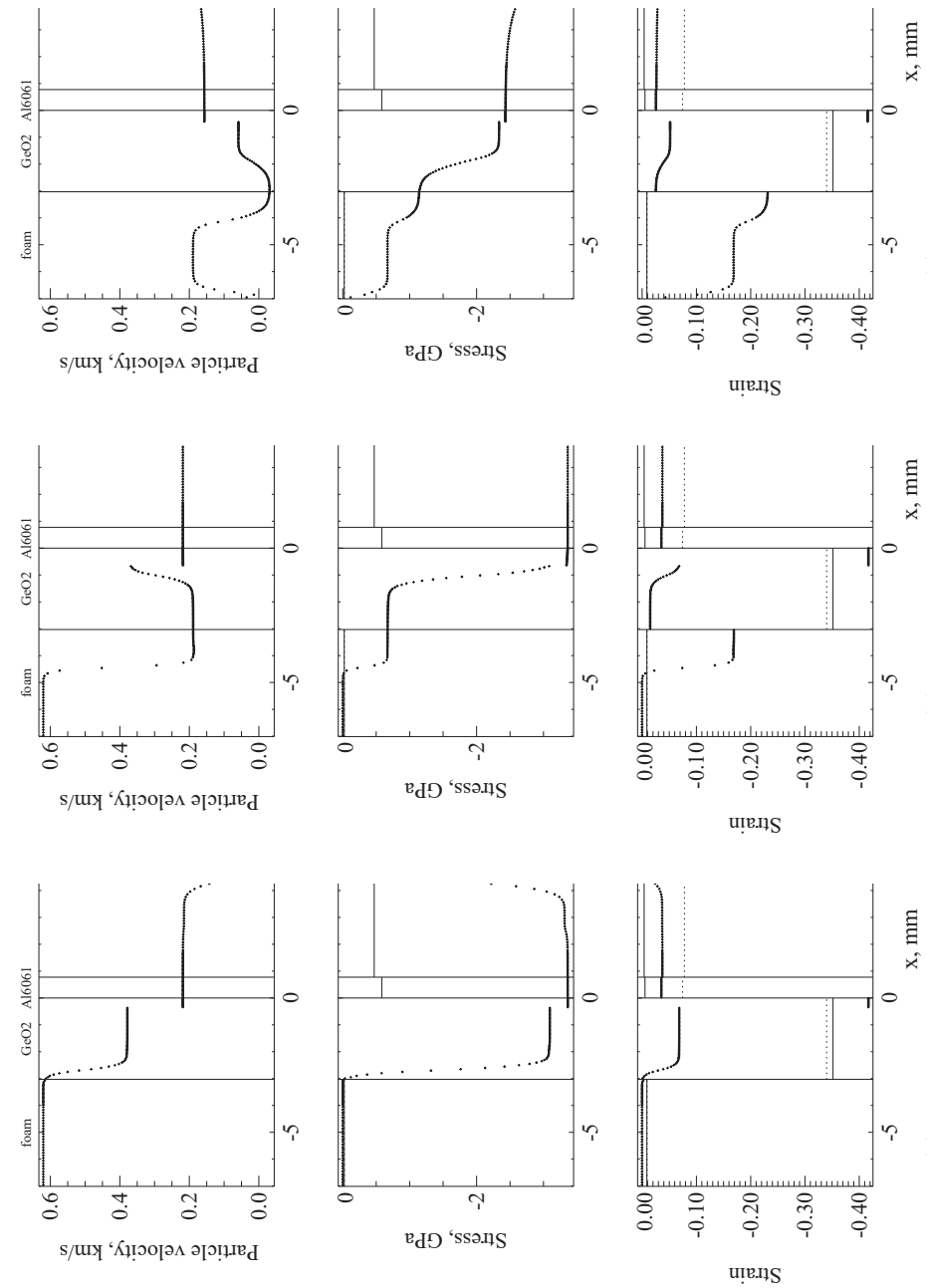

(a) t=0.758 μs (b) t=1.415 μs (c) t=2.476 μs

Figure 7.11: Sequence of spatial distributions in Shot 965 at late times, showing that the phase boundary reverses direction for the kinetic relations $\mathcal{F}_{31}(\dot{s}) = 0.300$, $\mathcal{F}_{13}(\dot{s}) = 0$. Compare this to Figure 7.12.

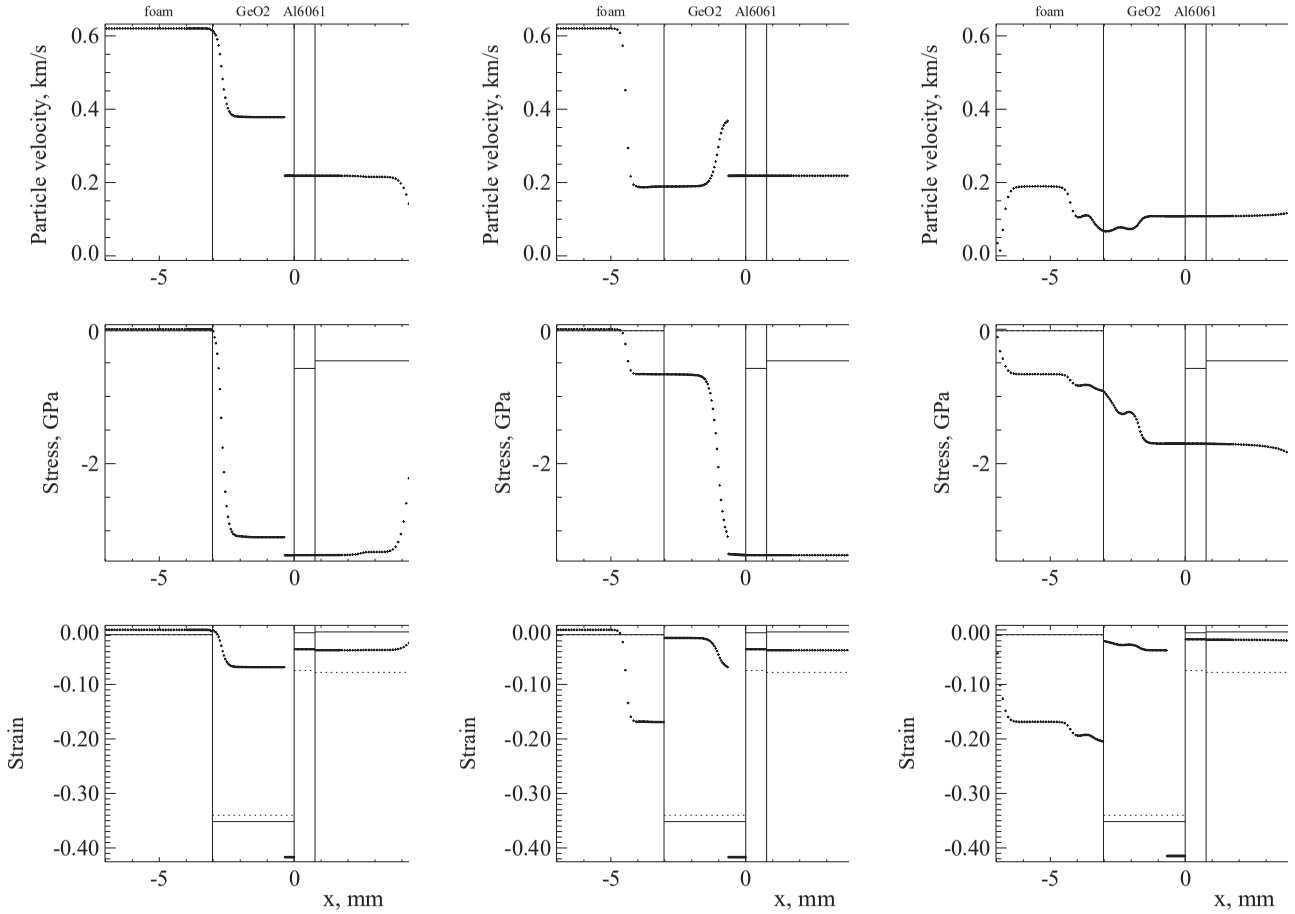

(a) t=0.758 μs (b) t=1.415 μs (c) t=2.476 μs

Figure 7.12: Sequence of spatial distributions in Shot 965 at late times, showing that the phase boundary does not reverse direction for the kinetic relations $\mathcal{F}_{31}(\dot{s}) = 0.300$, $\mathcal{F}_{13}(\dot{s}) = \mathcal{F}_{13}^{\text{roof}}(\dot{s})$. Compare this to Figure 7.11.

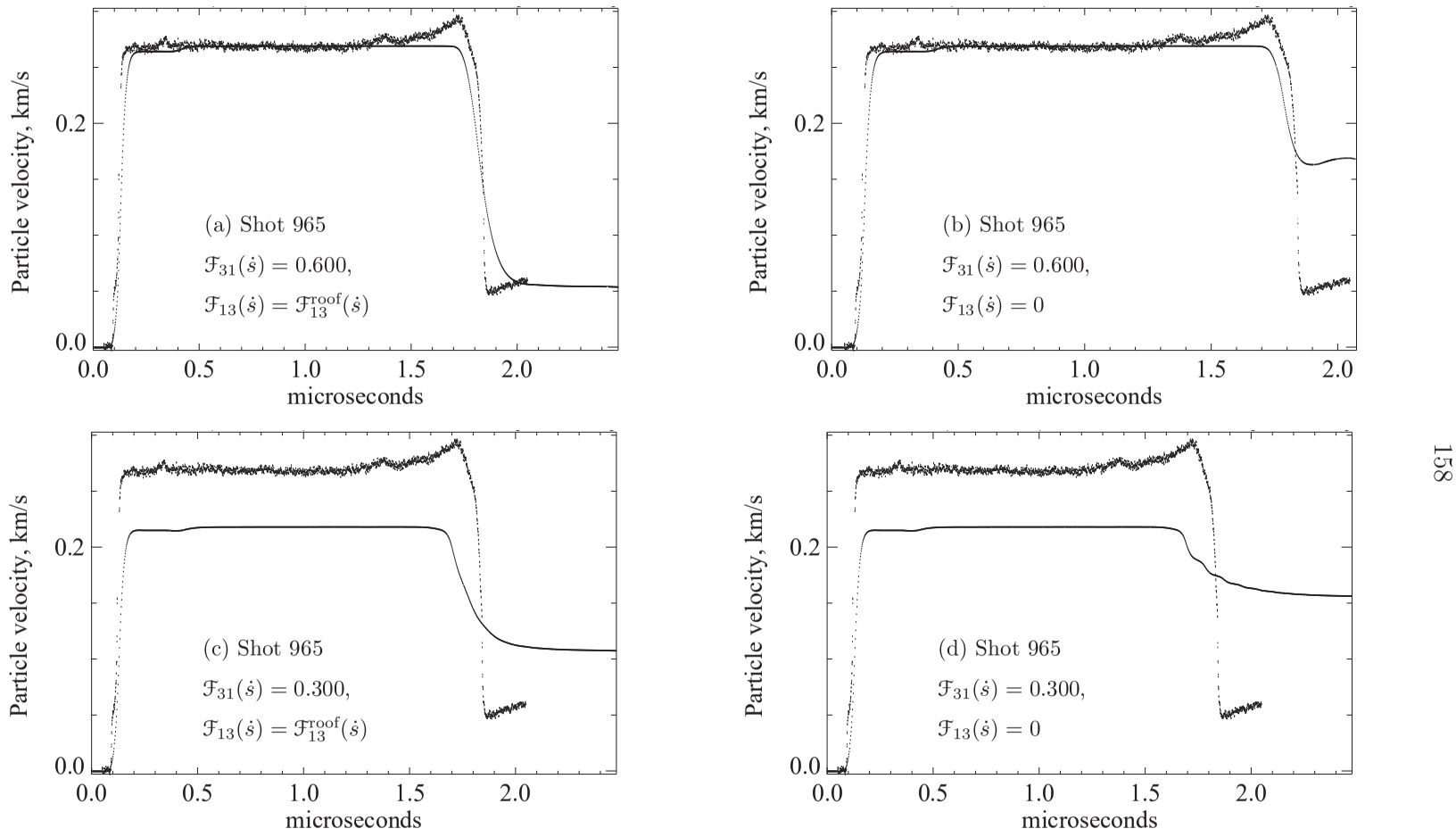

Figure 7.13: Predicted particle-velocity histories for Shot 965 using maximum dissipation (left) and dissipation-free (right) kinetic relations for the reverse transformation (from the high pressure phase to the low pressure phase) for two different choices of forward kinetic relations (top and bottom). Note the differences between the figures on the left and the right for $t > 1.5$ μs.

7.4 Shot 957

The contact loci for this shot, Figure 7.14, are similar to those we examined for Shot 965: their intersection occurs in the region ABC and the contact locus of the aluminum crosses the AB boundary of this region. Thus, the impact will produce a subsonic phase boundary in the GeO_2 when a critical driving traction f_{31}^c below some threshold value is enforced, but not when the critical driving traction is above this threshold.

Proceeding as for Shot 965, we estimate from the curves of constant driving traction in Figure 7.14(b) that the threshold value of the critical driving traction is less than $f_{31}^c = 2.363\,\text{GPa}$. The velocity of the fastest phase boundary that can be induced by the impact is slightly less than 3.528 km/s, and will occur with the dissipation-free forward kinetic relation $f = 0$.

Figure 7.15 shows predictions for four different forward kinetic relations, using the roof for all reverse kinetic relations. This is one of the shots in which the GeO_2 was thought to be fractured before impact [106], so the experimental record is suspect. We will select Figure 7.15(b) as the best match, because it does a fair job in matching the recorded peak velocities. The results were unchanged for this simulation when the reverse kinetic relationship was varied.

One could easily argue that Figure 7.15(c) is a better match because the duration of the particle-velocity history it predicts is closer to the experimental record.

The increase in the predicted particle-velocity near the end of the plateau in Figure 7.15(d) is a delightful result. Recall that an increase in the particle velocity at the end of the plateau is also seen in the experimental VISAR record of Shot 965. (Even in the experimental record for Shot 957 there is an increase, but since the GeO_2 may be damaged before the impact we shouldn't place too much stock in it.) At first, it's difficult to believe that the dramatic spike in Figure 7.15(d) has any relation to the more subtle increase seen experimentally—indeed, it was ignored as irrelevant for a long time—but we must remind ourselves that the linear high pressure phase of our model is much stiffer than the real material at these pressures,

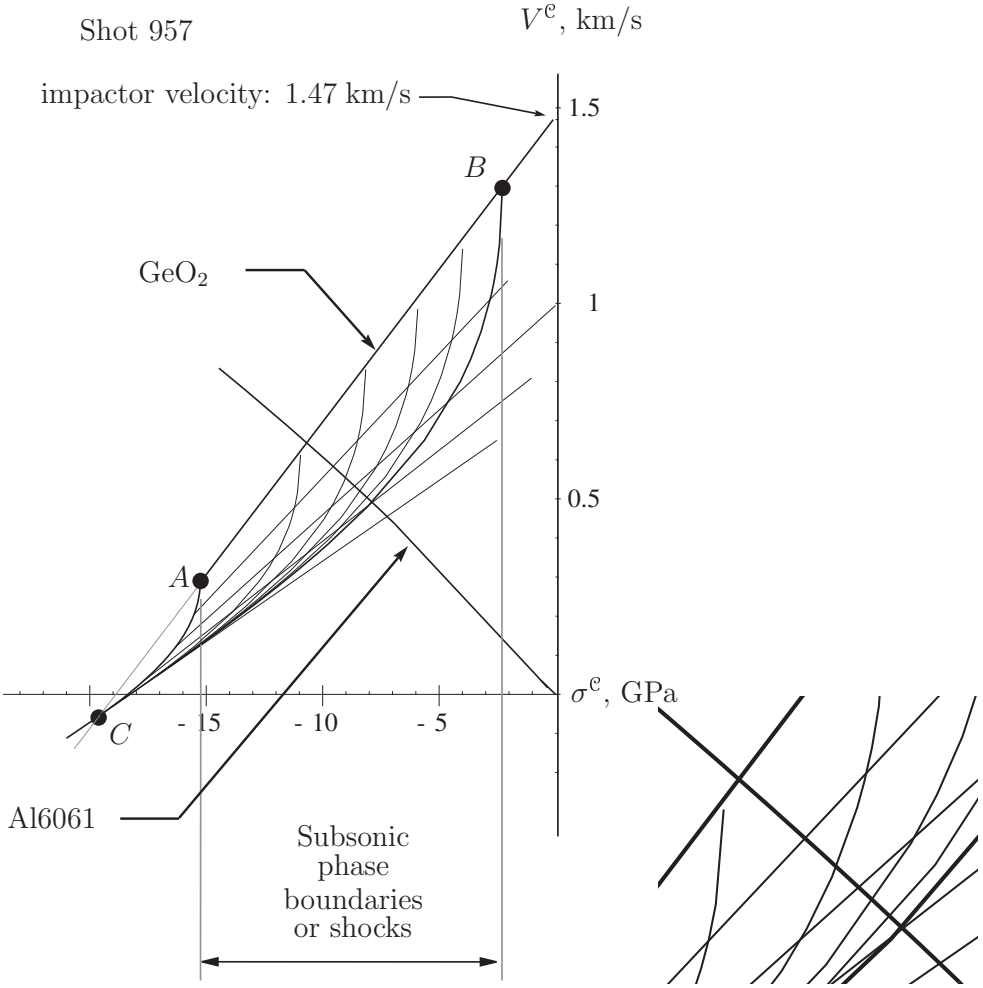

(a) Contact loci.

(b) Enlargement around the intersection of the loci.

Figure 7.14: The contact loci for the initial impact of Shot 957.

and it cannot generate the fans that the real high pressure phase does.

With our trilinear model, this spike is the result of a *tensile* wave that precedes the phase boundary initiated by the impact: see the stress and strain distributions in Figure 7.16(a). This expansive wave reflects as a compressive wave from the surface of the foam at its interface with the GeO_2, Figure 7.16(b). This compressive wave is partially transmitted into the high pressure phase of the GeO_2, Figure 7.16(c), and causes the increase in the predicted particle-velocity record at $t \approx 1.8$ μs. But the compressive wave also partially reflects back into the low pressure phase and then reflects again from the interface with the foam. When it again encounters the high pressure phase, it causes the increase in the predicted particle-velocity profile at $t \approx 2.1$ μs. At last, the phase boundary reaches the foam and the reflected signal from this event causes the large drop from this peak.

The dissipation-free kinetic relationship $\mathcal{F}_{31}(\dot{s}) = 0$ (not shown) produced similar results, though the increases in particle-velocity were much greater and occurred earlier.

If we were able to use a more realistic description of the high pressure phase of the GeO_2, and perhaps account for plasticity in the aluminum buffer, spikes like these might become less sharp and begin to resemble the experimental recording for Shot 965. If so, this would raise the intriguing possibility that an expansive wave can precede a compressive phase boundary. The author is unaware of any experimental evidence of this reported in the shock compression literature. Unfortunately, with only one experiment clearly showing this effect, and with our commitment to the present stress response models, further examination of this exciting possibility was deemed beyond the scope of this work.

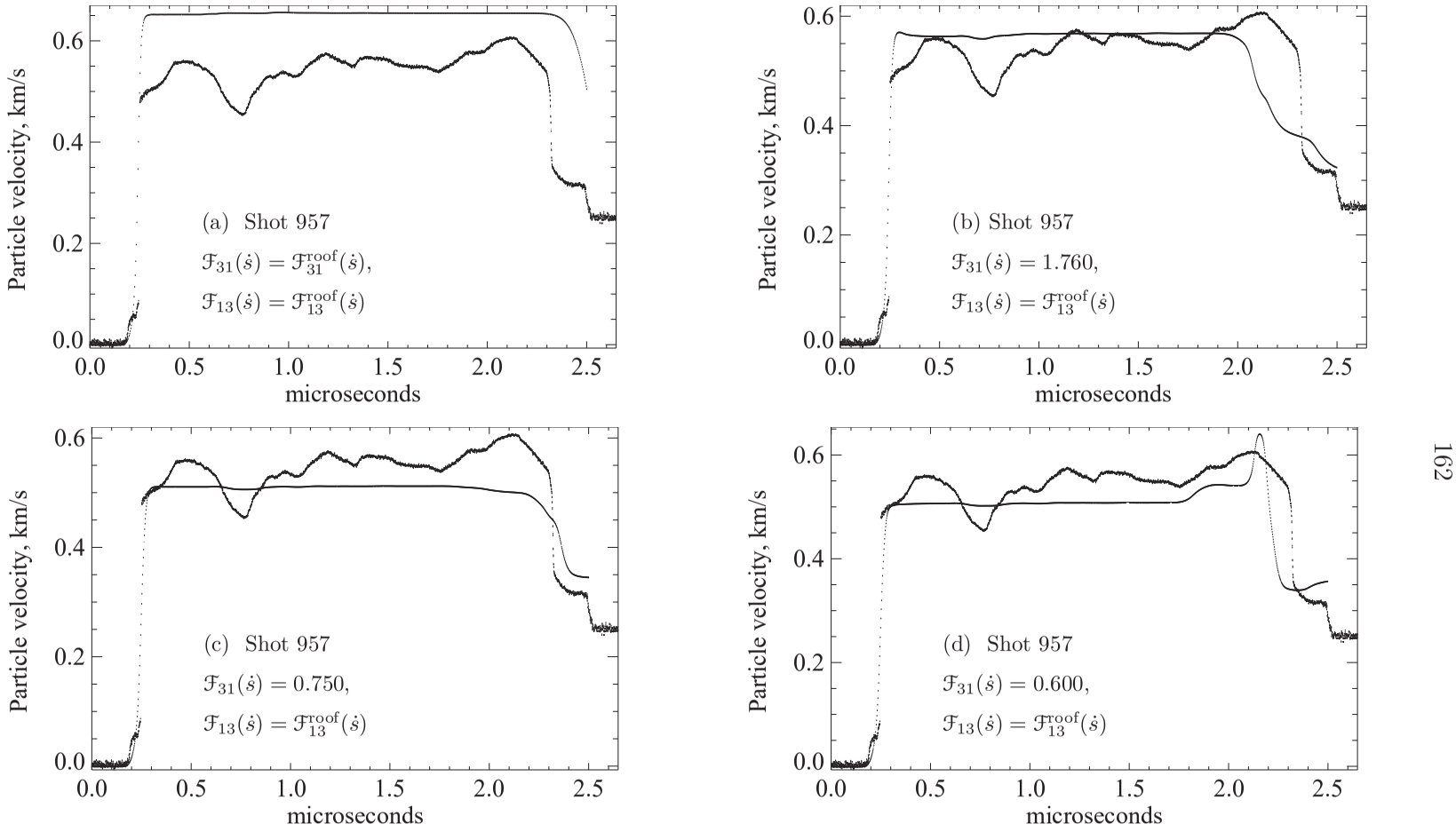

Figure 7.15: Predicted particle-velocity histories for Shot 957 using different kinetic relationships for the transformation from the low pressure phase to the high pressure phase.

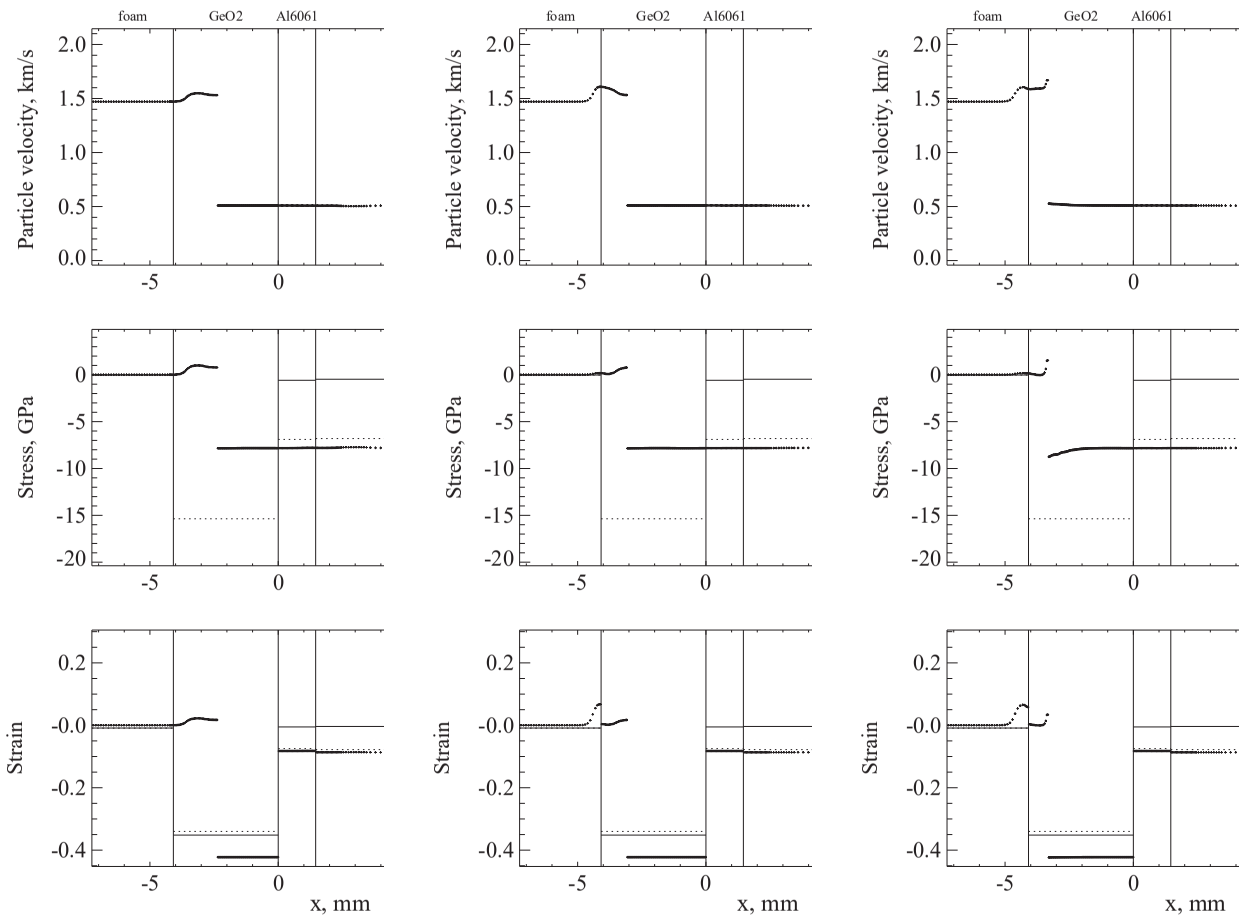

(a) $t = 1.010$ µs (b) $t = 1.313$ µs (c) $t = 1.414$ µs

Figure 7.16: Spatial distributions in Shot 957 with $\mathcal{F}_{31}(\dot{s}) = 0.600$, $\mathcal{F}_{31}(\dot{s}) = \mathcal{F}_{31}^{\text{roof}}(\dot{s})$, showing that the expansive wave ahead of the phase boundary is responsible for the increase in particle-velocity near the end of the VISAR profile.

7.5 Shot 958

Like the other two reverse shots, the intersection of the contact loci for the initial impact of Shot 958 is in the region ABC, and the contact locus of the aluminum crosses the AB boundary. Thus, once again, the impact produces a subsonic phase boundary when a critical driving traction f_{31}^c for nucleation that lies below some threshold value is prescribed, but not when the prescribed critical driving traction is above this threshold.

The contact locus of the aluminum crosses the AB boundary of the contact locus of GeO_2 between the curve of constant driving traction $f = 2.363$ GPa and the point A, where $f = \mathcal{F}_{31}(0^+) = 2.954$ GPa for this trilinear model. Thus, we know that the threshold value of the critical driving traction will be between these two values.

Since the contact locus of the aluminum cross the BC boundary of the contact locus for the GeO_2 between the two lines of constant phase boundary velocity $\dot{s} = 1.772$ km/s and $\dot{s} = 2.363$ km/s, we anticipate that the velocity of the fastest phase boundary that can be induced by the impact will be between these limits.

Simulations confirmed that the threshold value of the critical driving traction is in the range expected: the roof did not induce a phase transition, but all $\mathcal{F}_{31}(\dot{s}) = g_{31} \leq 2.690$ GPa did.

Figure 7.18 shows predicted particle-velocity histories for different forward kinetic relationships. As mentioned in Chapter 2, it was suspected that the flyer plate was fractured before impact in this experiment [106]. With this in mind, we will chose Figure 7.18(c) as the best fit to the experiment because both the predicted particle-velocity and duration of the plateau are similar to those of the experimental record.

The large spike that peaks at $t \approx 1.7$ μs in Figure 7.18(d)—like the spike of Figure 7.15(d) discussed in the previous section—is the result of a compressive wave that precedes the phase boundary. The second spike at $t \approx 2.3$ μs is caused by a partial reflection of the first spike back into the GeO_2 at the aluminum buffer. This partially reflected spike reverberates in the GeO_2 partially reflecting from

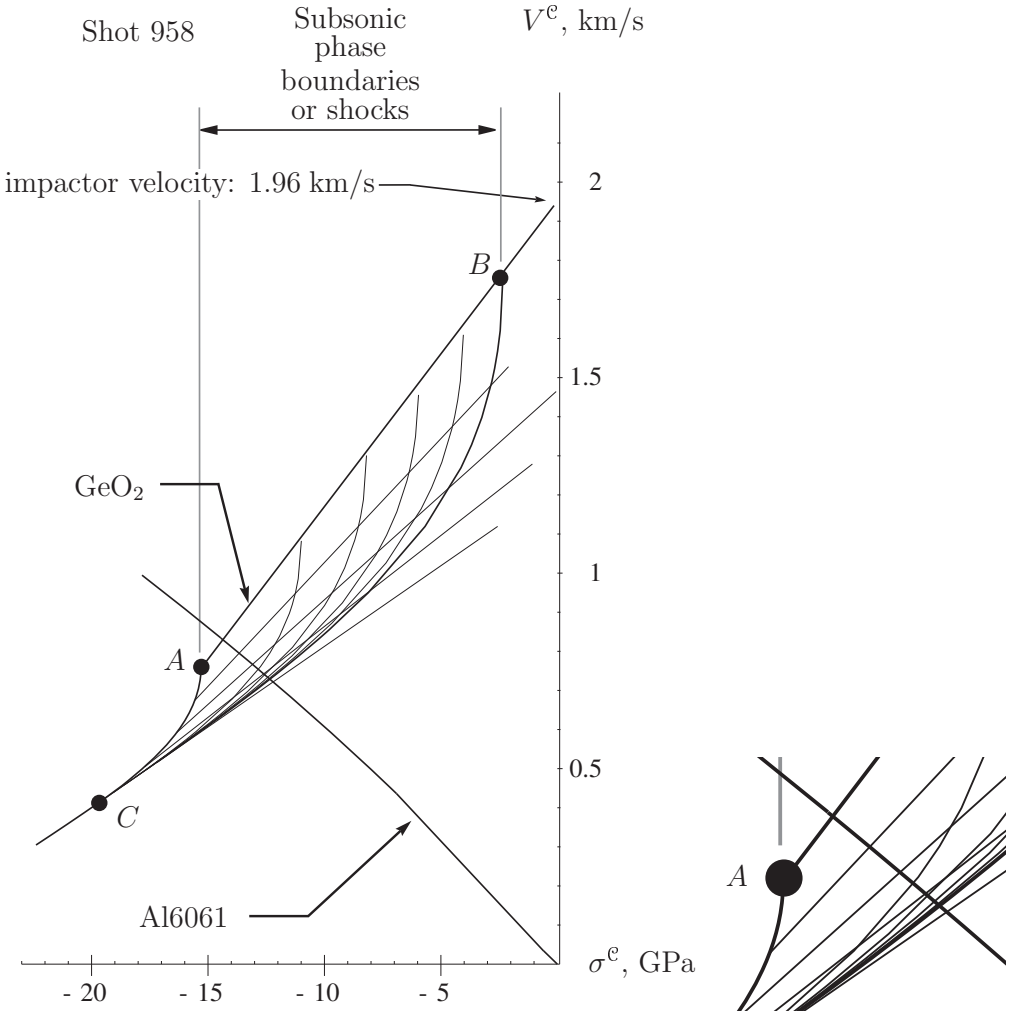

(a) Contact loci.

(b) Enlargement around the intersection of the loci.

Figure 7.17: The contact loci for the initial impact of Shot 958.

the interface between the foam and the GeO_2 then partially transmitting into the aluminum, generating the second spike. More spikes would appear if the simulation were carried out for a longer time, because the spike continues to reverberate from surface to surface within the GeO_2. Only one spike was seen in Figure 7.15(d): more would have appeared there too if the simulation had been carried out longer.

Figure 7.19 shows the predicted particle-velocity history when the kinetic relationship $\mathcal{F}_{13}(\dot{s})$ of the reverse transformation was varied with $\mathcal{F}_{31}(\dot{s}) = 1.760$ fixed for the forward transformation.

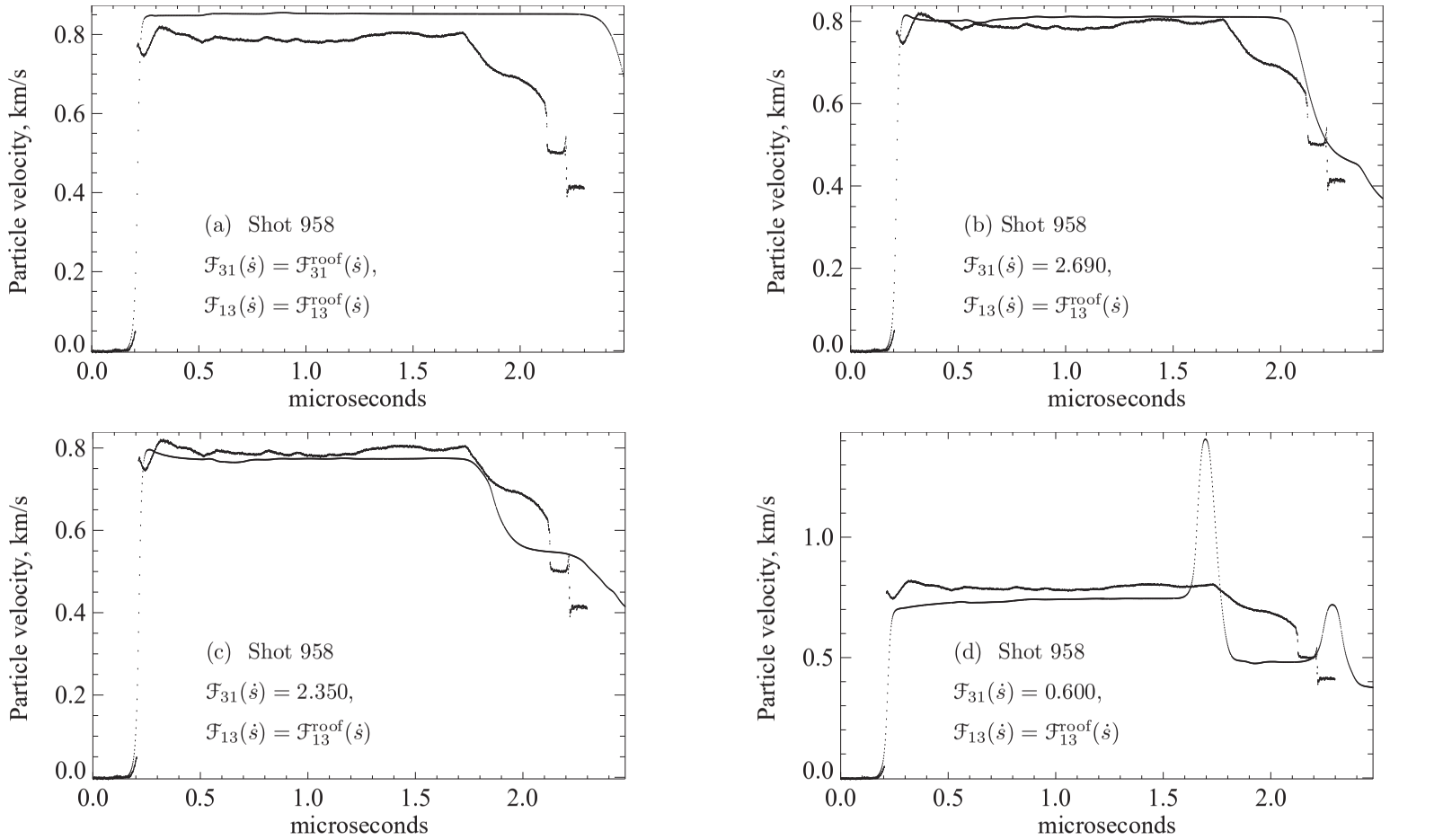

Figure 7.18: Predicted particle-velocity histories for Shot 958 using different kinetic relationships for the transformation from the low pressure phase to the high pressure phase.

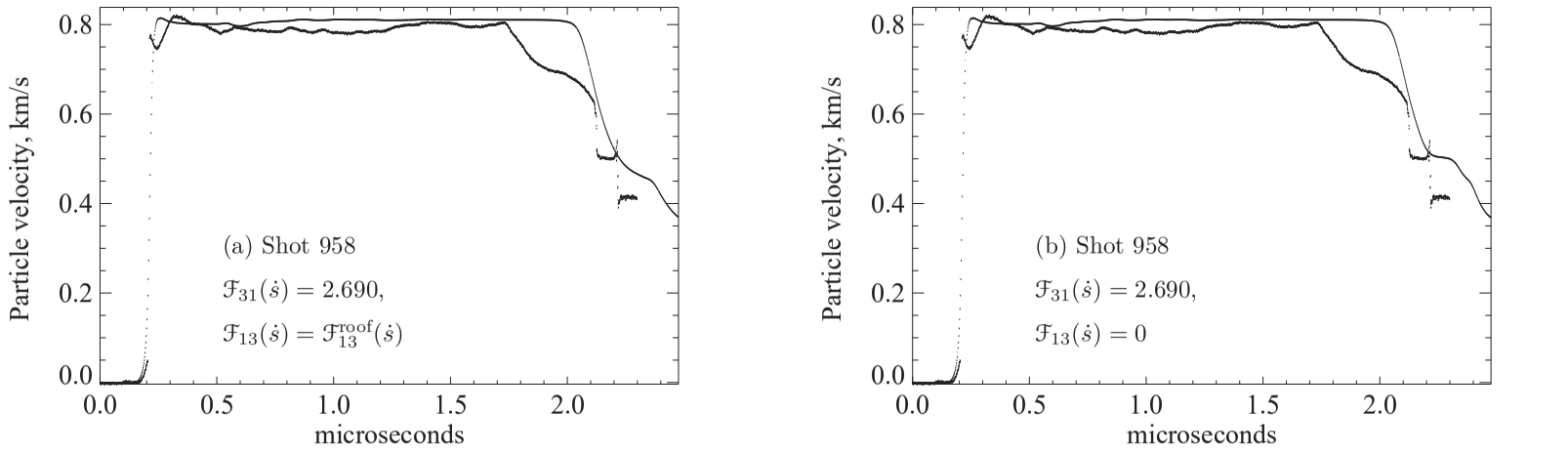

Figure 7.19: Predicted particle-velocity histories for Shot 958 using different kinetic relationships for the transformation from the high pressure phase to the low pressure phase. Slight differences appear for $t > 2.1$ μs.

7.6 Kinetic relations with non-constant dependence on phase boundary velocity

This section describes efforts, only partially successful, to prescribe kinetic relationships with a linear dependence on the phase boundary velocity in simulations.

7.6.1 A linear kinetic relation derived from the best predictions of the shots

We would like to prescribe a forward kinetic relationship with a linear dependence on $\dot{s}$, namely $\mathcal{F}_{31}(\dot{s}) = g_{31} + h_{31}\dot{s}$ where $h_{31} \neq 0$. We will select the parameters g_{31} and h_{31} from the four simulations of Shots 953, 965, 957 and 958 that gave the best match to the VISAR records. We cannot use Shot 955 here because simulations for this shot predicted a supersonic rather than a subsonic phase boundary.

With the possible exception of Shot 965, it is difficult to select the best predictions for these shots. All of the predictions for Shot 953 are poor, at least in part because of the limitations imposed by the linear stress-strain relationship in our model's high pressure phase. In the high velocity reverse experiments, Shots 957 and 958, the GeO_2 flyer plate was suspected of being fractured before impact, and the VISAR records may not represent uniaxial deformation.

Nonetheless, let us boldly dare to suggest that the best simulations are depicted in Figures 7.6(d), 7.9(b), 7.15(b) and 7.18(c): the reason each was picked is described in the section for that shot.

With the help of the Riemann solvers in our program, we can find the velocity $\dot{s}$ of the phase boundary nucleated at impact for each of these simulations. Furthermore, since the prescribed kinetic relationship had no dependence on $\dot{s}$ for each of these simulations, we know that the driving traction on each phase boundary was the prescribed $f = g_{31}$. Table 7.1 summarizes the $(\dot{s},\ f)$ pairs for these simulations.

A straight line was fit to these $(\dot{s},\ f)$ pairs by the least-squares method, resulting in the expression $f = 0.76 + 0.582\dot{s}$. But we are not interested in this kinetic

Shot	$\lvert f \rvert$, GPa	$\lvert \dot{s} \rvert$, km/s
965	0.6	0.119
957	1.76	1.309
958	2.350	2.233
953	2.275	3.119

Table 7.1: Driving traction and propagation velocity of the subsonic phase boundary induced by impact in the "best" simulations.

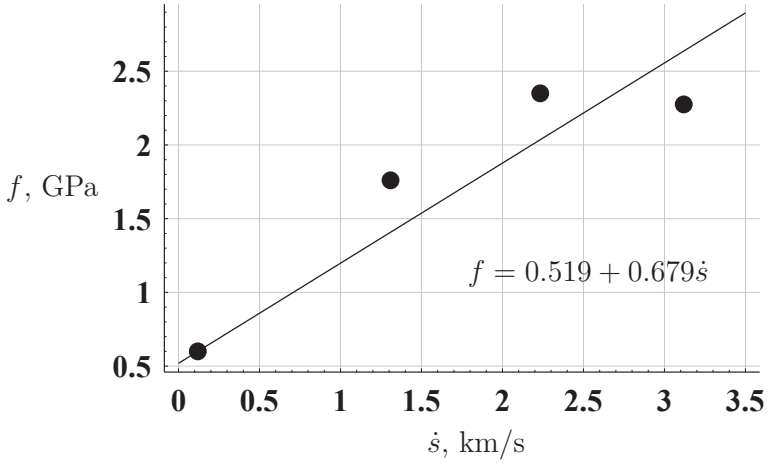

Figure 7.20: Least squares fit to the driving traction and propagation-velocity pairs of the subsonic phase boundary induced by impact in the best simulations, with the constraint the line must pass through ($\dot{s}$, f) pair for Shot 965. In order of increasing $\dot{s}$, the points shown are from Shots 965, 957, 958, and 953.

relationship because it will not allow a phase boundary to nucleate in Shot 965. So it was decided that another line should be chosen to fit the data points. This was accomplished by forcing the line to pass through the ($\dot{s}$, f) pair for Shot 965, and choosing its slope by a least squares fit to the remaining ($\dot{s}$, f) pairs. This resulted in the expression $f = 0.519 + 0.679\dot{s}$, as shown in Figure 7.20. This expression was then prescribed as the linear kinetic relation for a simulation of each shot. The unexpected result was the production of oscillations in particle velocity, stress

and strain behind the subsonic phase boundary predicted for each shot. These oscillations were clearly non-physical, as they appeared before the phase boundary encountered any disturbance, Figure 7.21. As foretold in Section 6.1.2, the result was disastrous: the oscillations caused spurious phase boundaries to nucleate, the time-steps decreased and the program became so slow that even Methuselahs might have given up hope of seeing them complete. The simulations were aborted.

Non-physical oscillations and spurious phase transitions: a brief investigation

Having encountered the non-physical oscillations and the disastrous phase transitions they nucleate, several other linear kinetic relationships, fit to various subsets of the $(\dot{s},\ f)$ pairs of Table 7.1 were formulated and prescribed in simulations in the hopes that the difficulties would somehow be avoided. For all of these kinetic relations, the program predicted that a subsonic phase boundary nucleated upon impact for Shots 953, 957, and 958. For some of these kinetic relations, no phase boundary was predicted in Shot 965, and the simulation of this shot was halted if no phase boundary appeared.

Of the kinetic relations tested, there were a few for which the program ran to completion with no difficulty for Shot 953. For a subset of these, the program also ran to completion for Shot 958. In all simulations of Shot 957 and 965 in which a phase boundary was predicted, the time-steps became very small, and the decision was made to stop the simulation.

Since no problems of this sort were encountered for any kinetic relation of the form $\mathcal{F}_{31}$ = constant, the suspicion arose that the oscillations and spurious phase boundaries might be related to the coefficient h_{31} in the kinetic relation $\mathcal{F}_{31}(\dot{s}) = g_{31} + h_{31}\dot{s}$. So a sensitivity study was conducted holding g_{31} fixed while varying h_{31} for simulations of Shots 953, 957, and 958. The constant $g_{31} = 1.49$ was chosen: this is its value in a least-squares fit of the linear kinetic relation to the $(f,\ \dot{s})$ pairs of Table 7.1 for Shots 953, 957, and 958.

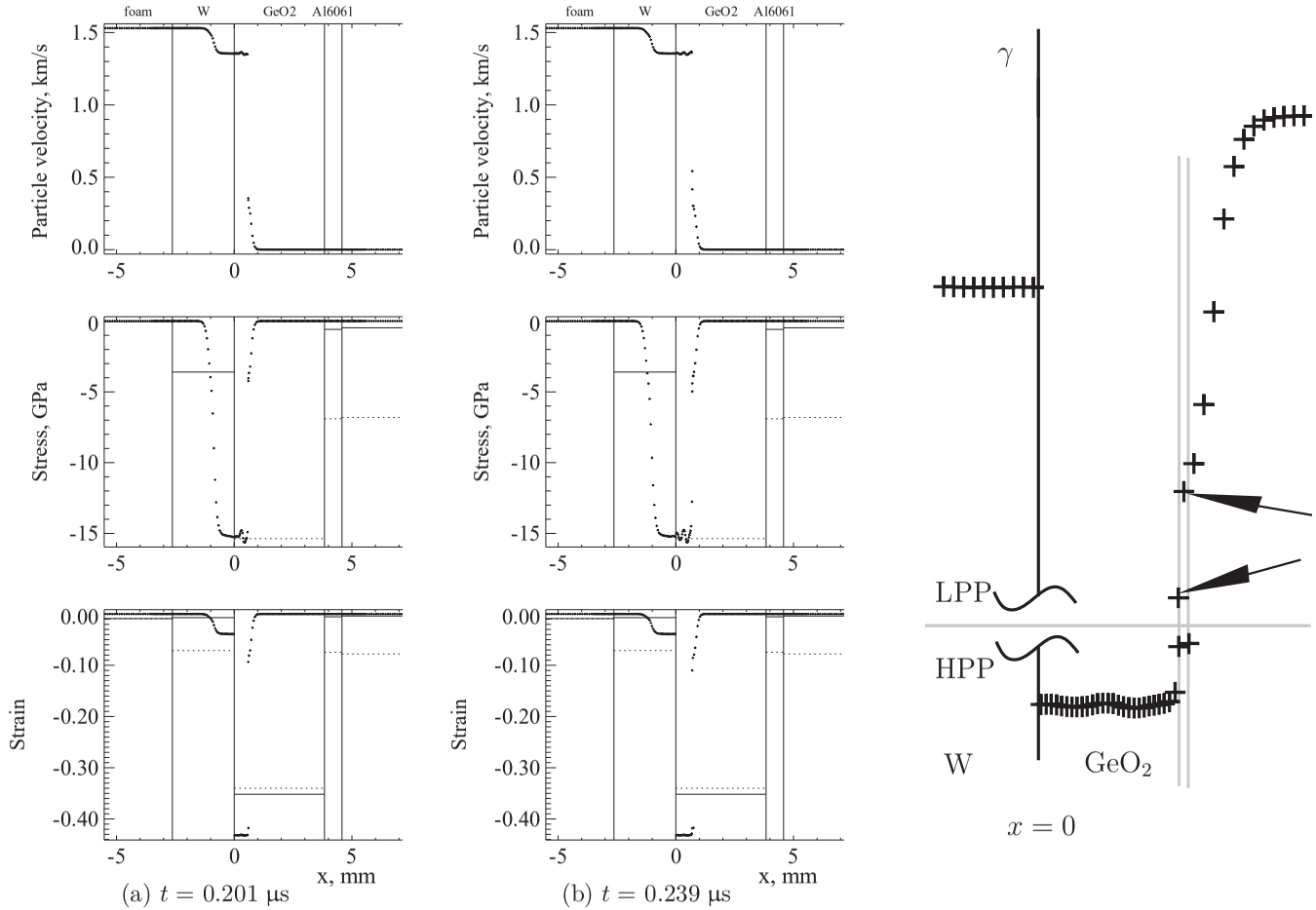

(a) $t = 0.201$ μs (b) $t = 0.239$ μs

Figure 7.21: Oscillations and spurious phase transitions in simulation of Shot 953 for kinetic relation of Figure 7.20. (a) Oscillations, between $x = 0$–0.6 mm, are most visible in the stress frame. Nucleation of low pressure phase from high pressure phase is imminent. (b) Oscillations are more pronounced. Spurious phase boundaries have nucleated, seen in the enlargement. Enlargement shows strains near the analytical phase boundary: the middle portion of the strain axis has been removed. Arrows point to isolated and non-adjacent cells of the LPP.

The sensitivity study supported this suspicion: time-step problems appeared at early times for h_{31} "large enough," but not for h_{31} "small enough," Figure 7.22. Furthermore, the value of h_{31} above which this time-step problem appeared was smallest for Shot 957—the least intense of these shots—and greatest for Shot 953—the most intense of these shots. Oscillations producing spurious phase boundaries are suspected in all instances where time-steps became small for h_{31} "large enough."

The cause of these oscillations has not yet been determined, although there is reason to suspect that they may be related to the specified precision to which a root is found in the various root-finding routines.

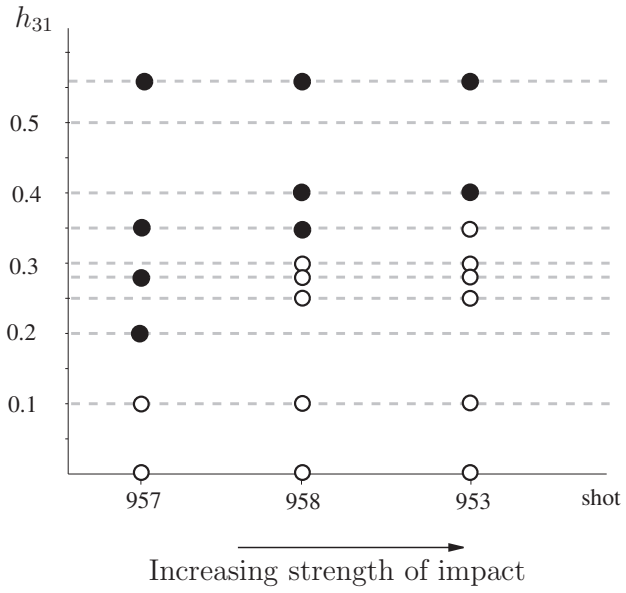

Figure 7.22: Results of the sensitivity study described in the text suggest that spurious phase boundaries caused by the spatial oscillations occur for sufficiently large values of the coefficient h_{31}. The kinetic relation tested was $\mathcal{F}_{31}(\dot{s}) = 1.49 + h_{31}\dot{s}$. Filled circles indicate values of h_{31} for which spurious phase boundaries of the type shown in Figure 7.21 appeared, open circles indicate values of h_{31} for which these spurious phase boundaries did not appear.

Predictions from successful simulations

Predictions from simulations of Shots 953, 957, and 958 that *did* run to completion with a non-zero h_{31} were very similar to predictions from simulations with $h_{31} = 0$, provided the comparison is between simulations that predict identical short-time results near the interface prior to any wave reflections. This was anticipated because in these shots, the phase boundary is typically predicted to propagate largely undisturbed for much of the time. In the absence of a disturbance, the phase boundary velocity remains constant, providing no demonstration of the kinetic relationship's dependence on phase boundary velocity. In a typical example, Figure 7.23, the predicted particle-velocity histories are visually indistinguishable.

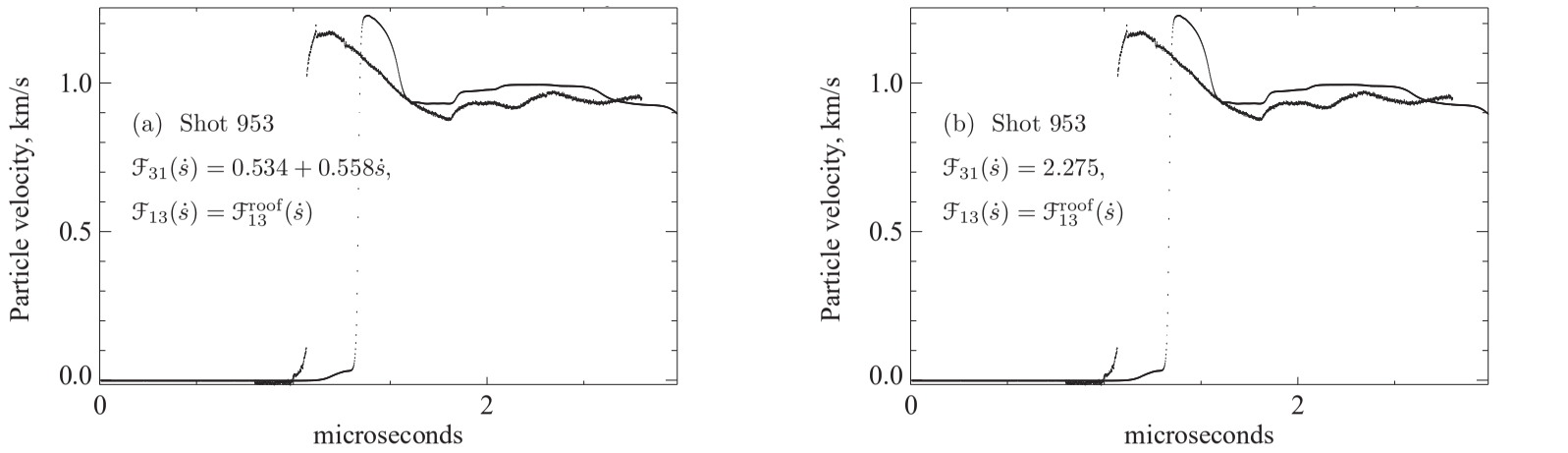

Figure 7.23: Comparison between predicted particle-velocity histories of Shot 953 using a forward kinetic relation with a dependence on the phase boundary velocity and one with no dependence on the phase boundary velocity. The results are very similar because the short-time solution to the impact problem was very nearly identical for these two kinetic relations. This was by design: the kinetic relationship in (a) intersects the $(\dot{s},\, f)$ pair given in Table 7.1 for this shot, which are from the simulation that produced (b).

7.7 A change to the GeO_2 model to force reverse phase changes

The high pressure phase of the model we have been using can exist in tension up to $\sigma_M =$ 48.86 GPa. This makes it difficult for a transition from the high pressure phase to the low pressure phase to nucleate. We can force this reverse phase change by decreasing σ_M sufficiently. Here we modify our model for GeO_2 by choosing γ_M =-0.41525, σ_M = -1.908 GPa to force a reverse phase change in the simulation of Shot 955.

Prescribing a reverse kinetic relationship $\mathcal{F}_{13}(\dot{s}) = 0.050$, this modified trilinear model caused the low pressure phase to nucleate from the high pressure phase at the interface between the tungsten and the GeO_2 when a release wave from the tungsten-foam interface reached the GeO_2. The predicted particle velocity profile is shown in Figure 7.24.

The low pressure phase first nucleated from the high pressure phase sometime between t = 1.20–1.25 μs, and disappeared between t = 1.76–1.81 μs, Figure 7.25. (Spatial distributions are saved at increments of $\Delta t \approx$0.05μs, so times are not known more precisely. It is even possible that a forward and reverse transformation could be entirely missed in this interval.) The low pressure phase never occupied more than one cell in the computations: its maximum width could not have exceeded 0.1 mm. Yet the prediction of particle velocity is clearly affected by this thin interval of material in the low pressure phase, as we see by comparing Figures 7.24(a) and 7.24(b).

Because of the limited fidelity of our trilinear model, we make no judgement on whether Figure 7.24(a) or Figure 7.24(b) is a better match to the experimental record. Rather, we comment that, given a predicted or actual particle-velocity record, one might be hard-pressed to recognize the manifestation of a reverse phase transformation in that record if Figure 7.24(a) is any indication of the surprises we might encounter.

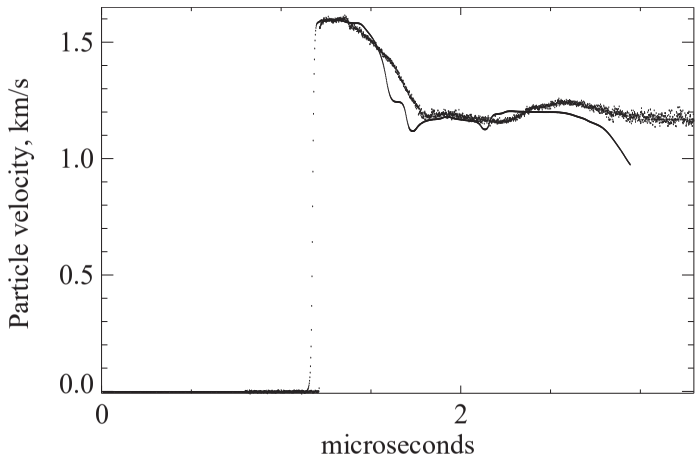

(a) Predicted particle-velocity history using the modified trilinear model. A reverse phase transition was predicted to nucleate, but the newly produced low pressure phase survived no more than 0.611 μs before fully transforming back to the high pressure phase. The prescribed kinetic relations were $\mathcal{F}_{31}(\dot{s}) = \mathcal{F}_{31}^{\text{roof}}(\dot{s})$, $\mathcal{F}_{13}(\dot{s}) = 0.050$.

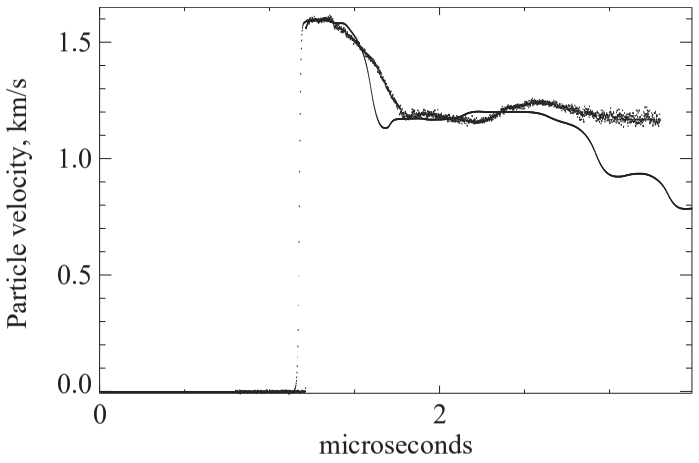

(b) Prediction with original trilinear model. No reverse phase transformation occurred.

Figure 7.24: Predicted particle-velocity history for Shot 955. (a) With the modified trilinear model a reverse phase transformation occurred, versus (b) no reverse phase transformation with the original trilinear model.

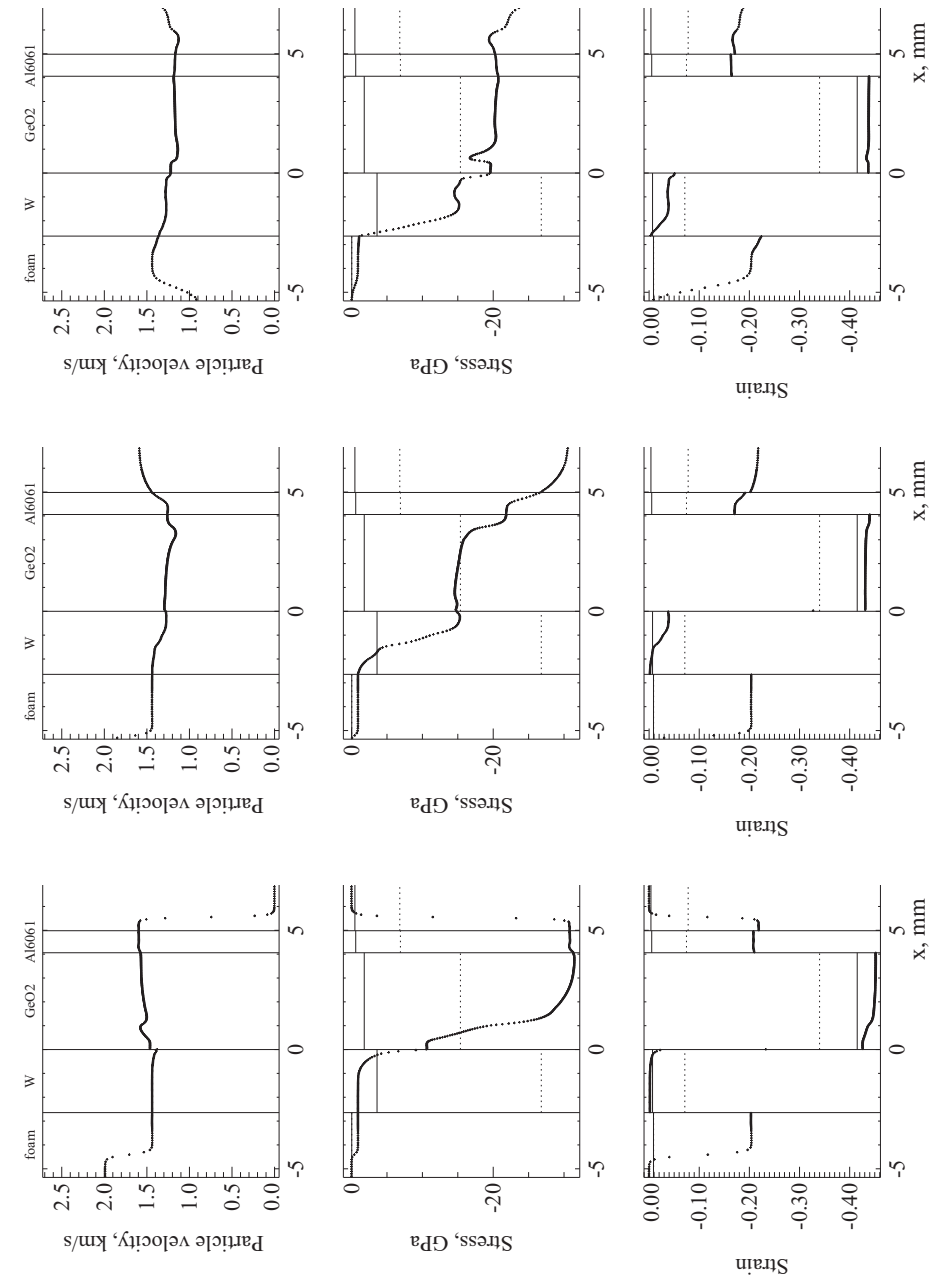

(a) $t = 1.254$ µs (b) $t = 1.558$ µs (c) $t = 1.810$ µs

Figure 7.25: Spatial distributions showing that the low pressure phase has nucleated from the high pressure phase. (a) The low pressure phase has just nucleated: it occupies one cell next to the tungsten at $\gamma = -0.21$. (b) The low pressure phase occupies the same cell at $\gamma = -0.32$. (c) The low pressure phase has just disappeared.

7.8 A change to the GeO_2 model to suppress phase changes

We have seen predictions with no phase change for the reverse shots, but the impact conditions of the forward shots necessarily nucleate phase boundaries with the trilinear model we have been using. To satisfy our curiosity about what the predicted results of these shots would be with no phase change, we must modify the trilinear model.

To completely suppress the possibility of phase boundaries in Shots 953 and 955, we extend the low pressure phase and force the high pressure phase closer to $\gamma = -1$. Our new model is:

$$\rho_\circ = 3.629 \text{ g/cm}^3 \tag{7.1}$$

$$\hat{\sigma}(\gamma)[\text{GPa}] = \begin{cases} \text{undefined} & \text{for } \gamma < -0.95 \text{ ,} \\ \hat{\sigma}_1(\gamma) = 550\gamma + 472.5 & \text{for } -0.95 \leq \gamma \leq -0.85 \text{ ,} \\ \hat{\sigma}_2(\gamma) = -823.2\gamma - 694.72 \text{ ,} & \text{for } -0.85 < \gamma < -0.8 \text{ ,} \\ \hat{\sigma}_3(\gamma) = 45.2\gamma \text{ ,} & \text{for } -0.8 \leq \gamma \leq 100.0, \\ \text{undefined} & \text{for } \gamma > 100.0 \text{ .} \end{cases} \tag{7.2}$$

This model lengthens the shock locus of the low pressure phase in the σ, V plane. It also moves the point B of the region ABC to a much lower stress: the Maxwell stress, where B lies, is $\sigma_\circ$ = -25.3 GPa. This makes it impossible to nucleate a phase boundary upon impact in *any* of the shots, regardless of the nucleation criterion used for the GeO_2.

Figure 7.26 shows the predictions for Shots 953 and 955 using this model. As expected, the simulations produced no phase boundaries. The match to the experimental record is poor.

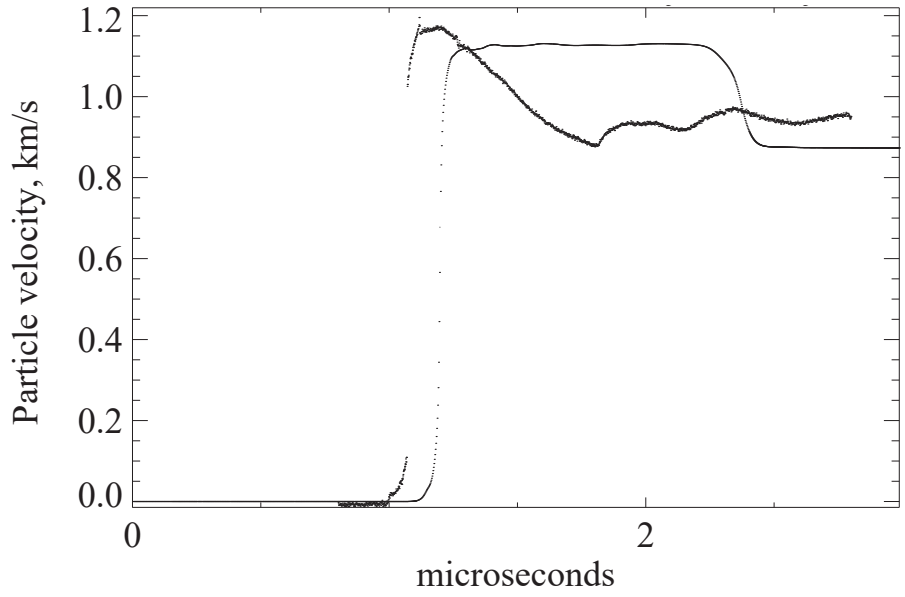

(a) Shot 953.

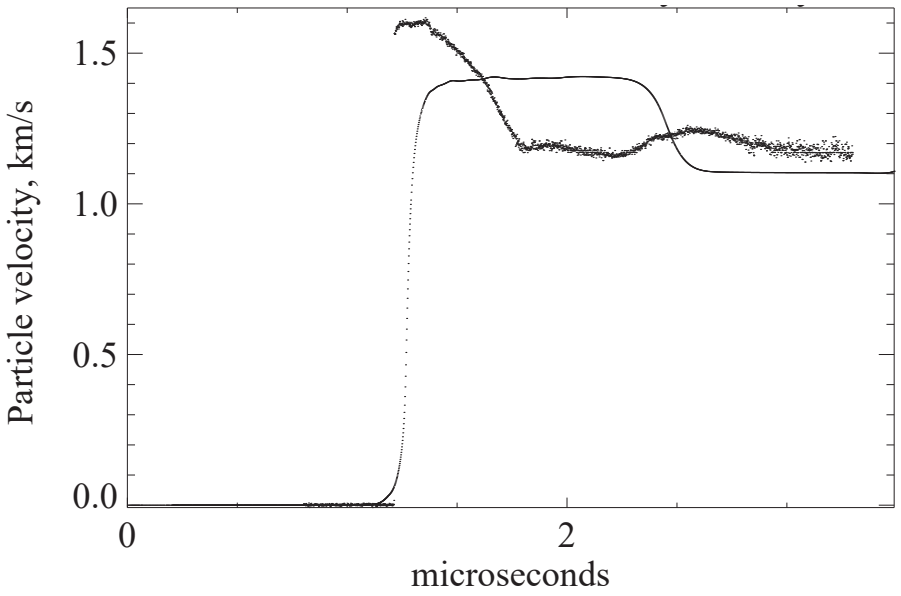

(b) Shot 955.

Figure 7.26: Particle-velocity predictions for Shots 953 and 955 when the trilinear model is modified to prevent any transformation to the high pressure phase.

Chapter 8

Closing remarks

The theories of Abeyaratne and Knowles have been applied in a finite-difference algorithm to examine impact experiments on GeO_2, a material known to experience a phase transformation under compression.

Simple constitutive models based on finite elasticity were developed to describe the response of the materials to one-dimensional deformation. The trilinear model used for the GeO_2 is incapable of developing fans, and this made it impossible for simulations to reproduce certain notable features of the experimental records. Despite this limitation, the simulations were able to reproduce many of the dominant features of the experimental records. This perhaps is the most remarkable finding: that—without accounting for important phenomena like thermal effects or plasticity, and even lacking the capability to develop fans in the material we are studying—these very simple models perform as well as they do.

When a subsonic phase boundary is nucleated within the GeO_2 during a simulation, the predictions become very sensitive to the kinetic relations that are prescribed to govern the propagation of the phase boundary. The kinetic relations can be tuned to best match the experimental record. The forward kinetic relation tends to dominate the predictions, the influence of the reverse kinetic relation appearing later in time.

The theories of Abeyaratne and Knowles appear to offer a plausible description of the experiments. Their performance would likely improve if the curvature known

to exist in the stress-response function of the high-pressure phase of the GeO_2 were introduced. It is not that surprising that these theories should do well: many results in the shock compression literature have been explained with assumptions that are special cases of a kinetic relationship, though they are not always recognized as such. Utilizing a broader definition of a kinetic relationship that encompasses these special cases can only improve the explanation of the results.

The numerical method developed in this work makes no use of adaptive meshing nor of sub-cycling in time. These techniques would greatly reduce the computational time of the simulations, and allow more practical analysis of certain problems associated with very slow phase boundaries. Their use is strongly recommended for future work.

Appendix A

Fundamentals of discontinuities and fans

This appendix presents some fundamental relationships for discontinuities and fans in our setting of one-dimensional strain for an elastic material.

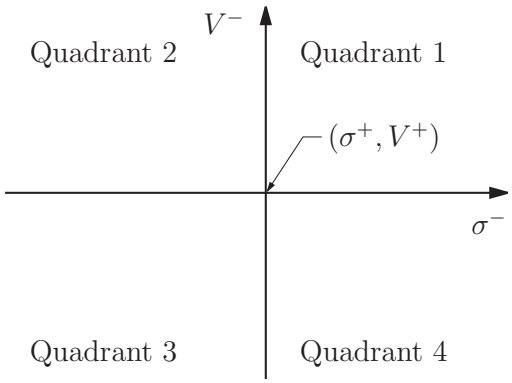

Figure A.1: The σ, V plane. Quadrants are labeled relative to the front state coordinates, (σ^+, V^+).

We shall seek the loci of states available behind a *single* discontinuity or fan for a fixed front state. The front state is denoted (γ^+, V^+, σ^+), and the back state is (γ^-, V^-, σ^-). Results are represented in a σ, V plane depicting the available (V^-, σ^-) pairs behind the discontinuity or fan, Figure A.1.

Stress, σ, is plotted in the horizontal direction, increasing from left to right. Particle velocity, V, is plotted in the vertical direction, increasing from bottom to top. References to *the quadrants* of the σ, V plane indicate the quadrants relative

to the point (σ^+, V^+).

A.1 Relations for discontinuities

Consider a discontinuity in an elastic material.

Eliminating $[\![V]\!]$ from the jump conditions, (3.38) and (3.39), we have

$$W^2 = \frac{[\![\sigma]\!]}{\rho_\circ [\![\gamma]\!]} \ . \tag{A.1}$$

Requiring W to be a real number necessitates that

$$\text{sign}\,([\![\sigma]\!]) = \text{sign}\,([\![\gamma]\!]) \ . \tag{A.2}$$

Also by the jump conditions, we have

$$\text{sign}\,([\![V]\!]) = -\text{sign}\,(W[\![\sigma]\!]) \ . \tag{A.3}$$

If the front state stress and particle velocity, σ^+ and V^+ are given, equation (A.3) prescribes that a pair of $\sigma \cdot V$ quadrants are accessible across any single discontinuity, Figure A.2. For a discontinuity moving to the left, (σ^- ,V^-) can lie in quadrants 1 or 3. For a discontinuity moving to the right, (σ^-, V^-) can lie in quadrants 2 or 4.

Eliminate W from the jump conditions and solve for V^-. We have

$$V^- = V^+ + \text{sign}\,(W[\![\sigma]\!])\,\frac{1}{\sqrt{\rho_\circ}}\sqrt{[\![\sigma]\!][\![\gamma]\!]}\ , \tag{A.4}$$

where (A.3) was used to determine the sign of the radical.

For the remainder of this section, assume that the phase behind the discontinuity is in some phase i, which is not spinodal over a range of strain, $\gamma_I < \gamma < \gamma_J$:

$$\hat{\sigma}\,'_i(\gamma) \geq 0 \quad \text{for } \gamma_I < \gamma < \gamma_J \ . \tag{A.5}$$

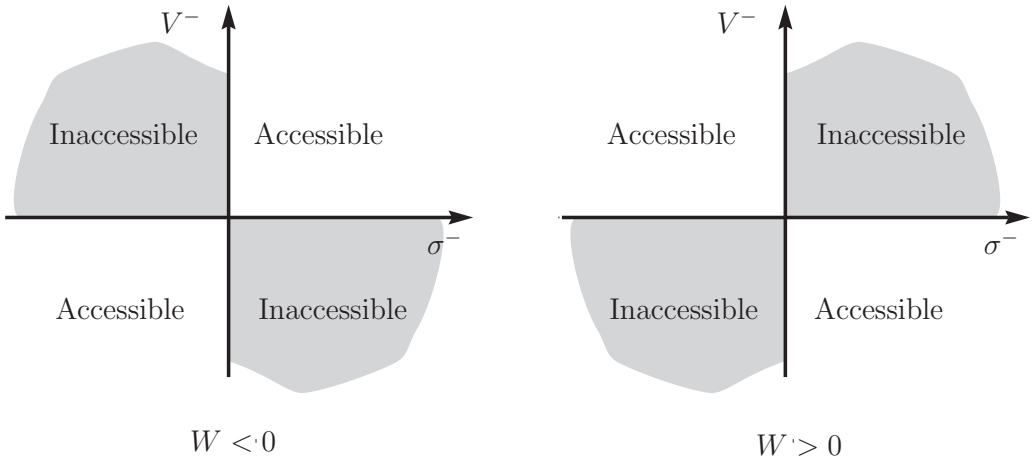

Figure A.2: Odd quadrants are accessible behind a discontinuity traveling to the left ($W < 0$), even quadrants are accessible behind a discontinuity traveling to the right ($W > 0$).

The phase behind the discontinuity need not be the same as that ahead of it: the following applies to shocks or phase boundaries.

Label the stresses at γ_I and γ_J by

$$\sigma_I = \hat{\sigma}_i(\gamma_I) \,, \qquad \sigma_J = \hat{\sigma}_i(\gamma_J) \,. \tag{A.6}$$

The expression $\hat{\sigma}_i(\gamma)$ is invertible, and we let $\hat{\gamma}_i(\sigma)$ be its inverse. We have

$$\hat{\gamma}_i'(\sigma) \geq 0 \quad \text{for } \sigma_I < \sigma < \sigma_J \,, \tag{A.7}$$

$$\hat{\gamma}_i''(\sigma) = -\hat{\sigma}_i''(\gamma) \,. \tag{A.8}$$

Consider how V^- and σ^- are related for a fixed front state, $(\gamma^+, \sigma^+, V^+)$, when γ^- lies in our non-spinodal phase i. Equation (A.4) can be written as a function of the back state stress, σ^-:

$$\hat{V}(\sigma^-) = V^+ + \operatorname{sign}\left(W[\![\sigma]\!]\right) \frac{1}{\sqrt{\rho_\circ}} \sqrt{[\![\sigma]\!]\left(\gamma^+ - \hat{\gamma}_i(\sigma^-)\right)} \,. \tag{A.9}$$

Examining the derivatives of $\hat{V}(\sigma^-)$ gives insight into its behaviour. Letting $'$ denote differentiation with respect to σ^-,

$$\hat{V}\,'(\sigma^-) = \text{sign}\,(W[\![\sigma]\!])\,\frac{1}{2\sqrt{\rho_\circ[\![\sigma]\!][\![\gamma]\!]}}([\![\sigma]\!]'[\![\gamma]\!] + [\![\sigma]\!][\![\gamma]\!]') \ . \tag{A.10}$$

But,

$$[\![\sigma]\!]' = (\sigma^+ - \sigma^-)' = -1 \ , \quad [\![\gamma]\!]' = (\gamma^+ - \hat{\gamma}_i(\sigma^-))' = -\hat{\gamma}_i\,'(\sigma^-) \ .$$

Equation (A.10) becomes,

$$\hat{V}'(\sigma^-) = \text{sign}\,(W[\![\sigma]\!])\,\frac{1}{2\sqrt{\rho_\circ[\![\sigma]\!][\![\gamma]\!]}}\left([\![\gamma]\!] + [\![\sigma]\!]\hat{\gamma}_i\,'(\sigma^-)\right) \ . \tag{A.11}$$

Considering the sign of this expression, we have

$$\text{sign}\left(\hat{V}\,'(\sigma^-)\right) = -\text{sign}\,(W) \ , \tag{A.12}$$

where (A.2) and (A.5) were utilized to arrive at this.

For a given front state, (A.12) implies that $\hat{V}(\sigma^-)$ is monotonically increasing for left-traveling discontinuities ($W < 0$), and monotonically decreasing for right-traveling discontuities ($W > 0$). Thus, for a discontinuity traveling in a prescribed direction, if the material behind the discontinuity is in a non-spinodal phase, then specifying σ^- or V^- selects a unique solution in that phase if the solution exists.

A.2 Relations for fans

A *fan* is a similarity solution which satisfies the continuity and momentum conditions where fields are smooth.

A fan may occur between two strains, γ^+ and γ^-, in the same non-spinodal phase, provided there is no inflection point of $\hat{\sigma}(\gamma)$ between γ^+ and γ^-. Inflections

at γ^+ and/or γ^- are allowed.

Again consider a material in a fixed front state, (γ^+, σ^+, V^+). What can we determine about the $\sigma \cdot V$ pairs that can be achieved behind a fan that passes through the material?

Seek similarity solutions to (3.36)–(3.37) by letting $\xi = x/t$ and substituting $\hat{\gamma}(\xi) = \gamma(x,t)$, $\hat{V}(\xi) = V(x,t)$. Equations (3.36) and (3.37) become

$$V_\xi + \xi\gamma_\xi = 0 \,, \tag{A.13}$$

$$\rho_\circ \xi V_\xi + \sigma_\gamma \gamma_\xi = 0 \,. \tag{A.14}$$

Solving for the slope of the characteristics,

$$\xi = \pm\sqrt{\frac{\hat{\sigma}\,'(\gamma)}{\rho_\circ}} \,, \tag{A.15}$$

where the sign is positive for fans propagating in the $+x$ direction, and negative for fans propagating in the $-x$ direction. In what follows, *we keep track of the sign by reserving the upper position for fans propating to the* $+x$ *direction, and the lower position for fans propagating to the* $-x$ *direction.*

The front of the fan and the back of the fan propagate with the respective velocities

$$\xi^+ = \pm\sqrt{\frac{\hat{\sigma}\,'(\gamma^+)}{\rho_\circ}} \,, \qquad \xi^- = \pm\sqrt{\frac{\hat{\sigma}\,'(\gamma^-)}{\rho_\circ}} \,. \tag{A.16}$$

By (A.13) and (A.15),

$$\int_{\xi^+}^{\xi^-} V_\xi d\xi = \mp\frac{1}{\sqrt{\rho_\circ}} \int_{\xi^+}^{\xi^-} \sqrt{\sigma_\xi}\gamma_\xi d\xi \,.$$

Integrating the left side, and eliminating ξ on the right,

$$V^- - V^+ = \mp \frac{1}{\sqrt{\rho_\circ}} \int_{\gamma^+}^{\gamma^-} \sqrt{\hat{\sigma}\,'(\gamma)} d\gamma \; . \tag{A.17}$$

Since we are working within a non-spinodal phase, $\hat{\sigma}(\gamma)$ can be inverted to provide $\hat{\gamma}(\sigma)$, and (A.17) can be considered to provide V^- as a function of σ^- for a fixed front state. Denoting this function $\hat{V}(\sigma)$, and using the chain rule to differentiate it with respect to σ^-,

$$\hat{V}\,'(\sigma^-) = \mp \frac{\sqrt{\hat{\gamma}\,'(\sigma^-)}}{\sqrt{\rho_\circ}}. \tag{A.18}$$

Of course,

$$\text{sign}\left(\hat{V}\,'(\sigma^-)\right) = \mp 1. \tag{A.19}$$

Recalling that the upper sign is for fans propagating to the right, and the lower sign is for fans propagating to the left, we have that quadrants 2 and 4 are accessible to a right-traveling fan, quadrants 1 and 3 are accessible to a left-traveling fan, and V^- is monotonically related to σ^-.

We can establish the curvature of the loci back states for a fixed front state. Differentiating (A.18),

$$\hat{V}\,''(\sigma^-) = \mp \frac{\hat{\gamma}\,''(\sigma)}{2\sqrt{\rho_\circ \hat{\gamma}\,'(\sigma)}} \; . \tag{A.20}$$

The sign of this expression becomes

$$\text{sign}\left(\hat{V}\,''(\sigma^-)\right) = \pm \hat{\sigma}\,''(\gamma) \; . \tag{A.21}$$

A.3 Fans compared to shocks

Which solution traces out a steeper curve in the σ, V plane for a fixed front state, the loci of back states for a shock or for a fan? From (A.11) and (A.18), we write the ratio of the square of their slopes,

$$\begin{aligned}\left\{\frac{V_{shock}{}'(\sigma^-)}{V_{fan}{}'(\sigma^-)}\right\}^2 &= \frac{[\![\gamma]\!]^2 + 2[\![\gamma]\!][\![\sigma]\!]\hat{\gamma}\,'(\sigma^-) + \{[\![\sigma]\!]\hat{\gamma}\,'(\sigma^-)\}^2}{4\hat{\gamma}\,'(\sigma^-)[\![\sigma]\!][\![\gamma]\!]} \\ &= \frac{\{[\![\gamma]\!] - [\![\sigma]\!]\hat{\gamma}\,'(\sigma^-)\}^2}{4\hat{\gamma}'(\sigma^-)[\![\sigma]\!][\![\gamma]\!]} + 1 \\ &\geq 1\,.\end{aligned} \tag{A.22}$$

We see that states attainable by a fan never trace out a steeper curve in the σ, V plane than do states attainable by a shock with the same front state. Furthermore, their curves are tangent at the front state, as found by considering the limit $[\![\gamma]\!] \to 0$, $[\![\sigma]\!] \to 0$ of (A.22). Elsewhere, their slopes are identical when

$$\hat{\sigma}\,'(\gamma^-) = \frac{[\![\sigma]\!]}{[\![\gamma]\!]}\,. \tag{A.23}$$

Thus, the $\hat{V}(\sigma^-)$ curves for a shock and a fan have identical slopes when a line connecting the front and back states on the $\hat{\sigma}(\gamma)$ curve is tangent to $\hat{\sigma}(\gamma)$ at $\sigma = \sigma^-$. In particular, the slopes are identical for all back state stresses if the material has a linear $\hat{\sigma}(\gamma)$ relation.

A.4 Shock or fan? Uniqueness in single-phase solutions

In the previous two sections, we found that both fans and discontinuities can satisfy the balance equations for a given front state when the front and back states are of the same phase. Here, we review how to determine whether a shock or a fan is the admissible similarity solution. Figure A.3 summarizes the results.

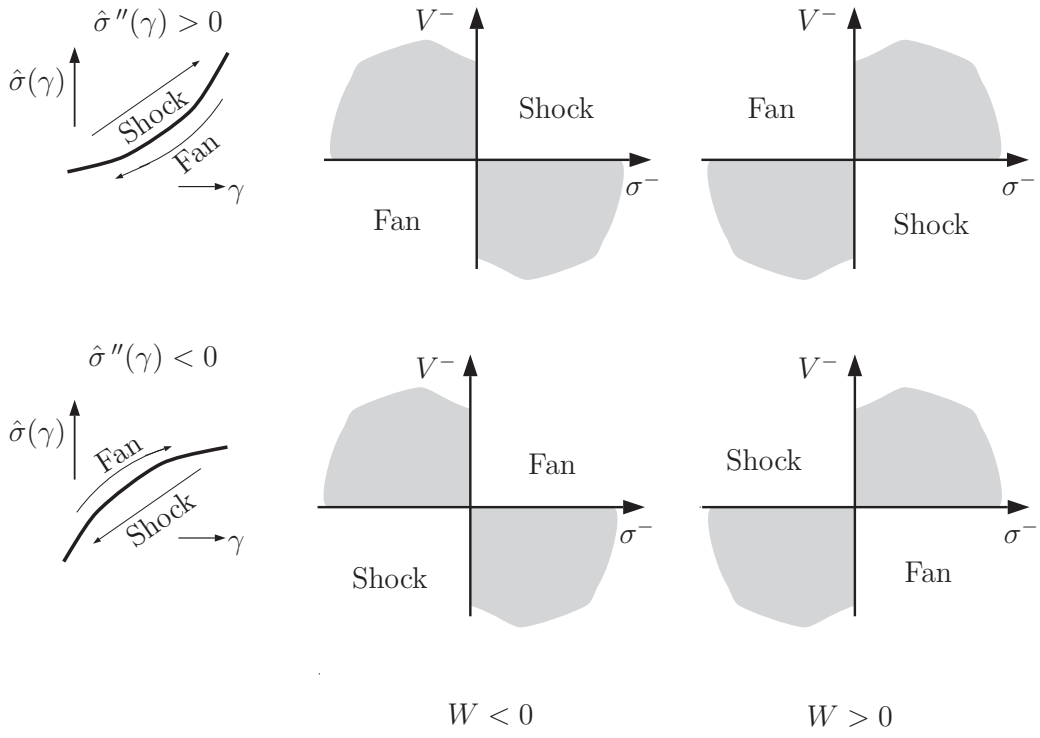

Figure A.3: The curvature of $\hat{\sigma}(\gamma)$ determines whether a shock or a fan is the unique similarity solution. The arrows in in the $\hat{\sigma}(\gamma)$ diagrams indicate valid solutions, pointing from (γ^+, σ^+) to (γ^-, σ^-).

First consider a fan. Recall that the propagation velocities of the front and the back of the fan are given by (A.16). To ensure that the front of the fan propagates faster than its back, we require that $\hat{\sigma}'(\gamma^-) \leq \hat{\sigma}'(\gamma^+)$. This leads to

$$\text{for a fan} \begin{cases} \text{if } \hat{\sigma}''(\gamma) > 0 & \text{then } \gamma^+ > \gamma^- \ , & \text{(A.24a)} \\ \text{if } \hat{\sigma}''(\gamma) < 0 & \text{then } \gamma^+ < \gamma^- \ . & \text{(A.24b)} \end{cases}$$

Now consider a shock. Enforcing the entropy inequality eliminates those strain jumps with the same sign as the changes in strain that can be obtained by fans,

(A.24a) and (A.24b), leaving

$$\text{for a shock} \begin{cases} \text{if } \hat{\sigma}''(\gamma) > 0 & \text{then } \gamma^+ < \gamma^- \ , & \text{(A.25a)} \\ \text{if } \hat{\sigma}''(\gamma) < 0 & \text{then } \gamma^+ > \gamma^- \ . & \text{(A.25b)} \end{cases}$$

Thus, within a single phase, the sign of the curvature of $\hat{\sigma}(\gamma)$ determines whether we have compressive shocks and rarefactive fans—the usual case—or vice versa.

Bibliography

[1] Rohan Abeyaratne, C. Chu, and R. D. James. Kinetics of materials with wiggly energies–theory and application to the evolution of twinning microstructures in a Cu-Al-Ni shape-memory alloy. *Philosophical Magazine A Physics of Condensed Matter Structure Defects and Mechanical Properties*, 73(2):457–497, 1996.

[2] Rohan Abeyaratne, S. J. Kim, and James K. Knowles. A one-dimensional continuum model for shape-memory alloys. *International Journal of Solids and Structures*, 31(16):2229–2249, Aug 1994.

[3] Rohan Abeyaratne and James K. Knowles. On the driving traction acting on a surface of strain discontinuity in a continuum. *Journal of the Mechanics and Physics of Solids*, 38(3):345–360, 1990.

[4] Rohan Abeyaratne and James K. Knowles. Implications of viscosity and strain-gradient effects for the kinetics of propagating phase boundaries in solids. *SIAM Journal on Applied Mathematics*, 51(5):1205–1221, 1991.

[5] Rohan Abeyaratne and James K. Knowles. Kinetic relations and the propagation of phase boundaries in solids. *Archive for Rational Mechanics and Analysis*, 114(2):119–154, 1991.

[6] Rohan Abeyaratne and James K. Knowles. On the propagation of maximally dissipative phase boundaries in solids. *Quarterly of Applied Mathematics*, 50(1):149–172, 1992.

[7] Rohan Abeyaratne and James K. Knowles. Wave-propagation in linear, bilinear and trilinear elastic bars. *Wave Motion*, 15(1):77–92, 1992.

[8] Rohan Abeyaratne and James K. Knowles. A continuum model of a thermoelastic solid capable of undergoing phase transitions. *Journal of the Mechanics and Physics of Solids*, 41(3):541–571, 1993.

[9] Rohan Abeyaratne and James K. Knowles. Dynamics of propagating phase boundaries: Adiabatic theory for thermoelastic solids. *Physica D*, 79(2-4):269–288, 1994.

[10] Rohan Abeyaratne and James K. Knowles. Dynamics of propagating phase boundaries: Thermoelastic solids with heat conduction. *Archive for Rational Mechanics and Analysis*, 126(3):203–230, 1994.

[11] Rohan Abeyaratne and James K. Knowles. Impact-induced phase transitions in thermoelastic solids. *Philosophical Transactions of the Royal Society of London Series A Mathematical, Physical and Engineering Sciences*, 355(1726):843–867, 1997.

[12] Rohan Abeyaratne and James K. Knowles. On the kinetics of an austenite→martensite phase transformation induced by impact in a Cu-Al-Ni shape-memory alloy. *Acta Materialia*, 45(4):1671–1683, 1997.

[13] Thomas J. Ahrens. Shock wave techniques for geophysics and planetary physics. In Charles G. Sammis and Thomas Louis Henyey, editors, *Geophysics, Laboratory measurements*, volume 24A of *Methods of experimental physics*, chapter 6, pages 185–235. Academic Press, Inc., 1986-1987.

[14] Thomas J. Ahrens. Equation of state. In Asay and Shahinpoor [17], chapter 4, pages 75–114.

[15] Thomas J. Ahrens, editor. *Mineral physics and crystallography: a handbook of physical constants*. American Geophysical Union, 1995.

[16] Thomas J. Ahrens and Mary L. Johnson. Shock wave data for minerals. In Ahrens [15], pages 143–184.

[17] James R. Asay and Mohsen Shahinpoor, editors. *High-pressure shock compression of solids*. Springer-Verlag, 1992.

[18] Michael F. Ashby and David R.H. Jones. *Engineering materials 1: an introduction to their properties and applications*. Pergamon Press, 1 edition, 1989.

[19] J. B. Bell, Phillip Colella, and J. A. Trangenstein. Higher-order Godunov methods for general systems of hyperbolic conservation laws. *Journal of Computational Physics*, 82(2):362–397, 1989.

[20] H. A. Bethe. The theory of shock waves for an arbitrary equation of state. Technical Report 545, Office of Scientific Research and Development, 1942.

[21] P. Chadwick. *Continuum Mechanics*. Halsted Press, 1976.

[22] G. Q. Chen, T. J. Ahrens, W. Yang, and J. K. Knowles. Effect of irreversible phase change on shock-wave propagation. *Journal of the Mechanics and Physics of Solids*, 47(4):763–783, April 1999.

[23] Weinong Chen. *Dynamic failure behavior of ceramics under multiaxial compression*. Ph.D. thesis, California Institute of Technology, 1995.

[24] Phillip Colella. A direct Eulerian MUSCL scheme for gas-dynamics. *SIAM Journal on Scientific and Statistical Computing*, 6(1):104–117, 1985.

[25] Phillip Colella and Paul R. Woodward. The piecewise parabolic method (PPM) for gas-dynamical simulations. *Journal of Computational Physics*, 54(1):174–201, 1984.

[26] Peter A. Darnell and Philip E. Margolis. *C, a software engineering approach*. Springer-Verlag, 3 edition, 1996.

[27] Thomas S. Duffy and Thomas J. Ahrens. Compressional sound velocity, equation of state, and constitutive response of shock-compressed magnesium oxide. *Journal of Geophysical Research Solid Earth*, 100(B1):529–542, 1995.

[28] J. E. Dunn. On Hugoniot structure. In Joanne L. Wegner and Frederick R. Norwood, editors, *Nonlinear waves in solids : IUTAM Symposium, University of Victoria*, volume 46 of *Applied Mechanics Reviews*. International Union of Theoretical and Applied Mechanics, Aug 1993.

[29] J. E. Dunn, Roger Fosdick, and Marshall Slemrod, editors. *Shock Induced Transitions and Phase Structures in General Media*, volume 52 of *The IMA Volumes in Mathematics and Its Applications Series*. Springer-Verlag, 1993.

[30] S. Eidelman, Phillip Colella, and R. P. Shreeve. Application of the Godunov method and its 2nd-order extension to cascade flow modeling. *AIAA Journal*, 22(11):1609–1615, 1984.

[31] J. L. Ericksen. Equilibrium of bars. *Journal of Elasticity*, 5(3-4):191–201, November 1975.

[32] J. D. Eshelby. The continuum theory of lattice defects. In Frederick Seitz and David Turnbull, editors, *Solid state physics*, volume 3, pages 79–144. Academic Press, 1956.

[33] J. D. Eshelby. Energy relations and the energy-momentum tensor in continuum mechanics. In Melvin F. Kanninen, William F. Adler, Alan R. Rosenfield, and Robert I. Jaffee, editors, *Inelastic behavior of solids*, pages 77–115. McGraw-Hill, 1970.

[34] J. D. Eshelby. The elastic energy-momentum tensor. *Journal of Elasticity*, 5:321, 1975.

[35] H. Fujisawa, E. Ito, O. Ohtaka, and T. Yamanaka. Elastic wave velocities of

high density pressure-induced amorphous GeO_2. *Geophysical Research Letters*, 21(14):1499–1502, July 1994.

[36] S. K. Godunov. A difference scheme for numerical computation of discontinuous solution of hydrodynamic equations. *Matematiceskij Sbornik*, 1959. In Russian.

[37] J. B. Goodman and R. J. LeVeque. A geometric approach to high-resolution TVD schemes. *SIAM Journal on Numerical Analysis*, 25(2):268–284, 1988.

[38] D. E. Grady and M. D. Furnish. Shock- and release-wave properties of MJ-2 grout. Sandia Report SAND88–1642, Sandia National Laboratories, 1988.

[39] A. Harten. High-resolution schemes for hyperbolic conservation-laws. *Journal of Computational Physics*, 49(3):357–393, 1983.

[40] H. Hattori. The Riemann problem for a van der Waals fluid with entropy rate admissibility criterion–nonisothermal case. *Journal of Differential Equations*, 65(2):158–174, 1986.

[41] H. Hattori. The Riemann problem for a van der Waals fluid with entropy rate admissibility criterion–isothermal case. *Archive for Rational Mechanics and Analysis*, 92(3):247–263, 1986.

[42] Charles Hirsch. *Numerical Computation of Internal and External Flows*, volume 2. Wiley, 1988.

[43] H. Horii and S. Nematnasser. Brittle failure in compression–splitting, faulting and brittle-ductile transition. *Philosophical Transactions of the Royal Society of London, Series A, Mathematical and Physical Sciences*, 319(1549):337–374, 1986.

[44] Ivor Horton. *The beginner's guide to C*. WROX Press, 1994.

[45] J. P. Itie, A. Polian, G. Calas, J. Petiau, A. Fontaine, and H. Tolentino. Pressure-induced coordination changes in crystalline and vitreous GeO_2. *Physical Review Letters*, 63(4):398–401, 1989.

[46] Ian Jackson and Thomas J. Ahrens. Shock-wave compression of vitreous and rutile- type GeO_2: A comparative study. *Physics of the Earth and Planetary Interiors*, 20:60–70, 1979.

[47] R. D. James. The propagation of phase boundaries in elastic bars. *Archive for Rational Mechanics and Analysis*, 73:125–158, 1980.

[48] R. D. James and M. Wuttig. Alternative smart materials. In V. V. Varadan and J. Chandra, editors, *Proceedings SPIE Symposium on "Mathematics and Control in Smart Structures"*, volume 2715, pages 420–426, 1996.

[49] R. D. James and Manfred Wuttig. Magnetostriction of martensite. *Philosophical Magazine A*, 77:1273–1299, 1998.

[50] R. Jeanloz. Differential finite-strain equations of state. In Syono and Manghnani [95], pages 147–156.

[51] Raymond Jeanloz and Richard Grover. Birch-Murnaghan and U_s-u_p equations of state. In S. C. Schmidt and N. C. Holmes, editors, *Shock Compression of Condensed Matter*, 1987.

[52] Qing Jiang. On the electromechanical response of electrically active materials. *Journal of Intelligent Material Systems and Structures*, 6(2):181–190, 1995.

[53] Qing Jiang and James K. Knowles. A thermoelastic model for an experiment involving a solid-solid phase transition. *Continuum Mechanics and Thermodynamics*, 7(1):97–110, 1995.

[54] Cornelis Klein and Cornelius S. Hurlbut, Jr. *Manual of mineralogy (after James D. Dana)*. Wiley, 21 edition, 1993.

[55] Elise Knittle. Static compression measurements of equations of state. In Ahrens [15], pages 65–74.

[56] James K. Knowles. On the dissipation associated with equilibrium shocks in finite elasticity. *Journal of Elasticity*, 9(2):131–158, 1978.

[57] P. D. Lax. *Hyperbolic systems of conservation laws and the mathematical theory of shock waves*. Number 11 in Regional Conference Series in Applied Mathematics. SIAM, Philadelphia, 1973.

[58] Yier Lin. *Dynamics of a continuum characterized by a non-convex energy function*. Ph.D. thesis, Massachusetts Institute of Technology, June 1993.

[59] J. Lipkin and J. R. Asay. Reshock and release of shock-compressed 6061-T6 aluminum. *Journal of Applied Physics*, 48(1):182–189, 1977.

[60] Lin-gun Liu and William A. Bassett. *Elements, oxides, silicates. High-pressure phases with implications for the Earth's interior*. Oxford University Press, 1986.

[61] Lin-gun Liu, William A. Bassett, and John Sharry. New high-pressure modifications of GeO_2 and SiO_2. *Journal of Geophysical Research*, 83(B5):2301–2306, May 1978.

[62] Mark T. Lusk. *Martensitic phase transitions with surface effects*. Ph.D. thesis, California Institute of Technology, 1992.

[63] E. N. Mamiya and J. C. Simo. Numerical-simulation of equilibrium shocks in maximally dissipative elastic-systems. 1. The one-dimensional case. *Journal of elasticity*, 35:175–211, 1994.

[64] E. N. Mamiya and J. C. Simo. Stress-induced phase transformations in elastic solids under anti-plane deformations: dissipative constitutive models and numerical simulation. *Computer Methods in Applied Mechanics and Engineering*, 133(1-2):47–77, 1996.

[65] Jerrold E. Marsden and Thomas J. R. Hughes. *Mathematical foundations of elasticity*. Dover, 1994.

[66] Stanley P. Marsh, editor. *LASL shock Hugoniot data*. Los Alamos series on dynamic material properties. University of California Press, 1980.

[67] R. Menikoff and B.J. Plohr. The Riemann problem for fluid-flow of real materials. *Reviews of Modern Physics*, 61(1):75–130, 1989.

[68] Marc A. Meyers. *Dynamic Behavior of Materials*. John Wiley & Sons, 1994.

[69] Gregory Hale Miller and Elbridge Gerry Puckett. A high-order Godunov method for multiple condensed phases. *Journal of Computational Physics*, 128(1):134–164, 1996.

[70] L. C. Ming and M. H. Manghnani. High-pressure phase transformations in vitreous and crystalline GeO_2 (rutile). *Physics of the Earth and Planetary Interiors*, 33(1):26–30, 1983.

[71] A. Navrotsky. Enthalpies of transformation among the tetragonal, hexagonal, and glassy modifications of GeO_2. *Journal of Inorganic and Nuclear Chemistry*, 33:1119–1124, 1971.

[72] C. S. Ngan and Lev Truskinovsky. Thermal trapping and kinetics of martensitic phase boundaries. *Journal of the Mechanics and Physics of Solids*, submitted.

[73] O. A. Oleinik. On the uniqueness of the generalized solution of the Cauchy problem for a nonlinear system of equations occuring in mechanics. *Uspekhi Matematicheskii Nauk*, 12(6):169–176, 1957. In Russian.

[74] Thomas J. Pence. On the mechanical dissipation of solutions to the Riemann problem for impact involving a two-phase elastic material. *Archive for Rational Mechanics and Analysis*, 117(1):1–52, 1992.

[75] Thomas J. Pence. The dissipation topography associated with solutions to a Riemann problem involving elastic materials undergoing phase transitions. In Dunn et al. [29], pages 169–183.

[76] Jean Paul Poirier. *Introduction to the physics of the Earth's interior*. Cambridge, 1991.

[77] Phoebus Rosakis. Compact zones of shear transformation in an anisotropic solid. *Journal of the Mechanics and Physics of Solids*, 40(6):1163–1195, 1992.

[78] Phoebus Rosakis. An equal-area rule for dissipative kinetics of propagating strain discontinuities. *SIAM Journal on Applied Mathematics*, 55(1):100–123, 1995.

[79] Phoebus Rosakis and James K. Knowles. Unstable kinetic relations and the dynamics of solid-solid phase transitions. *Journal of the Mechanics and Physics of Solids*, 45:2055–2081, 1997.

[80] C. G. Sammis and J. L. Dein. On the possibility of transformational superplasticity in the Earth's mantle. *Journal of Geophysical Research*, 79:2961–2965, 1974.

[81] James F. Sarver and F. A. Hummel. Alpha to Beta transition in germania quartz and a pressure-temperature diagram for GeO_2. *Journal of the American Ceramic Society*, 43(6):336, 1960.

[82] M. Shearer. The Riemann problem for a class of conservation laws of mixed type. *Journal of Differential Equations*, 46(3):426–443, 1982.

[83] M. Shearer. Nonuniqueness of admissible solutions of Riemann initial value problems for a system of conservation laws of mixed type. *Archive for Rational Mechanics and Analysis*, 93(1):45–59, 1986.

[84] M. Shearer. Dynamic phase transitions in a van der Waals gas. *Quarterly of Applied Mathematics*, 46(4):631–636, 1988.

[85] Miroslav Šilhavý. *The Mechanics and Thermodynamics of Continuous Media (Texts and Monographs in Physics)*. Springer Verlag, 1997.

[86] Stuart A. Silling. Finite difference modeling of phase changes and localization in elasticity. *Computer Methods in Applied Mechanics and Engineering*, 70(3):251–273, 1988.

[87] Stuart A. Silling. Dynamic growth of martensitic plates in an elastic-material. *Journal of Elasticity*, 28(2):143–164, 1992.

[88] M. Slemrod. Admissibility criteria for propagating phase boundaries in a van der Waals fluid. *Archive for Rational Mechanics and Analysis*, 81(4):301–315, 1983.

[89] M. Slemrod. Dynamic phase transitions in a van der Waals fluid. *Journal of Differential Equations*, 52(1):1–23, 1984.

[90] M. Slemrod and A. E. Tzavaras. A limiting viscosity approach for the Riemann problem in isentropic gas-dynamics. *Indiana University Mathematics Journal*, 38(4):1047–1074, 1989.

[91] Daniel J. Steinberg. Equation of state and strength properties of selected materials. Technical Report UCRL-MA-106439, Lawrence Livermore National Laboratory, Livermore, CA 94551, 1996.

[92] E.M. Stolper and Thomas J. Ahrens. On the nature of pressure-induced coordination changes in silicate melts and glasses. *Geophysical Research Letters*, 14(12):1231–1233, 1987.

[93] K. Suito, M. Miyoshi, T. Saskura, and H. Fujisawa. Elastic properties of obsidian, vitreous SiO_2 and vitreous GeO_2. In Murli H. Manghnani and Yasuhiko Syono, editors, *High Pressure Research in Mineral Physics*, pages 493–501. Terra Scientific Publishing Company / American Geophysical Union, 1987.

Third U.S.-Japan Seminar on High-Pressure Research in Mineral Physics held in Kahuku, Oahu, Hawaii, January 13-16, 1986.

[94] J. W. Swegle. Irreversible phase transitions and wave propagation in silicate geologic materials. *Journal of Applied Physics*, 68(4):1563–1579, August 1990.

[95] Yasuhiko Syono and Murli H. Manghnani, editors. *High pressure research: application to earth and planetary sciences*. Terra Scientific Publishing Company / American Geophysical Union, 1992.

[96] R. Tickle, R. D. James, T. Shield, P. Schumacher, M. Wuttig, and V. V. Kokorin. Ferromagnetic shape memory in the NiMnGa system. *Journal of Applied Physics*, Submitted.

[97] Lev Truskinovskii. Dynamics of non-equilibrium phase boundaries in a heat conducting non-linearly elastic medium. *PMM Journal of Applied Mathematics and Mechanics*, 51(6):777–784, 1987.

[98] L. Truskinovsky. Kinks versus shocks. In Dunn et al. [29], pages 185–229.

[99] Lev Truskinovsky. About the normal growth approximation in the dynamical theory of phase transitions. *Continuum Mechanics and Thermodynamics*, 6(3):185–208, 1994.

[100] Lev Truskinovsky and Giovanni Zanzotto. Ericksen's bar revisited: Energy wiggles. *Journal of the Mechanics and Physics of Solids*, 44(8):1371–1408, 1996.

[101] Sergio Turteltaub. *Dynamics of phase transformations in thermoelastic solids*. Ph.D. thesis, California Institute of Technology, June 1997.

[102] Bram van Leer. Towards the ultimate conservative difference scheme. IV. A new approach to numerical convection. *Journal of Computational Physics*, 23:276–299, 1977.

[103] Bram van Leer. Towards the ultimate conservative difference scheme. V. A second-order sequel to Godunov's method. *Journal of Computational Physics*, 32:101–136, 1979.

[104] Herbert Wang and Gene Simmons. Elasticity of some mantle crystal structures 2. Rutile GeO_2. *Journal of Geophysical Research*, 78(8):1262–1273, Mar 1973.

[105] George H. Wolf, Shuju Wang, Chris A. Herbst, Dan J. Durben, William F. Oliver, Z. C. Kang, and Kris Halvorson. Pressure induced collapse of the tetrahedral framework in crystalline and amorphous GeO_2. In Syono and Manghnani [95], pages 503–517.

[106] Wenbo B. Yang. Personal communication.

[107] Wenbo B. Yang and Thomas J. Ahrens. Personal communication. Unpublished experiments conducted 1994-1995.

[108] Xiaoguang Zhong. *Continuum dynamics of solid-solid phase transitions*. Ph.D. thesis, California Institute of Technology, June 1995.

[109] Xiaoguang Zhong, Thomas Y. Hou, and Philippe G. LeFloch. Computational methods for propagating phase boundaries. *Journal of Computational Physics*, 124(1):192–216, Mar 1 1996.